May 2019

Simulations of the 3-Dimensional Velocity Distribution of Halo Weakly Interacting Massive Particles for Directional Dark Matter Detection Experiments

Chung-Lin Shan

Physics Division, National Center for Theoretical Sciences
No. 101, Sec. 2, Kuang-Fu Road, Hsinchu City 30013, Taiwan, R.O.C.

E-mail: clshan@phys.nthu.edu.tw

Abstract

In this paper, as a preparation of developing data analysis procedures for using 3-dimensional information offered by directional Dark Matter (DM) detection experiments, we study the patterns of the angular distribution of the Monte Carlo–generated 3-D velocity of halo Weakly Interacting Massive Particles (WIMPs) as well as apply the Bayesian fitting technique to reconstruct the radial distribution of the 3-D WIMP velocity. Besides the diurnal modulation of the angular WIMP velocity distribution, the so–called "directionality" of DM signals proposed in literature, we will also demonstrate possible "annual" modulations of both of the angular and the radial distributions of the 3-D WIMP velocity. Our Bayesian reconstruction results of (the annual modulation of) the radial WIMP velocity distribution will also be discussed in detail. For readers' reference, the angular distribution patterns of the 3-D WIMP velocity in the "laboratory (location)–dependent" reference frames of several underground laboratories are given in the Appendix.

Contents

1 Introduction

So far Weakly Interacting Massive Particles (WIMPs) χ arising in several extensions of the Standard Model of particle physics are still one of the most favorite candidates for cosmological Dark Matter (DM). In the last (more than) three decades, a large number of experiments has been built and is being planned to search for different WIMP candidates by direct detection of the scattering recoil energy of ambient WIMPs off target nuclei in low–background underground laboratory detectors (see Refs. [1, 2, 3, 4, 5, 6] for reviews).

Among these direct detection experiments measuring recoil energies deposited in detectors, the "directional" detection of Galatic DM particles has been proposed more than one decade to be a promising experimental strategy for discriminating signals from backgrounds by using additional 3-dimensional information (the recoil tracks and/or the head–tail senses) of (elastic) WIMP–nucleus scattering events (see Refs. [7, 8, 9, 10, 11, 12, 13]). Several experimental collaborations investigate different detector materials and techniques and have achieved recently great progress [11, 13].

For instance, as the first directional detection experiment, the DRIFT Collab. demonstrated the reconstruction ability of the range component signature by using their DRIFT–IId detector with a gas mixture of CS_2 + CF_4 + O_2 [14, 15, 16, 17, 18, 19, 20, 21]. Meanwhile, the MIMAC experiment started with ^{3}He as detector material for searching for light WIMPs [22, 23, 24], but turned later to develop micromegas μTPC detetor with a gas mixture of CF_4 + CHF_3 + C_4H_{10} and also demonstrated the ability of determining 3-D positions of primary ionization electrons for reconstructing in turn the track of the recoiled nucleus [25, 26, 27, 28, 29].

In contrast to the use of gas mixtures, pure CF_4 gas has also been studied by the NEWAGE Collab. with also the μTPC technique [30, 31, 32] as well as by the DMTPC Collab. using an optical (CCD pixel image) readout combined with a transient charge readout [33, 34, 35, 36, 37, 38, 39]. Recently, while the D3 Collab. considers SF_6 gas with sulfur as target nucleus [40, 41], the NEWSdm Collab. investigates the nuclear emulsion technique with AgBr(I) as detector material [42, 43, 44]. Furthermore, a larger CYGNUS Collab. has been built for combining members, efforts and achievements from different experimental collaborations [45].

The basic concept of directional Dark Matter detection is based on the rotation of the Earth. As sketched in Figs. 1, there are two kinds of possible "diurnal" modulation of WIMP signals to observe: the diurnal modulation of the main incident direction of WIMP events, the so–called "directionality" of the WIMP wind, as well as that of the number (scattering rate) of WIMP events caused by Earth's shielding of the WIMP flux. Directional DM detection experiments aim hence, as the first step, to identify positive *modulated anisotropic* WIMP signals and discriminate them from theoretically (approximately) isotropic background events.

Once positive WIMP signals could be observed and more and more events could be accumulated, reconstructions of particle and/or astronomical properties of halo WIMPs would be considered as the next stage. For this purpose, different methods have been developed. In literature, a large number of earlier studies is focused on (the use of) the distribution patterns of the nuclear recoil energy and the WIMP flux, e.g., works done by N. Bozorgnia, G. B. Gelmini and P. Gondolo [46, 47, 48, 49] as well as by B. Morgan, A. M. Green, C. A. J. O'Hare and B. J. Kavanagh [50, 51, 52, 53, 54, 55, 56]. Meanwhile, J. Billard, F. Mayet and D. Santos developed their Bayesian analysis, which considers not only the 3-D velocity dispersion of the local WIMP velocity distribution and the main direction of the recoiled nucleus, but also the WIMP mass and the WIMP–nucleon cross section as fitting parameters simultaneously [57, 58, 59]. Moreover, some authors focused on theoretically analyzing of the (local) Dark Matter velocity distribution, e.g., works done by S. K. Lee and A. H. G. Peter [60, 61].

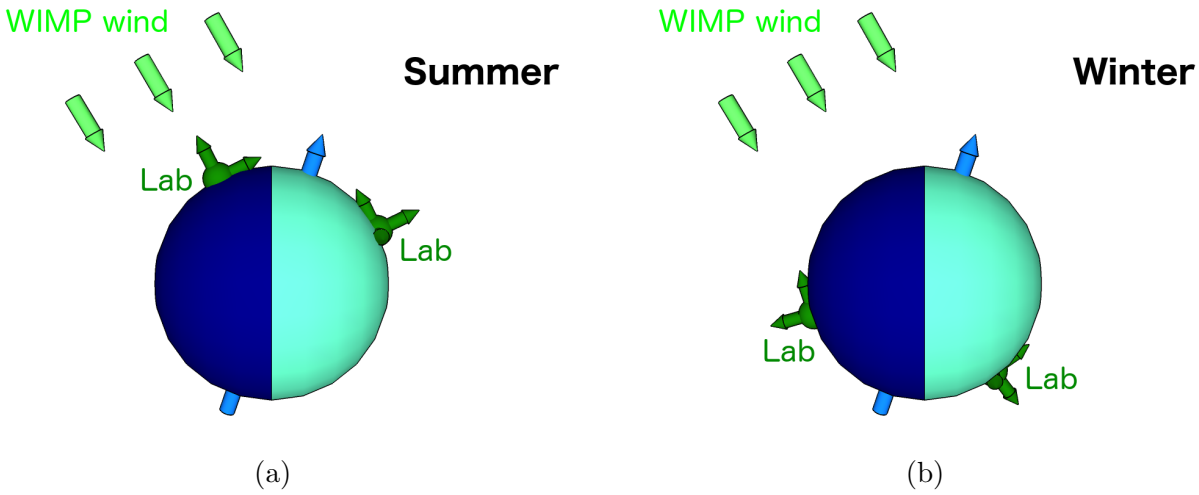

(a) (b)

Figure 1: Sketches of the basic concepts of directional Dark Matter detection: (a) the diurnal modulation of the main direction of incident WIMPs, the so–called "directionality" of the WIMP wind, for a laboratory located in the Northern Hemisphere (in Summer); (b) except of the directionality of the WIMP wind, the event number of WIMP signals observed at a laboratory located in the Southern Hemisphere (in Winter) could also have the diurnal modulation caused by the Earth's shielding of the WIMP flux. The darkened/lightened (left/right–hand) spheres indicate that the laboratory of interest is in the night/day. See Figs. 10 and 11 as well as the text there for more details.

Besides these works, in this paper, as a preparation for our future study on the development of data analysis procedures for using and/or combining 3-D information offered by directional detection experiments, to, e.g., reconstruct the 3-dimensional WIMP velocity distribution, we investigate the patterns of the angular distribution of the Monte Carlo–generated 3-dimensional WIMP velocity as well as apply the Bayesian fitting technique to reconstruct the radial distribution (magnitude) of the 3-D WIMP velocity. Not only the diurnal modulation of the angular WIMP velocity distribution mentioned above, we will also demonstrate possible "annual" modulations of both of the angular and the radial distributions of the 3-D WIMP velocity.

The remainder of this paper is organized as follows. In Sec. 2, we describe all needed tools for our simulations and analysis procedures presented in this paper: our definitions of different celestial coordinate systems, the event generation process based on the Monte Carlo method, as well as the Bayesian fitting procedure used for reconstructing the radial component of the 3-dimensional WIMP velocity distribution. Then we present at first the (annual/diurnal modulated) patterns of the angular WIMP velocity distribution in different celestial coordinate systems one by one in Sec. 3 and the reconstructions of (the annual modulation of) the radial WIMP velocity distribution in both of the Equatorial and the Galactic coordinate systems in Sec. 4. In Sec. 5, we raise the total number of generated WIMP events and demonstrate the simulation results with an improved analysis resolution. We conclude in Sec. 6. Some technical details for our analyses and a summary of the laboratory–dependent simulation results will be given in Appendix.

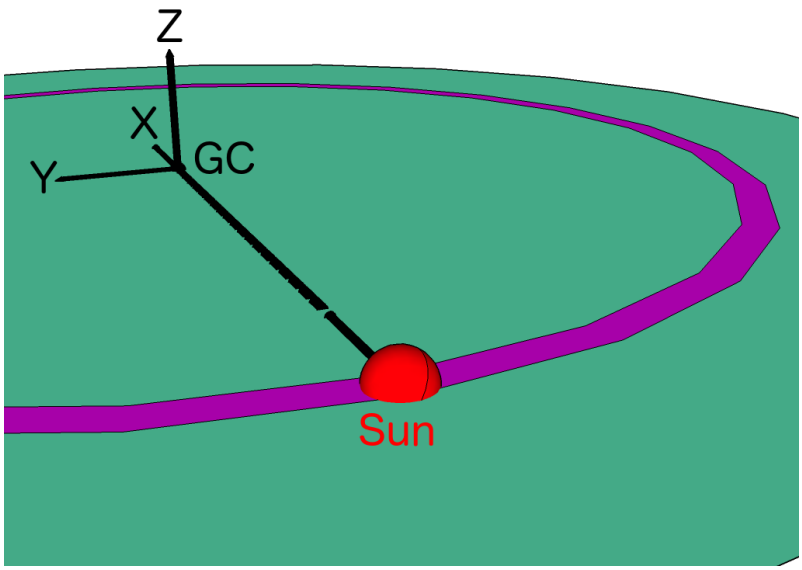

Figure 2: The sketch of the definition of the (black) Galactic coordinate system: the origin is at the Galactic Center (GC) (not the center of the Sun), the primary direction (the $\mathbf{X}_{\rm G}$–axis) points from the Solar center to the approximate center of our Galaxy, the $\mathbf{Z}_{\rm G}$–axis points to the Galactic North Pole (GNP), and the $\mathbf{Y}_{\rm G}$–axis is then defined by the right–handed convention. The fundamental $(\mathbf{X}_{\rm G} - \mathbf{Y}_{\rm G})$ plane is the approximate Galactic plane and the magenta circular band indicates an approximate path of the orbital motion of the Solar system in the Galaxy.

2 Toolbox

In this section, we describe all tools needed in our simulations and data analyses presented in this paper. At first we give our definitions of different celestial coordinate systems considered for demonstrating the 3-dimensional WIMP velocity distribution. Then we describe the event generation process based on the Monte Carlo method as well as the Bayesian fitting procedure used for reconstructing the radial distribution of the 3-D WIMP velocity.

2.1 Our definitions of different celestial coordinate systems

In this subsection, we give our definitions of four "laboratory–independent" (Galactic, Ecliptic, Equatorial and Earth) and two "laboratory–dependent" (horizontal and laboratory) coordinate systems[1]. The analytic and/or the numerical forms of all transformation matrices between these coordinate systems will be derived in detail in Appendix A.

2.1.1 Definition of the Galactic coordinate system

As shown in Fig. 2, the Galactic coordinate system in our simulations presented in this paper is defined as follows: the origin is at the Galactic Center (GC), the primary direction (the $\mathbf{X}_{\rm G}$–axis) points from the Solar center to the approximate center of our Galaxy, and the $\mathbf{Z}_{\rm G}$–axis points to the Galactic North Pole (GNP). As usual, the right–handed convention is used for defining the $\mathbf{Y}_{\rm G}$–axis and the fundamental $(\mathbf{X}_{\rm G} - \mathbf{Y}_{\rm G})$ plane is the approximate Galactic plane [62]. Note

[1] Note that some of our definitions are different from their astronomical conventions, but would be more convenient for our data analyses, in particular, for comparing results obtained by using data from different underground laboratories.

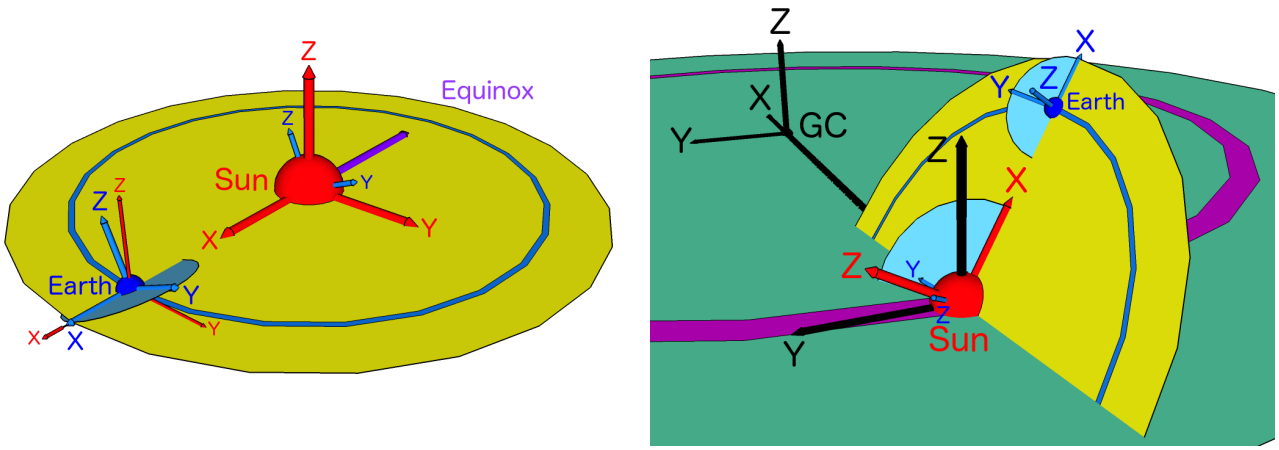

(a) (b)

Figure 3: (a) The sketch of the definitions of the (red) Ecliptic and the (blue) Equatorial coordinate systems: their origins are located at the center of the Sun and that of the Earth, respectively, the common primary direction (the $\mathbf{X}_{\rm S}/\mathbf{X}_{\rm Eq}$–axis) is the direction pointing from the Solar center to that of the Earth at 12 midnight (the end) of the date of the vernal equinox, the $\mathbf{Z}_{\rm S}$– and the $\mathbf{Z}_{\rm Eq}$–axes are perpendicular to the (yellow) Ecliptic or the (blue) Equatorial plane, respectively, and their $\mathbf{Y}_{\rm S}$– and $\mathbf{Y}_{\rm Eq}$–axes are then defined as usual by the right–handed convention. The blue circular band indicates the Earth's orbit around the Sun. The purple arrow points to the celestial Equinox, which is the conventional (common) primary direction of the Ecliptic and the Equatorial coordinate systems. (b) The sketch of the relative orientations between the (black) Galactic, the (red) Ecliptic and the (blue) Equatorial coordinate systems (on the date of the vernal equinox).

that, as discussed in detail in Appendix A.3.3 and sketched in Fig. A5, the direction of the Solar movement towards the CYGNUS constellation is *not parallel to*, but only *approximately along* the $\mathbf{Y}_{\rm G}$–axis of the Galactic coordinate system.

2.1.2 Definitions of the Ecliptic and the Equatorial coordinate systems

As shown in Fig. 3(a), the Ecliptic and the Equatorial coordinate systems are defined as follows: their origins are located at the center of the Sun and that of the Earth, respectively, the common primary direction (the $\mathbf{X}_{\rm S}/\mathbf{X}_{\rm Eq}$–axis) is the direction pointing from the Solar center to that of the Earth at 12 midnight (the *end*) of the date of the vernal equinox[2], the $\mathbf{Z}_{\rm S}$– and the $\mathbf{Z}_{\rm Eq}$–axes are perpendicular to the Ecliptic or the Equatorial plane, respectively, and their $\mathbf{Y}_{\rm S}$– and $\mathbf{Y}_{\rm Eq}$–axes are then defined as usual by the right–handed convention.

Additionally, in Fig. 3(b), we sketch the relative orientations between the Galactic, the Ecliptic and the Equatorial coordinate systems (on the date of the vernal equinox). Note that, the Ecliptic and the Equatorial coordinate systems only move, but do not rotate with the Sun nor with the Earth.

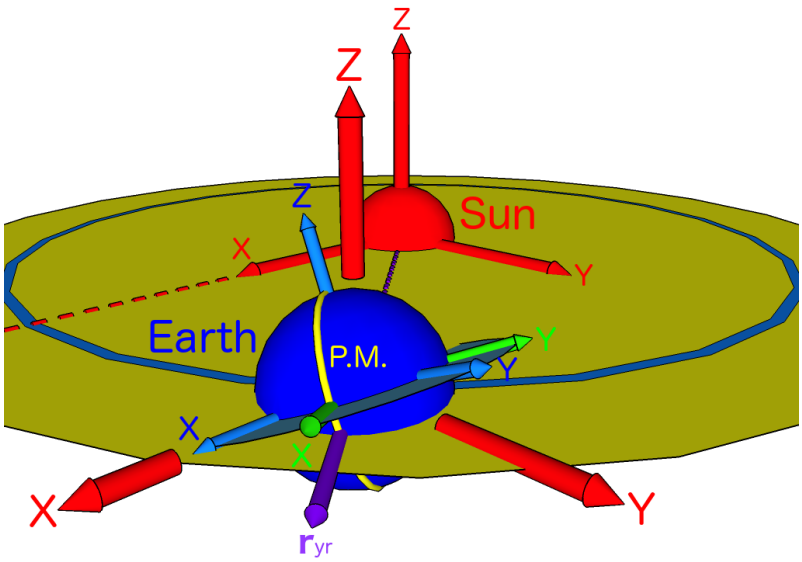

Figure 4: The sketch of the definition of the (light–green) Earth coordinate system: while the origin is also located at the Earth's center and the $\mathbf{Z}_{\rm E}$–axis is still the Earth's north polar axis, the primary direction (the $\mathbf{X}_{\rm E}$–axis) points now from the Earth's center to the (yellow) Prime Meridian (the longitude 0°) at 12 midnight (i.e., the moment when the Prime Meridian passes the purple arrow pointing from the Solar center to that of the Earth, $\mathbf{r}_{\rm yr}$) of "each single" day. Finally, the fundamental $(\mathbf{X}_{\rm E} - \mathbf{Y}_{\rm E})$ plane is also the (blue) Equatorial plane and the right–hand convention is used to define the $\mathbf{Y}_{\rm E}$–axis (see also Figs. 5 and 6). The (red) Ecliptic and the (blue) Equatorial coordinate systems as well as the (blue) Earth's orbit around the Sun are also given here.

2.1.3 Definition of the Earth coordinate system

As shown in Fig. 4, we define the Earth coordinate system as follows: while the origin is also located at the Earth's center and the $\mathbf{Z}_{\rm E}$–axis is still the Earth's north polar axis, the primary direction (the $\mathbf{X}_{\rm E}$–axis) points now from the Earth's center to the Prime Meridian (the longitude 0°) at 12 midnight (i.e., the moment when the Prime Meridian passes the direction pointing from the Solar center to that of the Earth) of "each single" day. Finally, the fundamental $(\mathbf{X}_{\rm E} - \mathbf{Y}_{\rm E})$ plane is also the Equatorial plane and the right–hand convention is used to define the $\mathbf{Y}_{\rm E}$–axis (see also Figs. 5 and 6).

Note that, the Earth coordinate system is fixed but *rotates* with the Earth, during the Earth's orbital motion around the Sun. Hence, in our simulations presented in this paper, we consider the position of the Earth coordinate system at 12 midnight (the *beginning*) of (the Coordinated Universal Time (UTC) of) each single "Solar" day[3]. This means then that our Earth coordinate system changes daily and *discretely* (see Table 1 for the summary of the styles of the movement and the rotation of different coordinate systems).

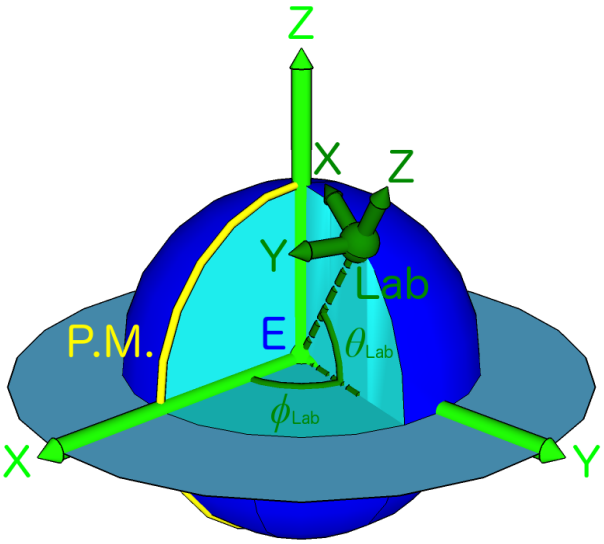

Figure 5: The sketch of the definition of the (dark–green) horizontal coordinate system: the origin is the geographic location of the laboratory of interest at 12 midnight (the beginning) of (the UTC time of) each single day, the primary direction (the $\mathbf{X}_{\rm H}$–axis) and the $\mathbf{Z}_{\rm H}$–axis point towards north and the zenith, respectively, and the right–handed convention is used for defining the $\mathbf{Y}_{\rm H}$–axis. Our (light–green) Earth coordinate system is also given here and $\phi_{\rm Lab}$ and $\theta_{\rm Lab}$ indicate the longitude and the latitude of the location of the laboratory, respectively.

2.1.4 Definition of the horizontal coordinate system

Moreover, for demonstrating (the annual modulation of) the angular distribution of the 3-D WIMP velocity observed in a specified underground laboratory, we define first the horizontal coordinate system with the origin at the geographic location of the laboratory of interest at 12 midnight (the *beginning*) of (the UTC time of) each single day, the primary direction (the $\mathbf{X}_{\rm H}$–axis) and the $\mathbf{Z}_{\rm H}$–axis pointing towards north and the zenith, respectively, and the right–handed convention for defining the $\mathbf{Y}_{\rm H}$–axis (see Fig. 5). Note that, as the Earth coordinate system, for each single Solar day, our horizontal coordinate system is fixed at 12 midnight (the beginning) of the day and thus changes daily and discretely (see Table 1 for the summary of the movement and the rotation styles of different coordinate systems).

2.1.5 Definition of the laboratory coordinate system

Finally, considering the long running time of (directional) direct Dark Matter detection experiments as well as for identifying the diurnal modulation of the angular WIMP velocity distribution, we define, besides the discretely variated horizontal coordinate system, the laboratory coordinate system by taking into account the *instantaneous* measuring time of each recorded WIMP scattering event. This means that our laboratory coordinate system is defined basically the same as the horizontal coordinate system, but rotates with the laboratory of interest around the Earth's north polar ($\mathbf{Z}_{\rm Eq}/\mathbf{Z}_{\rm E}$–)axis instantaneously by an angle of $\omega t_{\rm PM}$ (see Fig. 6), where

[2] Note that, in our simulations presented in this paper, this date has been fixed exactly as the 79th day (the May 20th) of a 365-day year.

[3] Originally, the Earth coordinate system was defined for connecting the horizontal and the laboratory coordinate systems (defined in Secs. 2.1.4 and 2.1.5) with the Equatorial and the Ecliptic coordinate systems [63].

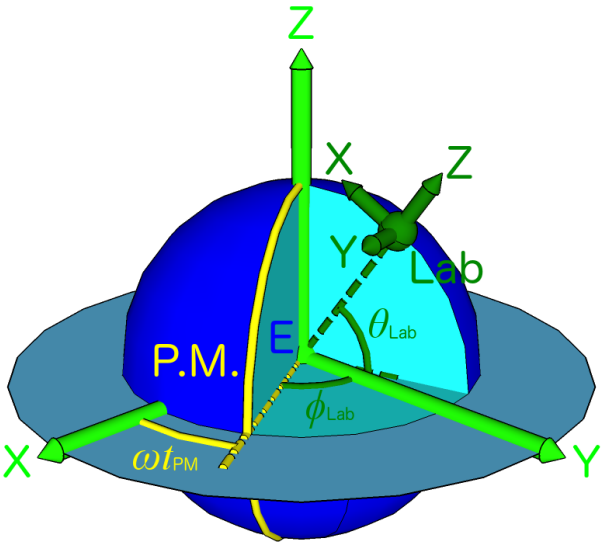

Figure 6: The sketch of the definition of the (dark–green) laboratory coordinate system: the same as the horizontal coordinate system in Fig. 5, but rotates with the laboratory of interest around the Earth's north polar ($\mathbf{Z}_{\rm Eq}/\mathbf{Z}_{\rm E}$–)axis *instantaneously*. $\omega t_{\rm PM}$ indicates the rotated angle of the (yellow) Prime Meridian from 12 midnight (the beginning) of (the UTC time of) each single day. Our (light–green) Earth coordinate system is also given here.

we define

$$\omega \equiv \frac{2\pi}{1\ \text{day}}\,, \tag{1}$$

and $t_{\rm PM}$ indicates the fractional part of the measuring UTC time t of each recorded WIMP event in unit of day. Note that, our laboratory coordinate system changes (rotates around the Earth's north polar axis) *event by event*.

In Table 1, we summarize the styles of the movement and the rotation of all six celestial coordinate systems defined in our simulations presented in this paper. Note that, except of the "linear + orbital $\rightarrow$ spiral" motion of the Equatorial coordinate system, the Earth, the horizontal and the laboratory coordinate systems are fixed on the Earth and only rotate around the Earth's north polar (i.e., $\mathbf{Z}_{\rm Eq}/\mathbf{Z}_{\rm E}$–)axis. Hence, the radial component (magnitude) of the 3-D WIMP velocity distribution in these three coordinate systems are equal to that in the Equatorial coordinate system.

2.2 Event generation in the Galactic coordinate system

In this subsection, we describe the generation procedure of the 3-dimensional information on the WIMP velocity (the magnitude and the direction as well as the measuring time) in the Galactic coordinate system based on the Monte Carlo method. These generated 3-D WIMP velocities will be transformed into different celestial coordinate systems for data analyses and distribution reconstructions presented in Secs. 3, 4, and 5 as well as in Appendices B and C.

Coordinate system	Movement	Rotation	Style
Galactic	$\times$	$\times^{\dagger}$	—
Ecliptic	$\surd$	$\times$	Orbital $\rightarrow$ approximately linear
Equatorial	$\surd$	$\times$	Linear + orbital $\rightarrow$ spiral
Earth	$\times^{\ddagger}$	$\surd$	Daily and discrete
Horizontal	$\times^{\ddagger}$	$\surd$	Daily and discrete
Laboratory	$\times^{\ddagger}$	$\surd$	Instantaneous and continuous

Table 1: The summary of the styles of the movement and the rotation of all six celestial coordinate systems defined in our simulations presented in this paper.
†: The tiny angle swept by the connection between the Solar and the Galactic centers during the orbital motion of the Solar system in the Galaxy is ignored here.
‡: Fixed on the Earth and combined additionally with the "linear + orbital $\rightarrow$ spiral" movement of the Equatorial coordinate system.

2.2.1 Radial component of the 3-D WIMP velocity distribution

For generating the radial component (magnitude) of the 3-D WIMP velocity in the Galactic coordinate system, we consider the simple Maxwellian velocity distribution truncated at the Galactic escape velocity [1]:

$$f_{1,\mathrm{Gau}}(v) = \begin{cases} N_{\mathrm{Gau}} \left(\dfrac{v^2}{v_0^3}\right) e^{-v^2/v_0^2}\,, & \text{for } v \leq v_{\mathrm{esc}}\,, \\ 0\,, & \text{for } v > v_{\mathrm{esc}}\,, \end{cases} \tag{2}$$

with the normalization constant

$$N_{\mathrm{Gau}} = \left[\left(\frac{\sqrt{\pi}}{4}\right) \mathrm{erf}\left(\frac{v_{\mathrm{esc}}}{v_0}\right) - \left(\frac{v_{\mathrm{esc}}}{2v_0}\right) e^{-v_{\mathrm{esc}}^2/v_0^2}\right]^{-1}\,, \tag{3}$$

where $v_0 \simeq 220$ km/s is the Solar orbital speed around the Galactic center and 498 km/s $< v_{\mathrm{esc}} < 608$ km/s is the escape velocity from our Galaxy at the position of the Solar system [64].

In Fig. 7, we show the radial distribution of the 3-dimensional WIMP velocity in the Galactic coordinate system generated by Eqs. (2) to (6). One entire year (0 to 365 day) for the measuring time of WIMP events has been considered. 50 total events on average in one experiment have been generated and binned into 8 bins. 5,000 experiments have been simulated. The solid red curve is the generating simple Maxwellian velocity distribution $f_{1,\mathrm{Gau}}(v)$ given in Eq. (2) with the Solar Galactic velocity $v_0 = 220$ km/s, while the dashed black histogram shows the generated WIMP velocities and the thin vertical dashed black lines indicate the 1σ Poisson statistical uncertainties on the recorded event numbers in the v–bins. The Galactic escape velocity has been set as $v_{\mathrm{esc}} = 550$ km/s. Not surprisingly, the recorded event numbers (averaged by all simulated experiments) in all v–bins match our generating simple Maxwellian velocity distribution perfectly.

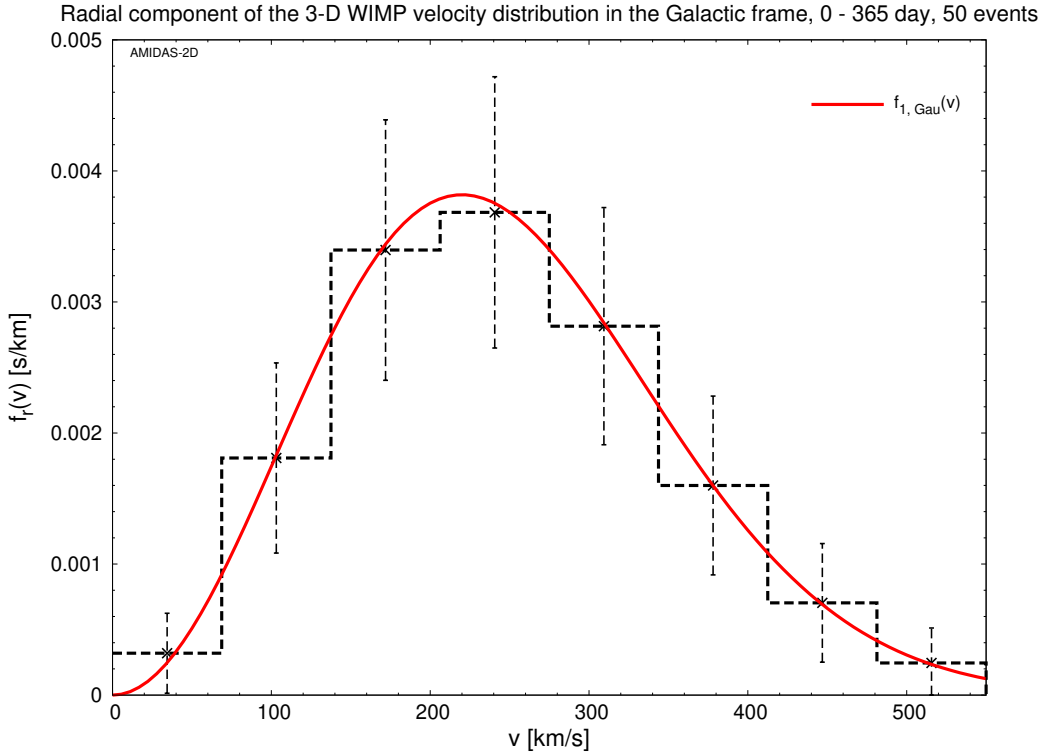

Figure 7: The radial distribution of the 3-dimensional WIMP velocity in the Galactic coordinate system generated by Eqs. (2) to (6). 50 total events on average in one experiment (in one entire year) have been generated and binned into 8 bins. The solid red curve is the generating simple Maxwellian velocity distribution $f_{1,\mathrm{Gau}}(v)$ given in Eq. (2) with the Solar Galactic velocity $v_0 = 220$ km/s, while the dashed black histogram shows the generated WIMP velocities and the thin vertical dashed black lines indicate the 1σ Poisson statistical uncertainties on the recorded event numbers in the v–bins. The Galactic escape velocity has been set as $v_{\mathrm{esc}} = 550$ km/s. See the text for further details.

2.2.2 Angular component of the 3-D WIMP velocity distribution

Since the simplest model of the Galactic Dark Matter halo is assumed to be isothermal, spherical and isotropic, the angular distribution of the 3-D WIMP velocity in the Galactic coordinate system has been considered to be isotropic and thus the velocity directions (i.e., the ϕ– and θ–angles in the longitude and the latitude directions, respectively) are generated with a constant probability in our simulations:

$$f_{\phi,\mathrm{G}}(\phi) = 1\,, \qquad \phi \in (-\pi,\ \pi]\,, \tag{4}$$

and

$$f_{\theta,\mathrm{G}}(\theta) = 1\,, \qquad \theta \in [-\pi/2,\ \pi/2]\,. \tag{5}$$

In Fig. 8, we show the angular distribution of the 3-dimensional WIMP velocity in the Galactic coordinate system generated by Eqs. (2) to (6). 50 total events on average in one experiment have been binned into 6 $\times$ 6 bins in the longitude and the latitude directions, respectively. The horizontal color bar on the top of the plot indicates the mean value of the

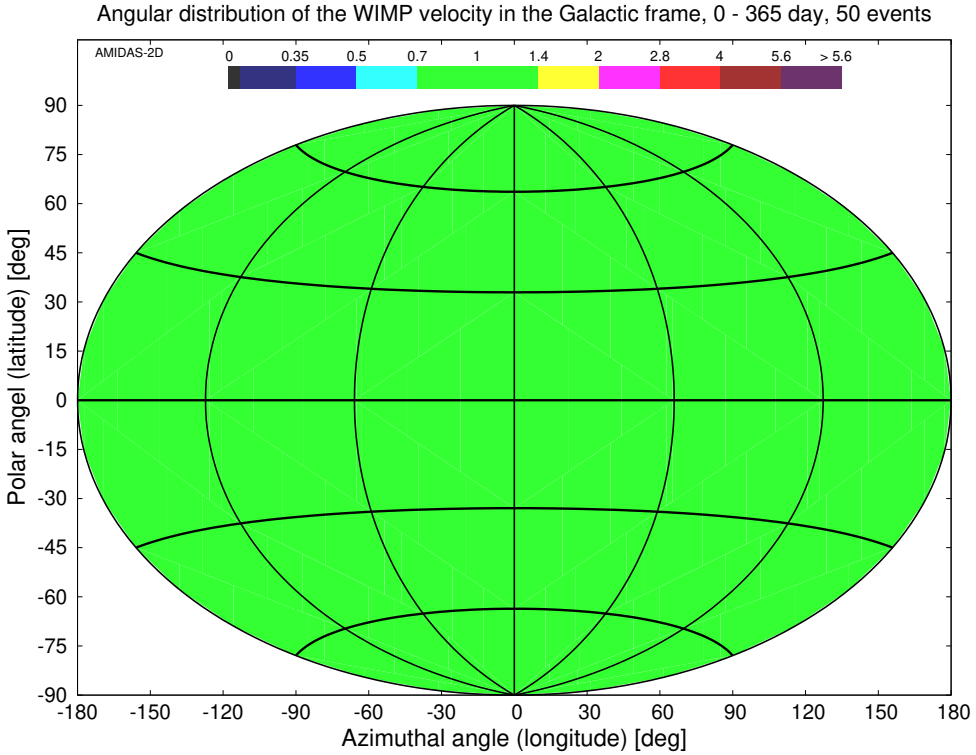

Figure 8: The angular distribution of the 3-dimensional WIMP velocity in the Galactic coordinate system generated by Eqs. (2) to (6). 50 total events on average in one experiment (in one entire year) have been generated and binned into 6 × 6 bins in the longitude and the latitude directions, respectively. The horizontal color bar on the top of the plot indicates the mean value of the recorded event number (averaged over all simulated experiments) in each angular bin in unit of the all–sky average value (50 events / 36 bins ≅ 1.39 events/bin here). See the text for further details.

recorded event number (averaged over all simulated experiments) in each angular bin in unit of the all–sky average value (50 events / 36 bins ≅ 1.39 events/bin here).

As expected, the event numbers in all angular bins are between 70% and 1.4 times of the all–sky average value (0.97 events/bin to 1.94 events/bin). More exactly, with $\mathcal{O}(50)$ total WIMP events, the maximal perturbation of the angular distribution of the simulated isotropic WIMP halo would be less than ±2.5% of the all–sky average.

2.2.3 Measuring time and observation periods/shifts of WIMP events

Although due to the orbital motion of the Earth around the Sun and the Earth's rotation around its axis, the theoretically predicted radial and angular WIMP velocity distributions as well as the event rate for WIMP–nucleus scattering should be time–dependent (the so–called "annual modulation") [65], in the Galactic point of view, WIMP–nucleus scattering events should be observed randomly and constantly. Hence, in our simulations we considered a constant probability for generating the measuring UTC time of the recorded WIMP scattering events:

$$f_{t,\mathrm{G}}(t) = 1\,, \qquad t \in [t_{\mathrm{start}},\ t_{\mathrm{end}}]\,. \tag{6}$$

For generating the WIMP events shown in Figs. 7 and 8, the observation period has been set as

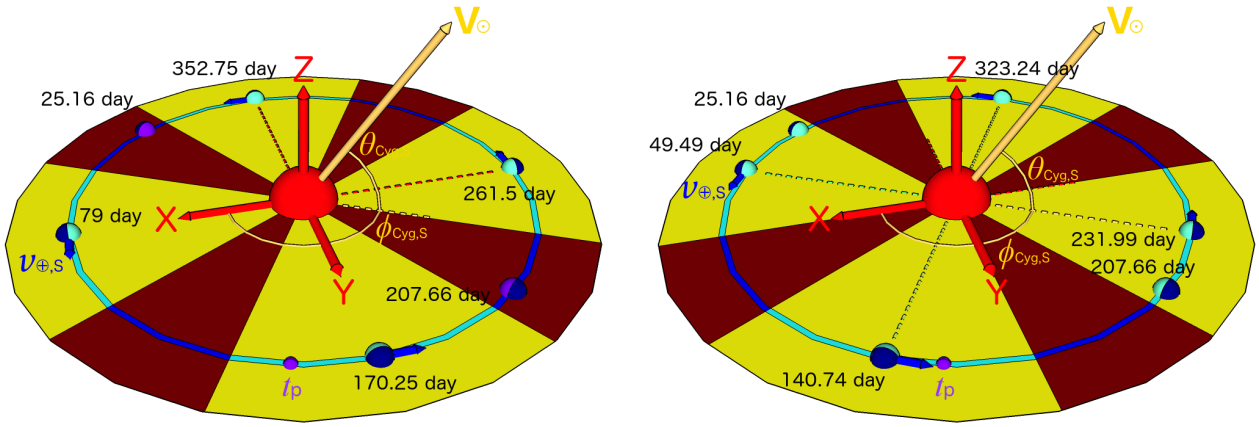

Figure 9: The sketches of two options for the observation periods (lightened areas) considered in our simulations presented in this paper (see also Table 2). (a) Four normal seasons with a common 60-day period on the central dates of 79.0 day, 170.25 day, 261.50 day, and 352.75 day, respectively. (b) Four "advanced" seasons with a 60-day period on the central dates of 49.49 day, 140.74 day, 231.99 day, and 323.24 day, respectively. The golden arrow indicates the moving direction of the Solar system towards the CYGNUS constellation with the velocity of $v_0 \simeq 220$ km/s, and the four short dark–blue arrows (in front of the Earths) indicate the (average) orbital velocity of the Earth, $|\mathbf{v}_{\oplus,\mathrm{S}}| \simeq 30$ km/s, on the central dates of four normal or four advanced seasons. While the small purple point at the bottom of each sketch indicates the location, where the Earth's orbital speed is maximal on the date around June 2nd ($t_\mathrm{p} = 152.5$ day) [65], two Earths without the velocity arrow indicate the locations, where the theoretical main direction of the WIMP wind (the opposite direction of the Solar movement) points straightly to the Prime Meridian in the night (207.66 day) or the day (25.16 day), corresponding (approximately) to the locations drawn in Figs. 1, 10, and 11. Other notations are the same as in Fig. 3(a). See the text as well as Appendices A.3.4 and A.3.6 for further details.

$[t_\mathrm{start},\ t_\mathrm{end}] = [0, 365\ \mathrm{day}]$.

Annual modulation of the 3-D WIMP velocity

As shown in Fig. 9(a), on the central dates of four normal seasons, the orbital velocity of the Earth's rotation around the Sun in the Ecliptic coordinate system is along the $\mathbf{X}_\mathrm{S}$– or the $\mathbf{Y}_\mathrm{S}$–axis. This would thus be the most natural choice for demonstrating the annual modulation of the Earth's velocity relative to the Dark Matter halo. However, as shown in Fig. 9(b) and discussed in detail in Appendix A.3.4, the relative velocity of the Earth to the DM halo should be the maximum (minimum), when its orbital velocity is (anti–)parallel to the projection of the direction of the Solar movement on the Ecliptic plane, namely, on the date around the 21st of May (140.74 day) (the 20th of November, 323.24 day). Hence, for demonstrating the annual modulation of the radial and angular distributions of the 3-D WIMP velocity, besides the 60-day ($\pm$ 30 days) observation periods of four normal seasons on the central dates of 79.0 day, 170.25 day, 261.50 day, and 352.75 day, respectively, we considered also the periods of four "advanced" ($\sim$ 30 days earlier) seasons on the central dates of 49.49 day, 140.74 day, 231.99 day, and 323.24 day, respectively. In Figs. 9, we sketch these two simulation options as the lightened areas.

Option	Central date (day)	Period (day)
One entire year	—	0 – 365
Four normal seasons	79.0	49.0 – 109.0
	170.25	140.25 – 200.25
	261.50	231.50 – 291.50
	352.75	322.75 – 382.75 (= 17.75)
Four advanced seasons	49.49	19.49 – 79.49
	140.74	110.74 – 170.74
	231.99	201.99 – 261.99
	323.24	293.24 – 353.24
For diurnal modulation	207.66	177.66 – 237.66
	390.16 (= 25.16)	360.16 – 420.16 (= 55.16)

Table 2: The list of four options for the observation periods in a 365-day year considered in our simulations presented in this paper. Note that, first, in each of the normal and advanced season, a period of 60 days (±30 days) has been set. This means that each pair of the corresponding season has an overlap of around 30 days (see the lightened and darkened areas in two sketches of Figs. 9). Second, the last option is considered only for demonstrating the diurnal modulation of the angular distribution of the 3-D WIMP velocity (see Appendix A.3.6 for the detailed calculation).

Moreover, in Table 2 we list, including the normal and the advanced seasons, four different options for the observation periods considered in our simulations presented in this paper. Note that, since in each of the normal and the advanced season, a period of 60 days (±30 days) has

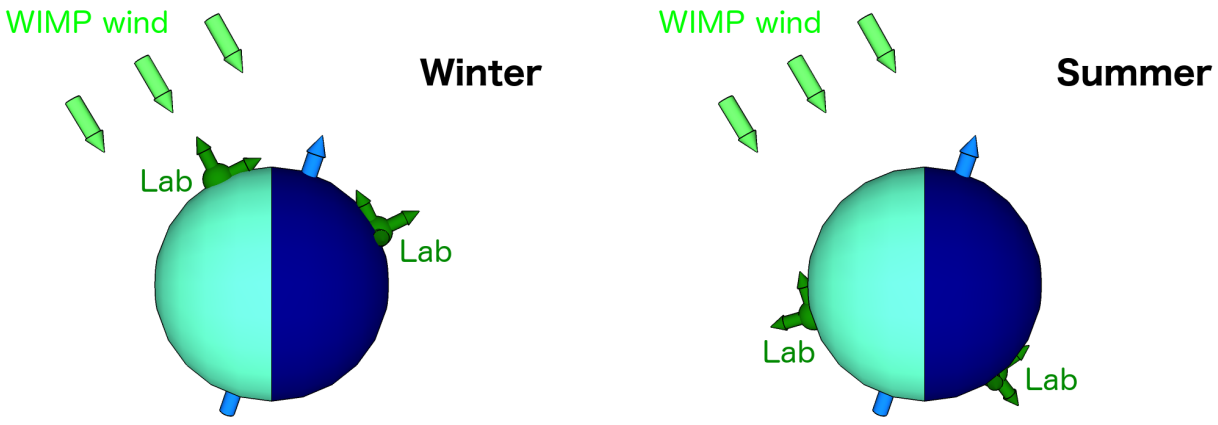

(a) (b)

Figure 10: As in Figs. 1, except that the laboratory in the Northern Hemisphere is now in Winter (a), while that in the Southern Hemisphere is in Summer (b).

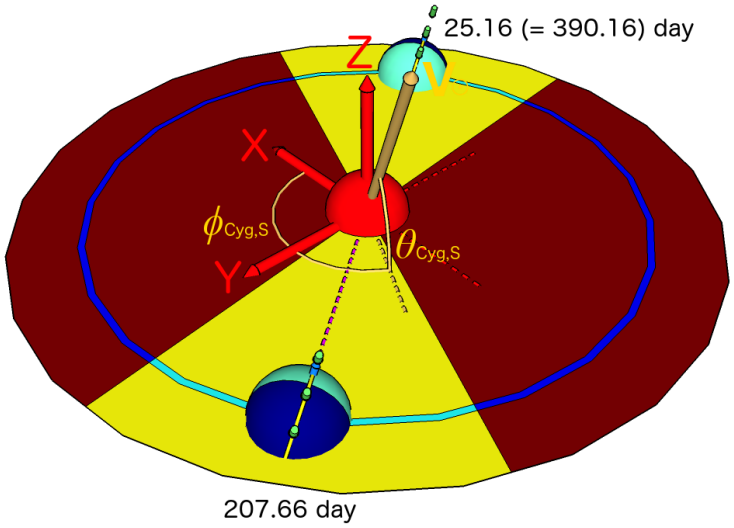

Figure 11: The sketch of two options for the observation periods (lightened areas) considered for demonstrating the diurnal modulation of the angular distribution of the 3-D WIMP velocity presented in this paper (see also Table 2): two 60-day ($\pm$ 30 days) observation period on the central date of 207.66 day and 25.16 (= 390.16) day, respectively, on which the (light–green) WIMP wind points straightly to the (yellow) Prime Meridian in the night (207.66 day) or the day (25.16 day), corresponding (approximately) to the locations drawn in Figs. 1 and 10, respectively. Other notations are the same as in Figs. 9. Note that the angle of view in this sketch turns $\sim 63^\circ$ counterclockwise from the sketches in Figs. 9. See the text and Appendix A.3.6 for further details.

been set, each pair of the corresponding season has an overlap of around 30 days (compare two sketches in Figs. 9).

Diurnal modulation of the 3-D WIMP velocity

Due to the very small unexcluded WIMP–nucleus cross section, nowadays it is required to run a direct Dark Matter detection experiment for a (very) long period, especially for directional low–mass gas detectors. Then, by comparing Figs. 1 with Figs. 10 and as shown in detail in Figs. 9 and 11, one can find that the orignial motivation of directional DM detection experiments — identifying the directionality of incident WIMPs — could be (strongly) reduced or even vanish. For demonstrating however the orignial motivation of directional detection experiments, we considered four observation intervals of 4 hours ($\pm$2 hours) at the central (*local*, not the UTC) times of 0 o'clock, 6 o'clock, 12 o'clock, and 18 o'clock, respectively (see Table 3), in the 60-day periods centered on the 207.66 day and 390.16 (= 25.16) day, respectively (see Table 2 and Fig. 11), on which the theoretical main direction of the WIMP wind points straightly to the Prime Meridian in the night (207.66 day) or the day (25.16 day)[4], corresponding (approximately) to the locations drawn in Figs. 1 and 10, respectively (see Appendix A.3.6 for the detailed calculation).

In Figs. 11, we sketch these two specified observation periods as the lightened areas (see also

[4] Note that these pure theoretically estimated dates (under some simplified assumptions) have in fact an $\sim$ 8-hour difference from the midnight or the noon, respectively, which could nevertheless be neglected in the 60-day observation periods.

Option	Central time (hour)	Interval (hour)
One entire day	—	0 – 24
Four daily shifts	0	0 – 2, 22 – 24
	6	4 – 8
	12	10 – 14
	18	16 – 20

Table 3: The list of two options for the observation intervals in a (Solar) day considered for demonstrating the diurnal modulation of the angular distribution of the 3-D WIMP velocity presented in this paper. Note that, in each shift of the second option, an interval of 4 hours (± 2 hours) has been set.

Table 2). And in Table 3, we list two options for the observation intervals in a (Solar) day considered for demonstrating (the diurnal modulation of) the angular distribution of the 3-D WIMP velocity presented in this paper.

2.3 Bayesian reconstruction of the radial distribution of the 3-D WIMP velocity

In this subsection, we describe briefly the Bayesian fitting procedure applied for reconstructing the radial component (magnitude) of the 3-D WIMP velocity distribution presented in Secs. 4 and 5.2 as well as in Appendix C.

2.3.1 Bayesian analysis

We start with the basic formula for Bayesian analysis [66]:

$$\mathrm{p}(\Theta|\mathrm{data}) = \frac{\mathrm{p}(\mathrm{data}|\Theta)}{\mathrm{p}(\mathrm{data})} \cdot \mathrm{p}(\Theta)\,. \tag{7}$$

Here $\Theta = \{a_1, a_2, \cdots, a_{N_{\mathrm{Bayesian}}}\}$ denotes a specified (combination of the) value(s) of the fitting parameter(s); $\mathrm{p}(\Theta)$, called the "prior probability", represents our degree of belief about Θ being the true value(s) of fitting parameter(s), which is often given in form of (the multiplication of) the probability distribution(s) of the fitting parameter(s). $\mathrm{p}(\mathrm{data})$, called the "evidence", is the total probability of obtaining the particular set of data, which is in practice irrespective of the actual value(s) of the parameter(s) and can be treated as a normalization constant; it will not be of interest in our analysis presented in this paper. $\mathrm{p}(\mathrm{data}|\Theta)$ denotes the probability of the observed result, once the specified (combination of the) value(s) of the fitting parameter(s) happens, which can usually be described by the likelihood function of Θ, $\mathcal{L}(\Theta)$. Finally, $\mathrm{p}(\Theta|\mathrm{data})$, called the "posterior probability density function" for Θ, representes the probability of that the specified (combination of the) value(s) of the fitting parameter(s) happens, given the observed result.

2.3.2 Bayesian reconstruction of $f_{\mathrm{r}}(v)$

Below we describe the procedure of our Bayesian reconstruction of the radial distribution of the 3-D WIMP velocity in detail.

First, as shown in Figs. 7 and 25, the magnitudes of the (transformed) 3-D velocity of the recorded WIMP scattering events are binned into B bins as

$$v_{n,\rm min} \equiv v_n - \frac{b_v}{2} \leq v_{n,i} \leq v_n + \frac{b_v}{2} \equiv v_{n,\rm max}\,, \qquad i = 1,\ 2,\ \cdots,\ N_n,\ n = 1,\ 2,\ \cdots,\ B. \tag{8}$$

Here the entire velocity range below the maximal cut–off ($v_{\rm esc}$ in the Galactic coordinate system and $v_{\rm max}$ in the Equatorial coordinate system) has been divided into B bins with central points v_n and a common width b_v. In the nth bin, N_n events are recorded and

$$N_{\rm tot} = \sum_{n=1}^{B} N_n \tag{9}$$

is the number of total WIMP events in the dataset to be analyzed. This means that in the nth v–bin $[v_{n,\rm min}, v_{n,\rm max}]$, the *normalized* event number is

$$f_{\rm r,expt}(v_n) = \frac{1}{N_{\rm tot}} \left(\frac{N_n}{b_v}\right)\,. \tag{10}$$

Choosing a theoretical prediction of the one–dimensional WIMP velocity distribution: $f_{\rm r,th}(v; a_1, a_2, \cdots, a_{N_{\rm Bayesian}})$, where $(a_1, a_2, \cdots, a_{N_{\rm Bayesian}})$ are the $N_{\rm Bayesian}$ fitting parameters, and since the recorded event number in each v–bin should be Poisson–distributed around the theoretical predictions $f_{\rm r,th}(v_n; a_1, a_2, \cdots, a_{N_{\rm Bayesian}})$, the likelihood function for p(data|Θ) can be defined by

$$\begin{aligned} &\mathcal{L}\Big(f_{\rm r,expt}(v_n),\ n = 1,\ 2,\ \cdots,\ B;\ a_i,\ i = 1,\ 2,\ \cdots,\ N_{\rm Bayesian}\Big) \\ &\equiv \prod_{n=1}^{B} {\rm Poi}\Big(v_n, f_{\rm r,expt}(v_n); a_1, a_2, \cdots, a_{N_{\rm Bayesian}}\Big)\,, \end{aligned} \tag{11}$$

where

$$\begin{aligned} &{\rm Poi}\Big(v_n, f_{\rm r,expt}(v_n); a_1, a_2, \cdots, a_{N_{\rm Bayesian}}\Big) \\ &\equiv \frac{f_{\rm r,th}^{f_{\rm r,expt}(v_n)}\Big(v_n; a_1, a_2, \cdots, a_{N_{\rm Bayesian}}\Big)\, e^{-f_{\rm r,th}\left(v_n; a_1, a_2, \cdots, a_{N_{\rm Bayesian}}\right)}}{\Gamma\left(f_{\rm r,expt}(v_n) + 1\right)}\,, \end{aligned} \tag{12}$$

and

$$\Gamma(x) = \int_0^\infty t^{x-1} e^{-t}\, dt \tag{13}$$

is the gamma function. Then the posterior probability density on the left–hand side of Eq. (7) can be given as

$$\begin{aligned} &{\rm p}\Big(a_i,\ i = 1,\ 2,\ \cdots,\ N_{\rm Bayesian} \,\Big|\, f_{\rm r,expt}(v_n),\ n = 1,\ 2,\ \cdots,\ B\Big) \\ &\propto \mathcal{L}\Big(f_{\rm r,expt}(v_n),\ n = 1,\ 2,\ \cdots,\ B;\ a_i,\ i = 1,\ 2,\ \cdots,\ N_{\rm Bayesian}\Big) \prod_{i=1}^{N_{\rm Bayesian}} {\rm p}_i(a_i)\,. \end{aligned} \tag{14}$$

Regarding our degree of belief about each fitting parameter a_i, i.e. ${\rm p}_i(a_i)$ in Eq. (14), two probability distribution functions have been considered. The simplest one is the flat–distribution:

$${\rm p}_i(a_i) = 1\,, \qquad\qquad \text{for } a_{i,\rm min} \leq a_i \leq a_{i,\rm max}, \tag{15}$$

where $a_{i,(\min,\max)}$ denote the minimal and maximal bounds of the scanning interval of the fitting parameter a_i. On the other hand, for the case that we have already prior knowledge about one fitting parameter, a Gaussian–distribution:

$$\mathrm{p}_i(a_i;\mu_{a,i},\sigma_{a,i}) = \frac{1}{\sqrt{2\pi}\,\sigma_{a,i}}\, e^{-(a_i-\mu_{a,i})^2/2\sigma_{a,i}^2} \tag{16}$$

with the expectation value $\mu_{a,i}$ of and the 1σ uncertainty $\sigma_{a,i}$ on the fitting parameter a_i is used. Note that, in one simulated experiment, we scan the parameter space $(a_1, a_2, \cdots, a_{N_{\rm Bayesian}})$ in the volume $a_i \in [a_{i,\min}, a_{i,\max}]$, $i = 1, 2, \cdots, N_{\rm Bayesian}$, to find a particular point $(a_1^*, a_2^*, \cdots, a_{N_{\rm Bayesian}}^*)$, which maximizes (the numerator of) the posterior probability density: $\mathrm{p}\Big(a_i,\ i=1,\ 2,\ \cdots,\ N_{\rm Bayesian}\ \Big|\ f_{\rm r,expt}(v_n),\ n=1,\ 2,\ \cdots,\ B\Big)$. And after that all simulations have been done, we determine the mean value of the event number in each v–bin from all simulated experiments, denoted as $N_{n,\rm mean}$, and define then

$$f_{\rm r,mean}(v_n) = \frac{1}{N_{\rm tot,ave}}\left(\frac{N_{n,\rm mean}}{b_v}\right) , \tag{17}$$

where $N_{\rm tot,ave}$ is the expectation value of the event number in one simulated experiment[5]. Hence, we can define further

$$\begin{aligned} &\mathrm{P}_{\rm mean}\left(a_i,\ i=1,\ 2,\ \cdots,\ N_{\rm Bayesian}\right) \\ &\equiv \mathrm{p}\left(a_i,\ i=1,\ 2,\ \cdots,\ N_{\rm Bayesian}\ \Big|\ f_{\rm r,mean}(v_n),\ n=1,\ 2,\ \cdots,\ B\right) , \end{aligned} \tag{18}$$

and scan the points $(a_1^*, a_2^*, \cdots, a_{N_{\rm Bayesian}}^*)$ obtained from all simulated experiments one–by–one to find the "best–fit" point $(a_{1,\rm Pmax}, a_{2,\rm Pmax}, \cdots, a_{N_{\rm Bayesian},\rm Pmax})$, which maximizes $\mathrm{P}_{\rm mean}(a_i,\ i = 1,\ 2,\ \cdots,\ N_{\rm Bayesian})$.

2.3.3 Fitting velocity distribution $f_{\rm r,th}(v)$

By taking into account the orbital motion of the Solar system around our Galaxy as well as that of the Earth around the Sun, the shifted Maxwellian velocity distribution has been derived in detail by Lewin and Smith [67]:

$$f_{1,\rm sh,vesc}(v) = \begin{cases} N_{\rm sh,vesc}\left(\dfrac{v}{v_0 v_{\rm e}}\right)\left[e^{-(v-v_{\rm e})^2/v_0^2} - e^{-(v+v_{\rm e})^2/v_0^2}\right], & \text{for } v \le v_{\rm esc} - v_{\rm e}\,, \\ N_{\rm sh,vesc}\left(\dfrac{v}{v_0 v_{\rm e}}\right)\left[e^{-(v-v_{\rm e})^2/v_0^2} - e^{-v_{\rm esc}^2/v_0^2}\right], & \text{for } v_{\rm esc} - v_{\rm e} \le v \le v_{\rm esc} + v_{\rm e}\,, \\ 0\,, & \text{for } v \ge v_{\rm esc} + v_{\rm e} \equiv v_{\rm max}\,, \end{cases} \tag{19}$$

with the normalization constant

$$N_{\rm sh,vesc} = \left[\sqrt{\pi}\,\mathrm{erf}\left(\frac{v_{\rm esc}}{v_0}\right) - \left(\frac{2v_{\rm esc}}{v_0}\right) e^{-v_{\rm esc}^2/v_0^2}\right]^{-1} . \tag{20}$$

Here $v_{\rm e}$ is the time–dependent Earth's speed in the Galactic frame, which has been given in Ref. [65] by

$$v_{\rm e}(t) = v_0\left[1.05 + 0.07\cos\left(\frac{2\pi(t-t_{\rm p})}{1\ \rm yr}\right)\right] , \tag{21}$$

[5] Note that in our numerical simulations presented in this paper, the total number of the generated WIMP events in each experiment, $N_{\rm tot}$, is Poisson–distributed around the expectation value $N_{\rm tot,ave}$.

with $t_{\rm p} \simeq$ June 2nd (the purple points sketched in Figs. 9), and, since the Galactic escape velocity has been set as $v_{\rm esc} = 550$ km/s in our simulations, the maximal cut–off on the radial distribution of the 3-D WIMP velocity in the Equatorial coordinate system is given as $v_{\rm max} = 781$ km/s. Meanwhile, a simplified expression for the shifted Maxwellian velocity distribution $f_{\rm 1,sh,vesc}(v)$ given in Eq. (19) is often adopted in literature [1]:

$$f_{\rm 1,sh}(v) = \begin{cases} N_{\rm sh} \left(\frac{v}{v_0 v_{\rm e}}\right) \left[e^{-(v-v_{\rm e})^2/v_0^2} - e^{-(v+v_{\rm e})^2/v_0^2}\right], & \text{for } v \leq v_{\rm max}\,, \\ 0\,, & \text{for } v > v_{\rm max}\,, \end{cases} \tag{22}$$

with the normalization constant

$$N_{\rm sh} = \left\{ \left(\frac{\sqrt{\pi}}{2}\right) \left[{\rm erf}\left(\frac{v_{\rm max}+v_{\rm e}}{v_0}\right) + {\rm erf}\left(\frac{v_{\rm max}-v_{\rm e}}{v_0}\right)\right] + \left(\frac{v_0}{2v_{\rm e}}\right) \left[e^{-(v_{\rm max}+v_{\rm e})^2/v_0^2} - e^{-(v_{\rm max}-v_{\rm e})^2/v_0^2}\right] \right\}^{-1} . \tag{23}$$

In Appendix D, we will show that, with the Galactic escape velocity of $v_{\rm esc} = 500$ km/s, the shape difference between the exact analytic expression $f_{\rm 1,sh,vesc}(v)$ given in Eq. (19) and the simplified form $f_{\rm 1,sh}(v)$ in Eq. (22) is pretty tiny and negligible compared to the annual variation of two expressions as well as the much larger statistical uncertainties on the recorded WIMP events (shown in e.g., Fig. 25); this tiny shape difference could even vanish once the Galactic escape velocity would be as large as $v_{\rm esc} = 600$ km/s. Hence, for our Bayesian reconstruction of the radial distribution of the 3-D WIMP velocity presented in this paper, we took the simplified expression (22) and considered the following four fitting distribution functions.

The first one is the "one–parameter" shifted Maxwellian velocity distribution with the Solar Galactic velocity v_0 as the unique fitting parameter [68]:

$$f_{\rm 1,sh,}{}_{v_0}(v; v_0) = N_{\rm sh}(v_0) \left(\frac{v}{v_0 v_{\rm e}}\right) \left[e^{-(v-v_{\rm e})^2/v_0^2} - e^{-(v+v_{\rm e})^2/v_0^2}\right], \tag{24}$$

and the constraint on $v_{\rm e}$:[6]

$$v_{\rm e} = 1.05\, v_0\,. \tag{25}$$

Considering the (annual) variation of the Earth's Galactic velocity in different observation periods, we introduce a "v_0–fixed" shifted Maxwellian velocity distribution with now the Earth's Galactic velocity $v_{\rm e}$ as the fitting parameter:

$$f_{\rm 1,sh,}{}_{v_{\rm e}}(v; v_{\rm e}) = N_{\rm sh}(v_{\rm e}) \left(\frac{v}{v_0 v_{\rm e}}\right) \left[e^{-(v-v_{\rm e})^2/v_0^2} - e^{-(v+v_{\rm e})^2/v_0^2}\right], \tag{26}$$

and the constraint of $v_0 = 220$ km/s. Moreover, in order to obtain reconstruction results which can match the recorded radial WIMP velocity distribution as well as possible, the simplified shifted Maxwellian velocity distribution with v_0 and v_e as two *independent* fitting parameters should certainly be considered:

$$f_{\rm 1,sh}(v; v_0, v_{\rm e}) = N_{\rm sh}(v_0, v_{\rm e}) \left(\frac{v}{v_0 v_{\rm e}}\right) \left[e^{-(v-v_{\rm e})^2/v_0^2} - e^{-(v+v_{\rm e})^2/v_0^2}\right]. \tag{27}$$

[6] Although in Appendix A.3.4 we will show that the first–order term of the time–dependence between v_0 and $v_{\rm e}$ would only be 1.0078, we took still the commonly used value of 1.05 for our reconstructions presented in this paper.

And, finally, as the auxiliary fitting function for confirming and/or improving our reconstruction results, the "modified" shifted Maxwellian velocity distribution with v_0 and $\Delta v \equiv v_{\rm e} - v_0$ as two independent fitting parameters introduced in our earlier work [68] has also be used:

$$f_{1,{\rm sh},\Delta v}(v; v_0, \Delta v) = N_{\rm sh}(v_0, \Delta v) \left[\frac{v}{v_0\,(v_0 + \Delta v)}\right] \left\{e^{-[v-(v_0+\Delta v)]^2/v_0^2} - e^{-[v+(v_0+\Delta v)]^2/v_0^2}\right\}. \quad (28)$$

3 Angular distributions of the 3-D WIMP velocity in different coordinate systems

In this section, we present the angular distributions of the (transformed) 3-D WIMP velocity in three "laboratory–independent" (Ecliptic, Equatorial, and Earth) coordinate systems and then in two "laboratory–dependent" (horizontal and laboratory) coordinate systems one by one. As readers' reference, a summary of the angular distributions observed in the horizontal and laboratory coordinate systems of different underground laboratories will be given in Appendix B.

3.1 Angular WIMP velocity distribution in the Ecliptic frame

In this subsection, we present at first the angular distribution of the 3-D WIMP velocity in the Ecliptic coordinate system. Remind that the Ecliptic coordinate system only moves (approximately) linearly with the Solar Galactic orbital velocity $v_0 \simeq 220$ km/s and its tiny rotation is imperceptible.

In our simulations presented in this paper, the ith 3-D WIMP velocity transformed from the ith velocity generated in the Galactic coordinate system to the Ecliptic coordinate system can be given by

$$\mathbf{v}_{\chi,i,{\rm S}} = \mathbf{M}_{{\rm G}\to{\rm S}}\left(\mathbf{v}_{\chi,i,{\rm G}} - \mathbf{v}_{\odot,{\rm G}}\right), \quad (29a)$$

where $\mathbf{M}_{{\rm G}\to{\rm S}}$ is the transformation matrix given in Eq. (A24a) and $\mathbf{v}_{\odot,{\rm G}}$ is the moving velocity of the Solar system in the Galactic coordinate system given in Eq. (A33). Conversely, for analyzing real data provided by experimental collaborations (hopefully) in the future, the ith 3-D velocity in the Galactic coordinate system can by transformed from that in the Ecliptic coordinate system by

$$\mathbf{v}_{\chi,i,{\rm G}} = \mathbf{M}_{{\rm S}\to{\rm G}}\mathbf{v}_{\chi,i,{\rm S}} + \mathbf{v}_{\odot,{\rm G}}, \quad (29b)$$

where the transformation matrix $\mathbf{M}_{{\rm S}\to{\rm G}}$ is given in Eq. (A24b).

In Fig. 12, we show the angular distribution of the 3-D WIMP velocity transformed from events shown in Fig. 8 to the Ecliptic coordinate system by Eq. (29a). One entire year (0 to 365 day) and 50 total events on average in one experiment have been considered. It can be found that, while in the most part of the northern sky and a small part of the southern sky, the numbers of WIMP events would be less than 35% (0.49 events/bin) of the all–sky average value (1.39 events/bin), the event numbers in the bins from the center (i.e., the direction of the $\mathbf{X}_{\rm S}$–axis) to southwest would be larger than 1.4 times (1.94 events/bin) of the all–sky average value; in particular, in the dark–red and dark–purple bins in the southern sky, the numbers of WIMP events are at least 4 times (5.56 events/bin) or even larger than 5.6 times (7.78 events/bin) of the all–sky average value, respectively. This means that the average event numbers from the center to the southwest part could be at least 4 times or even 16 times larger than the rest part

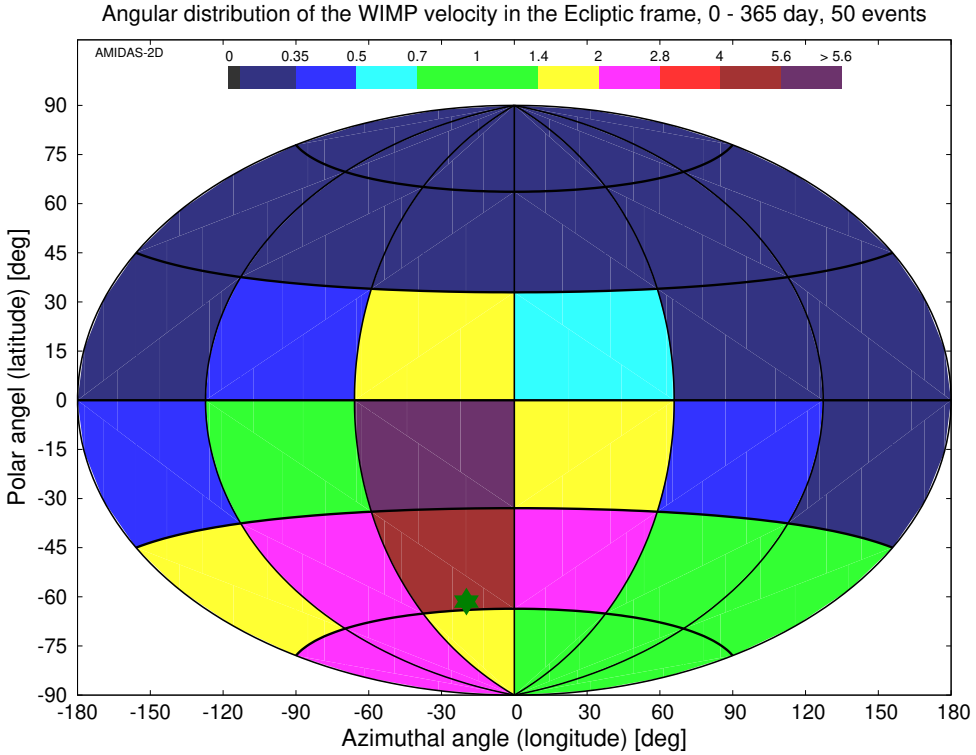

Figure 12: The angular distribution of the 3-D WIMP velocity transformed from events shown in Fig. 8 to the Ecliptic coordinate system by Eq. (29a). The dark–green star indicates the theoretical main direction of incident WIMPs (the opposite direction of the Solar Galactic movement) in the Ecliptic coordinate system: 57.40°S, 29.10°W. All simulation setup and other notations are the same as in Fig. 8. See the text for further details.

of the sky and would hence be a clear identification of the anisotropy of the incident direction of Galactic WIMPs.

However, comparing with the dark–green star on the map, which indicates the theoretical main direction of incident WIMPs (the opposite direction of the Solar Galactic movement) in the Ecliptic coordinate system: 57.40°S, 29.10°W,[7] the (dark–purple) bin with the most WIMP events would not match the theoretically predicted direction of the WIMP wind and has a 30° to 40° northward deviation. In Sec. 5.1.1, we will see that, with $\mathcal{O}(500)$ total WIMP events and a higher analysis resolution, this systematic bias could be strongly reduced, but a small amount of deviation would still exist.

3.2 Angular WIMP velocity distribution in the Equatorial frame

In this subsection, we present the angular distribution of the 3-D WIMP velocity in the Equatorial coordinate system. Remind that the Equatorial coordinate system moves orbitally around (and also linearly with) the Sun, but doesn't rotate. Thus its axes are fixed.

Similar to Eqs. (29a) and (29b), in our simulations presented in this paper, the ith 3-D WIMP velocity transformed from the ith velocity in (transformed to) the Ecliptic coordinate

[7] See Appendix A.3.3 for the detailed calculation.

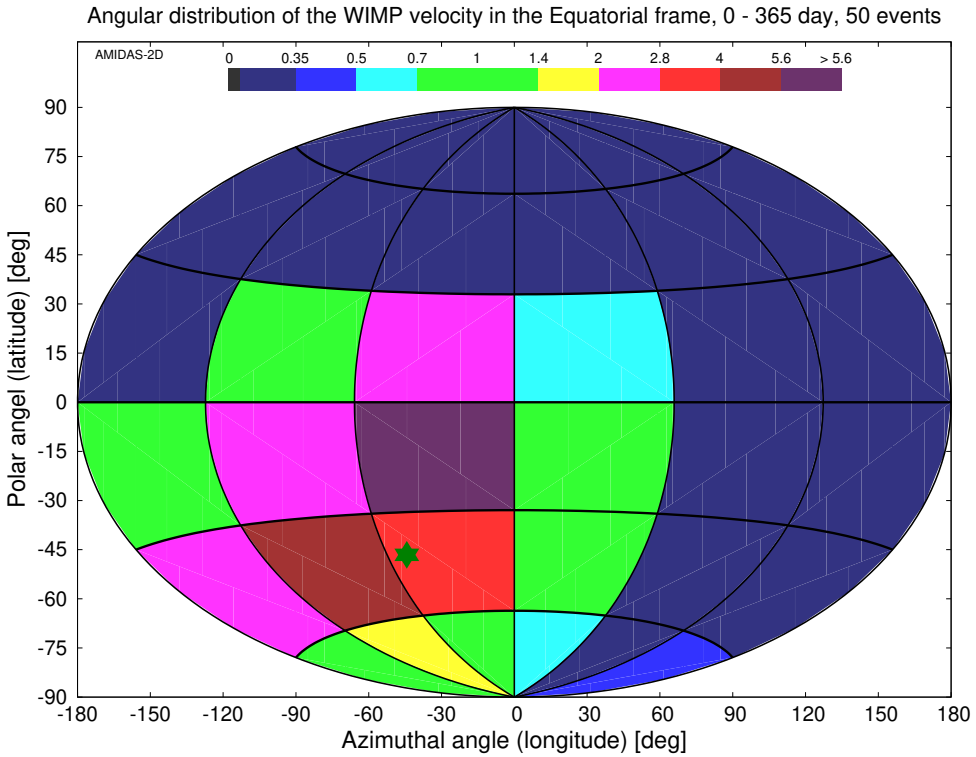

Figure 13: The angular distribution of the 3-D WIMP velocity transformed from events shown in Fig. 12 to the Equatorial coordinate system by Eq. (30a). The dark–green star indicates now the theoretical main direction of incident WIMPs in the Equatorial coordinate system [63]: 42.00°S, 50.70°W. All simulation setup and other notations are the same as in Fig. 12.

system to the Equatorial coordinate system can be given by

$$\mathbf{v}_{\chi,i,\mathrm{Eq}} = \mathbf{M}_{\mathrm{S}\to\mathrm{Eq}}\Big[\mathbf{v}_{\chi,i,\mathrm{S}} - \mathbf{v}_{\oplus,\mathrm{S}}(t_i)\Big]\,, \tag{30a}$$

where t_i is the generated observation time of the ith WIMP event, $\mathbf{M}_{\mathrm{S}\to\mathrm{Eq}}$ is the transformation matrix given in Eq. (A6a) and $\mathbf{v}_{\oplus,\mathrm{S}}(t)$ is the time–dependent Earth's orbital velocity around the Sun in the Ecliptic coordinate system given in Eq. (A16). Conversely, for analyzing real data provided by experimental collaborations in the future, the ith 3-D velocity in the Ecliptic coordinate system can by transformed from the ith velocity measured at time t_i in the Equatorial coordinate system by

$$\mathbf{v}_{\chi,i,\mathrm{S}} = \mathbf{M}_{\mathrm{Eq}\to\mathrm{S}}\mathbf{v}_{\chi,i,\mathrm{Eq}} + \mathbf{v}_{\oplus,\mathrm{S}}(t_i)\,, \tag{30b}$$

where the transformation matrix $\mathbf{M}_{\mathrm{Eq}\to\mathrm{S}}$ is given in Eq. (A6b).

In Fig. 13, we show the angular distribution of the 3-D WIMP velocity transformed from events shown in Figs. 8 and 12 to the Equatorial coordinate system by Eq. (30a). One entire year (0 to 365 day) and 50 total events on average in one experiment have been considered. As in Fig. 12, it can also be seen clearly here that, while in the most part of the northern and the eastern skies, the numbers of WIMP events would be less than 35% (0.49 events/bin) of the all–sky average value (1.39 events/bin), the event numbers in the southwest part of the sky would be at least 2 times (2.78 events/bin) or even more than 5.6 times (7.78 events/bin) of the all–sky average value, respectively. This means that the average event numbers from the center

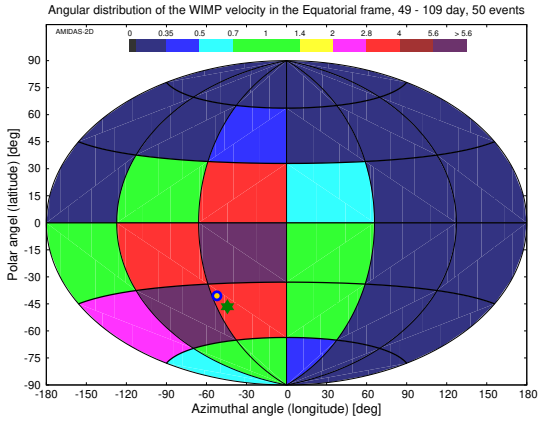

(a) 49.0 – 109.0 day

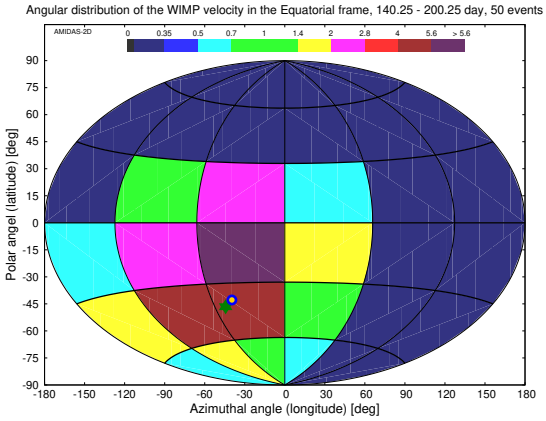

(b) 140.25 – 200.25 day

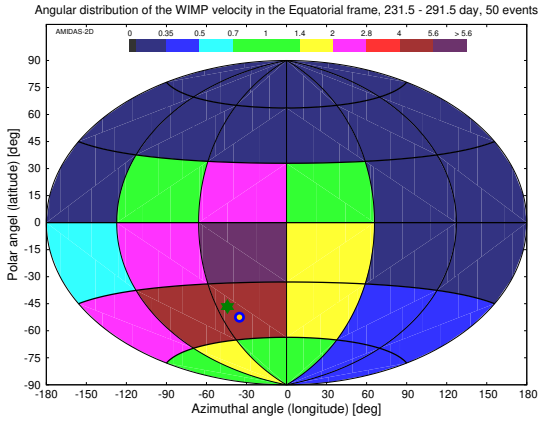

(c) 231.50 – 291.50 day

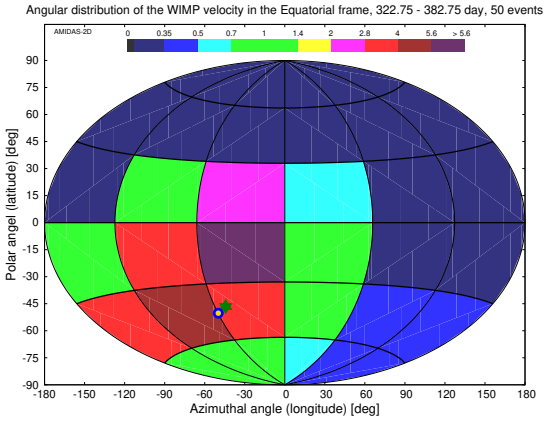

(d) 322.75 – 382.75 day

Figure 14: The angular distributions of the 3-D WIMP velocity in the Equatorial coordinate system. Four observation periods of the normal seasons listed in Table 2 and sketched in Fig. 9(a) as well as 50 total events on average in each 60-day observation period have been considered. Besides the dark–green star indicating the theoretical main direction of incident WIMPs, the blue–yellow point in each plot indicates the opposite direction of the Earth's velocity relative to the Dark Matter halo on the central date of the observation period (listed in Table A2). All other simulation setup and notations are the same as in Fig. 13.

(i.e., the direction of the $\mathbf{X}_{\rm Eq}$–axis) to the southwest part could be at least 5.7 times or even 16 times larger than the rest part of the sky and would hence also be a clear identification of the anisotropy of the incident direction of Galactic WIMPs.

In Fig. 13, we also put a dark–green star to indicate the theoretical main direction of incident WIMPs in the Equatorial coordinate system [63]: 42.00°S, 50.70°W. Now the deviation between the (dark–purple) bin with the most WIMP events and the theoretically predicted direction of the WIMP wind would only be $\sim 10^\circ$ northwestward, but they can still not match each other. In Sec. 5.1.2, we will show that, with $\mathcal{O}(500)$ total WIMP events and a higher analysis resolution, a small deviation might still exist.

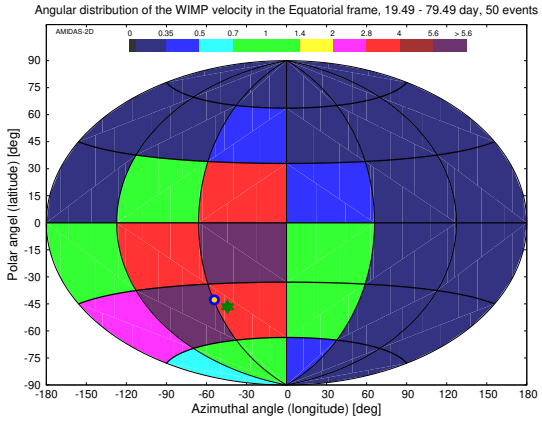

(a) 19.49 – 79.49 day

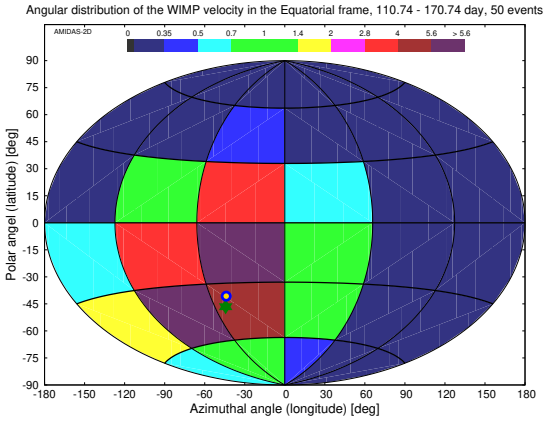

(b) 110.74 – 170.74 day

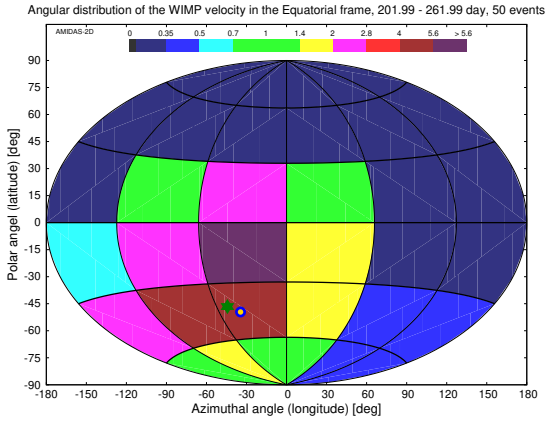

(c) 201.99 – 261.99 day

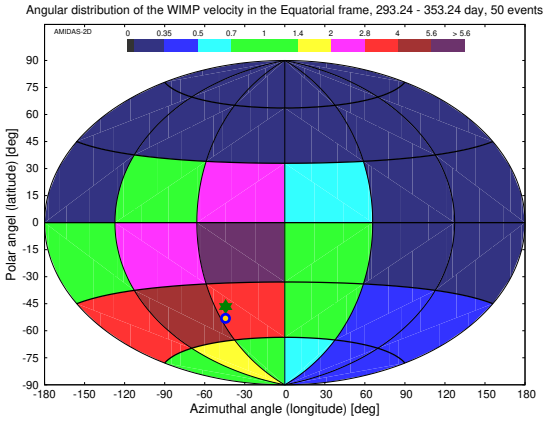

(d) 293.24 – 353.24 day

Figure 15: As in Figs. 14, except that four observation periods of the advanced seasons listed in Table 2 and sketched in Fig. 9(b) have been considered.

3.2.1 Annual modulation of the angular velocity distribution in the Equatorial frame

Moreover, in order to demonstrate the annual modulation of the angular distribution pattern of the 3-D WIMP velocity, we show in Figs. 14 and 15 the angular distributions in the Equatorial coordinate system in four observation periods of the normal and the advanced seasons listed in Table 2 and sketched in Figs. 9, respectively. Note that 50 total events on average in each 60-day observation period have been simulated. This means although that $\sim$ 300 total events in one year would be required, considering the laboratory–independence of the Equatorial coordinate system, we could in practice collect the WIMP events observed in several different underground laboratories for such an analysis.

In each plot of Figs. 14 and 15, besides the dark–green star indicating the theoretical main direction of incident WIMPs, we also put a blue–yellow point to indicate the opposite direction of the Earth's velocity relative to the Dark Matter halo on the central date of the observation period[8]. By comparing the plots in four normal and four advanced seasons carefully, one could

[8] See Appendix A.3.4 for the detailed calculations.

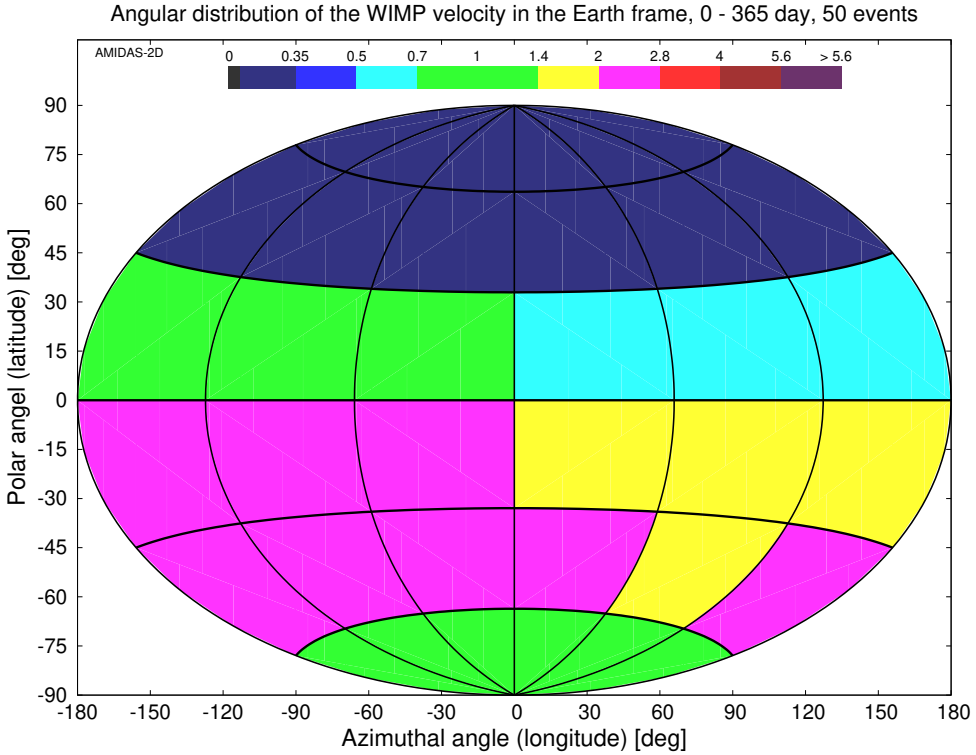

Figure 16: The angular distribution of the 3-D WIMP velocity transformed from events shown in Fig. 13 to the Earth coordinate system by Eq. (31a). All simulation setup and notations are the same as in Fig. 13.

find that the event numbers indeed variate (become more and then fewer) slightly and this variation follows also the circular clockwise movement of the blue–yellow point. This would be, besides the pure anisotropy of the WIMP velocity, a second (important) characteristic for identifying directional WIMP signals and discriminating from any (unexpected) backgrounds with some specified incoming directions.

3.3 Angular WIMP velocity distribution in the Earth frame

In this subsection, we present the angular distribution of the 3-D WIMP velocity in the Earth coordinate system. Remind that the Earth coordinate system not only moves orbitally around (and also linearly with) the Sun, but also rotates daily and discretely.

As mentioned at the end of Sec. 2.1, the transformations of the ith 3-D WIMP velocity measured at time t_i between the Equatorial and the Earth coordinate systems are pure rotations, which can be given by

$$\mathbf{v}_{\chi,i,\mathrm{E}} = \mathbf{M}_{\mathrm{Eq}\to\mathrm{E}}(t_i)\,\mathbf{v}_{\chi,i,\mathrm{Eq}}\,, \tag{31a}$$

and, conversely,

$$\mathbf{v}_{\chi,i,\mathrm{Eq}} = \mathbf{M}_{\mathrm{E}\to\mathrm{Eq}}(t_i)\,\mathbf{v}_{\chi,i,\mathrm{E}}\,, \tag{31b}$$

where the transformation matrices $\mathbf{M}_{\mathrm{Eq}\to\mathrm{E}}(t)$ and $\mathbf{M}_{\mathrm{E}\to\mathrm{Eq}}(t)$ are given in Eqs. (A14a) and (A14b).

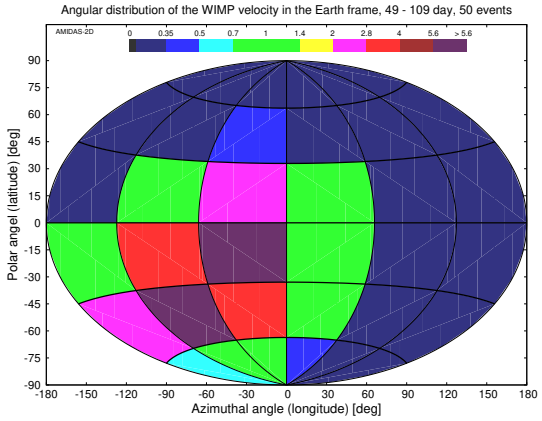

(a) 49.0 – 109.0 day

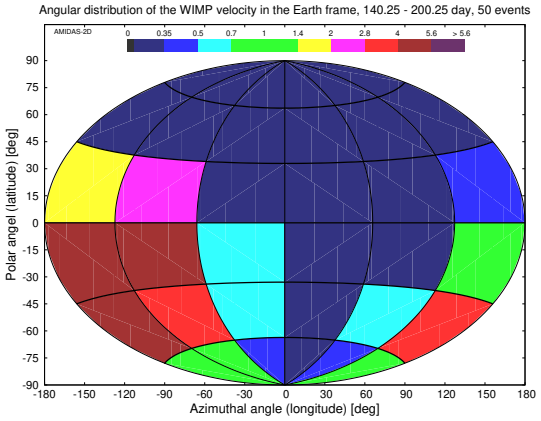

(b) 140.25 – 200.25 day

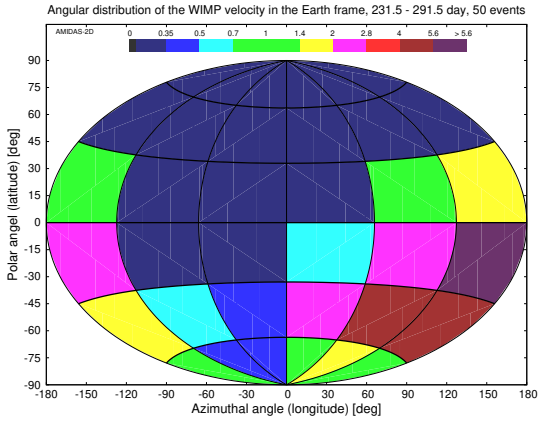

(c) 231.50 – 291.50 day

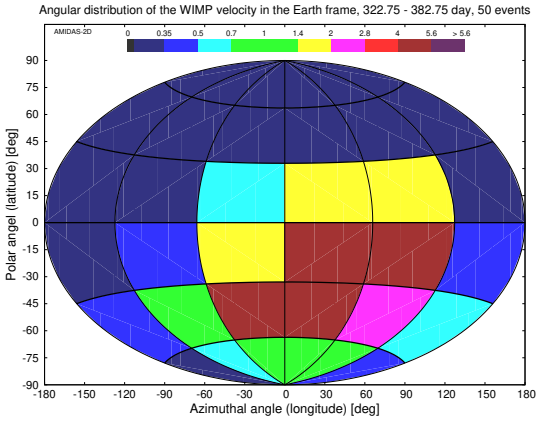

(d) 322.75 – 382.75 day

Figure 17: The angular distributions of the 3-D WIMP velocity in the Earth coordinate system. Four observation periods of the normal seasons as well as 50 total events on average in each 60-day observation period have been considered. All other simulation setup and notations are the same as in Fig. 16.

In Fig. 16, we show the angular distribution of the 3-D WIMP velocity transformed from events shown in Figs. 8, 12, and 13 to the Earth coordinate system by Eq. (31a). One entire year (0 to 365 day) with 50 total events on average have been considered. It could be seen that, first, due to the Earth's orbital motion around the Sun and thus the Earth coordinate system rotates daily, (the anisotropy of) the angular distribution of the 3-D WIMP velocity spreads out latitudinally. However, one could still find that the event numbers are at fewest (less than 35% of the all–sky average value, < 0.49 events/bin among $\mathcal{O}(50)$ total events) in the bins more northern than 60°N, and at least 2 times of the all–sky average (> 2.78 events/bin) in the southwest part of the sky.

3.3.1 Annual modulation of the angular velocity distribution in the Earth frame

In Figs. 17 and 18, we show the angular distributions of the 3-D WIMP velocity in the Earth coordinate system in four observation periods of the normal and the advanced seasons, respectively. Remind that, as in Figs. 14 and 15, 50 total events on average in each 60-day observation

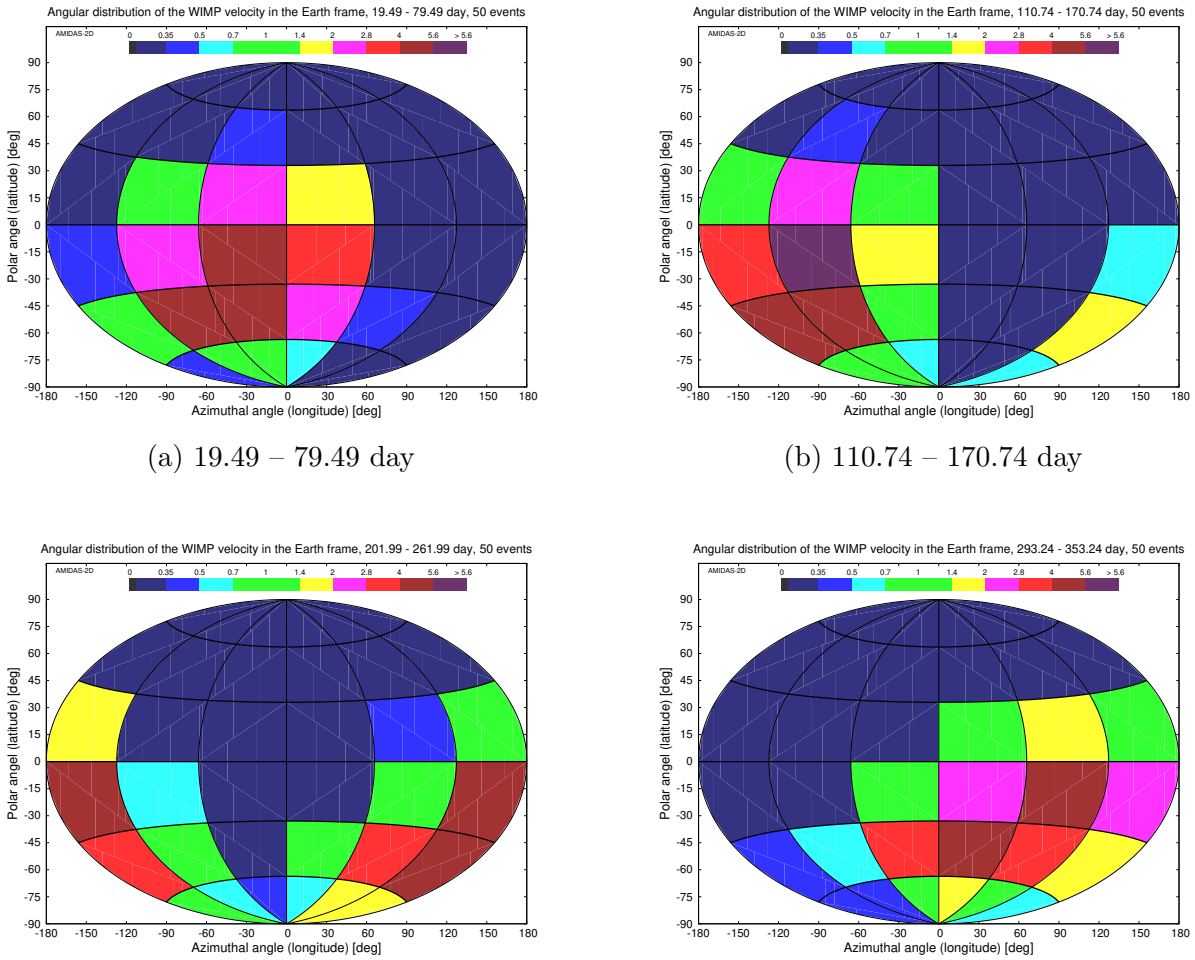

(a) 19.49 – 79.49 day

(b) 110.74 – 170.74 day

(c) 201.99 – 261.99 day

(d) 293.24 – 353.24 day

Figure 18: As in Figs. 17, except that four observation periods of the advanced seasons have been considered.

period have been simulated.

By comparing with Figs. 14 and 15, one can see clearly the similarity between the angular distribution patterns of the 3-D WIMP velocity observed in each 60-day observation period. The reason is understandable: since by definition the Earth coordinate system rotates daily with a one–year period, the directions of the $\mathbf{X}_{\rm E}$–axis on the central dates of the observation period in four plots shown in Fig. 17 or 18 rotates 90° eastwards on the celestial Equator. Hence, four distribution patterns in the normal and the advanced seasons rotates 90° westwards around the $\mathbf{Z}_{\rm E}$–axis. Due to the same reason, the distribution patterns in each pair of the normal and the advanced seasons would also rotate $\sim 30°$ westwards. In general, the angular distribution patterns in the Earth coordinate system should approximately be those in the Equatorial coordinate system combined with a westward rotation of a one–year period. This periodic variation of the anisotropic angular distribution of the 3-D WIMP velocity could be observed more clearly in our simulations with $\mathcal{O}(500)$ total WIMP events and a higher analysis resolution given in Sec. 5.1.3.

3.4 Angular WIMP velocity distribution in the horizontal frame

In this subsection, we present the angular distribution of the 3-D WIMP velocity in the laboratory–dependent horizontal coordinate system. Remind that, as the Earth coordinate system, the horizontal coordinate system not only moves orbitally around (and also linearly with) the Sun, but also rotates daily and discretely.

Similar to Eqs. (31a) and (31b), the transformations (pure rotations) of the ith 3-D WIMP velocity between the Earth and the horizontal coordinate systems can be given by

$$\mathbf{v}_{\chi,i,\mathrm{H}} = \mathbf{M}_{\mathrm{E}\to\mathrm{H}}(\phi_{\mathrm{Lab}}, \theta_{\mathrm{Lab}})\, \mathbf{v}_{\chi,i,\mathrm{E}}\,, \tag{32a}$$

and, conversely,

$$\mathbf{v}_{\chi,i,\mathrm{E}} = \mathbf{M}_{\mathrm{H}\to\mathrm{E}}(\phi_{\mathrm{Lab}}, \theta_{\mathrm{Lab}})\, \mathbf{v}_{\chi,i,\mathrm{H}}\,, \tag{32b}$$

where the transformation matrices $\mathbf{M}_{\mathrm{E}\to\mathrm{H}}(\phi_{\mathrm{Lab}}, \theta_{\mathrm{Lab}})$ and $\mathbf{M}_{\mathrm{H}\to\mathrm{E}}(\phi_{\mathrm{Lab}}, \theta_{\mathrm{Lab}})$ depending on the longitude and the latitude of the laboratory $(\phi_{\mathrm{Lab}}, \theta_{\mathrm{Lab}})$ are given in Eqs. (A2b) and (A2a).

3.4.1 Annual modulation of the angular velocity distribution in the horizontal frame

In Figs. 19, we show the angular distributions of the 3-D WIMP velocity transformed from events shown in Figs. 16 and 18 to the horizontal coordinate system at the location of the LNGS laboratory (42.45°N, 13.58°E) as a demonstration for an underground laboratory located in the Northern Hemisphere. 50 total events on average in one experiment in one entire year (a) and in each of four 60-day observation periods of the *advanced* seasons (b – e) have been considered.

From the sketch of an underground laboratory located in the Northern Hemisphere in Winter in Fig. 10(a) combined with the sketches of the Earth's positions in Figs. 9(b) and 11, one can find that, first, during the observation period of the advanced Spring (see Fig. 19(b)), the main direction of incident WIMPs should be approximately towards the $-\mathbf{X}_{\mathrm{H,\,LNGS}}$–axis. Thus the highest–WIMP–flux bins is between 30°N and 30°S, from 150°E to 180°. Note here that there is a difference of ~ 24 days between the central date of the advanced Spring (49.49 day) and the date sketched in Fig. 10(a) (25.16 day). This corresponds to a shift of the angular distribution pattern of $\sim 24°$ westwards. Additionally, by definition of the horizontal coordinate system, the geographical difference between the LNGS laboratory and the Prime Meridian enlarge the shift of the angular distribution pattern by 13.58°. Totally, the overall shift of the angular distribution observed at the LNGS laboratory in the advanced Spring is $\sim 38°$ westwards.

Similar reason can explain the angular distribution of the advanced Winter (Fig. 19(e)). A difference of ~ 67 days between the central date of the advanced Winter (323.24 day) and the date sketched in Fig. 10(a) (390.16 day) corresponds to a shift of the angular distribution pattern of $\sim 66°$ eastwards now. In addition, in this observation period, more events should *come from* the direction *above* the horizon and result in the angular distribution with slightly higher event numbers in the *southern* sky.

On the other hand, from the sketch of a laboratory in the Northern Hemisphere in Summer (Fig. 1(a)) combined with the sketches in Figs. 9(b) and 11, one can also conclude that, from the (advanced) Summer to the (advanced) Autumn, most WIMPs should come from the zenith and the most part in the northern sky in Figs. 19(c) and (d) would hence have the lowest event numbers.

Finally, the angular distribution shown in Fig. 19(a) in one entire year is approximately a combination of the plots of four advanced seasons. Hence, as the angular distribution shown

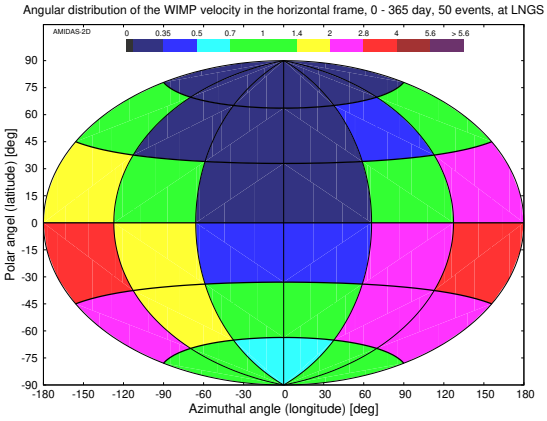

(a) 0 – 365 day

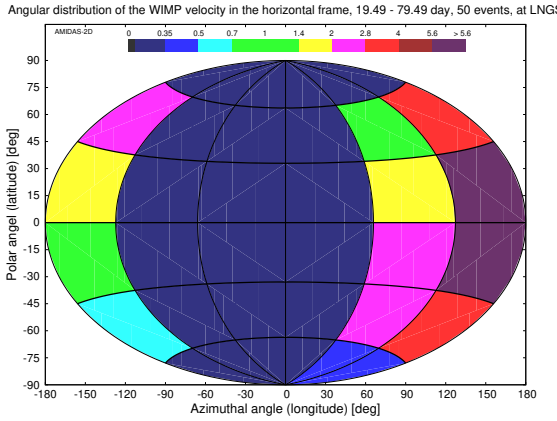

(b) 19.49 – 79.49 day

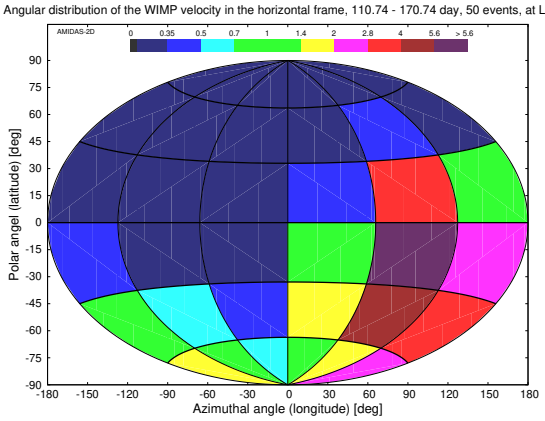

(c) 110.74 – 170.74 day

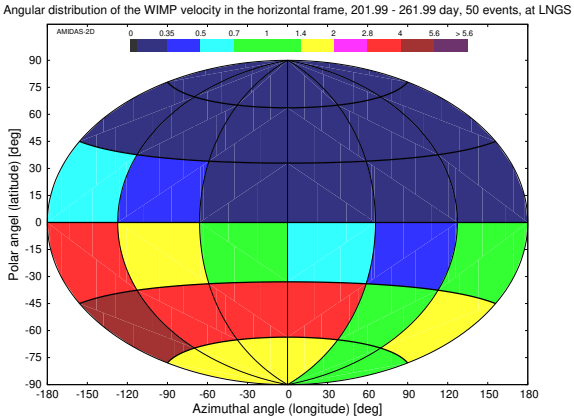

(d) 201.99 – 261.99 day

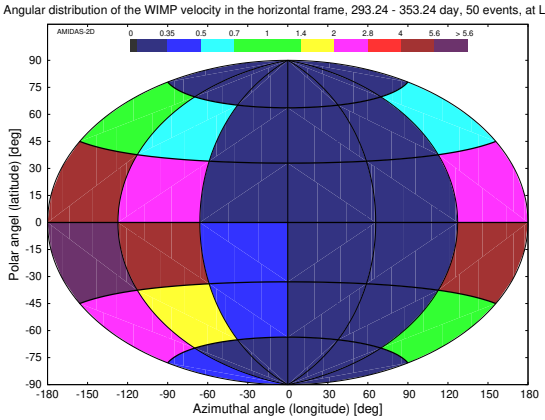

(e) 293.24 – 353.24 day

Figure 19: The angular distributions of the 3-D WIMP velocity in the horizontal coordinate system at the location of the LNGS laboratory (42.45°N, 13.58°E). 50 total events on average in one entire year (a) and in each of four *advanced* seasons (b – e) have been considered. All simulation setup and notations are the same as in Figs. 16 or 18, respectively.

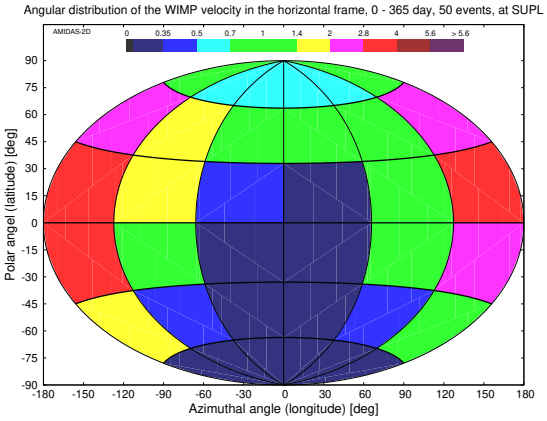

(a) 0 – 365 day

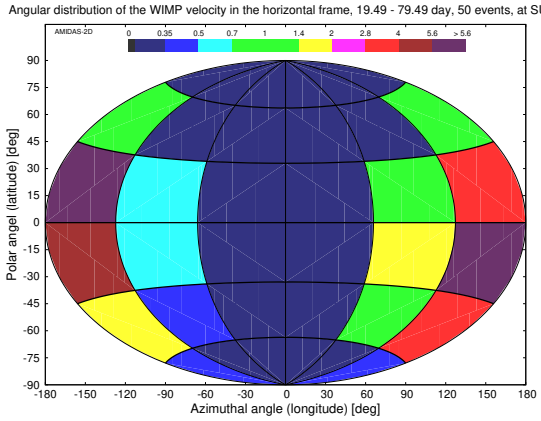

(b) 19.49 – 79.49 day

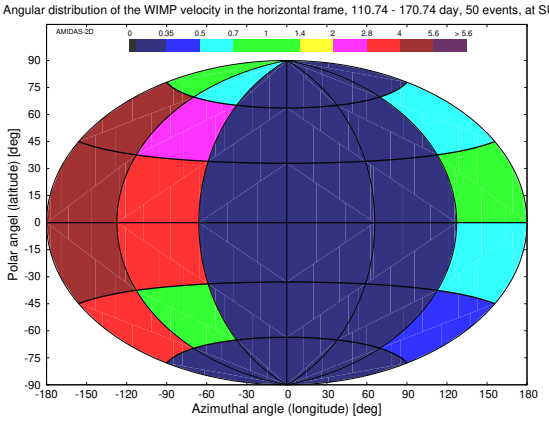

(c) 110.74 – 170.74 day

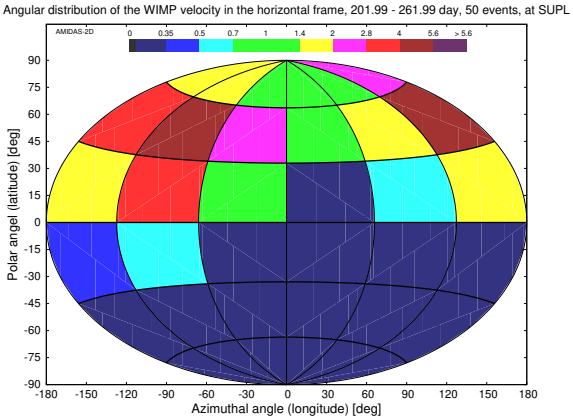

(d) 201.99 – 261.99 day

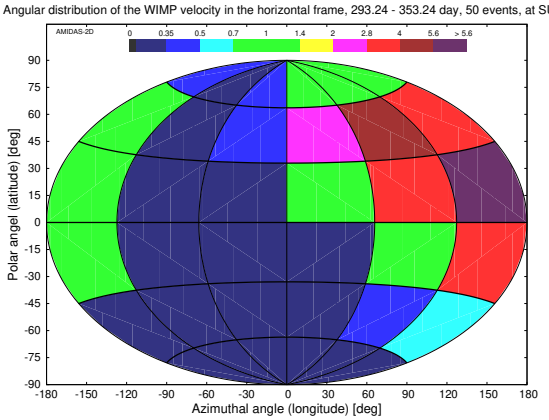

(e) 293.24 – 353.24 day

Figure 20: As in Figs. 19, except that the SUPL laboratory (37.07°S, 142.81°E), as the so far unique functionable underground laboratory in the Southern Hemisphere, has been considered.

in Fig. 16, due to the Earth's orbital motion around the Sun, the anisotropy of the incident direction of Galactic WIMPs would be averaged out, except of the lowest–WIMP–flux bins from the center (i.e., the north at the laboratory location) to the north pole (the zenith of the laboratory). From the sketches in Figs. 1(a) and 10(a) combined with the sketches in Figs. 9(b) and 11, one can find that these bins correspond exactly to the sky around the Earth's North Pole (see Fig. 16).

Moreover, in order to demonstrate the *location*–dependence of (the annual modulation of) the angular distribution pattern, in Figs. 20 we show also the angular distributions of the 3-D WIMP velocity in the horizontal coordinate system at the location of the SUPL laboratory (37.07°S, 142.81°E), which is so far the unique functionable underground laboratory in the Southern Hemisphere.

From Figs. 1(b) and 10(b) and the detailed discussions above, one would expect that, from the (advanced) Spring to the (advanced) Summer (Figs. 20(b) and (c)), the main direction of incident WIMPs should be towards the $-\mathbf{X}_{\mathrm{H,\,SUPL}}$–axis. This implies that the high–WIMP–flux bins should be close to the 180° longitude. Moreover, from the (advanced) Autumn to the (advanced) Winter, most WIMPs should come from the ground and thus the most part in the southern sky in Figs. 20(d) and (e) have the lowest event numbers. On the other hand, in contrast to Fig. 19(a), the angular distribution in one entire year in Fig. 20(a) shows the pattern with the lowest–WIMP–flux bins from the center to the south pole.

3.5 Angular WIMP velocity distribution in the laboratory frame

In this subsection, we present the angular distribution of the 3-D WIMP velocity in the laboratory coordinate system. Remind that the laboratory coordinate system not only moves orbitally around (and also linearly with) the Sun, but also rotates continuously. Thus the angular distribution in the laboratory coordinate system would also be averaged out, when a long observation period for accumulating enough WIMP events is required. Hence, in this subsection we only discuss the diurnal modulation of the angular distribution patterns. The angular distributions in one entire year and in four *advanced* seasons at the locations of several underground laboratories will be summarized in Appendix B as readers' reference.

Similar to Eqs. (32a) and (32b), the transformations (pure rotations) of the ith 3-D WIMP velocity between the horizontal and the laboratory coordinate systems can be given by

$$\mathbf{v}_{\chi,i,\mathrm{Lab}} = \mathbf{M}_{\mathrm{H}\to\mathrm{Lab}}(t_i, \phi_{\mathrm{Lab}}, \theta_{\mathrm{Lab}})\, \mathbf{v}_{\chi,i,\mathrm{H}}\,, \tag{33a}$$

and, conversely,

$$\mathbf{v}_{\chi,i,\mathrm{H}} = \mathbf{M}_{\mathrm{Lab}\to\mathrm{H}}(t_i, \phi_{\mathrm{Lab}}, \theta_{\mathrm{Lab}})\, \mathbf{v}_{\chi,i,\mathrm{Lab}}\,, \tag{33b}$$

where the transformation matrices $\mathbf{M}_{\mathrm{H}\to\mathrm{Lab}}(t, \phi_{\mathrm{Lab}}, \theta_{\mathrm{Lab}})$ and $\mathbf{M}_{\mathrm{Lab}\to\mathrm{H}}(t, \phi_{\mathrm{Lab}}, \theta_{\mathrm{Lab}})$ depending not only on the longitude and the latitude of the laboratory $(\phi_{\mathrm{Lab}}, \theta_{\mathrm{Lab}})$ but also on the measuring time t (t_{PM}) of each recorded WIMP event are given in Eqs. (A5b) and (A5a).

3.5.1 Diurnal modulation of the angular velocity distribution in the laboratory frame

In Figs. 21 and 22, we show the angular distributions of the 3-D WIMP velocity observed at the location of the LNGS laboratory (42.45°N, 13.58°E) in four daily shifts listed in Table 3[9] in

[9] Note that, in the simulations of the diurnal modulation of the angular WIMP velocity distribution presented in this paper, we have re–calculated the local time of each simulated event of the considered laboratory from the generated measuring UTC time.

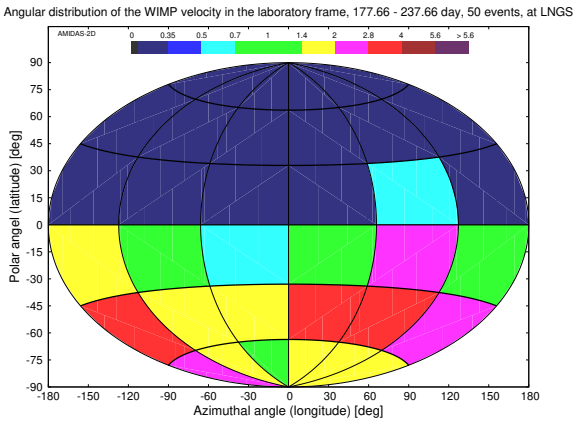

(a) 0 – 2 + 22 – 24 hour

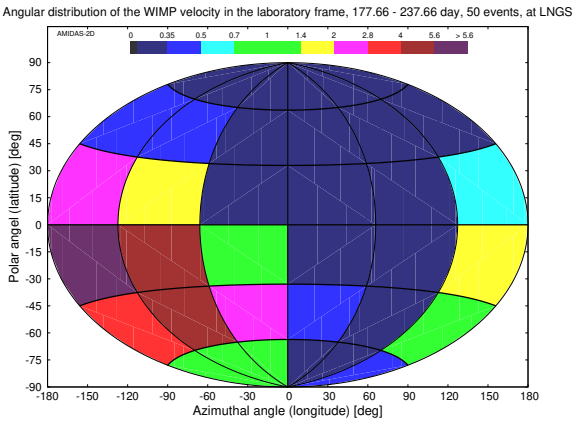

(b) 4 – 8 hour

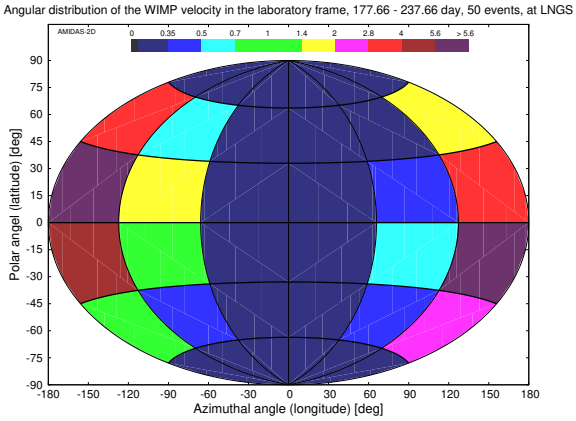

(c) 10 – 14 hour

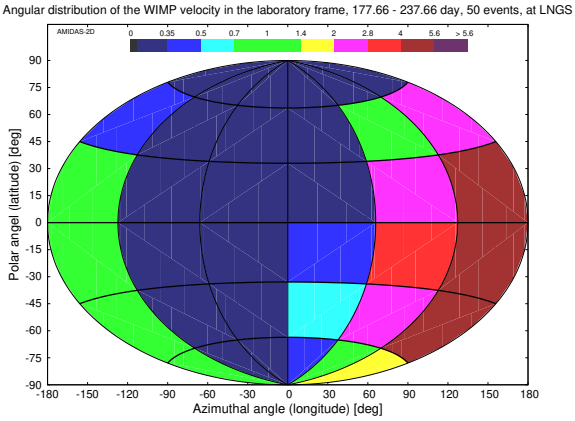

(d) 16 – 20 hour

Figure 21: The angular distributions of the 3-D WIMP velocity observed at the location of the LNGS laboratory (42.45°N, 13.58°E) in four daily shifts listed in Table 3 in the observation period of 177.66 – 237.66 day. 50 total events on average in each 4-hour daily shift in the 60-day observation period have been considered. All other simulation setup and notations are the same as in Figs. 19.

the observation period of 177.66 – 237.66 day and 360.16 – 420.16 (= 55.16) day, respectively. As usual, 50 total events on average in one experiment in each 4-hour daily shift in the 60-day observation period have been considered.

Not surprisingly, by comparing these two figures with each other, we can find first that, in two observation periods with a half–year time difference, the angular distribution patterns show indeed a 12-hour shift. Moreover, the diurnal modulations (from the midnight and morning shifts to the noon and evening shifts) in both of two periods look also similar to the annual modulation shown in Figs. 19 (b – e).

As in Sec. 3.4, in order to demonstrate the location–dependence of the diurnal modulation of the angular distribution of the 3-D WIMP velocity, in Figs. 23 and 24 we show also the angular distribution patterns observed at the location of the SUPL laboratory (37.07°S, 142.81°E) in four daily shifts in two observation periods. As expected, by comparing these two figures with each other and with Figs. 20, not only two observations described above, but also the location–

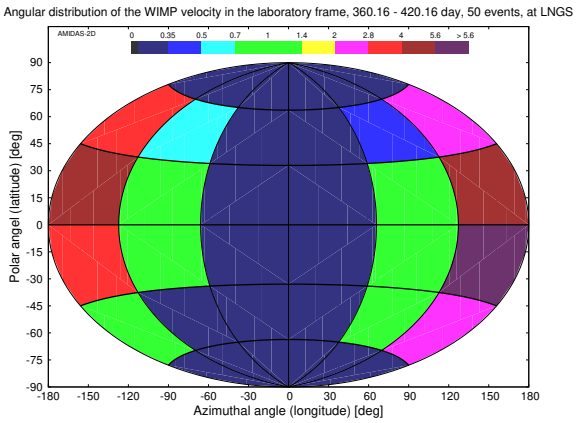

(a) 0 – 2 + 22 – 24 hour

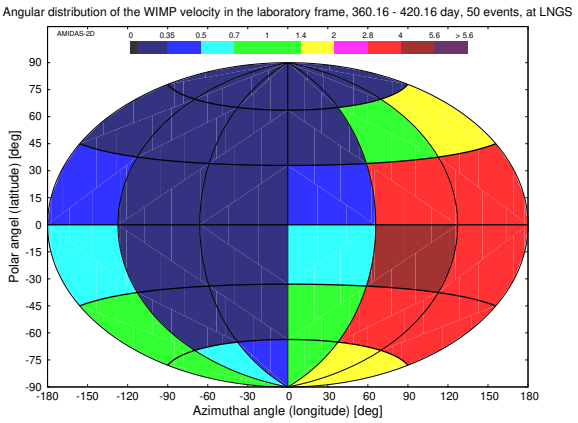

(b) 4 – 8 hour

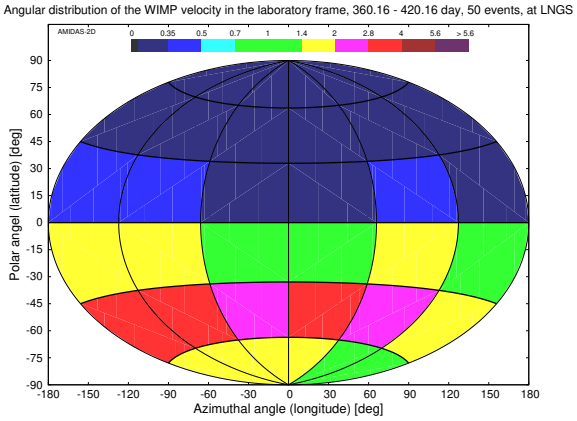

(c) 10 – 14 hour

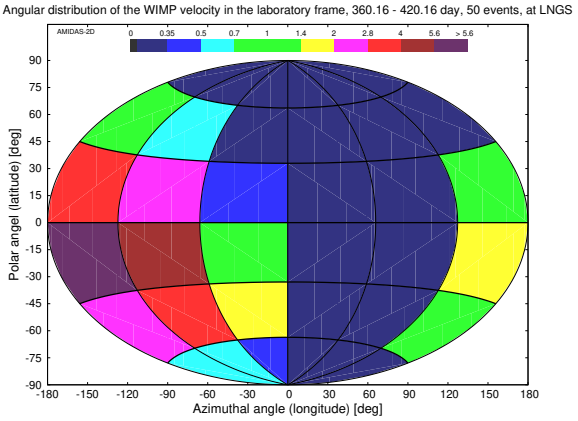

(d) 16 – 20 hour

Figure 22: As in Figs. 21, except that the observation period is now 360.16 – 420.16 (= 55.16) day.

dependence of (the annual modulation of) the angular distribution patterns observed in the horizontal coordinate system can be clearly confirmed.

In Appendix B, one can find more simulation results and discussions for other underground laboratories. Note only that, although the diurnal modulation in the laboratory coordinate system (or, in fact, in any laboratory's own reference frame) can be pretty clearly observed, a few tens of WIMP events accumulated in each a–few–hour daily shift in one observation period of a few tens of days would be required. This means in turn that a couple of thousands of WIMP events would be needed to observe in one or two years, which should be a very hard challenge for (directional) direct Dark Matter detection experiments in the near future.

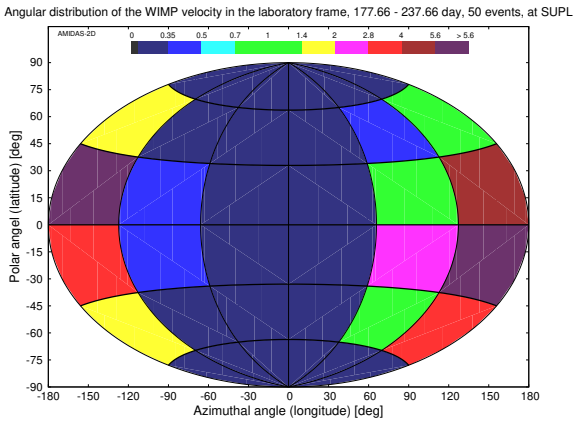

(a) 0 – 2 + 22 – 24 hour

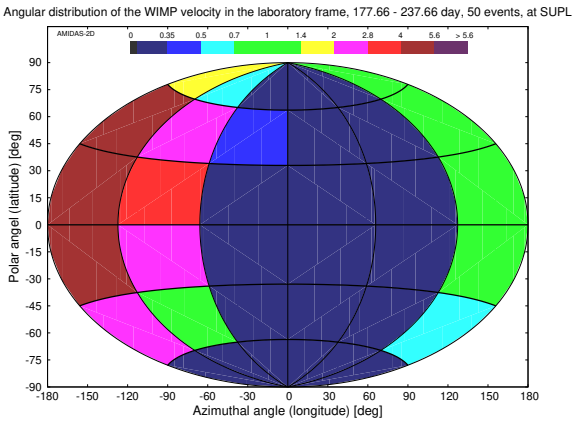

(b) 4 – 8 hour

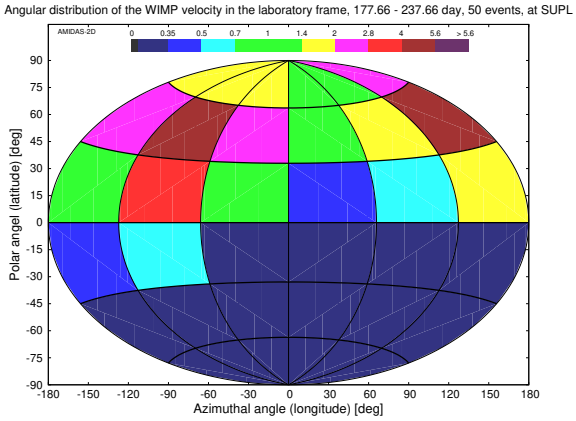

(c) 10 – 14 hour

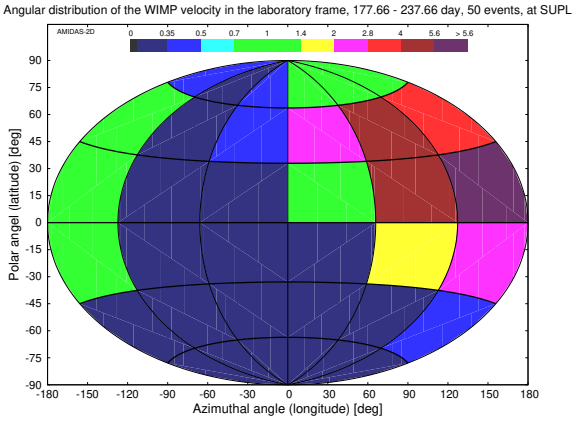

(d) 16 – 20 hour

Figure 23: As in Figs. 21, except that the SUPL laboratory (37.07°S, 142.81°E), as the so far unique functionable underground laboratory in the Southern Hemisphere, has been considered.

4 Bayesian reconstruction of the radial distribution of the 3-D WIMP velocity

In this section, we turn to analyze the radial distribution (magnitude) of the (transformed) 3-D WIMP velocity in the Equatorial coordinate system[10]. We discuss at first the radial distribution of the 3-D WIMP velocity transformed from events shown in Fig. 7 to the Equatorial coordinate system. Then we present the reconstruction results of (the annual modulation of) the radial WIMP velocity distribution by using the Bayesian fitting procedure described in Sec. 2.3.

4.1 Radial WIMP velocity distribution in the Equatorial frame

In Fig. 25 we show the radial distribution of the 3-D WIMP velocity transformed from events shown in Fig. 7 to the Equatorial coordinate system by using Eqs. (29a) and (30a). The solid

[10] Remind that the transformations between the Equatorial, the Earth, the horizontal, and the laboratory coordinate systems are only rotations. These vary thus only the directions (angular components) of the generated 3-D WIMP velocities, but keep their magnitudes (radial components) unchanged.

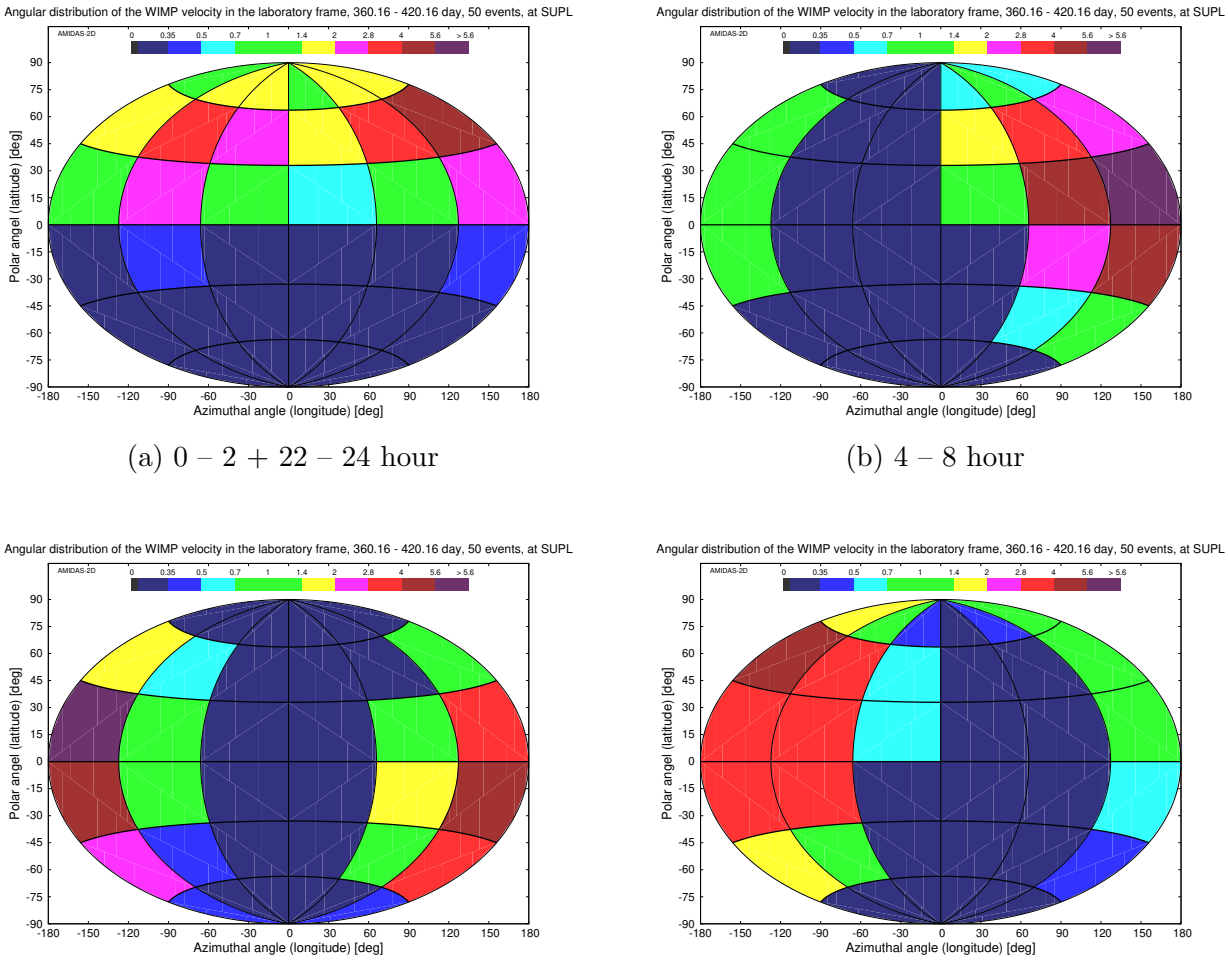

(a) 0 – 2 + 22 – 24 hour

(b) 4 – 8 hour

(c) 10 – 14 hour

(d) 16 – 20 hour

Figure 24: As in Figs. 23, except that the observation period is now 360.16 – 420.16 (= 55.16) day.

red curve is the shifted Maxwellian velocity distribution $f_{1,\mathrm{sh,vesc}}(v)$ given in Eq. (19) with the input value of $v_0 = 220$ km/s and $v_\mathrm{e} = 1.05\, v_0$, while the dashed black histogram shows the binned radial component of the transformed 3-D WIMP velocities and the thin vertical dashed black lines indicate the 1σ Poisson statistical uncertainties on the recorded event numbers in the v–bins. One entire year (0 to 365 day) and 50 total events on average in one experiment have been considered. Remind that the maximal cut–off velocity here is given by $v_\mathrm{max} = 781$ km/s.

It can be found that, firstly, although the theoretical (solid red) curve falls inside the 1σ statistical uncertainty range of the radial distribution of the 3-D WIMP velocity, the theoretical distribution seems to be slightly higher than the histogram in the velocity ranges of 100 km/s $\lesssim v \lesssim$ 200 km/s and 400 km/s $\lesssim v \lesssim$ 700 km/s, while in the velocity range around the peak (close to the average value) of the theoretical distribution (200 km/s $\lesssim v \lesssim$ 400 km/s), the radial distribution of the simulated WIMP velocity is obviously higher than the theoretical prediction. This indicates that there would be more WIMPs with middle–value velocities, but fewer WIMPs with relatively lower or higher velocities than theoretically predicted. In Sec. 5.2, we will see that, with $\mathcal{O}(500)$ total WIMP events and a higher analysis resolution, the difference between the simulated radial WIMP velocity distribution and the theoretical prediction would

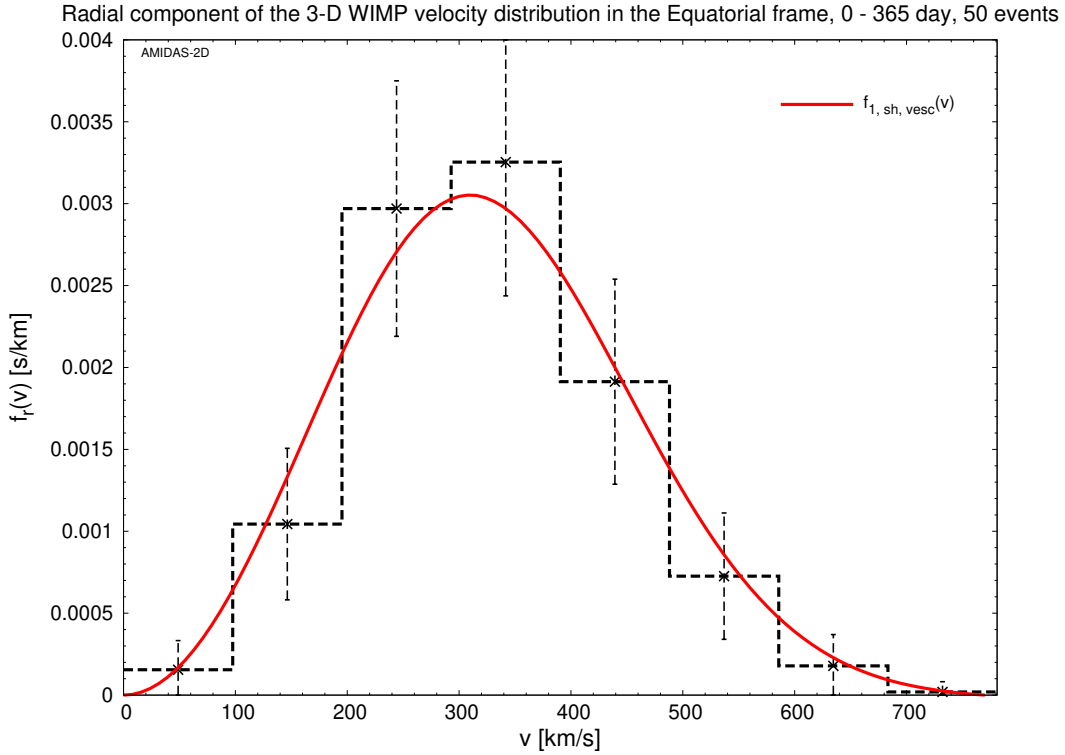

Figure 25: The radial distribution of the 3-D WIMP velocity transformed from events shown in Fig. 7 to the Equatorial coordinate system by using Eqs. (29a) and (30a). The solid red curve is the shifted Maxwellian velocity distribution $f_{1,\mathrm{sh,vesc}}(v)$ given in Eq. (19) with the input value of $v_0 = 220$ km/s and $v_\mathrm{e} = 1.05\, v_0$, while the dashed black histogram shows the binned radial component of the transformed 3-D WIMP velocities and the thin vertical dashed black lines indicate the 1σ Poisson statistical uncertainties on the recorded event numbers in the v–bins. One entire year (0 to 365 day) and 50 total events on average have been considered. Remind that the maximal cut–off velocity here is given by $v_\mathrm{max} = 781$ km/s.

become more obviously.

4.2 Fitted radial WIMP velocity distributions in the Equatorial frame

Since we found *unexpectedly* that the simulated radial WIMP velocity distribution in the Equatorial coordinate system could not match the theoretical prediction well, we considered then to apply the Bayesian fitting technique to reconstruct the radial component of the transformed 3-D WIMP velocity shown in Fig. 25, in order to find out the most suitable radial WIMP velocity distribution as well as to obtain the best–fit values of the Solar and Earth's Galactic velocities, v_0 and v_e. In this and the next subsections, we discuss our reconstruction results by using the Bayesian fitting procedure with four fitting velocity distributions given in Sec. 2.3.3.

4.2.1 With the one–parameter velocity distribution $f_{1,\mathrm{sh},v_0}(v; v_0)$

We consider at first the one–parameter shifted Maxwellian velocity distribution $f_{1,\mathrm{sh},v_0}(v; v_0)$ given by Eq. (24) with the constraint that $v_\mathrm{e} = 1.05\, v_0$. The fitting parameter v_0 has been scanned in the range of 160 km/s $\leq v_0 \leq$ 270 km/s.

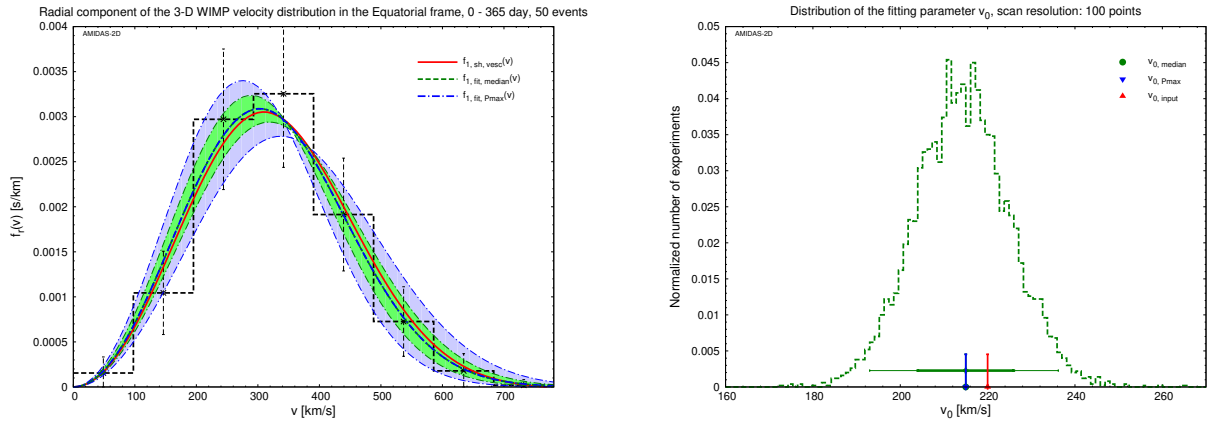

(a) (b)

Figure 26: (a) The reconstructed radial distributions of the 3-D WIMP velocity and the $1(2)\sigma$ statistical uncertainty bands by using the one–parameter shifted Maxwellian velocity distribution $f_{1,\mathrm{sh},v_0}(v;v_0)$ given by Eq. (24) to fit data shown in Fig. 25. The solid red curve is the shifted Maxwellian velocity distribution $f_{1,\mathrm{sh,vesc}}(v)$ given in Eq. (19) with the input value of $v_0 = 220$ km/s and $v_\mathrm{e} = 1.05\,v_0$. While the dashed green curve labeled with the subscript "median" indicates the reconstructed velocity distribution with the fitting parameter v_0 given by the median value of all simulated experiments, the dash–dotted blue curve labeled with the subscript "Pmax" indicates the reconstructed velocity distribution with v_0 maximizing $\mathrm{P}_\mathrm{mean}\,(a_i,\ i=1,\ 2,\ \cdots,\ N_\mathrm{Bayesian})$ defined in Eq. (18). (b) The distribution of the fitting parameter v_0 in all simulated experiments. The red vertical line labeled with the subscript "input" indicates the input value of v_0, whereas the green vertical line labeled with the subscript "median" and the blue one labeled with the subscript "Pmax" indicate the median value of the simulated results and the value which maximizes P_mean, respectively. In addition, the horizontal thick (thin) green bars show the $1(2)\sigma$ ranges of the reconstructed results. See the text for further details.

In Fig. 26(a), we show the reconstructed radial distributions of the 3-D WIMP velocity and the $1(2)\sigma$ statistical uncertainty bands by using $f_{1,\mathrm{sh},v_0}(v;v_0)$ to fit data shown in Fig. 25. The solid red curve is the shifted Maxwellian velocity distribution $f_{1,\mathrm{sh,vesc}}(v)$ given in Eq. (19) with the input value of $v_0 = 220$ km/s and $v_\mathrm{e} = 1.05 v_0$. While the dashed green curve labeled with the subscript "median" indicates the reconstructed velocity distribution with the fitting parameter v_0 given by the median value of all simulated experiments, the dash–dotted blue curve labeled with the subscript "Pmax" indicates the reconstructed velocity distribution with v_0 maximizing $\mathrm{P}_\mathrm{mean}\,(a_i,\ i=1,\ 2,\ \cdots,\ N_\mathrm{Bayesian})$ defined in Eq. (18).

Additionally, the light–green (light–blue) area shown here indicate the $1(2)\sigma$ statistical uncertainty bands of the Bayesian reconstructed velocity distribution, which has been determined as follows. After scanning the reconstructed fitting parameter v_0 obtained from all simulated experiments and ordering according to their P_mean values defined in Eq. (18) descendingly, we can not only determine the point which maximizes P_mean (labeled with the subscript "Pmax" in our plots hereafter), but also the smallest and largest values of the first 68.27% (95.45%) of all reconstructed v_0's. We then use the smallest (largest) value of the first 68.27% (95.45%) reconstructed v_0's to give the $1(2)\sigma$ lower (upper) boundaries of the Bayesian reconstructed velocity distribution. This means that all of the velocity distributions with v_0's which give the largest

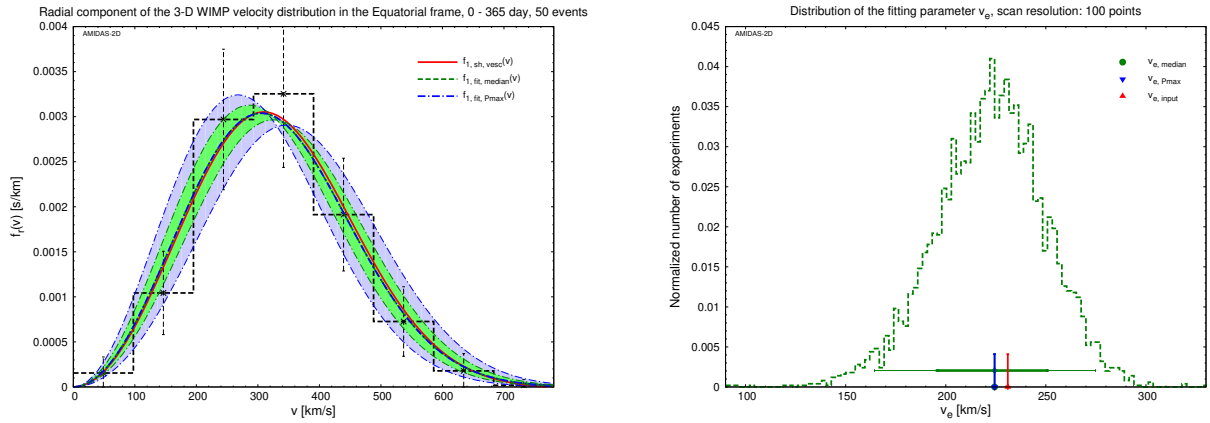

(a) (b)

Figure 27: (a) The reconstructed radial distributions of the 3-D WIMP velocity and the $1(2)\sigma$ statistical uncertainty bands by using the v_0–fixed shifted Maxwellian velocity distribution $f_{1,\mathrm{sh},v_\mathrm{e}}(v;v_\mathrm{e})$ given by Eq. (26) to fit data shown in Fig. 25. (b) The distribution of the fitting parameter v_e in all simulated experiments. The red vertical line labeled with the subscript "input" indicates the theoretical value of $v_\mathrm{e} = 1.05\,v_0 = 231$ km/s. Other notations are the same as in Figs. 26.

68.27% (95.45%) $\mathrm{P_{mean}}$ values should be in the $1(2)\sigma$ light–green (light–blue) areas.

Meanwhile, Fig. 26(b) shows the distribution of the fitting parameter v_0 in all simulated experiments. The red vertical line labeled with the subscript "input" indicates the input value of v_0, whereas the green vertical line labeled with the subscript "median" and the blue one labeled with the subscript "Pmax" indicate the median value of the simulated results and the value which maximizes $\mathrm{P_{mean}}$, respectively. In addition, the horizontal thick (thin) green bars show the $1(2)\sigma$ ranges of the reconstructed results.

It can be seen that the best–fit value of $v_0 = 215.0$ km/s is only a little bit (0.45σ, see Table 4) smaller than the input value of 220 km/s and thus the best–fit distribution curve would be very close to the theoretically derived shifted Maxwellian velocity distribution $f_{1,\mathrm{sh},v_\mathrm{esc}}(v)$. However, as found in Sec. 4.1, the best–fit velocity distribution shown here differs clearly from the simulated radial distribution of the 3-D WIMP velocity.

4.2.2 With the v_0–fixed velocity distribution $f_{1,\mathrm{sh},v_\mathrm{e}}(v;v_\mathrm{e})$

As shown in Sec. 4.2.1, by using v_0 as the unique fitting parameter with the fixed relation between v_0 and v_e, the reconstructed velocity distribution can *not* fit the simulated radial distribution of the 3-D WIMP velocity as well as we hoped. Hence, we consider here the v_0–fixed shifted Maxwellian velocity distribution $f_{1,\mathrm{sh},v_\mathrm{e}}(v;v_\mathrm{e})$ given by Eq. (26) with the input condition that $v_0 = 220$ km/s (although the best–fit value of v_0 obtained in Sec. 4.2.1 is 215.0 km/s) and scan the Earth's Galactic velocity v_e in the range of 90 km/s $\leq v_\mathrm{e} \leq$ 330 km/s.

In Fig. 27(a), we show the reconstructed radial distributions of the 3-D WIMP velocity and the $1(2)\sigma$ statistical uncertainty bands by using $f_{1,\mathrm{sh},v_\mathrm{e}}(v;v_\mathrm{e})$ to fit data shown in Fig. 25. Also, in Fig. 27(b), we give the distribution of the fitting parameter v_e in all simulated experiments. The red vertical line labeled with the subscript "input" indicates the theoretical value of $v_\mathrm{e} = 1.05\,v_0 = 231$ km/s. Unfortunately and unexpectedly, we have obtained a similar result as in Sec. 4.2.1: the best–fit value of $v_\mathrm{e} = 224.4$ km/s is only a little bit (0.25σ, see Table 4)

smaller than the theoretical value of 231 km/s, and thus the best–fit distribution curve would be very close to the theoretical derivation $f_{1,\mathrm{sh},v_{\mathrm{esc}}}(v)$, but *not* be improved to fit the simulated radial WIMP velocity distribution very much (as we hoped).

4.2.3 With the simplified velocity distribution $f_{1,\mathrm{sh}}(v; v_0, v_{\mathrm{e}})$

Our fitting results shown in Secs. 4.2.1 and 4.2.2 indicate that, although the best–fit values of $v_0 = 215.0$ km/s and $v_{\mathrm{e}} = 224.4$ km/s are only a little bit smaller than the theoretical values and thus the best–fit distribution curves would be very close to the theoretically predicted shifted Maxwellian velocity distribution $f_{1,\mathrm{sh},v_{\mathrm{esc}}}(v)$, there would obviously be some systematic bias between the theoretical derivation and our (Monte Carlo–simulated) radial velocity distribution. Hence, we release now the constraints on both of the fitting parameters v_0 and v_{e}, use the simplified shifted Maxwellian velocity distribution $f_{1,\mathrm{sh}}(v; v_0, v_{\mathrm{e}})$ given by Eq. (27) and scan the parameter plane of 80 km/s $\leq v_0 \leq$ 340 km/s and $0 \leq v_{\mathrm{e}} \leq$ 380 km/s in order to obtain a better–fitted WIMP velocity distribution[11].

In Fig. 28(a), we show the reconstructed radial distributions of the 3-D WIMP velocity and the $1(2)\sigma$ statistical uncertainty bands by using $f_{1,\mathrm{sh}}(v; v_0, v_{\mathrm{e}})$ to fit data shown in Fig. 25. It can be seen that, while the red theoretically derived velocity distribution (19) could still be covered by the 1σ statistical uncertainty band, except of in the ranges around two turning points: $v \sim 270$ km/s and $v \sim 550$ km/s, the best–fit velocity distributions would now clearly differ from the theoretical derivation, but indeed fit to our simulated radial distribution of the 3-D WIMP velocity much better.

Meanwhile, Fig. 28(b) shows the distribution of the fitting parameters v_0 and v_{e} in all simulated experiments on the $v_0 - v_{\mathrm{e}}$ plane. The light–green (light–blue, golden) square points indicate the $1(2, > 2)\sigma$ areas of the reconstructed combination of v_0 and v_{e}. While the red upward–triangle labeled with the subscript "input" indicates the theoretical values of $v_0 = 220$ km/s and $v_{\mathrm{e}} = 231$ km/s, the green disk labeled with the subscript "median" and the blue downward–triangle labeled with the subscript "Pmax" indicate the median values of the simulated results and the point which maximizes $\mathrm{P}_{\mathrm{mean}}$, respectively. Additionally, Figs. 28(c) and (d) show the distributions of the fitting parameters v_0 and v_{e} in all simulated experiments separately.

Corresponding to the reconstructed radial distributions, from these three plots one can find that, while the best–fit values of $v_0 \simeq 190$ km/s are $\sim 14\%$ smaller than the input value, those of $v_{\mathrm{e}} = 258.4$ km/s are now $\sim 12\%$ *larger* than its theoretical value (see also Table 4), although (the combination of) the theoretical values of our fitting parameters could still fall inside their 1σ statistical uncertainty (green) area/ranges. Consequently, the ratio between the best–fit values of v_0 and v_{e} is ~ 1.4, much larger than the commonly adopted theoretical value of 1.05 [65] and our estimate of 1.0078.[12] Note also that, due to the pretty small ($\mathcal{O}(50)$) simulated total event number and thus a large statistical fluctuation, there is a long distribution tail at the lower scanning boundary of v_{e} in Fig. 28(b). In Sec. 5.2, we will see that, once the total event number is raised to $\mathcal{O}(500)$ and thus the statistics is improved, this tail would disappear.

4.2.4 With the modified velocity distribution $f_{1,\mathrm{sh},\Delta v}(v; v_0, \Delta v)$

In Ref. [68], we introduced the modified shifted Maxwellian velocity distribution $f_{1,\mathrm{sh},\Delta v}(v; v_0, \Delta v)$ given by Eq. (28) for reducing the systematic bais of the best–fit results obtained by using the simplified velocity distribution $f_{1,\mathrm{sh}}(v; v_0, v_{\mathrm{e}})$. For checking and potentially also improving

[11] Note that the scanning ranges of both of v_0 and v_{e} are extended from those used for the one–parameter and the v_0–fixed velocity distributions in Secs. 4.2.1 and 4.2.2.

[12] See Appendix A.3.4 for the detailed calculation.

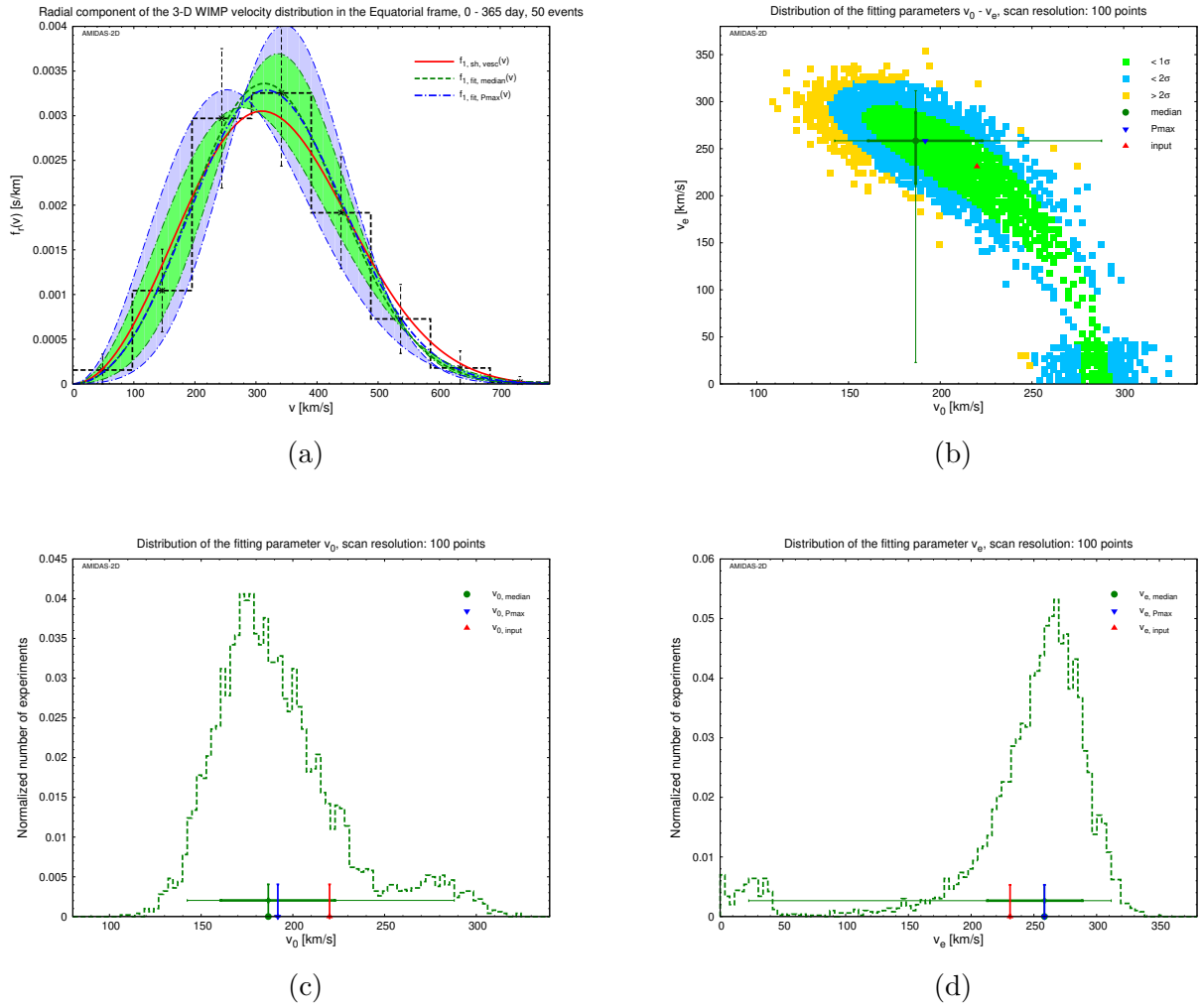

Figure 28: (a) The reconstructed radial distributions of the 3-D WIMP velocity and the $1(2)\sigma$ statistical uncertainty bands by using the simplified shifted Maxwellian velocity distribution $f_{1,\rm sh}(v; v_0, v_{\rm e})$ given by Eq. (27) to fit data shown in Fig. 25. Notations are the same as in Fig. 26(a). (b) The distribution of the fitting parameters v_0 and $v_{\rm e}$ in all simulated experiments on the $v_0 - v_{\rm e}$ plane. The light–green (light–blue, golden) square points indicate the $1(2, > 2)\sigma$ areas of the reconstructed combination of v_0 and $v_{\rm e}$. While the red upward–triangle labeled with the subscript "input" indicates the theoretical values of $v_0 = 220$ km/s and $v_{\rm e} = 231$ km/s, the green disk labeled with the subscript "median" and the blue downward–triangle labeled with the subscript "Pmax" indicate the median values of the simulated results and the point which maximizes $\rm P_{mean}$, respectively. The meaning of the horizontal and vertical thick (thin) green bars are the same as in Figs. 26(b) and 27(b). (c) As in Figs. 26(b). (d) As in Figs. 27(b).

our reconstruction results shown in Sec. 4.2.3, we apply now the modified velocity distribution $f_{1,{\rm sh},\Delta v}(v; v_0, \Delta v)$ and scan the parameter plane of 80 km/s $\leq v_0 \leq$ 340 km/s and -190 km/s $\leq \Delta v \leq$ 230 km/s.

In Fig. 29(a) we show the reconstructed radial distributions of the 3-D WIMP velocity and the $1(2)\sigma$ statistical uncertainty bands by using $f_{1,{\rm sh},\Delta v}(v; v_0, \Delta v)$ to fit data shown in Fig. 25. Not surprisingly, the reconstructed velocity distributions as well as the $1(2)\sigma$ statistical uncertainty bands have similar shapes as those shown in Fig. 28(a).

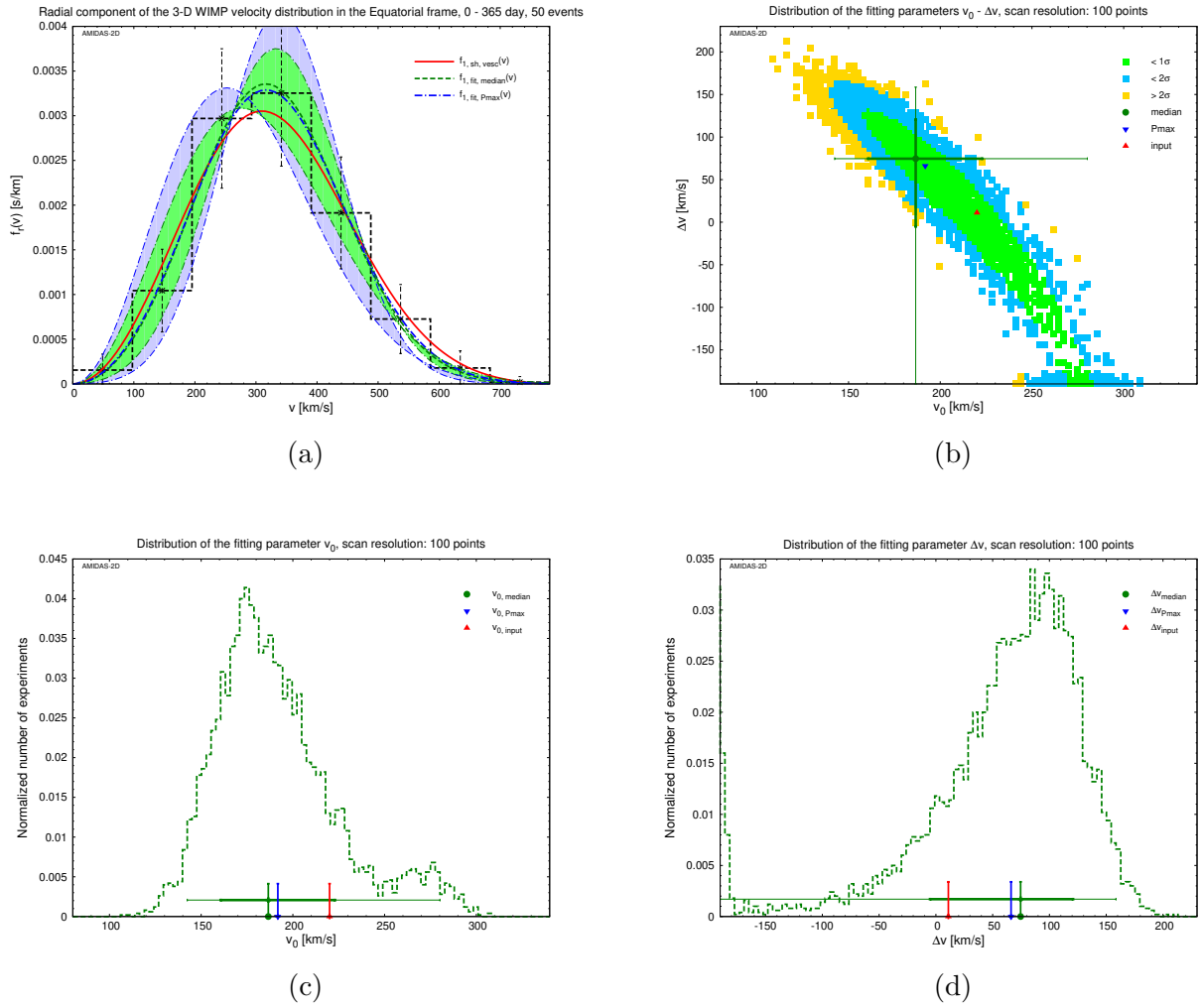

Figure 29: (a) The reconstructed radial distributions of the 3-D WIMP velocity and the $1(2)\sigma$ statistical uncertainty bands by using the modified shifted Maxwellian velocity distribution $f_{1,\mathrm{sh},\Delta v}(v; v_0, \Delta v)$ given by Eq. (28) to fit data shown in Fig. 25. Notations are the same as in Fig. 26(a). (b) The distribution of the fitting parameters v_0 and Δv in all simulated experiments on the $v_0 - \Delta v$ plane. The light–green (light–blue, golden) square points indicate the $1(2, > 2)\sigma$ areas of the reconstructed combination of v_0 and Δv. The red upward–triangle labeled with the subscript "input" indicates the theoretical values of $v_0 = 220$ km/s and $\Delta v = 11$ km/s. Other notations are the same as in Fig. 28(b). (c) As in Figs. 26(b). (d) As in Figs. 27(b).

Meanwhile, Fig. 29(b) shows the distribution of the fitting parameters v_0 and Δv in all simulated experiments on the $v_0 - \Delta v$ plane. The light–green (light–blue, golden) square points indicate the $1(2, > 2)\sigma$ areas of the reconstructed combination of v_0 and Δv. While the red upward–triangle labeled with the subscript "input" indicates the theoretical values of $v_0 = 220$ km/s and $\Delta v = 11$ km/s, the green disk labeled with the subscript "median" and the blue downward–triangle labeled with the subscript "Pmax" indicate the median values of the simulated results and the point which maximizes $\mathrm{P_{mean}}$, respectively. As shown in 28(b), one can also see here a long distribution tail at the lower scanning boundary of Δv. Additionally, Figs. 29(c) and (d) show the distribution of the fitting parameters v_0 and Δv in all simulated experiments separately.

Fitting dist.	Parameter	Max. $P_{\rm median}$	Median	1σ range	2σ range
$f_{1,{\rm sh},v_0}(v)$	v_0 [km/s]	215.0	$215.0 \pm 11.0\,(^{+21.2}_{-22.0})$	[204.0, 226.0]	[193.0, 236.2]
$f_{1,{\rm sh},v_{\rm e}}(v)$	$v_{\rm e}$ [km/s]	224.4	$224.4\,^{+26.4}_{-28.8}\,(^{+50.4}_{-60.0})$	[195.6, 250.8]	[164.4, 274.8]
$f_{1,{\rm sh}}(v)$	v_0 [km/s]	191.8	$186.6\,^{+36.4}_{-26.0}\,(^{+101.4}_{-\ 44.2})$	[160.6, 223.0]	[142.4, 288.0]
	$v_{\rm e}$ [km/s]	258.4	$258.4\,^{+30.4}_{-45.6}\,(^{+\ 53.2}_{-235.6})$	[212.8, 288.8]	[22.8, 311.6]
$f_{1,{\rm sh},\Delta v}(v)$	v_0 [km/s]	191.8	$186.6\,^{+36.4}_{-26.0}\,(^{+93.6}_{-44.2})$	[160.6, 223.0]	[142.4, 280.2]
	Δv [km/s]	66.2	$74.6\,^{+46.2}_{-79.8}\,(^{+\ 84.0}_{-264.6})$	[−5.2, 120.8]	[−190.0, 158.6]
50 total events on average in the observation period of 0 – 365 day					

Table 4: The summary of the reconstructed results of the fitting parameters and their $1(2)\sigma$ statistical uncertainty ranges of the median values by using four considered fitting velocity distributions with 50 total events on average in one entire year shown in Figs. 26, 27, 28, and 29.

From these three plots one can confirm that, first, the best–fit values of $v_0 \simeq 190$ km/s are the same as the results obtained by using the simplified velocity distribution (see also Table 4). Second, the best–fit values of $\Delta v \simeq 70$ km/s are also equal to the difference between v_0 and $v_{\rm e}$ obtained previously. Note however that, the $1(2)\sigma$ statistical uncertainties on Δv would be at least 1.5 times larger than those on $v_{\rm e}$ (see Table 4).

In Table 4, we summarize the reconstructed results of the fitting parameters and their $1(2)\sigma$ statistical uncertainty ranges of the median values with 50 total events on average in one entire year for all four considered fitting velocity distributions shown in Figs. 26, 27, 28, and 29.

4.3 Annual modulation of the radial distribution of the 3-D WIMP velocity

In this subsection, we discuss the annual modulation of the radial distribution of the 3-D WIMP velocity and present the reconstructed radial WIMP velocity distributions in the observation periods of four *advanced* seasons[13].

4.3.1 With the one–parameter velocity distribution $f_{1,{\rm sh},v_0}(v; v_0)$

As in Sec. 4.2, we consider at first the one–parameter velocity distribution $f_{1,{\rm sh},v_0}(v; v_0)$ with v_0 as the fitting parameter and the constraint that $v_{\rm e} = 1.05\, v_0$. Note however that, although the

[13] For the sake of completeness and readers' reference, the reconstructed radial WIMP velocity distributions for four normal seasons will be given in Appendix C.

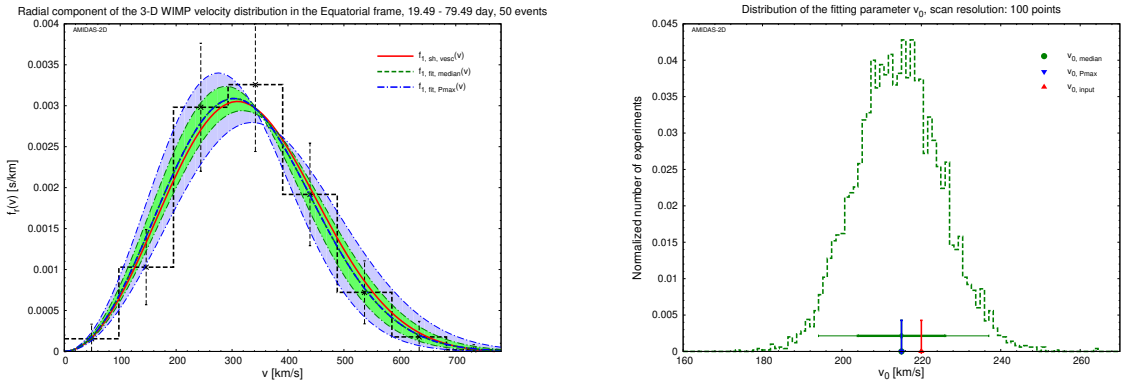

(a) 19.49 – 79.49 day

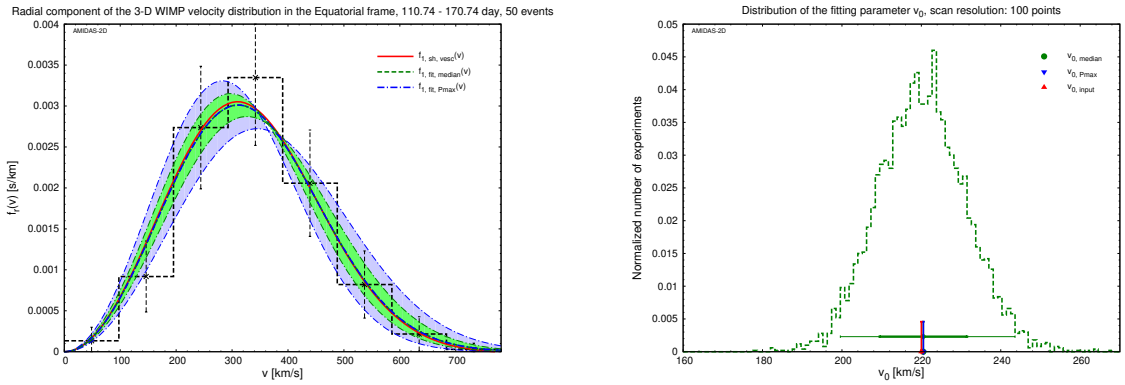

(b) 110.74 – 170.74 day

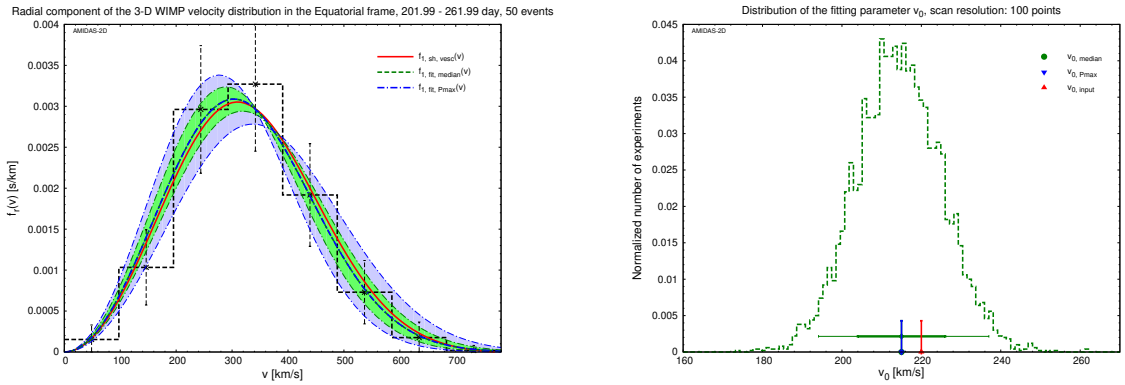

(c) 201.99 – 261.99 day

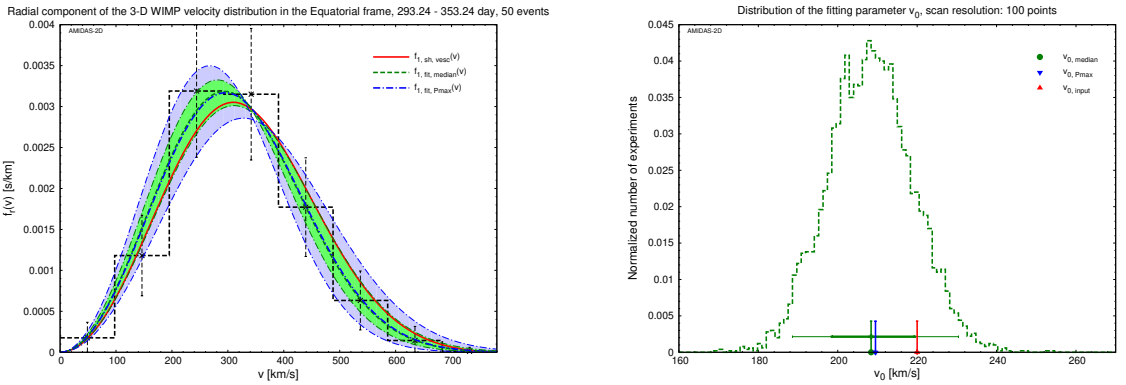

(d) 293.24 – 353.24 day

Figure 30: As in Figs. 26, reconstructed with the one–parameter velocity distribution $f_{1,\mathrm{sh},v_0}(v;v_0)$, except that four 60-day observation periods of the advanced seasons have been considered.

Fitting distribution: one–parameter velocity distribution $f_{1,\mathrm{sh},v_0}(v;v_0)$					
Central date (observation period) (day)	Parameter	Max. $\mathrm{P}_{\mathrm{median}}$	Median	1σ range	2σ range
49.49 (19.49 – 79.49)	v_0 [km/s]	215.0	$215.0 \pm 11.0\,(^{+22.0}_{-20.9})$	[204.0, 226.0]	[194.1, 237.0]
140.74 (110.74 – 170.74)	v_0 [km/s]	220.5	$220.5 \pm 11.0\,(^{+23.1}_{-20.9})$	[209.5, 231.5]	[199.6, 243.6]
231.99 (201.99 – 261.99)	v_0 [km/s]	215.0	$215.0 \pm 11.0\,(^{+22.0}_{-20.9})$	[204.0, 226.0]	[194.1, 237.0]
323.24 (293.24 – 353.24)	v_0 [km/s]	209.5	$208.4\,^{+11.0}_{-\ 9.9}\,(^{+22.0}_{-19.8})$	[198.5, 219.4]	[188.6, 230.4]
50 total events on average in one observation period of 60 days					

Table 5: The summary of the reconstructed results of the fitting parameter v_0 and their $1(2)\sigma$ statistical uncertainty ranges of the median values by using the one–parameter velocity distribution $f_{1,\mathrm{sh},v_0}(v;v_0)$ with 50 total events on average in each 60–day observation period of the advanced seasons.

fitting parameter v_0 is in fact the Solar Galactic velocity and should be fixed in the whole year, it has been used here as a normal fitting parameter[14].

In Figs. 30, we show the reconstructed radial WIMP velocity distributions and the $1(2)\sigma$ statistical uncertainty bands by using $f_{1,\mathrm{sh},v_0}(v;v_0)$ as well as the distributions of the fitting parameter v_0 in all simulated experiments for four advanced seasons. Firstly, from the plots in the left column of Figs. 30, one can see the variation of the radial distributions of the 3-D WIMP velocity in different seasons: the event numbers in the high–velocity bins ($v \gtrsim 290$ km/s) vary (from top to bottom) at first more and then fewer; in contrast, the event numbers in low–velocity bins ($v \lesssim 290$ km/s) at first fewer and then more. This can be observed in particularly clearly from the variation of the difference between the third and the forth v–bins around the distribution peak. This implies that the (average) velocity of the simulated WIMP events indeed increases at first to the maximum (in the advanced Summer) and then reduces to the minimum (in the advanced Winter). Secondly and more importantly, the reconstructed velocity distributions and their $1(2)\sigma$ statistical uncertainty bands follow the variation of the histogram in different seasons as tightly as possible. Note that the red theoretically derived curve shown in the left column of Figs. 30 is time–*independent*.

Moreover, from the plots in the right column of Figs. 30, the *symmetric periodic* variation of the fitting parameter v_0 of 215.0 ($\pm \sim 5.5$) km/s can also be seen clearly. It would be worth to notice here that the $\sim \pm 5.5$ km/s annual variation of the best–fit value of v_0 is $\sim 0.5\sigma$ of the statistical uncertainties on v_0 (see the summary given in Table 4) and approximately equal

[14] In Secs. 4.3.3 and 4.3.4, we will see that, once our constraints on v_0 and v_{e} are released and two fitting parameters, v_0 and v_{e} (or Δv), are used, the best–fit values of v_0 would indeed be a constant.

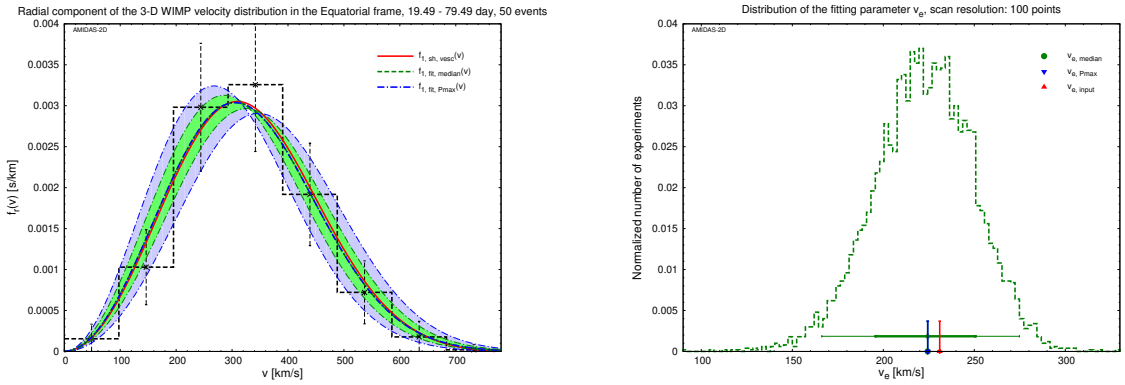

(a) 19.49 – 79.49 day

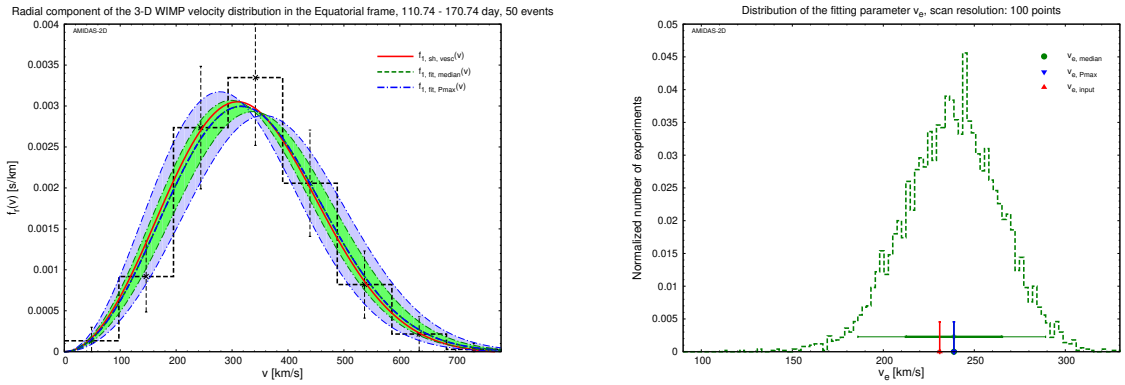

(b) 110.74 – 170.74 day

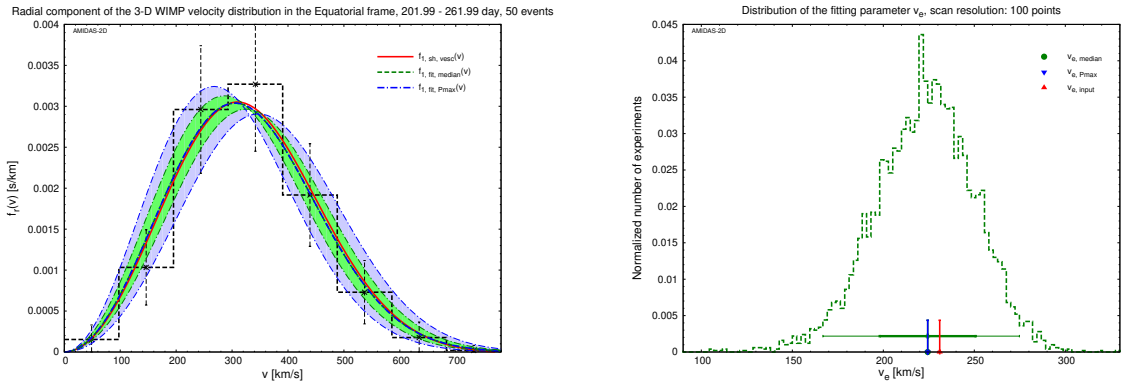

(c) 201.99 – 261.99 day

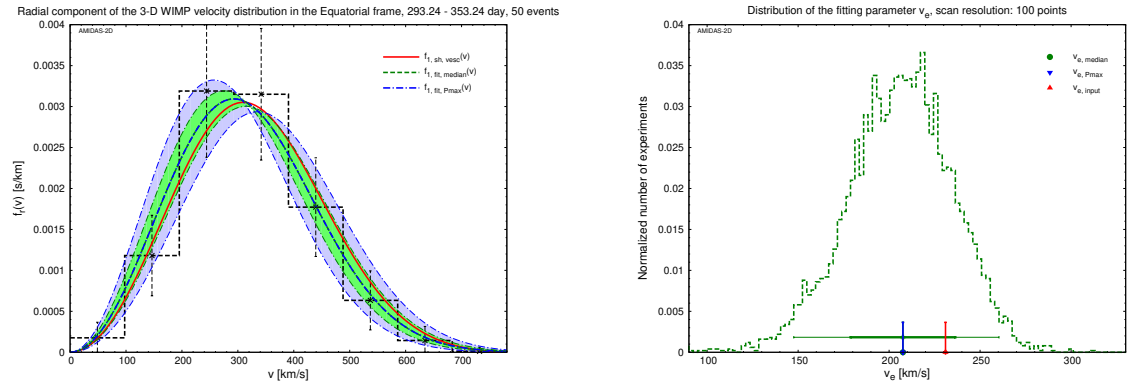

(d) 293.24 – 353.24 day

Figure 31: As in Figs. 27, reconstructed with the v_0–fixed velocity distribution $f_{1,\mathrm{sh},v_\mathrm{e}}(v;v_\mathrm{e})$, except that four 60-day observation periods of the advanced seasons have been considered.

Fitting distribution: v_0–fixed velocity distribution $f_{1,\mathrm{sh},v_\mathrm{e}}(v;v_\mathrm{e})$					
Central date (observation period) (day)	Parameter	Max. $\mathrm{P}_{\mathrm{median}}$	Median	1σ range	2σ range
49.49 (19.49 – 79.49)	v_e [km/s]	224.4	$224.4\,^{+26.4}_{-28.8}\,(^{+50.4}_{-58.2})$	[195.6, 250.8]	[166.2, 274.8]
140.74 (110.74 – 170.74)	v_e [km/s]	238.8	$238.8 \pm 26.4\,(^{+50.4}_{-52.8})$	[212.4, 265.2]	[186.0, 289.2]
231.99 (201.99 – 261.99)	v_e [km/s]	224.4	$224.4 \pm 26.4\,(^{+50.4}_{-57.6})$	[198.0, 250.8]	[166.8, 274.8]
323.24 (293.24 – 353.24)	v_e [km/s]	207.6	$207.6 \pm 28.8\,(^{+52.8}_{-60.0})$	[178.8, 236.4]	[147.6, 260.4]
50 total events on average in one observation period of 60 days					

Table 6: The summary of the reconstructed results of the fitting parameter v_e and their $1(2)\sigma$ statistical uncertainty ranges of the median values by using the v_0–fixed velocity distribution $f_{1,\mathrm{sh},v_\mathrm{e}}(v;v_\mathrm{e})$ with 50 total events on average in each 60–day observation period of the advanced seasons.

to the difference between the annual average value of $v_0 = 215.0$ km/s (see Table 4) and its theoretical value. In Sec. 5.2.2, we will show that, with $\mathcal{O}(500)$ total WIMP events and thus $\sim 1/3$ reduced statistical uncertainties on v_0, the annual variation of the fitting parameter v_0 and in turn that of the radial WIMP velocity distribution could be identified with a confidence level of 2σ to 3σ.

In Table 5, we summarize the reconstructed results of the fitting parameter v_0 and their $1(2)\sigma$ statistical uncertainty ranges of the median values by using the one–parameter velocity distribution $f_{1,\mathrm{sh},v_0}(v;v_0)$ with 50 total events on average in each 60-day observation period.

4.3.2 With the v_0–fixed velocity distribution $f_{1,\mathrm{sh},v_\mathrm{e}}(v;v_\mathrm{e})$

In order to check the identification possibility of the variation of the Earth's Galactic velocity v_e, we consider then the v_0–fixed velocity distribution $f_{1,\mathrm{sh},v_\mathrm{e}}(v;v_\mathrm{e})$ with v_e as the fitting parameter and the input condition that $v_0 = 220$ km/s.

In Figs. 31, we show the reconstructed radial WIMP velocity distributions and the $1(2)\sigma$ statistical uncertainty bands by using $f_{1,\mathrm{sh},v_\mathrm{e}}(v;v_\mathrm{e})$ as well as the distributions of the fitting parameter v_e in all simulated experiments for four advanced seasons. Firstly, from the plots in the left column of Figs. 31, one can find that the reconstructed velocity distributions and their $1(2)\sigma$ statistical uncertainty bands also follow the variation of the simulated radial velocity distribution in different seasons. Meanwhile, from the plots in the right column of Figs. 31, one can also see the (approximately) symmetric periodic variation of the fitting parameter v_e of 224.4 $(^{+14.4}_{-16.8})$ km/s clearly; this $^{+14.4}_{-16.8}$ km/s annual variation of the best–fit value of v_e is also $\sim 0.5\sigma$ of the statistical uncertainties on v_e (see the summary given in Table 4). In Sec. 5.2.2, we

will show that, with $\mathcal{O}(500)$ total WIMP events and thus $\sim 1/3$ reduced statistical uncertainties on $v_{\rm e}$, its annual variation could be identified with a confidence level of $> 2\sigma$.

In Table 6, we summarize the reconstructed results of the fitting parameter $v_{\rm e}$ and their $1(2)\sigma$ statistical uncertainty ranges of the median values by using the v_0–fixed velocity distribution $f_{1,{\rm sh},v_{\rm e}}(v;v_{\rm e})$ with 50 total events on average in each 60-day observation period.

4.3.3 With the simplified velocity distribution $f_{1,{\rm sh}}(v;v_0,v_{\rm e})$

Now we release the constraints on the fitting parameters v_0 and $v_{\rm e}$ and consider the simplified velocity distribution $f_{1,{\rm sh}}(v;v_0,v_{\rm e})$, in order to identify the variation of the Earth's Galactic velocity $v_{\rm e}$ as well as to check the *invariability* of the Solar Galactic velocity v_0 with the better–fitted radial WIMP velocity distributions in the advanced seasons.

In Figs. 32, we show the reconstructed radial WIMP velocity distributions and the $1(2)\sigma$ statistical uncertainty bands by using $f_{1,{\rm sh}}(v;v_0,v_{\rm e})$ as well as the distributions of the fitting parameters v_0 and $v_{\rm e}$ in all simulated experiments on the $v_0 - v_{\rm e}$ plane for four advanced seasons. Firstly, as found in Sec. 4.2.3, from the plots in the left column of Figs. 32, one can observe clearly that the reconstructed velocity distributions and their $1(2)\sigma$ statistical uncertainty bands indeed follow the variation of the simulated radial velocity distribution in different seasons (much tighter than those shown in Figs. 30 and 31 and) almost perfectly. Meanwhile, from the plots in the right column of Figs. 32 as well as our summary given in Table 7, we can find that, although the first fitting parameter v_0 is unconstraint, its best–fit values in four advanced seasons are indeed a constant equal to its annual average value with also the similar $1(2)\sigma$ statistical uncertainties. Remind however that, as its annual average value obtained in Secs. 4.2.3 and 4.2.4, the invariant best–fit value of $v_0 \simeq 190$ km/s is $\sim 14\%$ smaller than the input value.

In contrast, in four advanced seasons the best–fit values of the second fitting parameter $v_{\rm e}$ show clearly an (approximately) symmetric periodic variation of 258.4 $(^{+11.4}_{-15.2})$ km/s, also around its annual average value obtained in Sec. 4.2.3. As mentioned in Sec. 4.3.2, this $^{+11.4}_{-15.2}$ km/s annual variation of the best–fit value of $v_{\rm e}$ is $\sim 1/3$ of the statistical uncertainties on $v_{\rm e}$ (see the summary given in Table 4). This indicates that, with $\mathcal{O}(500)$ total WIMP events and thus $\sim 1/3$ reduced statistical uncertainties on $v_{\rm e}$, its annual variation could be identified with a confidence level of $\sim 1\sigma$ (see Sec. 5.2.2).

In Table 7, we summarize the reconstructed results of the fitting parameters v_0 and $v_{\rm e}$ as well as their $1(2)\sigma$ statistical uncertainty ranges of the median values by using the simplified velocity distribution $f_{1,{\rm sh}}(v;v_0,v_{\rm e})$ with 50 total events on average in each 60-day observation period.

4.3.4 With the modified velocity distribution $f_{1,{\rm sh},\Delta v}(v;v_0,\Delta v)$

Finally, as the confirmation of the invariability of the Solar Galactic velocity v_0 and that of the variation of the Earth's Galactic velocity $v_{\rm e}$ shown in Sec. 4.3.3, we consider here the modified velocity distribution $f_{1,{\rm sh},\Delta v}(v;v_0,\Delta v)$ with v_0 and Δv as two free fitting parameters.

In Figs. 33, we show the reconstructed radial WIMP velocity distributions and the $1(2)\sigma$ statistical uncertainty bands by using $f_{1,{\rm sh},\Delta v}(v;v_0,\Delta v)$ as well as the distributions of the fitting parameters v_0 and Δv in all simulated experiments on the $v_0 - \Delta v$ plane for four advanced seasons. Firstly, by comparing the plots in the left column of Figs. 33 with the plots in the left column of Figs. 32, one could see that, except of the 2σ statistical uncertainty bands[15], the

[15] Note that, due to the wide–extended distribution tails at the lower scanning boundaries of $v_{\rm e}$ and Δv, the lower bounds of the 2σ statistical uncertainties on $v_{\rm e}$ and Δv and in turn the shapes of the 2σ uncertainty bands are actually limited by our simulation setup for their scanning ranges. In Sec. 5.2.2 we will see that, with $\mathcal{O}(500)$ total WIMP events the $1(2)\sigma$ uncertainty contours become closed and the lower bounds of the 2σ uncertainties

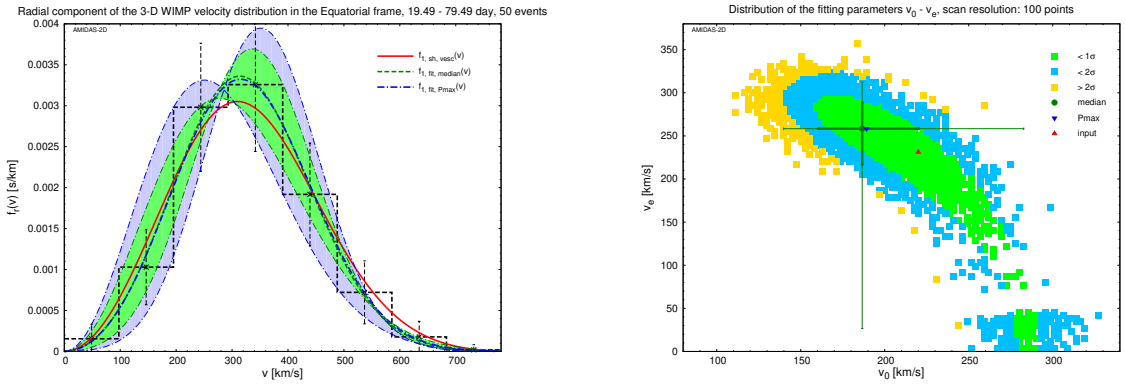

(a) 19.49 – 79.49 day

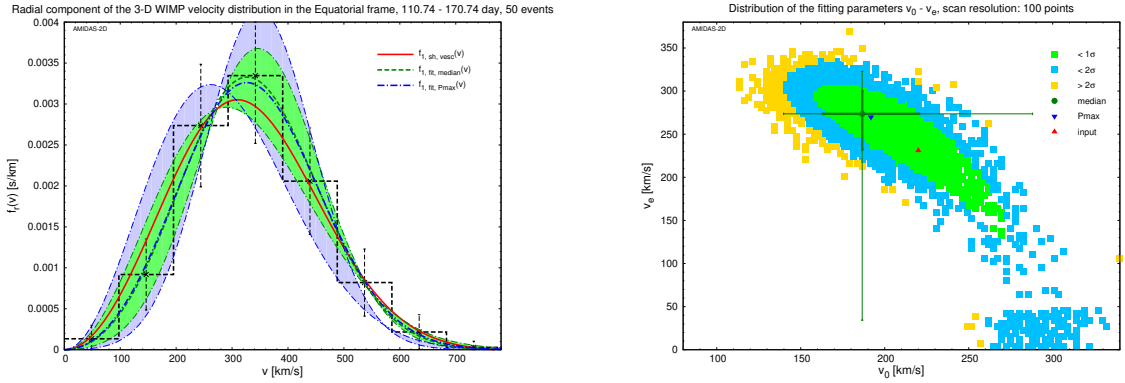

(b) 110.74 – 170.74 day

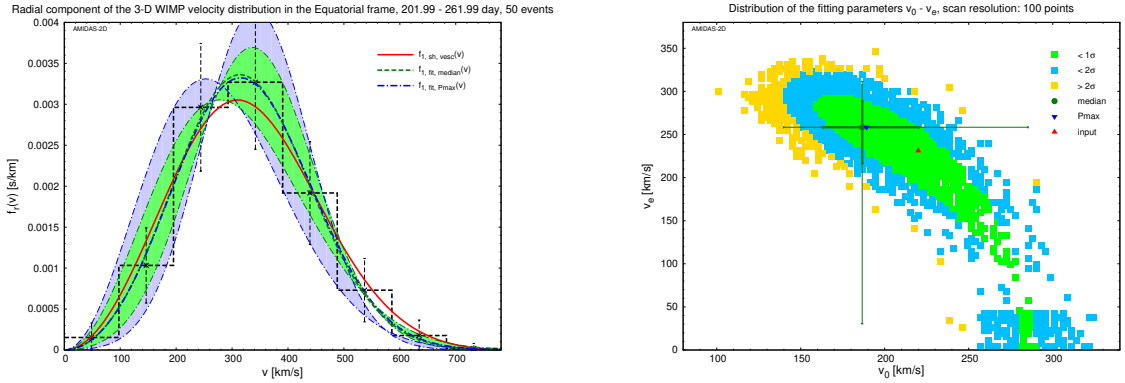

(c) 201.99 – 261.99 day

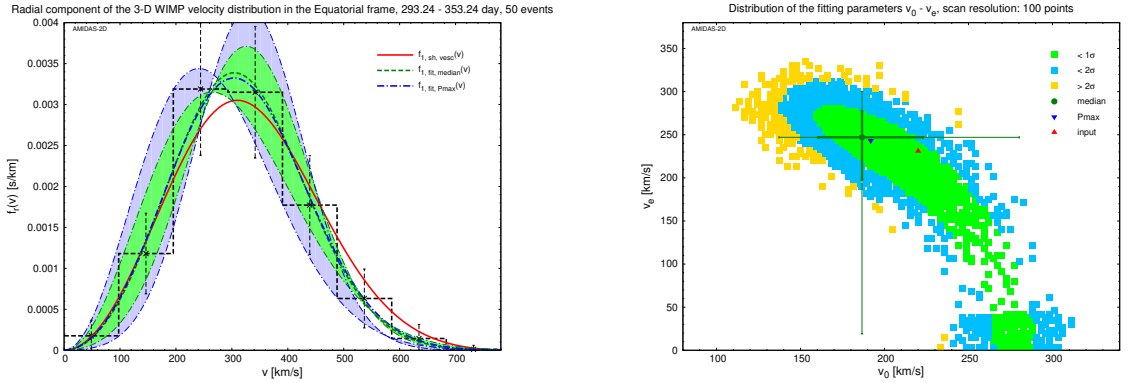

(d) 293.24 – 353.24 day

Figure 32: As in Figs. 28, reconstructed with the simplified velocity distribution $f_{1,\mathrm{sh}}(v; v_0, v_\mathrm{e})$, except that four 60-day observation periods of the advanced seasons have been considered.

Fitting distribution: simplified velocity distribution $f_{1,\mathrm{sh}}(v; v_0, v_\mathrm{e})$					
Central date (observation period) (day)	Parameter	Max. $\mathrm{P}_{\mathrm{median}}$	Median	1σ range	2σ range
49.49 (19.49 – 79.49)	v_0 [km/s]	189.2	$186.6\,^{+33.8}_{-26.0}\,(^{+96.2}_{-46.8})$	[160.6, 220.4]	[139.8, 282.8]
	v_e [km/s]	258.4	$258.4\,^{+30.4}_{-41.8}\,(^{+\ 54.2}_{-231.8})$	[216.6, 288.8]	[26.6, 312.6]
140.74 (110.74 – 170.74)	v_0 [km/s]	191.8	$186.6\,^{+33.8}_{-23.4}\,(^{+101.4}_{-\ 46.8})$	[163.2, 220.4]	[139.8, 288.0]
	v_e [km/s]	269.8	$273.6\,^{+26.6}_{-41.8}\,(^{+\ 49.4}_{-239.4})$	[231.8, 300.2]	[34.2, 323.0]
231.99 (201.99 – 261.99)	v_0 [km/s]	189.2	$186.6\,^{+33.8}_{-23.4}\,(^{+98.8}_{-46.8})$	[163.2, 220.4]	[139.8, 285.4]
	v_e [km/s]	258.4	$258.4\,^{+30.4}_{-41.8}\,(^{+\ 53.2}_{-228.0})$	[216.6, 288.8]	[30.4, 311.6]
323.24 (293.24 – 353.24)	v_0 [km/s]	191.8	$186.6\,^{+36.4}_{-26.0}\,(^{+93.6}_{-49.4})$	[160.6, 223.0]	[137.2, 280.2]
	v_e [km/s]	243.2	$247.0\,^{+30.4}_{-49.4}\,(^{+\ 53.2}_{-228.0})$	[197.6, 277.4]	[19.0, 300.2]
50 total events on average in one observation period of 60 days					

Table 7: The summary of the reconstructed results of the fitting parameters v_0 and v_e as well as their $1(2)\sigma$ statistical uncertainty ranges of the median values by using the simplified velocity distribution $f_{1,\mathrm{sh}}(v; v_0, v_\mathrm{e})$ with 50 total events on average in each 60–day observation period of the advanced seasons.

velocity distributions and their 1σ statistical uncertainty bands reconstructed with the simplified and the modified velocity distributions would be identical.

Additionally, from the plots in the right column of Figs. 33 as well as our summary given in Table 8, one could confirm that the best–fit values of the first fitting parameter v_0 in four advanced seasons are fixed around the annual average value of $v_0 \simeq 190$ km/s with the similar $1(2)\sigma$ statistical uncertainties. Meanwhile, the best–fit values of the second fitting parameter Δv show also clearly an (approximately) symmetric periodic variation of 70.4 $(^{+\ 8.4}_{-12.6})$ km/s in four advanced seasons, which is approximately equal to both of the annual average value of $\Delta v \simeq 70$ km/s (see Table 4) and the difference between the best–fit values of v_0 and v_e obtained in Sec. 4.3.3 (see Table 7). It would be worth to notice that, while the $^{+\ 8.4}_{-12.6}$ km/s annual variation of the best–fit value of Δv is smaller than the $^{+11.4}_{-15.2}$ km/s annual variation of v_e, the 1σ statistical uncertainties on Δv are in contrast much ($\gtrsim 1.5$ times) larger than those on v_e.

In Table 8, we summarize the reconstructed results of the fitting parameters v_0 and Δv as well as their $1(2)\sigma$ statistical uncertainty ranges of the median values by using the modified velocity distribution $f_{1,\mathrm{sh},\Delta v}(v; v_0, \Delta v)$ with 50 total events on average in each 60-day observation period.

on v_e and Δv can be determined accurately. Then the shape differences between the 2σ uncertainty bands of the WIMP velocity distributions reconstructed with the simplified and the modified velocity distributions becomes very tiny.

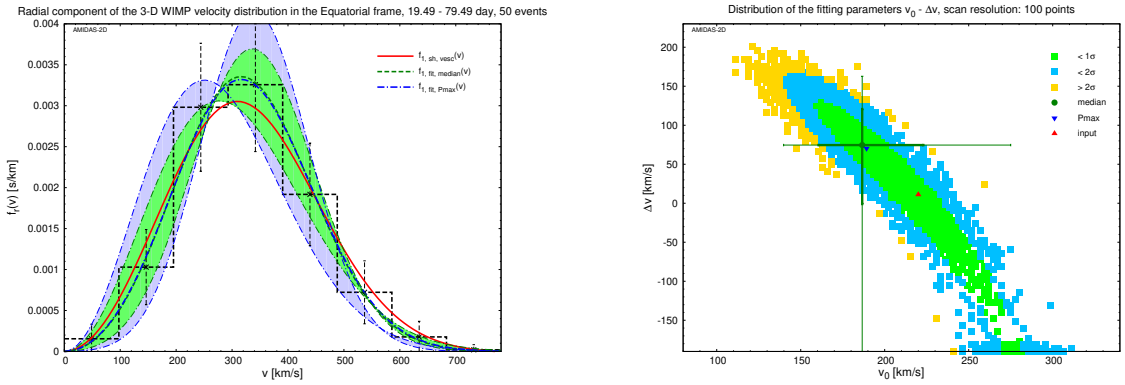

(a) 19.49 – 79.49 day

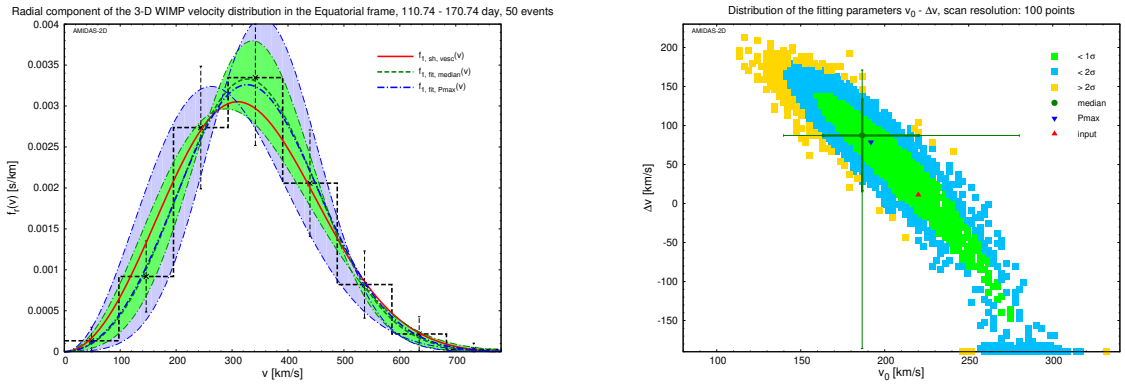

(b) 110.74 – 170.74 day

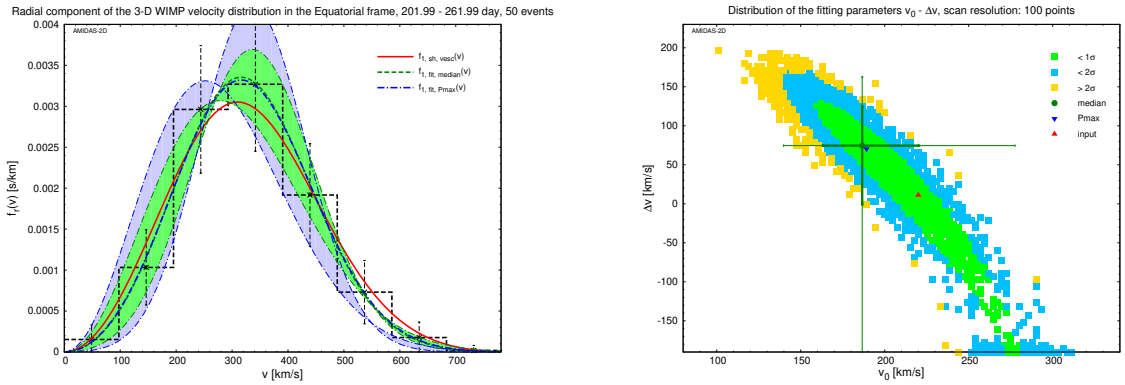

(c) 201.99 – 261.99 day

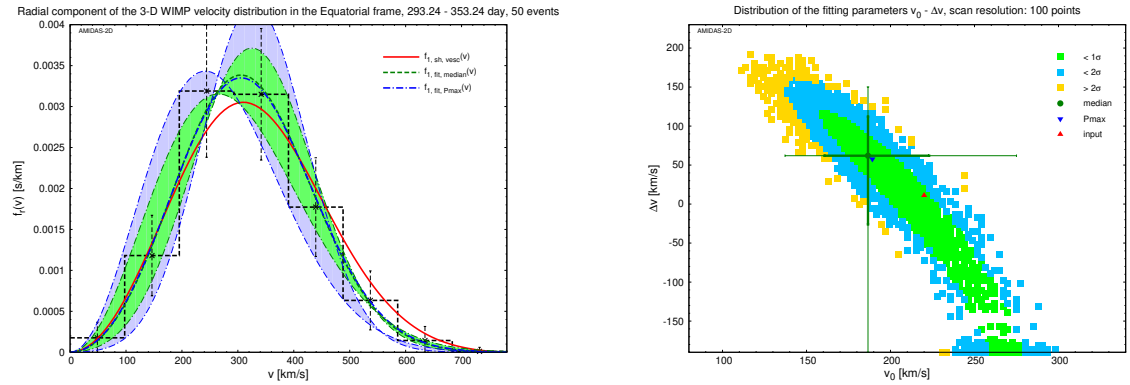

(d) 293.24 – 353.24 day

Figure 33: As in Figs. 29, reconstructed with the modified velocity distribution $f_{1,\mathrm{sh},\Delta v}(v; v_0, \Delta v)$, except that four 60-day observation periods of the advanced seasons have been considered.

Fitting distribution: modified velocity distribution $f_{1,\mathrm{sh},\Delta v}(v; v_0, \Delta v)$					
Central date (observation period) (day)	Parameter	Max. $\mathrm{P}_{\mathrm{median}}$	Median	1σ range	2σ range
49.49 (19.49 – 79.49)	v_0 [km/s]	189.2	$186.6\,^{+36.4}_{-26.0}\,(^{+88.4}_{-46.8})$	[160.6, 223.0]	[139.8, 275.0]
	Δv [km/s]	70.4	$74.6\,^{+46.2}_{-75.6}\,(^{+\ 88.2}_{-264.6})$	[−1.0, 120.8]	[−190.0, 162.8]
140.74 (110.74 – 170.74)	v_0 [km/s]	191.8	$186.6\,^{+33.8}_{-23.4}\,(^{+93.6}_{-46.8})$	[163.2, 220.4]	[139.8, 280.2]
	Δv [km/s]	78.8	$87.2\,^{+46.2}_{-71.4}\,(^{+\ 84.0}_{-273.0})$	[15.8, 133.4]	[−185.8, 171.2]
231.99 (201.99 – 261.99)	v_0 [km/s]	189.2	$186.6\,^{+33.8}_{-23.4}\,(^{+91.0}_{-46.8})$	[163.2, 220.4]	[139.8, 277.6]
	Δv [km/s]	70.4	$74.6\,^{+50.4}_{-75.6}\,(^{+\ 88.2}_{-264.6})$	[−1.0, 125.0]	[−190.0, 162.8]
323.24 (293.24 – 353.24)	v_0 [km/s]	189.2	$186.6\,^{+36.4}_{-26.0}\,(^{+88.4}_{-49.4})$	[160.6, 223.0]	[137.2, 275.0]
	Δv [km/s]	57.8	$62.0\,^{+50.4}_{-88.2}\,(^{+\ 88.2}_{-252.0})$	[−26.2, 112.4]	[−190.0, 150.2]
50 total events on average in one observation period of 60 days					

Table 8: The summary of the reconstructed results of the fitting parameters v_0 and Δv as well as their $1(2)\sigma$ statistical uncertainty ranges of the median values by using the modified velocity distribution $f_{1,\mathrm{sh},\Delta v}(v; v_0, \Delta v)$ with 50 total events on average in each 60–day observation period of the advanced seasons.

4.4 Fitted radial WIMP velocity distribution in the Galactic frame

As preparation for analyzing (future) real experimental data to understand the 3-dimensional velocity distribution of halo WIMPs, we have also tried to transform the saved 3-D velocity information of the simulated WIMP events (including measuring times) in the laboratory coordinate system back by using Eqs. (33b), (32b), (31b), (30b), and (29b) and reconstruct the radial WIMP velocity distribution in the Galactic coordinate system.

In Figs. 34, we show the reconstructed radial distributions of the 3-D WIMP velocity and the $1(2)\sigma$ statistical uncertainty bands by using the *simple* Maxwellian velocity distribution $f_{1,\mathrm{Gau}}(v)$ given by Eq. (2) to fit data shown in Fig. 7 as well as the distribution of the fitting parameter v_0 in all simulated experiments. Not surprisingly, our best–fit reconstruction distributions could match the input simple Maxwellian velocity distribution perfectly and the fitting parameter v_0 could also be pinned down very precisely[16] (see the summary given in Table 9).

5 With a raised total event number

In this section, we raise the simulated total event number in one observation period (365 days/year, 60 days/season, or 4 hours/shift × 60 days) to 500 events on average in one ex-

[16] The tiny difference of 0.2 km/s between the best–fit and the input values of v_0 is only due to the scanning resolution.

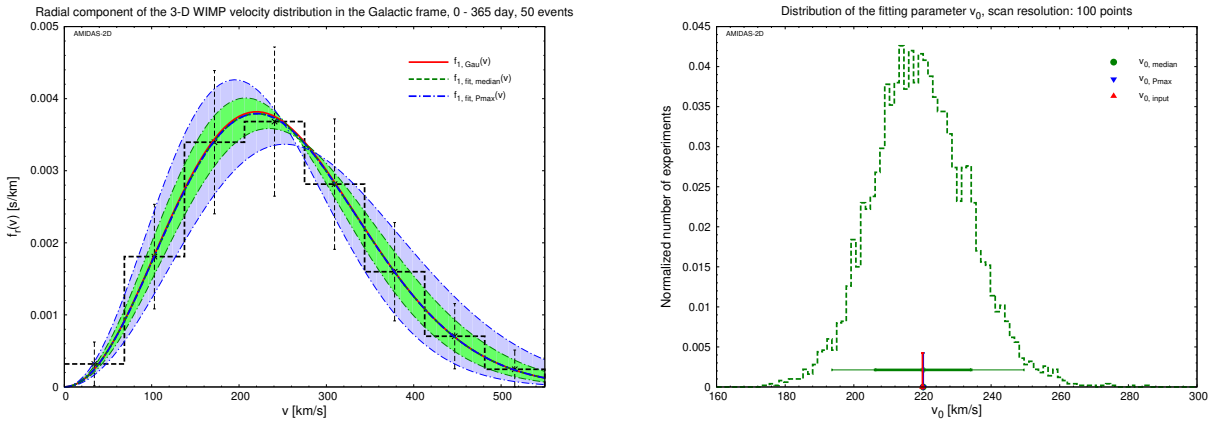

(a) (b)

Figure 34: (a) The reconstructed radial distributions of the 3-D WIMP velocity and the $1(2)\sigma$ statistical uncertainty bands by using the *simple* Maxwellian velocity distribution $f_{1,\mathrm{Gau}}(v)$ given by Eq. (2) to fit data shown in Fig. 7. The solid red curve is the input simple Maxwellian velocity distribution with the input value of $v_0 = 220$ km/s. (b) The distribution of the fitting parameter v_0 in all simulated experiments. Other notations are the same as in Figs. 26.

periment. We present at first the angular distribution patterns of the 3-dimensional WIMP velocity and then discuss the Bayesian reconstructions of its radial distributions.

5.1 Angular distributions of the 3-D WIMP velocity in the laboratory–independent frames

In this subsection, we present only the angular distributions of the (transformed) 3-D WIMP velocity in three laboratory–independent (Ecliptic, Equatorial, and Earth) coordinate systems. The angular distributions in two laboratory–dependent (horizontal and laboratory) coordinate systems observed in different underground laboratories can be found in Appendix B.

5.1.1 Angular WIMP velocity distribution in the Ecliptic frame

In Fig. 35, we show the angular distribution of the 3-D WIMP velocity transformed to the Ecliptic coordinate system. 500 total events on average in one experiment in one entire year

Fitting dist.	Parameter	Max. $\mathrm{P}_{\mathrm{median}}$	Median	1σ range	2σ range
$f_{1,\mathrm{Gau}}(v)$	v_0 [km/s]	220.2	$220.2 \pm 14\,(^{+29.4}_{-26.6})$	[206.2, 234.2]	[193.6, 249.6]
50 total events on average in the observation period of 0 – 365 day					

Table 9: The summary of the reconstructed results of the fitting parameter v_0 and their $1(2)\sigma$ statistical uncertainty ranges of the median values by using the simple Maxwellian velocity distribution with 50 total events on average in one entire year shown in Figs. 34.

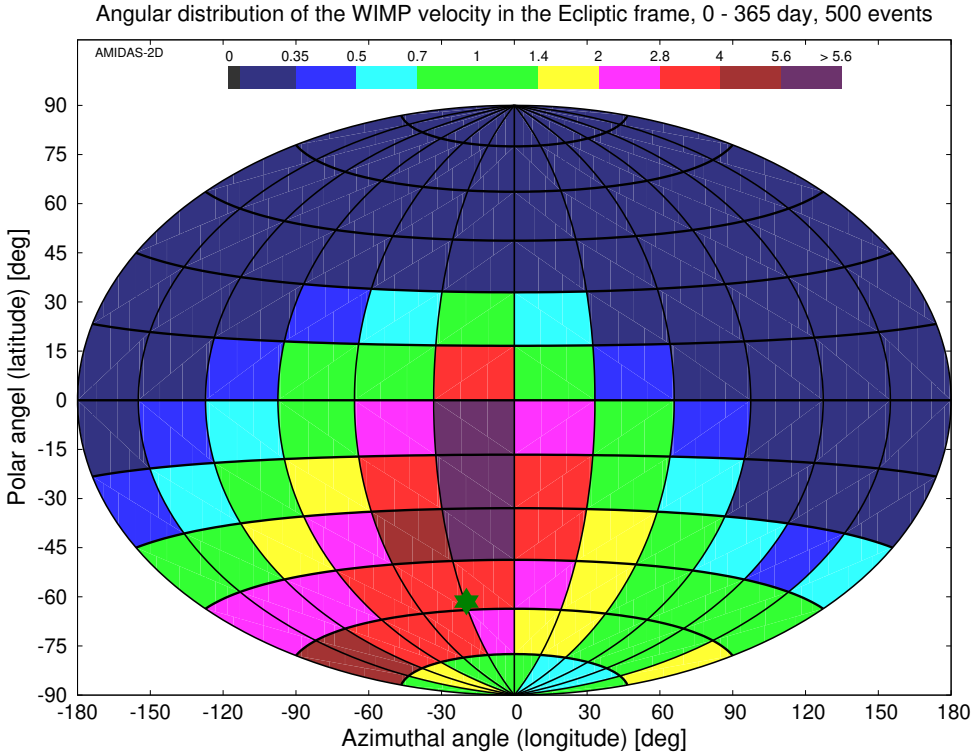

Figure 35: As in Fig. 12, the angular distribution of the 3-D WIMP velocity transformed to the Ecliptic coordinate system, except that 500 total events on average in one entire year have been generated and binned into 12 × 12 bins for the longitude and latitude directions, respectively.

have been generated and binned into 12 × 12 bins for the longitude and latitude directions, respectively.

It can be found that, first, with a higher analysis resolution, the bins with higher event numbers spreading from the center to the southwest part can be seen more obviously, including the bins with the highest event number (> 5.6 times of the all–sky average value of 500 events / 144 bins = 3.47 events/bin, i.e., > 19.44 events/bin) between 45°S and 0° latitude, 30°W and 0° longitude. Second, the deviation between the center of the band of the high–WIMP–flux bins and the theoretical main direction of incident WIMPs in the Ecliptic coordinate system (57.40°S, 29.10°W) (the dark–green star) would now be $\lesssim 15°$ and $\lesssim 30°$ in the latitude and the longitude direction, respectively.

5.1.2 Angular WIMP velocity distribution in the Equatorial frame

In Fig. 36, we show at first the angular distribution of the 3-D WIMP velocity transformed to the Equatorial coordinate system with 500 total events on average in one entire year. With a higher analysis resolution, one can also find that, first, as in the Ecliptic coordinate system, the bins with higher event numbers spreading from the center to the southwest part can be seen more obviously and there seems still to be a small deviation between the center of the band of the high–WIMP–flux bins and the theoretical main direction of incident WIMPs (in the Equatorial coordinate system, 42.00°S, 50.70°W) (the dark–green star). Second, not only the bins around the north pole (more northern than 45°N) and in the most part of the eastern sky, a few bins around the south pole (more southern than 75°S) would also be a "WIMP hole" with

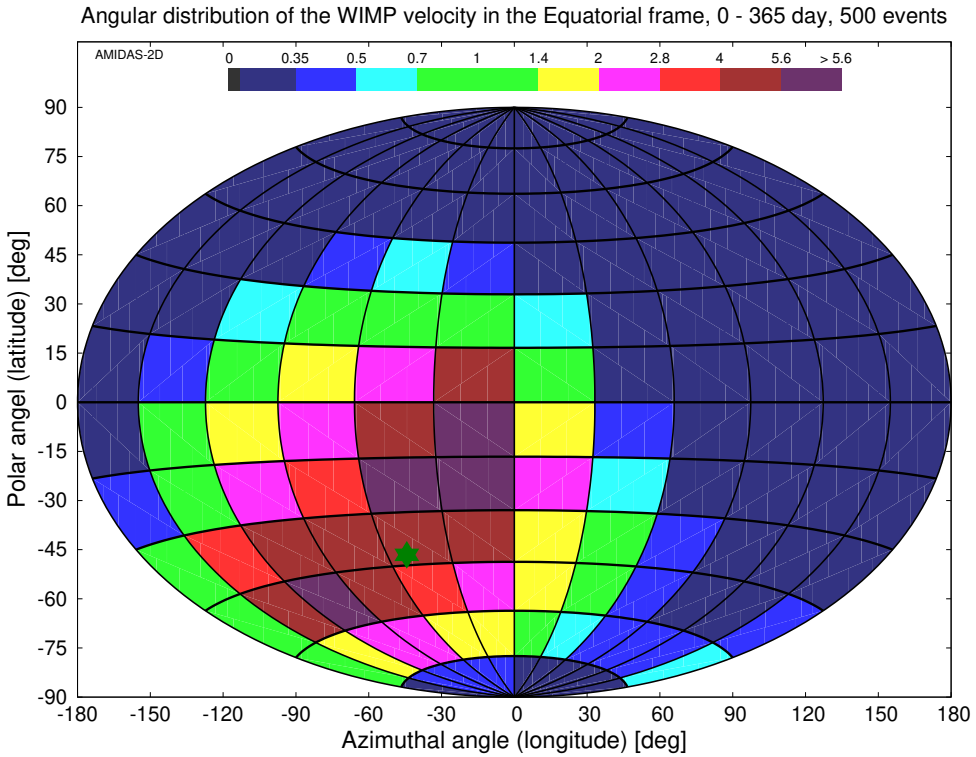

Figure 36: As in Fig. 13, the angular distribution of the 3-D WIMP velocity transformed to the Equatorial coordinate system, except that 500 total events on average in one entire year have been simulated.

event numbers less than 35% of the all–sky average (i.e., < 1.22 events/bin among $\mathcal{O}(500)$ total events).

Moreover, in order to demonstrate the annual modulation of the angular distribution pattern of the 3-D WIMP velocity, in Figs. 37 and 38 we show the angular distributions in the Equatorial coordinate system in four normal and four advanced seasons, respectively. Remind that 500 total events on average in each 60-day observation period have been simulated. Now, with a higher analysis resolution, the clockwise circular variation of the angular distribution patterns following the blue–yellow point around the theoretical main direction of incident WIMPs could be observed more clearly. In addition, the difference of the angular distribution patterns between the corresponding observation periods of four normal and four advanced seasons can already be observed. In fact, one could even combine all eight plots of the normal and the advanced seasons to build a more–detailed rotated pattern of the angular WIMP velocity distribution.

5.1.3 Angular WIMP velocity distribution in the Earth frame

In Fig. 39, we show the angular distribution of the 3-D WIMP velocity transformed to the Earth coordinate system with 500 total events on average in one entire year. With a higher analysis resolution, as in the Equatorial coordinate system, not only the bins around the north pole (more northern than 30°N), a few bins around the south pole (more southern than 75°S) would also be the "WIMP hole" with event numbers less than 35% of the all–sky average (i.e., < 1.22 events/bin among $\mathcal{O}(500)$ total events).

Moreover, in order to demonstrate the annual modulation of the angular distribution pattern

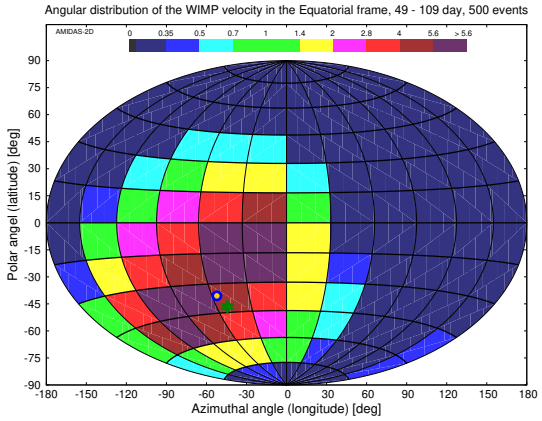

(a) 49.0 – 109.0 day

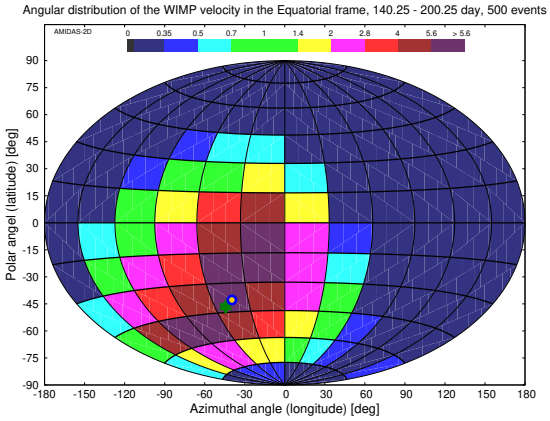

(b) 140.25 – 200.25 day

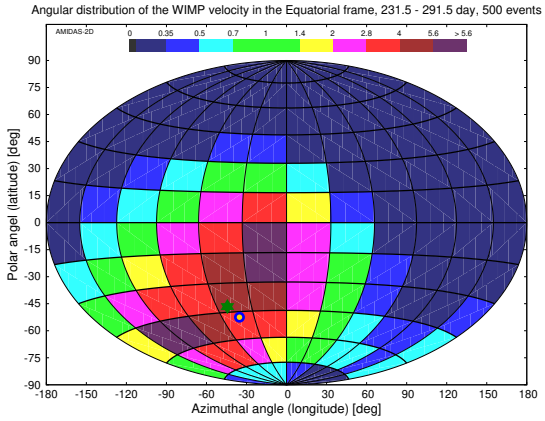

(c) 231.50 – 291.50 day

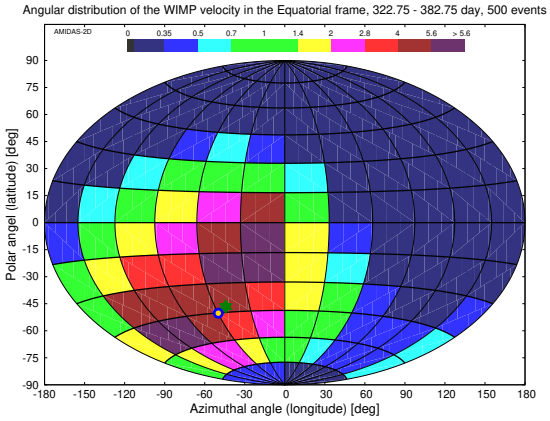

(d) 322.75 – 382.75 day

Figure 37: As in Figs. 14, the angular distributions of the 3-D WIMP velocity in the Equatorial coordinate system, except that 500 total events on average in each 60-day observation period of four normal seasons have been considered.

of the 3-D WIMP velocity, in Figs. 40 and 41 we show the angular distributions in the Earth coordinate system in four normal and four advanced seasons, respectively. Remind that 500 total events on average in each 60-day observation period have been simulated. Now, with a higher analysis resolution, the rotation of the angular distribution patterns around the $\mathbf{Z}_{\rm E}$–axis can be clearly observed, not only in four normal and four advanced seasons, but also between each pair of the corresponding seasons.

5.2 Bayesian reconstruction of the radial distribution of the 3-D WIMP velocity

In this subsection, we present our Bayesian reconstructions of the radial distribution of the (transformed) 3-D WIMP velocity in the Equatorial coordinate system. As in Sec. 4, we discuss at first the one–year simulations and then the results of the annual modulation in the observation

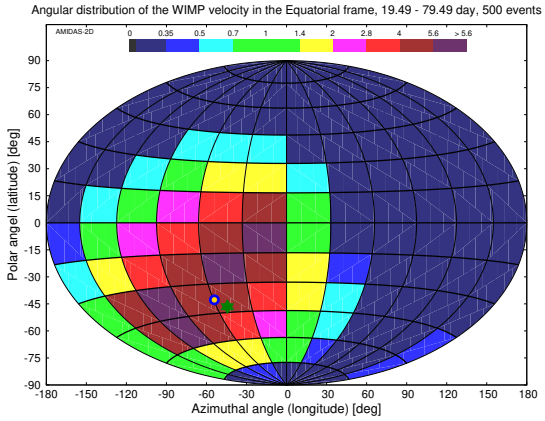

(a) 19.49 – 79.49 day

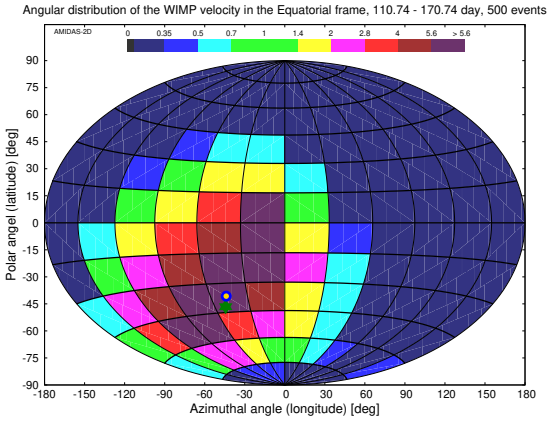

(b) 110.74 – 170.74 day

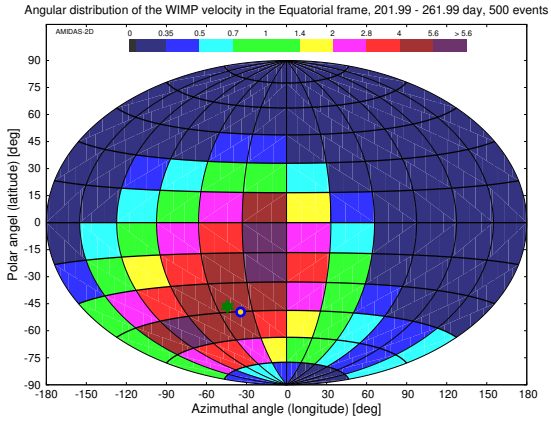

(c) 201.99 – 261.99 day

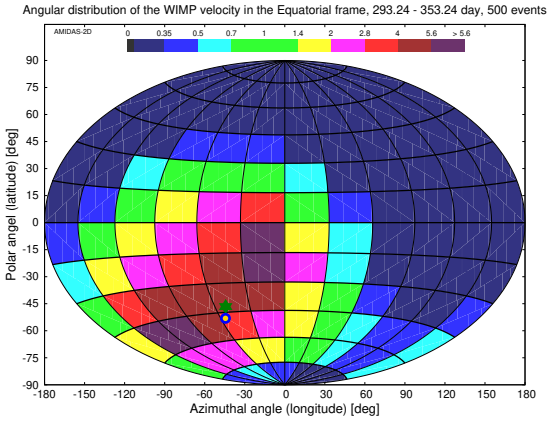

(d) 293.24 – 353.24 day

Figure 38: As in Figs. 15, the angular distributions of the 3-D WIMP velocity in the Equatorial coordinate system, except that 500 total events on average in each 60-day observation period of four advanced seasons have been considered.

periods of four advanced seasons[17]. All four fitting velocity distributions given in Sec. 2.3.3 will be considered. At the end of this subsection, we will also show the reconstruction result of the WIMP velocity distribution in the Galactic coordinate system.

5.2.1 Fitted radial WIMP velocity distributions in the Equatorial frame

We discuss at first our reconstruction results with 500 total events on average in one experiment recorded in one entire year.

With the one–parameter and the v_0–fixed velocity distributions $f_{1,\mathrm{sh},v_0}(v;v_0)$ and $f_{1,\mathrm{sh},v_e}(v;v_e)$

As in Secs. 4.2.1 and 4.2.2, we consider at first the one–parameter and the v_0–fixed velocity

[17] The reconstructed radial WIMP velocity distributions in the observation periods of four normal seasons will be given in Appendix C for readers' reference.

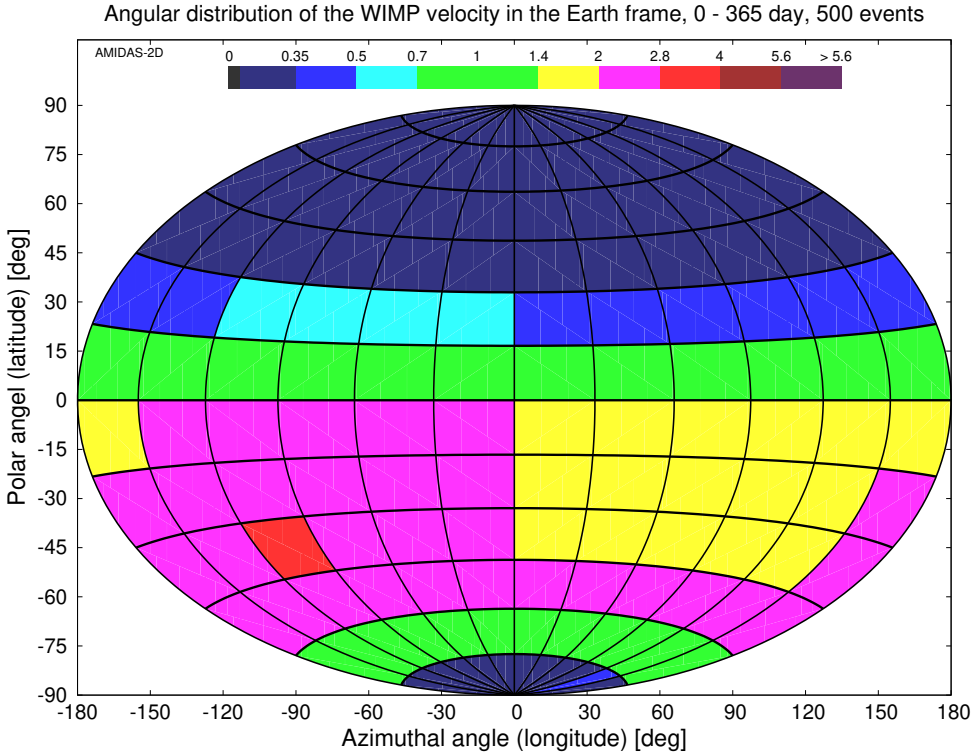

Figure 39: As in Fig. 16, the angular distribution of the 3-D WIMP velocity transformed to the Earth coordinate system, except that 500 total events on average in one entire year have been simulated.

distribution functions, $f_{1,\mathrm{sh},v_0}(v;v_0)$ and $f_{1,\mathrm{sh},v_\mathrm{e}}(v;v_\mathrm{e})$, with the constraints that $v_\mathrm{e} = 1.05\,v_0$ and $v_0 = 220$ km/s, respectively. Note that the scanning ranges of the fitting parameters have been shrunk to 190 km/s $\leq v_0 \leq$ 240 km/s or 180 km/s $\leq v_\mathrm{e} \leq$ 270 km/s, respectively.

In Figs. 42 and 43, we show the reconstructed radial distributions of the 3-D WIMP velocity and the $1(2)\sigma$ statistical uncertainty bands by using the one–parameter and the v_0–fixed velocity distributions, respectively. One can find that, although two 1σ statistical uncertainty bands could still cover the theoretical (solid red) velocity distribution, the difference between the best–fit and the input values of v_0 is already $\sim 1.6\sigma$, while the difference between these two values of v_e is also $\sim 0.7\sigma$ (see the summary given in Table 10). More importantly, both of the theoretical velocity distribution and those reconstructed with two fitting distribution functions are now clearly $\sim 1\sigma$ deviated from the radial distribution of the simulated 3-D WIMP velocity in most of the v–bins. These would imply that the radial distribution of the 3-D WIMP velocity in the Equatorial as well as in the laboratory coordinate systems would differ from the theoretically derived analytic form $f_{1,\mathrm{sh,vesc}}(v)$ given in Eq. (19) [67].

With the simplified and the modified velocity distributions $\boldsymbol{f_{1,\mathrm{sh}}(v;v_0,v_\mathrm{e})}$ and $\boldsymbol{f_{1,\mathrm{sh},\Delta v}(v;v_0,\Delta v)}$

As in Secs. 4.2.3 and 4.2.4, we release now the constraints that $v_\mathrm{e} = 1.05\,v_0$ and $v_0 = 220$ km/s and consider the simplified and the modified velocity distribution functions, $f_{1,\mathrm{sh}}(v;v_0,v_\mathrm{e})$ and $f_{1,\mathrm{sh},\Delta v}(v;v_0,\Delta v)$. Note that the scanning ranges of the fitting parameters have been shrunk to

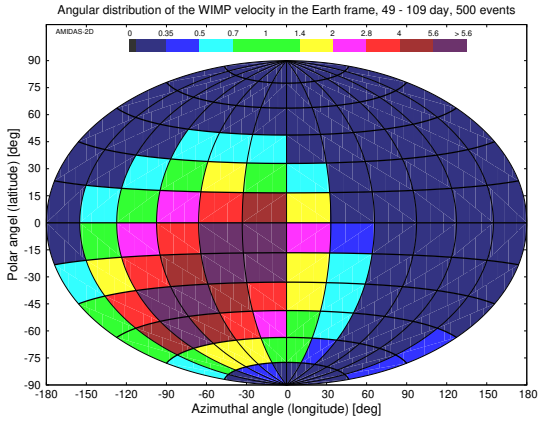

(a) 49.0 – 109.0 day

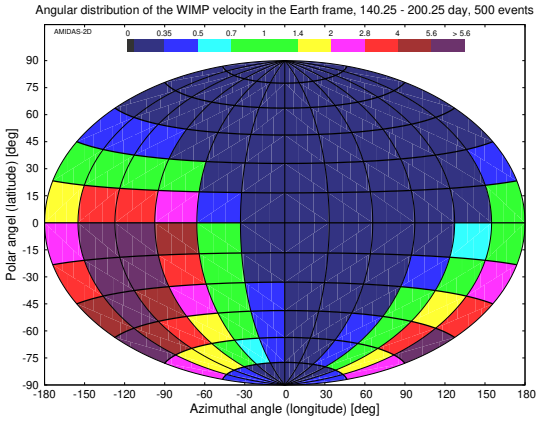

(b) 140.25 – 200.25 day

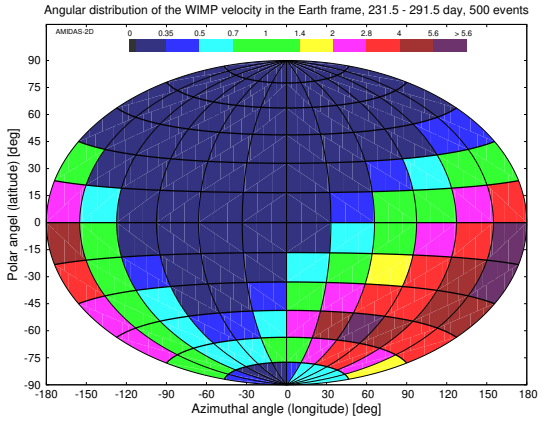

(c) 231.50 – 291.50 day

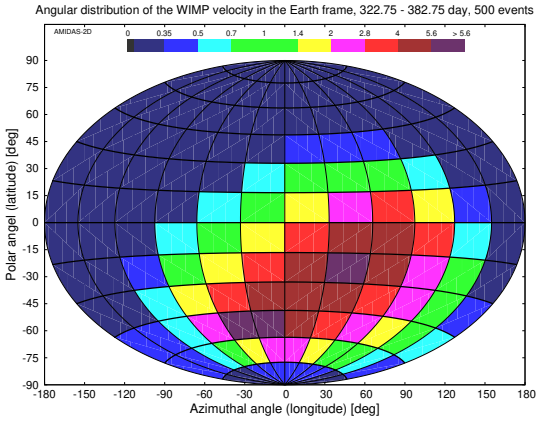

(d) 322.75 – 382.75 day

Figure 40: As in Figs. 17, the angular distributions of the 3-D WIMP velocity in the Earth coordinate system, except that 500 total events on average in each 60-day observation period of four normal seasons have been considered.

140 km/s $\leq v_0 \leq$ 240 km/s, 200 km/s $\leq v_e \leq$ 310 km/s, and -20 km/s $\leq \Delta v \leq$ 150 km/s.

In Figs. 44 and 45, we show the reconstructed radial distributions of the 3-D WIMP velocity and the $1(2)\sigma$ statistical uncertainty bands by using the simplified and the modified velocity distributions, respectively. One can find firstly that, although the long distribution tails at the lower scanning boundaries on the $v_0 - v_e$ and the $v_0 - \Delta v$ planes disappear now and the $1(2)\sigma$ statistical uncertainty contours become closed, two $1(2)\sigma$ uncertainty bands could not cover the theoretical (solid red) velocity distribution any more. Additionally, two reconstructed radial distributions as well as their $1(2)\sigma$ uncertainty bands seem not to fit the radial distribution of the simulated 3-D WIMP velocity in the velocity range of 200 km/s $\lesssim v \lesssim$ 300 km/s very well. Moreover, in Figs. 44(b) and 45(b), one can see that the theoretical values of the fitting parameters (the red upward–triangle) are now clearly out of the (light–blue) 2σ statistical uncertainty contours; the difference between the best–fit and the input values of v_0 becomes now $\sim 3.4\sigma$, and the difference between these two values of v_e is also enlarged to $\sim 2.8\sigma$ (see the summary given in Table 10). These would imply not only that the radial distribution of the 3-D WIMP velocity in the Equatorial as well as in the laboratory coordinate systems would differ

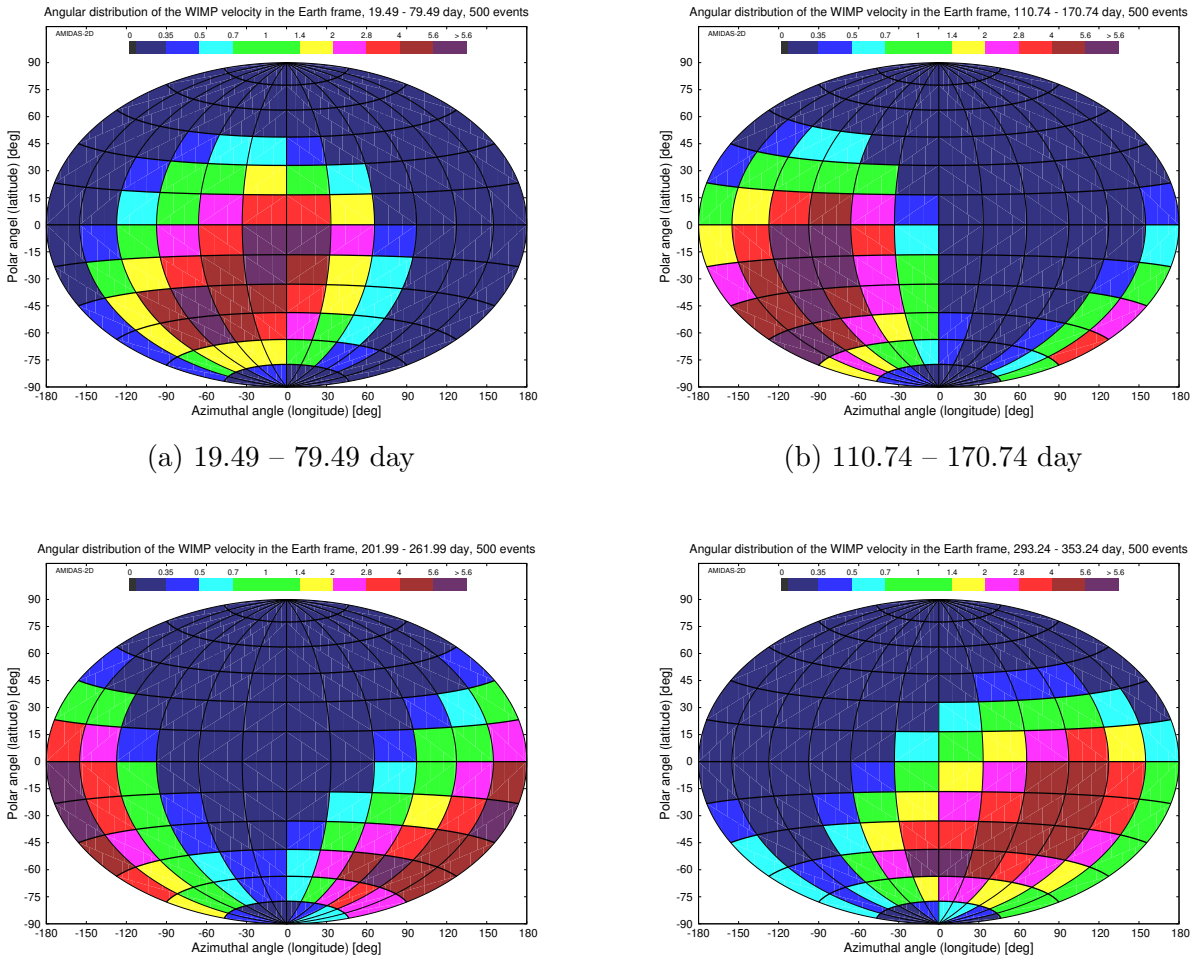

(a) 19.49 – 79.49 day

(b) 110.74 – 170.74 day

(c) 201.99 – 261.99 day

(d) 293.24 – 353.24 day

Figure 41: As in Figs. 18, the angular distributions of the 3-D WIMP velocity in the Earth coordinate system, except that 500 total events on average in each 60-day observation period of four advanced seasons have been considered.

from the theoretically derived analytic form (19) of $f_{1,\mathrm{sh,vesc}}(v)$, but also a requirement of the modification of the analytic form of the fitting velocity distribution function.

In Table 10, we summarize the reconstructed results of the fitting parameters and their $1(2)\sigma$ statistical uncertainty ranges of the median values with 500 total events on average in one entire year for all four considered fitting velocity distributions shown in Figs. 26, 27, 28, and 29.

5.2.2 Annual modulation of the radial WIMP velocity distribution

Now we come to present the reconstruction results of the annual modulation of the radial WIMP velocity distribution in the observation periods of four advanced seasons.

With the one–parameter and the v_0–fixed velocity distributions $f_{1,\mathrm{sh},v_0}(v; v_0)$ and $f_{1,\mathrm{sh},v_\mathrm{e}}(v; v_\mathrm{e})$

As in Secs. 4.3.1 and 4.3.2, we consider at first the one–parameter and the v_0–fixed velocity distribution functions, $f_{1,\mathrm{sh},v_0}(v; v_0)$ and $f_{1,\mathrm{sh},v_\mathrm{e}}(v; v_\mathrm{e})$, with the constraints that $v_\mathrm{e} = 1.05\, v_0$ and

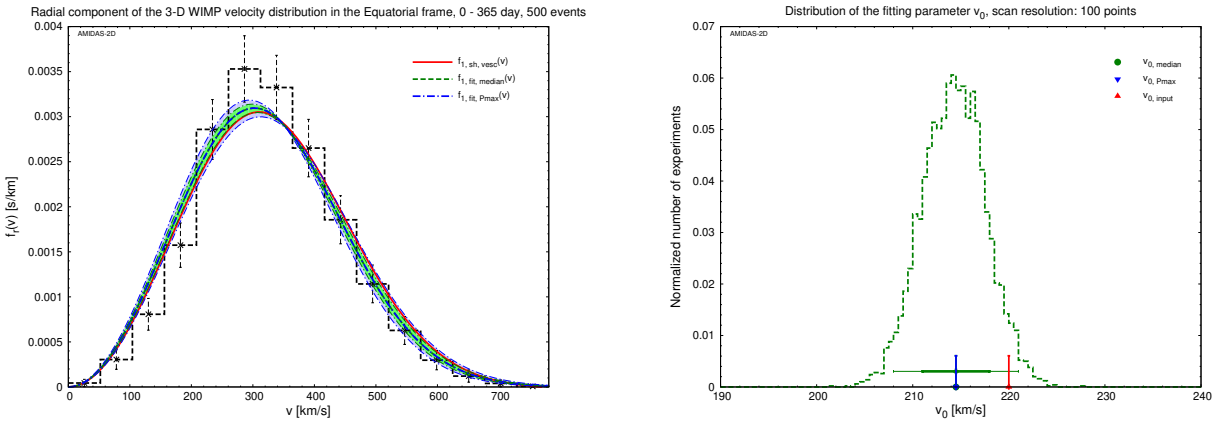

(a) (b)

Figure 42: As in Figs. 26, reconstructed with the one–parameter velocity distribution $f_{1,\mathrm{sh},v_0}(v;v_0)$, except that 500 total events on average in one entire year have been simulated. Note that the scanning range of the fitting parameter v_0 is shrunk to between 190 km/s and 240 km/s.

$v_0 = 220$ km/s, respectively.

In Figs. 46 and Figs. 47, we show the reconstructed radial distributions of the 3-D WIMP velocity and the $1(2)\sigma$ statistical uncertainty bands as well as the distributions of the fitting parameters v_0 and v_e in all simulated experiments by using the one–parameter and the v_0–fixed velocity distributions in four observation periods of the advanced seasons, respectively. It can be find that the (approximately) symmetric periodic variations of the fitting parameters v_0 and v_e observed in Secs. 4.3.1 and 4.3.2 can now be seen more obviously and pinned down more precisely as 214.5 ± 6.0 km/s and $225.0\ (^{+15.3}_{-17.1})$ km/s, respectively; the ±6.0 km/s and the $^{+15.3}_{-17.1}$ km/s annual variations of the best–fit values of v_0 and v_e are almost $\sim 2\sigma$ of their statistical uncertainties

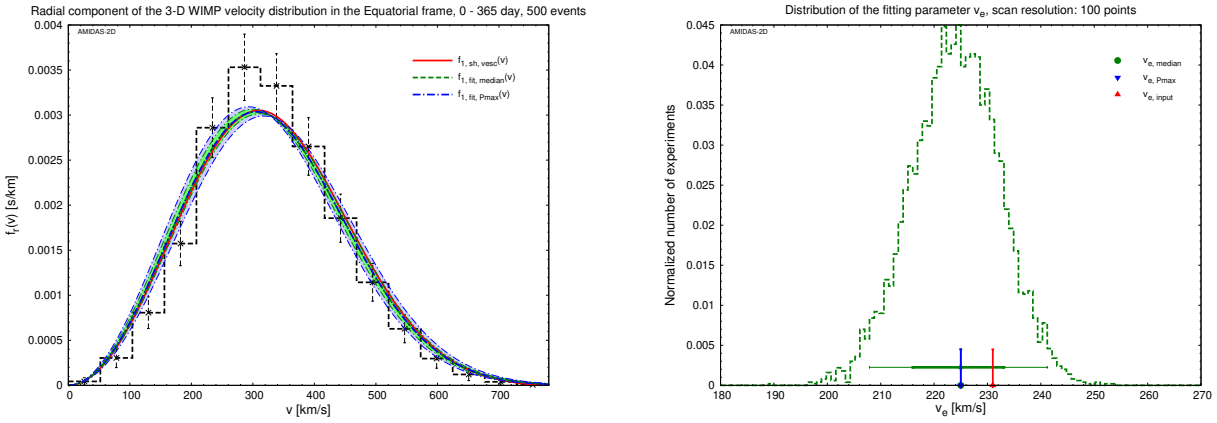

(a) (b)

Figure 43: As in Figs. 27, reconstructed with the v_0–fixed velocity distribution $f_{1,\mathrm{sh},v_\mathrm{e}}(v;v_\mathrm{e})$, except that 500 total events on average in one entire year have been simulated. Note that the scanning range of the fitting parameter v_e is shrunk to between 180 km/s and 270 km/s.

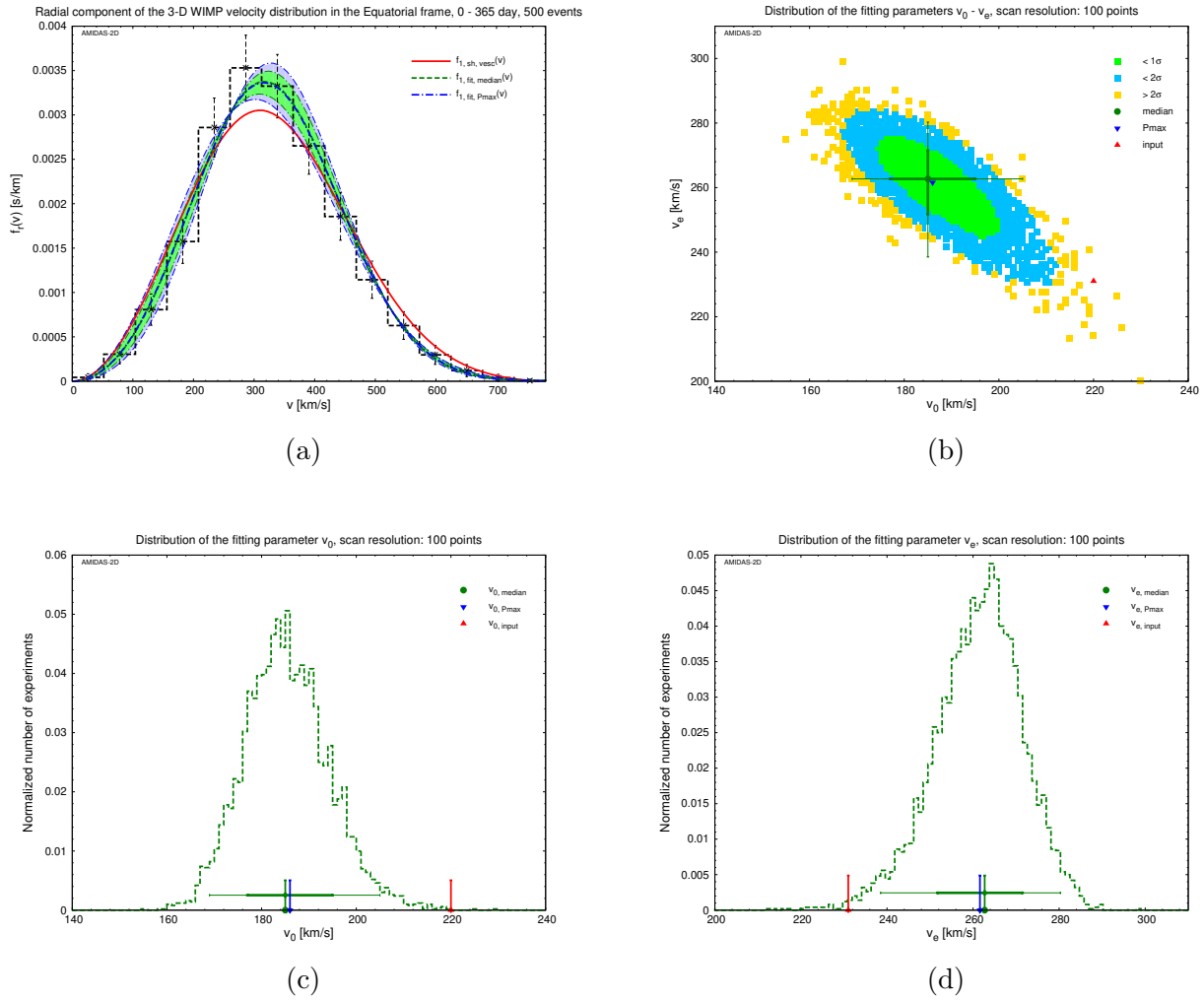

Figure 44: As in Figs. 28, reconstructed with the simplified velocity distribution $f_{1,\mathrm{sh}}(v; v_0, v_\mathrm{e})$, except that 500 total events on average in one entire year have been simulated. Note that the scanning ranges of the fitting parameters v_0 and v_e are shrunk to between 140 km/s and 240 km/s and between 200 km/s and 310 km/s, respectively.

(see Table 10). Additionally, it would be worth to also notice that, in (the advanced) Winter the deviations of the best–fit values of v_0 and v_e from their theoretical (annual–average) values of 220 km/s and 231 km/s could be as large as $\sim 3.3\sigma$ and $\sim 2.6\sigma$ of their statistical uncertainties, respectively.

In Tables 11 and 12, we summarize the reconstructed results of the fitting parameters v_0 and v_e as well as their $1(2)\sigma$ statistical uncertainty ranges of the median values by using the one–parameter and the v_0–fixed velocity distribution with 500 total events on average in each 60-day observation period of the advanced seasons, respectively.

With the simplified and the modified velocity distributions $\boldsymbol{f_{1,\mathrm{sh}}(v; v_0, v_\mathrm{e})}$ and $\boldsymbol{f_{1,\mathrm{sh},\Delta v}(v; v_0, \Delta v)}$

As in Secs. 4.3.3 and 4.3.4, we release now the constraints that $v_\mathrm{e} = 1.05\, v_0$ and $v_0 = 220$ km/s and consider the simplified and the modified velocity distribution functions, $f_{1,\mathrm{sh}}(v; v_0, v_\mathrm{e})$ and

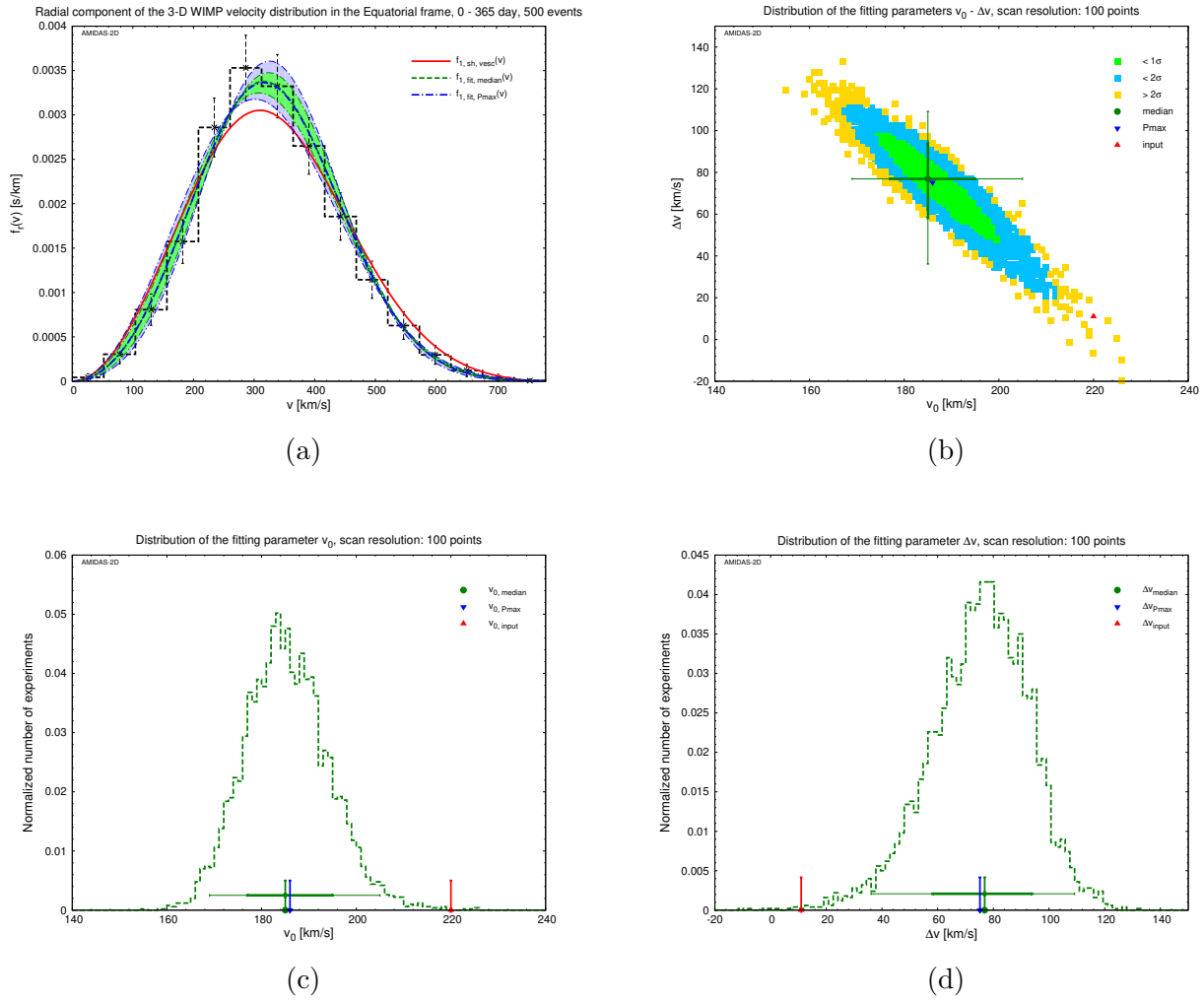

Figure 45: As in Figs. 29, reconstructed with the modified velocity distribution $f_{1,\mathrm{sh},\Delta v}(v; v_0, \Delta v)$, except that 500 total events on average in one entire year have been simulated. Note that the scanning ranges of the fitting parameters v_0 and Δv are shrunk to between 140 km/s and 240 km/s and between -20 km/s and 150 km/s, respectively.

$f_{1,\mathrm{sh},\Delta v}(v; v_0, \Delta v)$, respectively, in order to check the identification possibility of the invariability of the Solar Galactic velocity v_0 as well as that of the variation of the Earth's Galactic velocity v_e observed in Secs. 4.3.3 and 4.3.4.

In Figs. 48 and Figs. 49, we show the reconstructed radial distributions of the 3-D WIMP velocity and the $1(2)\sigma$ statistical uncertainty bands as well as the distributions of the fitting parameters v_0, v_e and Δv in all simulated experiments on the $v_0 - v_\mathrm{e}$ and $v_0 - \Delta v$ planes by using the simplified and the modified velocity distributions in four observation periods of the advanced seasons, respectively. As observed in Secs. 4.3.3 and 4.3.4, although the first fitting parameter v_0 is unconstraint, its best–fit values in four advanced seasons would be fixed as its annual average value of $\simeq$ 185 km/s, with the similar $1(2)\sigma$ statistical uncertainties of $^{+10.0}_{-\ 8.0}$ ($^{+20.0}_{-16.0}$) km/s. In contrast, in four advanced seasons the best–fit values of the second fitting parameter v_e and Δv show clearly the (approximately) symmetric periodic variations of 262.7 ($\pm \sim 13$) km/s and 78.6 ($\pm \sim 12$) km/s, respectively. Additionally, these annual variations would now be comparable with (or even larger than) their strongly reduced 1σ statistical uncertainties. Remind

Fitting dist.	Parameter	Max. $P_{\rm median}$	Median	1σ range	2σ range
$f_{1,{\rm sh},v_0}(v)$	v_0 [km/s]	214.5	$214.5 \pm 3.5\,(\pm 6.5)$	[211.0, 218.0]	[208.0, 221.0]
$f_{1,{\rm sh},v_{\rm e}}(v)$	$v_{\rm e}$ [km/s]	225.0	$225.0\,^{+8.1}_{-9.0}\,(^{+16.2}_{-17.1})$	[216.0, 233.1]	[207.9, 241.2]
$f_{1,{\rm sh}}(v)$	v_0 [km/s]	186.0	$185.0\,^{+10.0}_{-\ 8.0}\,(^{+20.0}_{-16.0})$	[177.0, 195.0]	[169.0, 205.0]
	$v_{\rm e}$ [km/s]	261.6	$262.7\,^{+\ 8.8}_{-11.0}\,(^{+17.6}_{-24.2})$	[251.7, 271.5]	[238.5, 280.3]
$f_{1,{\rm sh},\Delta v}(v)$	v_0 [km/s]	186.0	$185.0\,^{+10.0}_{-\ 8.0}\,(^{+20.0}_{-16.0})$	[177.0, 195.0]	[169.0, 205.0]
	Δv [km/s]	75.2	$76.9\,^{+17.0}_{-18.7}\,(^{+32.3}_{-40.8})$	[58.2, 93.9]	[36.1, 109.2]
500 total events on average in the observation period of 0 – 365 day					

Table 10: The summary of the reconstructed results of the fitting parameters and their $1(2)\sigma$ statistical uncertainty ranges of the median values by using four considered fitting velocity distributions with 500 total events on average in one entire year shown in Figs. 42, 43, 44, and 45.

that, as shown in Figs. 44(b) and 45(b), the theoretical values of the fitting parameters (the red upward–triangle) are now clearly out of the (light–blue) 2σ statistical uncertainty contours.

In Tables 13 and 14, we summarize the reconstructed results of the fitting parameters v_0, $v_{\rm e}$ and Δv as well as their $1(2)\sigma$ statistical uncertainty ranges of the median values by using the simplified and the modified velocity distribution with 500 total events on average in each 60-day observation period of the advanced seasons, respectively.

5.2.3 Fitted radial WIMP velocity distribution in the Galactic frame

Finally, we present here also our Bayesian reconstruction result of the radial distribution of the 3-D WIMP velocity in the Galactic coordinate system with 500 total events on average recorded in one entire year. Note that the scanning range of the fitting parameter has been shrunk to 190 km/s $\leq v_0 \leq$ 250 km/s.

In Figs. 50, we show the reconstructed radial distributions of the 3-D WIMP velocity and the $1(2)\sigma$ statistical uncertainty bands by using the simple Maxwellian velocity distribution $f_{1,{\rm Gau}}(v)$ given by Eq. (2). As in Sec. 4.4, our best–fit reconstruction distributions could match the input simple Maxwellian velocity distribution perfectly and the fitting parameter v_0 could also be pinned down very precisely with the $\sim 1/3$ reduced statistical uncertainties.

In Table 15, we summarize the reconstructed results of the fitting parameter v_0 and their $1(2)\sigma$ statistical uncertainty ranges of the median values by using the simple Maxwellian velocity distribution with 500 total events on average in one entire year shown in Figs. 50.

6 Summary and conclusions

In this paper, as a preparation for our future study aiming to develop data analysis procedures using and/or combining 3-dimensional information offered by directional Dark Matter detection

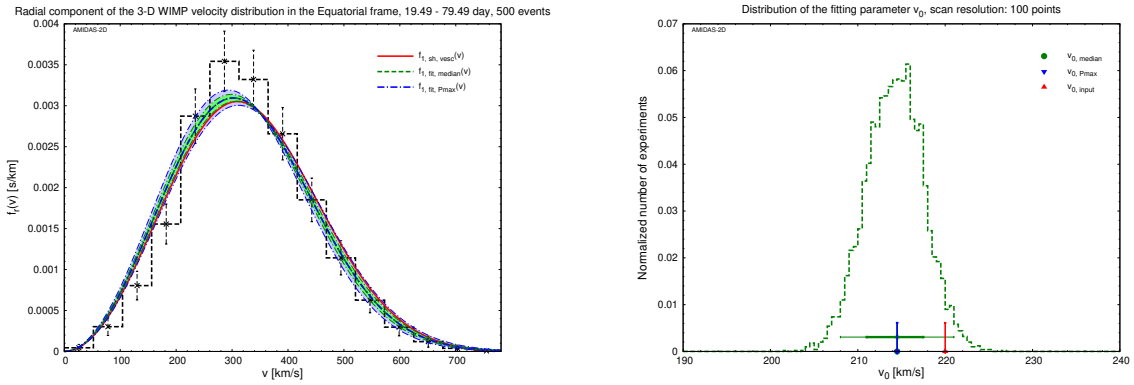

(a) 19.49 – 79.49 day

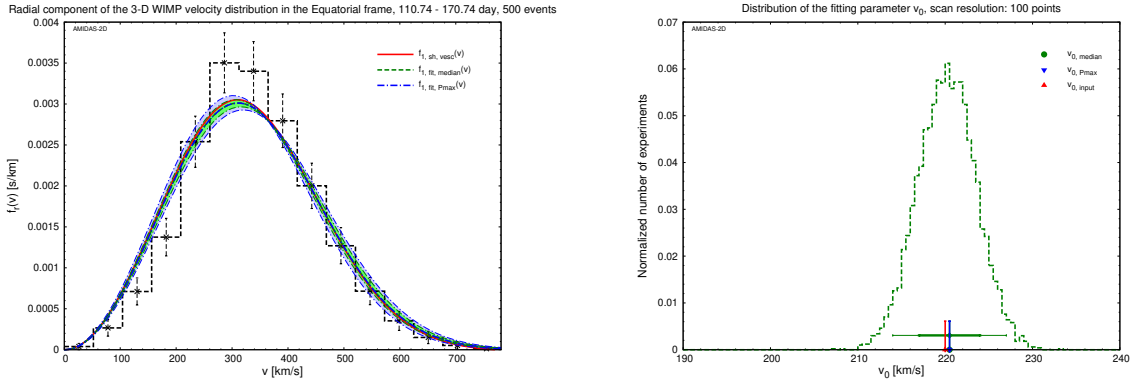

(b) 110.74 – 170.74 day

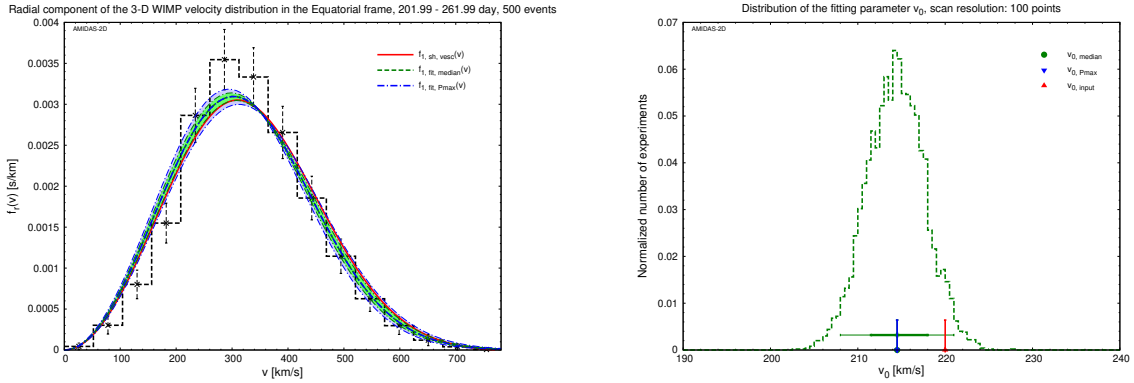

(c) 201.99 – 261.99 day

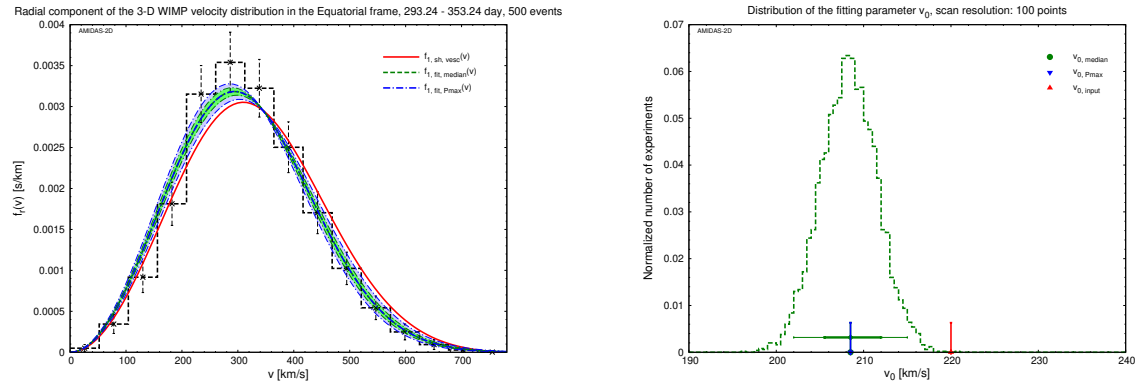

(d) 293.24 – 353.24 day

Figure 46: As in Figs. 30, reconstructed with the one–parameter velocity distribution $f_{1,\mathrm{sh},v_0}(v;v_0)$, except that 500 total events on average in each 60-day observation period of the advanced seasons have been simulated.

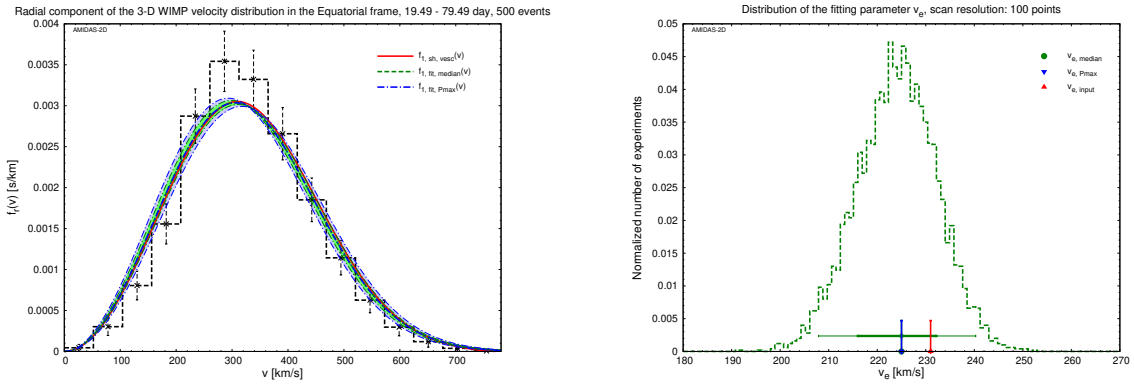

(a) 19.49 – 79.49 day

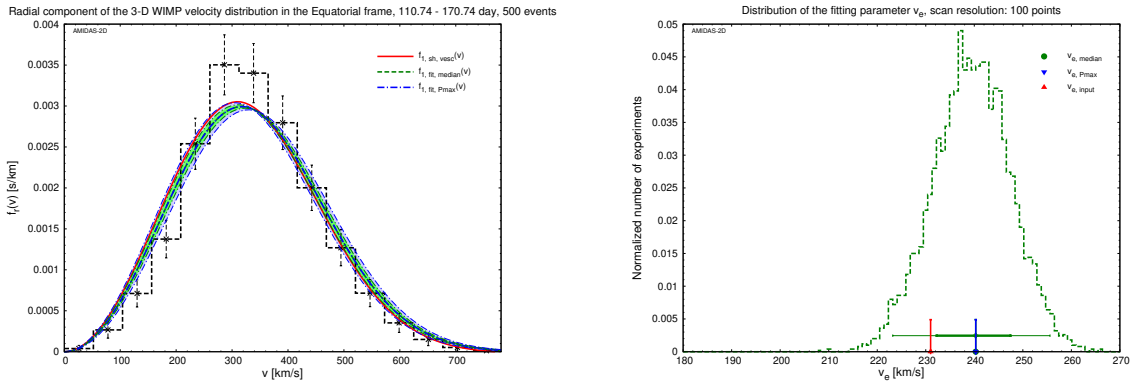

(b) 110.74 – 170.74 day

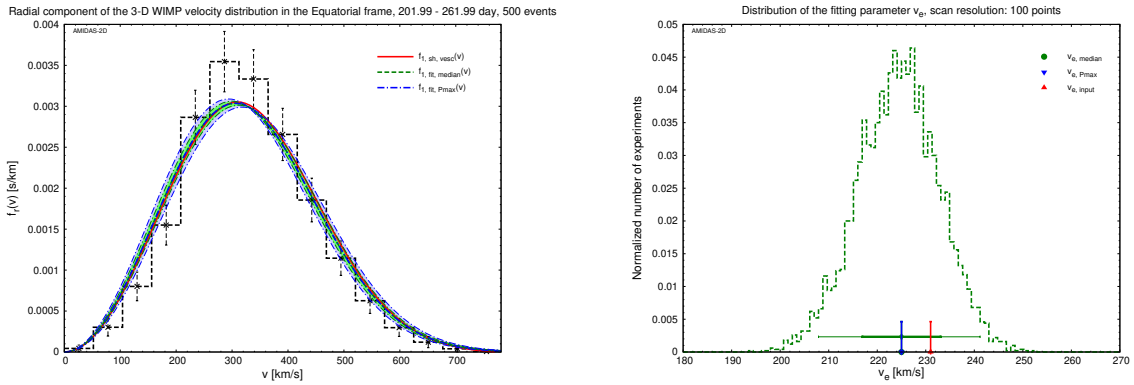

(c) 201.99 – 261.99 day

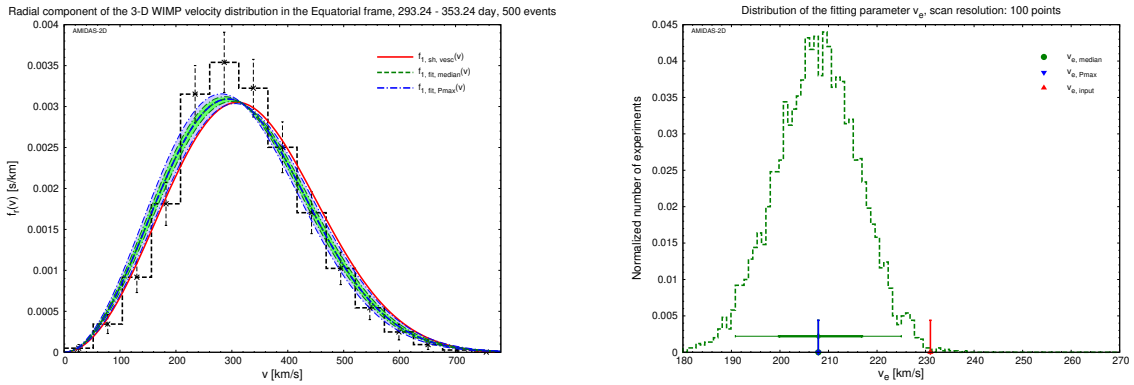

(d) 293.24 – 353.24 day

Figure 47: As in Figs. 31, reconstructed with the v_0–fixed velocity distribution $f_{1,\mathrm{sh},v_\mathrm{e}}(v;v_\mathrm{e})$, except that 500 total events on average in each 60-day observation period of the advanced seasons have been simulated.

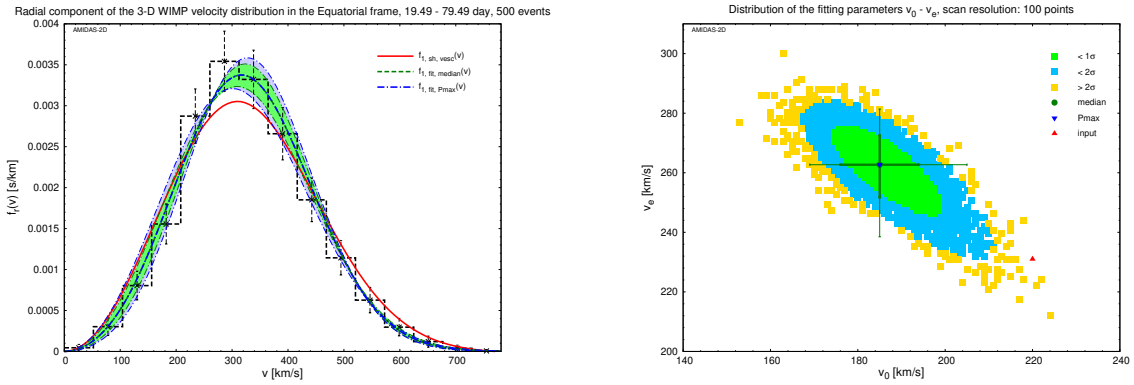

(a) 19.49 – 79.49 day

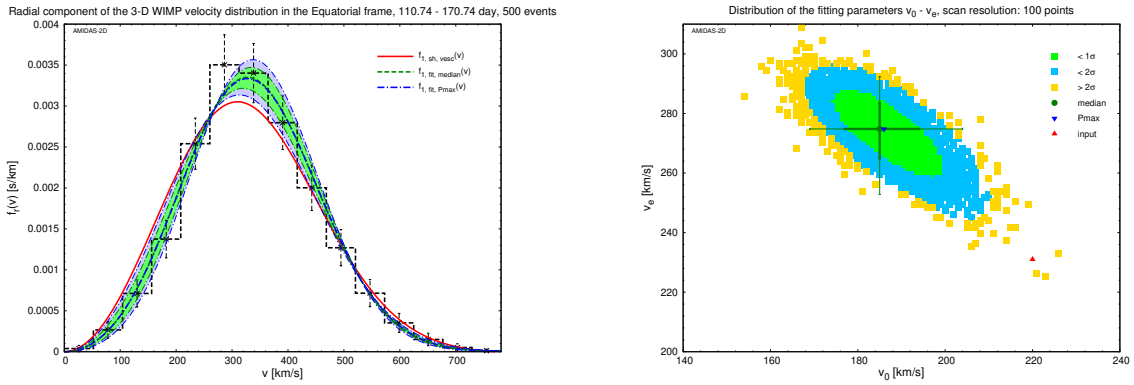

(b) 110.74 – 170.74 day

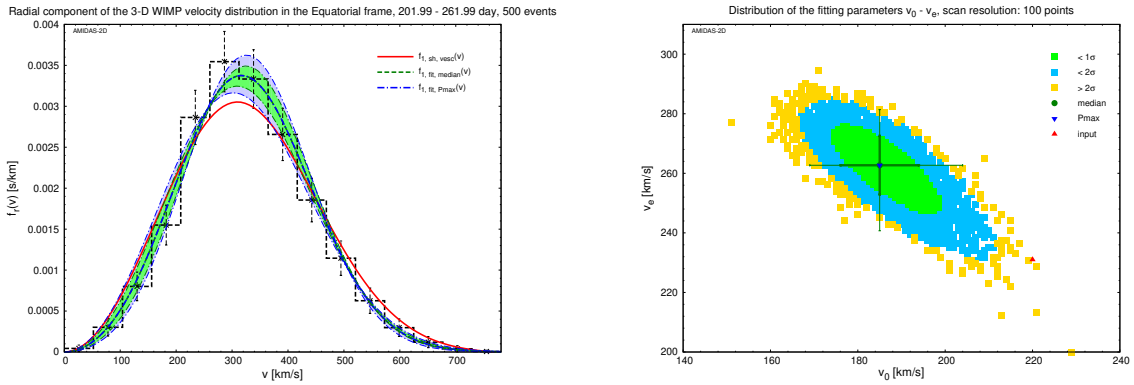

(c) 201.99 – 261.99 day

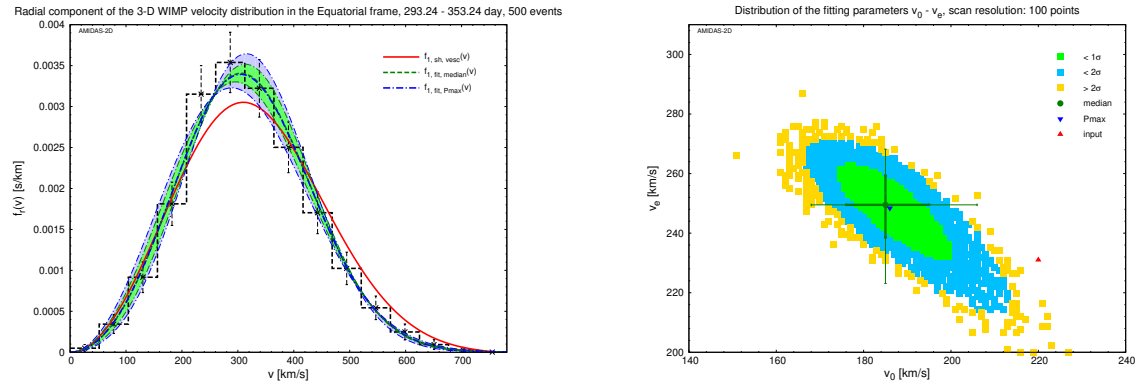

(d) 293.24 – 353.24 day

Figure 48: As in Figs. 32, reconstructed with the simplified velocity distribution $f_{1,\mathrm{sh}}(v; v_0, v_\mathrm{e})$, except that 500 total events on average in each 60-day observation period of the advanced seasons have been simulated.

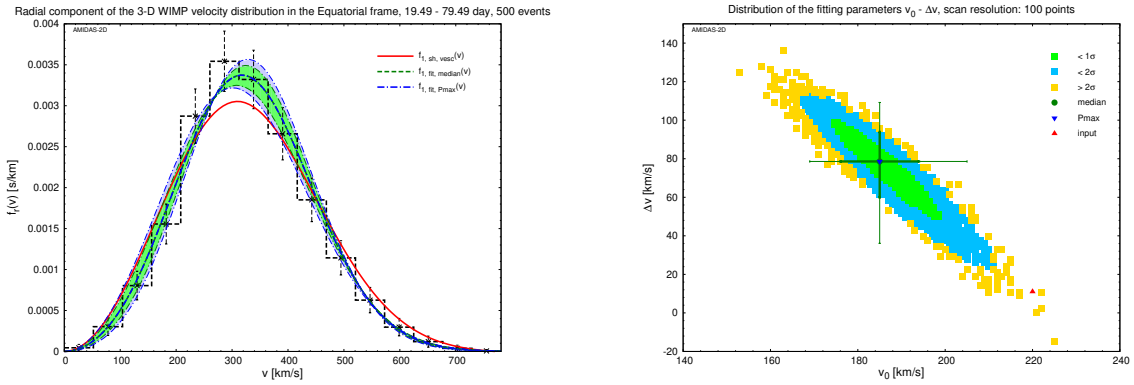

(a) 19.49 – 79.49 day

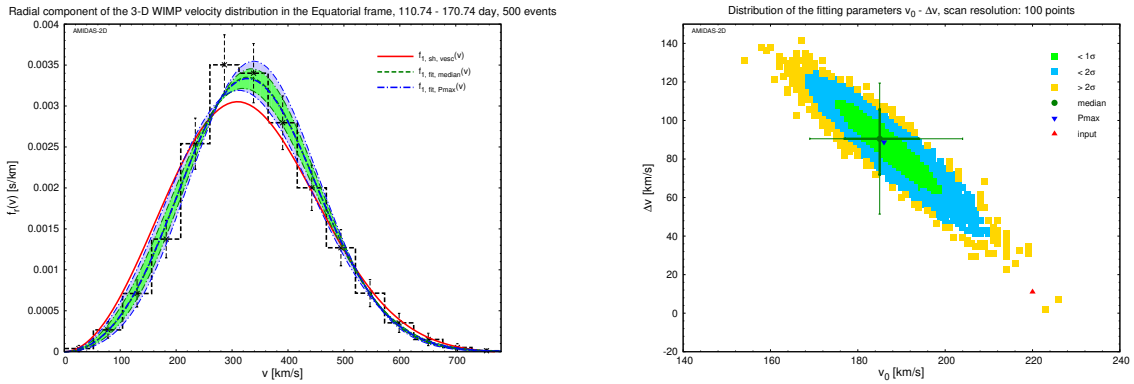

(b) 110.74 – 170.74 day

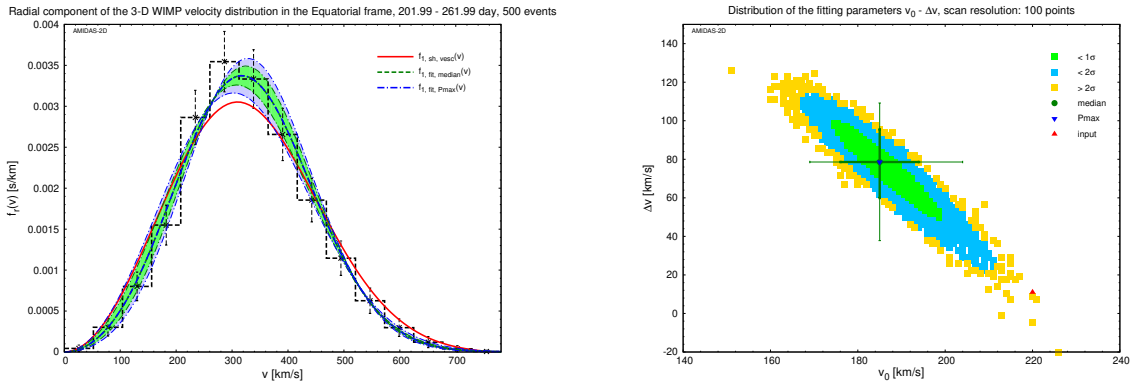

(c) 201.99 – 261.99 day

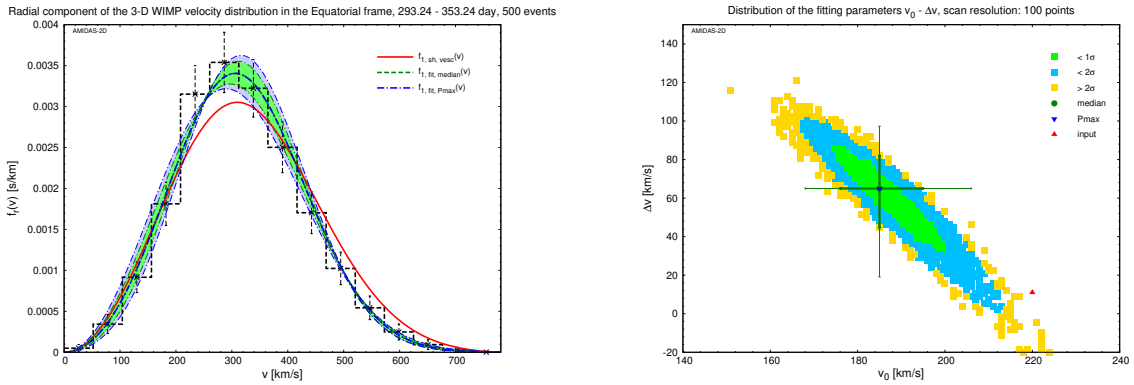

(d) 293.24 – 353.24 day

Figure 49: As in Figs. 33, reconstructed with the modified velocity distribution $f_{1,\mathrm{sh},\Delta v}(v; v_0, \Delta v)$, except that 500 total events on average in each 60-day observation period of the advanced seasons have been simulated.

Fitting distribution: one–parameter velocity distribution $f_{1,\mathrm{sh},v_0}(v;v_0)$					
Central date (observation period) (day)	Parameter	Max. $\mathrm{P_{median}}$	Median	1σ range	2σ range
49.49 (19.49 – 79.49)	v_0 [km/s]	214.5	$214.5\,^{+3.0}_{-3.5}\,(\pm 6.5)$	[211.0, 217.5]	[208.0, 221.0]
140.74 (110.74 – 170.74)	v_0 [km/s]	220.5	$220.5 \pm 3.5\,(\pm 6.5)$	[217.0, 224.0]	[214.0, 227.0]
231.99 (201.99 – 261.99)	v_0 [km/s]	214.5	$214.5\,^{+3.5}_{-3.0}\,(\pm 6.5)$	[211.5, 218.0]	[208.0, 221.0]
323.24 (293.24 – 353.24)	v_0 [km/s]	208.5	$208.5\,^{+3.5}_{-3.0}\,(\pm 6.5)$	[205.5, 212.0]	[202.0, 215.0]
500 total events on average in one observation period of 60 days					

Table 11: The summary of the reconstructed results of the fitting parameter v_0 and their $1(2)\sigma$ statistical uncertainty ranges of the median values by using the one–parameter velocity distribution $f_{1,\mathrm{sh},v_0}(v;v_0)$ with 500 total events on average in each 60–day observation period of the advanced seasons.

experiments, to, e.g., reconstruct the 3-dimensional WIMP velocity distribution, we simulated 3-D velocity information (magnitude, direction and measuring time) of WIMP events in the Galactic coordinate system, transformed them to different celestial coordinate systems, and

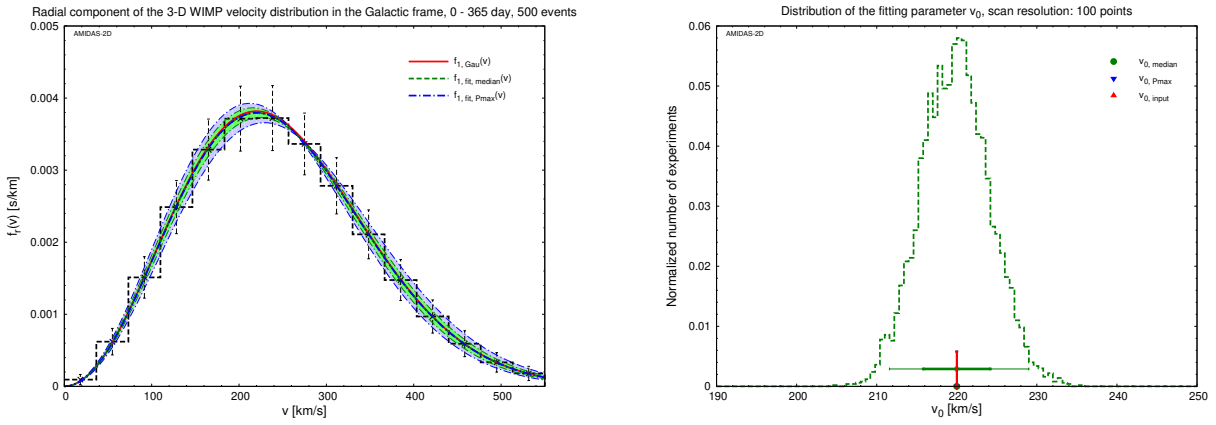

(a) (b)

Figure 50: As in Figs. 34, reconstructed with the simple Maxwellian velocity distribution $f_{1,\mathrm{Gau}}(v)$, except that 500 total events on average in one entire year have been simulated. Note that the scanning range of the fitting parameter v_0 is shrunk to between 190 km/s and 250 km/s.

Fitting distribution: v_0–fixed velocity distribution $f_{1,\mathrm{sh},v_\mathrm{e}}(v;v_\mathrm{e})$					
Central date (observation period) (day)	Parameter	Max. $\mathrm{P}_{\mathrm{median}}$	Median	1σ range	2σ range
49.49 (19.49 – 79.49)	v_e [km/s]	225.0	$225.0\,^{+7.2}_{-9.0}\,(^{+15.3}_{-17.1})$	[216.0, 232.2]	[207.9, 240.3]
140.74 (110.74 – 170.74)	v_e [km/s]	240.3	$240.3\,^{+7.2}_{-8.1}\,(^{+15.3}_{-17.1})$	[232.2, 247.5]	[223.2, 255.6]
231.99 (201.99 – 261.99)	v_e [km/s]	225.0	$225.0 \pm 8.1\,(^{+16.2}_{-17.1})$	[216.9, 233.1]	[207.9, 241.2]
323.24 (293.24 – 353.24)	v_e [km/s]	207.9	$207.9\,^{+9.0}_{-8.1}\,(\pm 17.1)$	[199.8, 216.9]	[190.8, 225.0]
500 total events on average in one observation period of 60 days					

Table 12: The summary of the reconstructed results of the fitting parameter v_e and their $1(2)\sigma$ statistical uncertainty ranges of the median values by using the v_0–fixed velocity distribution $f_{1,\mathrm{sh},v_\mathrm{e}}(v;v_\mathrm{e})$ with 500 total events on average in each 60–day observation period of the advanced seasons.

then investigated the angular distribution patterns of the 3-dimensional WIMP velocity as well as reconstructed its radial distribution (magnitude) by applying the Bayesian fitting technique.

Our simulations indicate that, first, with $\mathcal{O}(50)$ total WIMP events recorded in one entire year, the angular distribution patterns of the 3-D WIMP velocity transformed to the Ecliptic and Equatorial coordinate systems would already show clear anisotropy. And, more precisely, the most frequent directions of the 3-D WIMP velocity would be close to, but somehow deviate from the theoretically predicted direction of the WIMP wind, i.e., the opposite direction of the Solar movement in our Galaxy. Once $\mathcal{O}(500)$ total events could be accumulated and thus a higher analysis resolution would be used, the systematic bias could be reduced, but a small deviation might still exist.

Moreover, for demonstrating the "annual" modulation of the main direction of the WIMP wind due to the Earth's orbital motion around the Sun, we considered two sets of observation periods: four normal seasons and four advanced seasons, $\mathcal{O}(50)$ total recorded events in 60 observation days ($\pm$ 30 days from the central date) had been considered for each season. It has been found that, with only $\mathcal{O}(50)$ total WIMP events recorded in one season, the pattern of the angular distribution of the 3-D WIMP velocity in the Equatorial coordinate system would already vary slightly but clearly with a clockwise rotation around the theoretical main direction of the WIMP wind. This would be, besides the pure anisotropy of the WIMP velocity, a second (important) characteristic for identifying directional WIMP signals and discriminating from any (unexpected) backgrounds with some specified incoming directions. Meanwhile, the angular distribution pattern in our Earth coordinate system in both of four normal and four advanced seasons would also show clear anisotropy with an annually rotation.

In addition, in our laboratory–dependent horizontal coordinate system, as expected, our

Fitting distribution: simplified velocity distribution $f_{1,\mathrm{sh}}(v; v_0, v_\mathrm{e})$					
Central date (observation period) (day)	Parameter	Max. $\mathrm{P}_{\mathrm{median}}$	Median	1σ range	2σ range
49.49 (19.49 – 79.49)	v_0 [km/s]	185.0	$185.0 \pm 9.0\,(^{+20.0}_{-16.0})$	[176.0, 194.0]	[169.0, 205.0]
	v_e [km/s]	262.7	$262.7\,^{+\ 9.9}_{-11.0}\,(^{+18.7}_{-24.2})$	[251.7, 272.6]	[238.5, 281.4]
140.74 (110.74 – 170.74)	v_0 [km/s]	186.0	$185.0\,^{+9.0}_{-8.0}\,(^{+19.0}_{-16.0})$	[177.0, 194.0]	[169.0, 204.0]
	v_e [km/s]	274.8	$274.8\,^{+8.8}_{-9.9}\,(^{+17.6}_{-22.0})$	[264.9, 283.6]	[252.8, 292.4]
231.99 (201.99 – 261.99)	v_0 [km/s]	185.0	$185.0 \pm 9.0\,(^{+19.0}_{-16.0})$	[176.0, 194.0]	[169.0, 204.0]
	v_e [km/s]	262.7	$262.7 \pm 9.9\,(^{+18.7}_{-22.0})$	[252.8, 272.6]	[240.7, 281.4]
323.24 (293.24 – 353.24)	v_0 [km/s]	186.0	$185.0\,^{+10.0}_{-\ 9.0}\,(^{+21.0}_{-17.0})$	[176.0, 195.0]	[168.0, 206.0]
	v_e [km/s]	248.4	$249.5\,^{+\ 9.9}_{-11.0}\,(^{+18.7}_{-26.4})$	[238.5, 259.4]	[223.1, 268.2]
500 total events on average in one observation period of 60 days					

Table 13: The summary of the reconstructed results of the fitting parameters v_0 and v_e as well as their $1(2)\sigma$ statistical uncertainty ranges of the median values by using the simplified velocity distribution $f_{1,\mathrm{sh}}(v; v_0, v_\mathrm{e})$ with 500 total events on average in each 60–day observation period of the advanced seasons.

simulation results with $\mathcal{O}(50)$ total events recorded in each (60-day) season show clearly reversed distribution patterns for laboratories located in the Northern or the Southern Hemisphere. The simulations for different underground laboratories show also that, with more WIMP events and a higher analysis resolution, we might even be able to demonstrate a more detailed latitude–dependent pattern.

Regarding the original purpose of directional Dark Matter detection experiments, we demonstrated also the laboratory–dependent diurnal modulation of the angular WIMP velocity distribution pattern in our laboratory coordinate system with $\mathcal{O}(50)$ total WIMP events recorded in each 4-hour daily shift (in the 60-day observation period). Not surprisingly, such a laboratory–dependent diurnal modulation shows a similar variation pattern to the annual modulation in our horizontal coordinate system, requires however much more recorded events.

On the other hand, we found unexpectedly that, with only $\mathcal{O}(50)$ total WIMP events recorded in one entire year, the radial component of the transformed 3-D WIMP velocity would already show a distribution shape, which is a little bit more concentrated than the theoretically derived shifted Maxwellian velocity distribution in the range around the average WIMP velocity, but a little bit reduced in the lower and higher velocity ranges. By using the Bayesian fitting technique, we obtained the slightly–smaller best–fit values of the fitting parameter v_0 (under the constraint of $v_\mathrm{e} = 1.05\, v_0$) and v_e (under the constraint of $v_0 = 220$ km/s), although the reconstructed velocity distributions could match the theoretical velocity distribution very well.

However, once we release the constraints on v_0 and v_e and treat them as two independent

Fitting distribution: modified velocity distribution $f_{1,\mathrm{sh},\Delta v}(v; v_0, \Delta v)$					
Central date (observation period) (day)	Parameter	Max. $\mathrm{P}_{\mathrm{median}}$	Median	1σ range	2σ range
49.49 (19.49 – 79.49)	v_0 [km/s]	185.0	$185.0 \pm 9.0\,(^{+20.0}_{-16.0})$	[176.0, 194.0]	[169.0, 205.0]
	Δv [km/s]	78.6	$78.6\,^{+15.3}_{-18.7}\,(^{+30.6}_{-42.5})$	[59.9, 93.9]	[36.1, 109.2]
140.74 (110.74 – 170.74)	v_0 [km/s]	186.0	$185.0\,^{+9.0}_{-8.0}\,(^{+19.0}_{-16.0})$	[177.0, 194.0]	[169.0, 204.0]
	Δv [km/s]	88.8	$90.5\,^{+15.3}_{-18.7}\,(^{+28.9}_{-39.1})$	[71.8, 105.8]	[51.4, 119.4]
231.99 (201.99 – 261.99)	v_0 [km/s]	185.0	$185.0 \pm 9.0\,(^{+19.0}_{-16.0})$	[176.0, 194.0]	[169.0, 204.0]
	Δv [km/s]	78.6	$78.6\,^{+17.0}_{-18.7}\,(^{+30.6}_{-40.8})$	[59.9, 95.6]	[37.8, 109.2]
323.24 (293.24 – 353.24)	v_0 [km/s]	185.0	$185.0\,^{+10.0}_{-9.0}\,(^{+21.0}_{-17.0})$	[176.0, 195.0]	[168.0, 206.0]
	Δv [km/s]	65.0	$65.0\,^{+17.0}_{-20.4}\,(^{+32.3}_{-45.9})$	[44.6, 82.0]	[19.1, 97.3]
500 total events on average in one observation period of 60 days					

Table 14: The summary of the reconstructed results of the fitting parameters v_0 and Δv as well as their $1(2)\sigma$ statistical uncertainty ranges of the median values by using the modified velocity distribution $f_{1,\mathrm{sh},\Delta v}(v; v_0, \Delta v)$ with 500 total events on average in each 60–day observation period of the advanced seasons.

fitting parameters, the reconstructed velocity distributions would have a clearly different shape from the theoretical prediction, although, with only $\mathcal{O}(50)$ total events recorded in one entire year and thus a relatively large statistical uncertainties, the 1σ statistical uncertainty bands of the reconstructed velocity distributions could still cover the theoretical distribution in most part of the velocity range. The best–fit values of the fitting parameters v_0 and v_{e} would also be $\sim 16\%$ smaller and $\sim 14\%$ larger than their theoretical values, respectively.

Once we raise the event number to $\mathcal{O}(500)$ total WIMP events, the best–fit velocity distributions would differ pretty strongly from the theoretical distribution and their narrower 1σ

Fitting dist.	Parameter	Max. $\mathrm{P}_{\mathrm{median}}$	Median	1σ range	2σ range
$f_{1,\mathrm{Gau}}(v)$	v_0 [km/s]	220.0	$220.0 \pm 4.2\,(^{+9.0}_{-8.4})$	[215.8, 224.2]	[211.6, 229.0]
500 total events on average in the observation period of 0 – 365 day					

Table 15: The summary of the reconstructed results of the fitting parameter v_0 and their $1(2)\sigma$ statistical uncertainty ranges of the median values by using the simple Maxwellian velocity distribution with 500 total events on average in one entire year shown in Figs. 50.

statistical uncertainty bands could not cover the expected curve in most part of the velocity ranges; the fitting parameters v_0 and v_e would also be 3σ – 4σ smaller or larger than their theoretical values, respectively. Additionally, our reconstructed radial distributions as well as their $1(2)\sigma$ statistical uncertainty bands seem not to fit the radial distribution of the simulated 3-D WIMP velocity in the middle velocity range very well. These would imply not only that the radial distribution of the 3-D WIMP velocity in the Equatorial as well as the in laboratory coordinate systems would differ from the theoretically derived analytic form, but also a requirement of the modification of the analytic form of the fitting velocity distribution function.

Nevertheless, with $\mathcal{O}(50)$ total WIMP events recorded in each (60-day) season, the annual modulation of the radial distribution of the 3-D WIMP velocity could already be identified very clearly by observing the $\sim 5\%$ annual variation of the best–fit values of the second fitting parameter v_e. In contrast and interestingly, the best–fit values of the first fitting parameter v_0 in all observation periods stay fixed, although it is also unconstraint.

In our simulations presented in this paper, 50 and 500 total WIMP events on average in (one daily shift of) one observation period (365 days/year, 60 days/season, or 4 hours/shift $\times$ 60 days) have been considered. In this and probably the next decades, even only $\mathcal{O}(50)$ total WIMP signals (per year) to observe would be a strong challenge for all (non)directional direct Dark Matter detection experiments. Fortunately, the recorded 3-D velocity information of WIMP signals offered by different underground laboratories could (in principle) be transformed to all laboratory–independent (Galactic, Ecliptic, Equatorial, and Earth) coordinate systems. Hence, data offered by more than one directional DM detection experiment could be combined for:

- the identification of the anisotropy of the angular velocity distribution of incident WIMPs;
- the demonstration of the annual modulation of the angular velocity distribution pattern of incident WIMPs;
- the Bayesian reconstruction of the radial distribution of the 3-D WIMP velocity;
- the demonstration of the annual modulation of the (Bayesian reconstructed) radial distribution of the 3-D WIMP velocity.

These analyses could be applied for reconstructing the 3-dimensional WIMP velocity distribution in both of the Equatorial and Galactic coordinate systems, for checking our theoretical models of the Galactic Dark Matter halo.

In the long term, with enough WIMP events observed in one underground laboratory, the angular distribution patterns of the 3-D WIMP velocity in the laboratory–dependent (horizontal and laboratory) coordinate systems could be used to demonstrate:

- the diurnal modulation of the angular velocity distribution pattern of incident WIMPs;
- the latitude–dependence of the angular velocity distribution pattern of incident WIMPs.

Regarding the observation periods considered in our simulations presented in this paper, we used several approximations about the Earth's orbital motion in the Solar system. First, the Earth's orbit around the Sun is perfectly circular on the Ecliptic plane and the orbital speed is thus a constant. Second, the date of the vernal equinox is fixed exactly at the end of the 79th day (the May 20th) of a 365-day year and the few extra hours in an actual Solar year have been neglected. Nevertheless, considering the very low WIMP scattering event rate and thus only a few tens of total (combined) WIMP events required in at least a few tens of days (an

overall event rate of $\lesssim$ 1 event/day) for the first–phase analyses, these approximations should be acceptable.

For our simulations presented in this paper, we also assumed implicitly that 3-D information on the velocity of incident WIMPs (magnitudes and directions/angles) can be measured by using data from directional detection experiments. However, so far we could only measure, besides recoil energies, recoil tracks and in turn recoil angles of the recoiled nuclei. A way to use the experimental measurable data (recoil energies and recoil tracks/angles of the recoiled nuclei) to reconstruct 3-D WIMP velocities requires more investigations.

Furthermore, for generating the 3-D WIMP velocity we considered in this paper only the simplest isotropic Maxwellian velocity distribution. Effects of other theoretically predicted structures of the Galactic Dark Matter halo, including some possible streams and/or the bulk rotation discussed in literature, and the possibility of distinguishing these models would also be interesting to investigate.

In summary, we have begun to extend our earlier works and to study how to use information provided by directional Dark Matter detection experiments to understand the 3-dimensional (velocity) distribution of Galactic DM particles. Hopefully, this and more works achieved in the future could offer useful information on the structure of our Galaxy as well as for data analyses in indirect Dark Matter detection experiments.

Acknowledgments

The author appreciates N. Bozorgnia and P. Gondolo for useful discussions about the transformations between the celestial coordinate systems. The author would also like to thank the friendly hospitality of the Gran Sasso Science Institute, the School of Physics at the University of New South Wales, the School of Physics and Astronomy at the Monash University, and the Department of Nuclear Physics at the Australian National University during the completion and finalization of this work.

A Definitions of and transformations between the celestial coordinate systems

In this section, we describe the definitions of the celestial coordinate systems used in our simulations and data analyses presented in this paper as well as the transformation matrices between these coordinate systems in detail. In order to avoid possible confusion, the conventional astronomical definitions of these coordinate systems will also be mentioned.

A.1 Definitions of the horizontal and the laboratory coordinate systems

Firstly, in order to connect the celestial (laboratory–independent) (Galactic, Ecliptic, and Equatorial) coordinate systems with the geographic (laboratory–dependent) (horizontal and laboratory) coordinate systems, we defined particularly the Earth coordinate system as described in Sec. 2.1.3 and sketched in Fig. 4 [63].

Then we discuss here two coordinate systems depending on the geographic location of the underground laboratory of interest as well as the measuring time of WIMP scattering events.

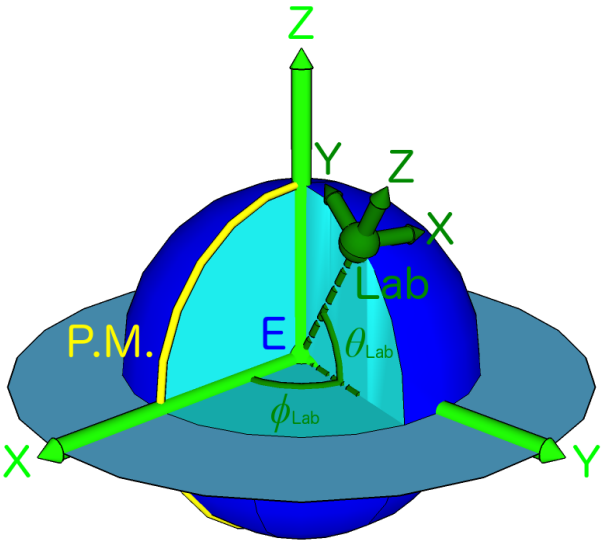

Figure A1: The sketch of the conventional definition of the (dark–green) horizontal/laboratory coordinate system: it is basically the same as our definition of the horizontal coordinate system described in Sec. 2.1.4 and sketched in Fig. 5, except that the primary direction (the $\mathbf{X}_{\rm H/Lab}$–axis) points here towards east. Our (light–green) Earth coordinate system is also given here.

A.1.1 Conventional definition

Conventionally, as shown in Fig. A1, the horizontal/laboratory coordinate system is defined with the origin at the geographic location of the laboratory of interest at, e.g., 12 midnight (the beginning) of (the UTC time of) each single Solar day, the primary direction (the $\mathbf{X}_{\rm H/Lab}$–axis) and the $\mathbf{Z}_{\rm H/Lab}$–axis pointing towards east and the zenith, respectively, and the right–handed convention for defining the $\mathbf{Y}_{\rm H/Lab}$–axis.

In Fig. A1, we sketch the conventionally defined horizontal/laboratory coordinate system with our Earth coordinate system together. It can easily find out that, by rotating the conventional horizontal/laboratory coordinate system at first $-(\pi/2-\theta_{\rm Lab})$ around the $\mathbf{X}_{\rm H/Lab}$–axis and then $-(\pi/2+\phi_{\rm Lab})$ around the $\mathbf{Z}_{\rm H/Lab}$–axis, one can obtain our Earth coordinate system. Hence, the transformation matrix from the conventional horizontal/laboratory coordinate system to our Earth coordinate system can be expressed by

$$\mathbf{M}_{\rm H\to E,conv}(\phi_{\rm Lab},\theta_{\rm Lab}) = \begin{bmatrix} \cos\left[-\left(\pi/2+\phi_{\rm Lab}\right)\right] & \sin\left[-\left(\pi/2+\phi_{\rm Lab}\right)\right] & 0 \\ -\sin\left[-\left(\pi/2+\phi_{\rm Lab}\right)\right] & \cos\left[-\left(\pi/2+\phi_{\rm Lab}\right)\right] & 0 \\ 0 & 0 & 1 \end{bmatrix} \times \begin{bmatrix} 1 & 0 & 0 \\ 0 & \cos\left[-\left(\pi/2-\theta_{\rm Lab}\right)\right] & \sin\left[-\left(\pi/2-\theta_{\rm Lab}\right)\right] \\ 0 & -\sin\left[-\left(\pi/2-\theta_{\rm Lab}\right)\right] & \cos\left[-\left(\pi/2-\theta_{\rm Lab}\right)\right] \end{bmatrix}$$

$$= \begin{bmatrix} -\sin\phi_{\rm Lab} & -\cos\phi_{\rm Lab}\sin\theta_{\rm Lab} & \cos\phi_{\rm Lab}\cos\theta_{\rm Lab} \\ \cos\phi_{\rm Lab} & -\sin\phi_{\rm Lab}\sin\theta_{\rm Lab} & \sin\phi_{\rm Lab}\cos\theta_{\rm Lab} \\ 0 & \cos\theta_{\rm Lab} & \sin\theta_{\rm Lab} \end{bmatrix}, \quad \text{(A1a)}$$

where $\phi_{\rm Lab}$ and $\theta_{\rm Lab}$ are the longitude and the latitude of the location of the laboratory, respectively. Conversely, the transformation matrix from our Earth coordinate system to the conventional horizontal/laboratory coordinate system can be given directly as

$$\mathbf{M}_{\rm E\to H,conv}(\phi_{\rm Lab},\theta_{\rm Lab}) = \mathbf{M}^{\rm T}_{\rm H\to E,conv}(\phi_{\rm Lab},\theta_{\rm Lab})$$
$$= \begin{bmatrix} -\sin\phi_{\rm Lab} & \cos\phi_{\rm Lab} & 0 \\ -\cos\phi_{\rm Lab}\sin\theta_{\rm Lab} & -\sin\phi_{\rm Lab}\sin\theta_{\rm Lab} & \cos\theta_{\rm Lab} \\ \cos\phi_{\rm Lab}\cos\theta_{\rm Lab} & \sin\phi_{\rm Lab}\cos\theta_{\rm Lab} & \sin\theta_{\rm Lab} \end{bmatrix}. \quad \text{(A1b)}$$

A.1.2 Our definitions

In order to understand and compare the angular distribution patterns of the 3-D WIMP velocity offered by different underground laboratories more easily, as sketched in Fig. 5, for our simulations presented in this paper we defined the horizontal coordinate system by rotating the conventional coordinates 90° around the $\mathbf{Z}_{\rm H(/Lab)}$–axis, so that the $\mathbf{X}_{\rm H}$–axis points now towards north. Remind that, as our Earth coordinate system, for each single Solar day, our horizontal coordinate system is fixed at 12 midnight (the beginning) of (the UTC time of) the day.

By this definition, the transformation from our horizontal coordinate system to the Earth coordinate system can be done by rotating at first $\pi/2-\theta_{\rm Lab}$ around the $\mathbf{Y}_{\rm H}$–axis and then $\pi-\phi_{\rm Lab}$ around the $\mathbf{Z}_{\rm H}$–axis. Thus the transformation matrix can be given by

$$\mathbf{M}_{\rm H\to E}(\phi_{\rm Lab},\theta_{\rm Lab}) = \begin{bmatrix} \cos(\pi-\phi_{\rm Lab}) & \sin(\pi-\phi_{\rm Lab}) & 0 \\ -\sin(\pi-\phi_{\rm Lab}) & \cos(\pi-\phi_{\rm Lab}) & 0 \\ 0 & 0 & 1 \end{bmatrix}$$
$$\times \begin{bmatrix} \cos(\pi/2-\theta_{\rm Lab}) & 0 & -\sin(\pi/2-\theta_{\rm Lab}) \\ 0 & 1 & 0 \\ \sin(\pi/2-\theta_{\rm Lab}) & 0 & \cos(\pi/2-\theta_{\rm Lab}) \end{bmatrix}$$
$$= \begin{bmatrix} -\cos\phi_{\rm Lab}\sin\theta_{\rm Lab} & \sin\phi_{\rm Lab} & \cos\phi_{\rm Lab}\cos\theta_{\rm Lab} \\ -\sin\phi_{\rm Lab}\sin\theta_{\rm Lab} & -\cos\phi_{\rm Lab} & \sin\phi_{\rm Lab}\cos\theta_{\rm Lab} \\ \cos\theta_{\rm Lab} & 0 & \sin\theta_{\rm Lab} \end{bmatrix}, \quad \text{(A2a)}$$

and then, conversely, we have

$$\mathbf{M}_{\rm E\to H}(\phi_{\rm Lab},\theta_{\rm Lab}) = \mathbf{M}^{\rm T}_{\rm H\to E}(\phi_{\rm Lab},\theta_{\rm Lab})$$
$$= \begin{bmatrix} -\cos\phi_{\rm Lab}\sin\theta_{\rm Lab} & -\sin\phi_{\rm Lab}\sin\theta_{\rm Lab} & \cos\theta_{\rm Lab} \\ \sin\phi_{\rm Lab} & -\cos\phi_{\rm Lab} & 0 \\ \cos\phi_{\rm Lab}\cos\theta_{\rm Lab} & \sin\phi_{\rm Lab}\cos\theta_{\rm Lab} & \sin\theta_{\rm Lab} \end{bmatrix}. \quad \text{(A2b)}$$

On the other hand, considering the long running time of (directional) direct Dark Matter detection experiments as well as for identifying the diurnal modulation of the angular WIMP velocity distribution, we also defined the laboratory coordinate system by taking into account the instantaneous measuring time of each recorded WIMP scattering event. As sketched in Fig. 6, it is defined by rotating our horizontal coordinate system of the laboratory of interest around the Earth's north polar ($\mathbf{Z}_{\rm Eq}/\mathbf{Z}_{\rm E}$–)axis instantaneously by the angle of $\omega t_{\rm PM}$, where we define

$$\omega \equiv \frac{2\pi}{1\ \text{day}}\,, \tag{1}$$

and $t_{\rm PM}$ indicates the fractional part of the measuring UTC time t of each recorded WIMP event in unit of day. Hence, by adding the longitude of the laboratory of interest in the transformation matrices (A2a) and (A2b) with this extra time–dependent term:

$$\phi_{\rm Lab} \longrightarrow \phi_{\rm Lab} + \omega t_{\rm PM}\,, \tag{A3}$$

we can obtain the transformation matrices between the laboratory and the Earth coordinate systems straightforwardly as

$$\begin{aligned}
&\mathbf{M}_{\rm Lab\to E}(t, \phi_{\rm Lab}, \theta_{\rm Lab}) \\
&= \begin{bmatrix}
-\cos\left(\phi_{\rm Lab} + \omega t_{\rm PM}\right)\sin\theta_{\rm Lab} & \sin\left(\phi_{\rm Lab} + \omega t_{\rm PM}\right) & \cos\left(\phi_{\rm Lab} + \omega t_{\rm PM}\right)\cos\theta_{\rm Lab} \\
-\sin\left(\phi_{\rm Lab} + \omega t_{\rm PM}\right)\sin\theta_{\rm Lab} & -\cos\left(\phi_{\rm Lab} + \omega t_{\rm PM}\right) & \sin\left(\phi_{\rm Lab} + \omega t_{\rm PM}\right)\cos\theta_{\rm Lab} \\
\cos\theta_{\rm Lab} & 0 & \sin\theta_{\rm Lab}
\end{bmatrix},
\end{aligned} \tag{A4a}$$

and

$$\begin{aligned}
&\mathbf{M}_{\rm E\to Lab}(t, \phi_{\rm Lab}, \theta_{\rm Lab}) \\
&= \begin{bmatrix}
-\cos\left(\phi_{\rm Lab} + \omega t_{\rm PM}\right)\sin\theta_{\rm Lab} & -\sin\left(\phi_{\rm Lab} + \omega t_{\rm PM}\right)\sin\theta_{\rm Lab} & \cos\theta_{\rm Lab} \\
\sin\left(\phi_{\rm Lab} + \omega t_{\rm PM}\right) & -\cos\left(\phi_{\rm Lab} + \omega t_{\rm PM}\right) & 0 \\
\cos\left(\phi_{\rm Lab} + \omega t_{\rm PM}\right)\cos\theta_{\rm Lab} & \sin\left(\phi_{\rm Lab} + \omega t_{\rm PM}\right)\cos\theta_{\rm Lab} & \sin\theta_{\rm Lab}
\end{bmatrix}.
\end{aligned} \tag{A4b}$$

Moreover, by combining Eq. (A4b) with Eq. (A2a), the transformation matrices between the horizontal and the laboratory coordinate systems can be found as

$$\begin{aligned}
&\mathbf{M}_{\rm H\to Lab}(t, \phi_{\rm Lab}, \theta_{\rm Lab}) \\
&= \mathbf{M}_{\rm E\to Lab}(t, \phi_{\rm Lab}, \theta_{\rm Lab})\,\mathbf{M}_{\rm H\to E}(\phi_{\rm Lab}, \theta_{\rm Lab}) \\
&= \begin{bmatrix}
\cos\omega t_{\rm PM}\sin^2\theta_{\rm Lab} + \cos^2\theta_{\rm Lab} & \sin\omega t_{\rm PM}\sin\theta_{\rm Lab} & \left(1 - \cos\omega t_{\rm PM}\right)\sin\theta_{\rm Lab}\cos\theta_{\rm Lab} \\
-\sin\omega t_{\rm PM}\sin\theta_{\rm Lab} & \cos\omega t_{\rm PM} & \sin\omega t_{\rm PM}\cos\theta_{\rm Lab} \\
\left(1 - \cos\omega t_{\rm PM}\right)\sin\theta_{\rm Lab}\cos\theta_{\rm Lab} & -\sin\omega t_{\rm PM}\cos\theta_{\rm Lab} & \cos\omega t_{\rm PM}\cos^2\theta_{\rm Lab} + \sin^2\theta_{\rm Lab}
\end{bmatrix},
\end{aligned} \tag{A5a}$$

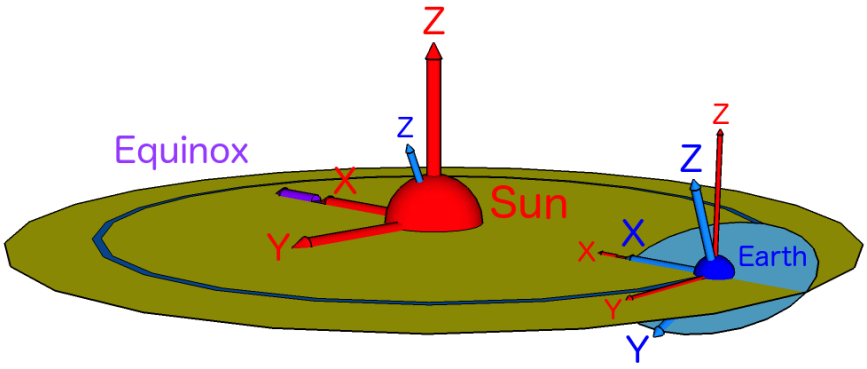

Figure A2: The sketch of the astronomical definitions of the (red) Ecliptic and the (blue) Equatorial coordinate systems: they are basically the same as our definitions described in Sec. 2.1.2 and sketched in Fig. 3(a), except that the common primary direction (the $\mathbf{X}_{\rm S}/\mathbf{X}_{\rm Eq}$–axis) is now the direction pointing from the Earth's center to that of the Sun at 12 noon of the date of the vernal equinox (i.e., pointing towards the celestial Equinox), and their $\mathbf{Y}_{\rm S}$– and $\mathbf{Y}_{\rm Eq}$–axes are then defined as usual by the right–handed convention.

and

$$\begin{aligned}
&\mathbf{M}_{\rm Lab\to H}(t,\phi_{\rm Lab},\theta_{\rm Lab}) \\
&= \mathbf{M}^{\rm T}_{\rm H\to Lab}(t,\phi_{\rm Lab},\theta_{\rm Lab}) \\
&= \begin{bmatrix}
\cos\omega t_{\rm PM}\sin^2\theta_{\rm Lab}+\cos^2\theta_{\rm Lab} & -\sin\omega t_{\rm PM}\sin\theta_{\rm Lab} & (1-\cos\omega t_{\rm PM})\sin\theta_{\rm Lab}\cos\theta_{\rm Lab} \\
\sin\omega t_{\rm PM}\sin\theta_{\rm Lab} & \cos\omega t_{\rm PM} & -\sin\omega t_{\rm PM}\cos\theta_{\rm Lab} \\
(1-\cos\omega t_{\rm PM})\sin\theta_{\rm Lab}\cos\theta_{\rm Lab} & \sin\omega t_{\rm PM}\cos\theta_{\rm Lab} & \cos\omega t_{\rm PM}\cos^2\theta_{\rm Lab}+\sin^2\theta_{\rm Lab}
\end{bmatrix}.
\end{aligned} \tag{A5b}$$

Note that the transformations between the horizontal and the laboratory coordinate systems are longitude ($\phi_{\rm Lab}$) independent and depend in fact only on the latitude of the laboratory location $\theta_{\rm Lab}$ (and the measuring time t).

A.2 Definitions of the Ecliptic and the Equatorial coordinate systems

Now we turn to define the most important coordinate systems in our data analysis procedures: the Ecliptic and the Equatorial coordinate systems. The transformation matrices between the Earth and these two coordinate systems will be derived in detail here.

A.2.1 Conventional definitions

As shown in Fig. A2, in astronomy the Ecliptic and the Equatorial coordinate systems are conventionally defined as follows: their origins are located at the center of the Sun and that of the Earth, respectively, the common primary direction (the $\mathbf{X}_{\rm S}/\mathbf{X}_{\rm Eq}$–axis) is now the direction pointing from the Earth's center to that of the Sun at 12 noon of the date of the vernal equinox (i.e., pointing towards the celestial Equinox), the fundamental ($\mathbf{X}_{\rm S}-\mathbf{Y}_{\rm S}$ and $\mathbf{X}_{\rm Eq}-\mathbf{Y}_{\rm Eq}$) planes are the Ecliptic plane and the Equatorial plane, respectively, the $\mathbf{Z}_{\rm S}$– and $\mathbf{Z}_{\rm Eq}$–axes are perpendicular to the Ecliptic or the Equatorial plane, respectively, and their $\mathbf{Y}_{\rm S}$– and $\mathbf{Y}_{\rm Eq}$–axes are then defined as usual by the right–handed convention.

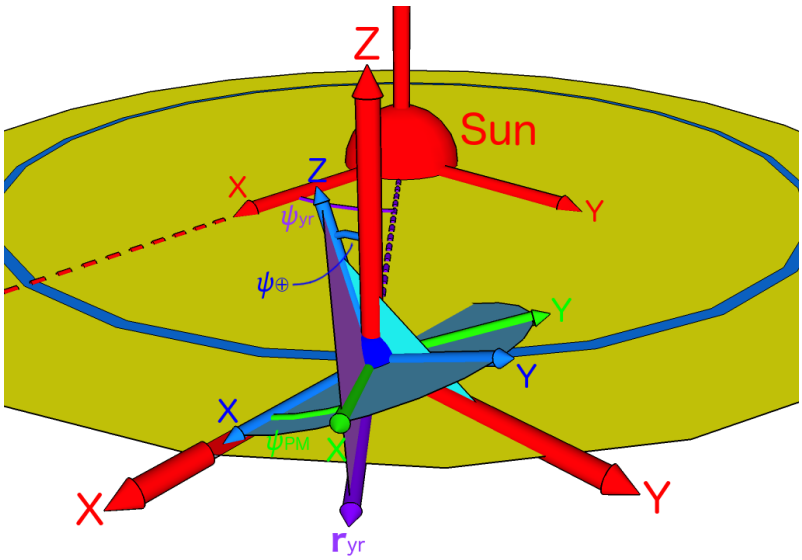

Figure A3: The sketch of the relations between the (light–green) Earth, the (blue) Equatorial, and the (red) Ecliptic coordinate systems (cf. Fig. 4). Here $\psi_{\rm yr}$ indicates the angle swept by the connection between the Solar and the Earth's centers, $\mathbf{r}_{\rm yr}$, from the day of the vernal equinox, $\psi_{\oplus} = 23.4^{\circ}$ is the Earth's obliquity, and $\psi_{\rm PM}$ is the angle between the $\mathbf{X}_{\rm Eq}$– and the $\mathbf{X}_{\rm E}$–axes. Other notations are the same as in Fig. 4.

A.2.2 Our definitions

Our definitions of the Ecliptic and the Equatorial coordinate systems are described in Sec. 2.1.2 and sketched in Fig. 3(a). Note only that, firstly, the Equatorial coordinate system is fixed and moves with the Earth, during the Earth's orbital motion around the Sun combined with the motion of the Solar system in the Galaxy. Secondly, since in our definitions the common primary direction (the $\mathbf{X}_{\rm S}/\mathbf{X}_{\rm Eq}$–axis) point towards the opposite direction of the conventional astronomical defintion, in our calculations given in Appendix A.3 there is always a 180° (or -90°) difference from the conventional data provided by, e.g., Ref. [62] (and those used in Ref. [63]).

In Fig. A3, we sketch the relations between the Earth, the Equatorial, and the Ecliptic coordinate systems (cf. Fig. 4). Here $\psi_{\rm yr}$ indicates the angle swept by the connection between the Solar and the Earth's centers, $\mathbf{r}_{\rm yr}$, from the day of the vernal equinox, $\psi_{\oplus} = 23.4^{\circ}$ is the Earth's obliquity, and $\psi_{\rm PM}$ is the angle between the $\mathbf{X}_{\rm Eq}$– and the $\mathbf{X}_{\rm E}$–axes. It can be found that, firstly, the Equatorial coordinate system can be obtained by simply rotating the Ecliptic coordinate system by the Earth's obliquity $\psi_{\oplus}$ around the common $\mathbf{X}_{\rm S}/\mathbf{X}_{\rm Eq}$–axis. Hence, the transformation matrix from the Ecliptic to the Equatorial coordinate system can be given directly as

$$\mathbf{M}_{\rm S\to Eq} = \begin{bmatrix} 1 & 0 & 0 \\ 0 & \cos\psi_{\oplus} & \sin\psi_{\oplus} \\ 0 & -\sin\psi_{\oplus} & \cos\psi_{\oplus} \end{bmatrix} = \begin{bmatrix} 1 & 0 & 0 \\ 0 & 0.91775 & 0.39715 \\ 0 & -0.39715 & 0.91775 \end{bmatrix}, \tag{A6a}$$

and, conversely,

$$\mathbf{M}_{\rm Eq\to S} = \mathbf{M}^{\rm T}_{\rm S\to Eq} = \begin{bmatrix} 1 & 0 & 0 \\ 0 & \cos\psi_{\oplus} & -\sin\psi_{\oplus} \\ 0 & \sin\psi_{\oplus} & \cos\psi_{\oplus} \end{bmatrix} = \begin{bmatrix} 1 & 0 & 0 \\ 0 & 0.91775 & -0.39715 \\ 0 & 0.39715 & 0.91775 \end{bmatrix} . \tag{A6b}$$

On the other hand, following the calculations done by A. Bandyopadhyay and D. Majumdar in Ref. [63], since $\mathbf{r}_{\rm yr}$ is the intersection vector of the (purple) $\mathbf{X}_{\rm E} - \mathbf{Z}_{\rm E}$ plane and the (yellow) Ecliptic ($\mathbf{X}_{\rm S} - \mathbf{Y}_{\rm S}$) plane, one has

$$\begin{aligned} \mathbf{r}_{\rm yr} &= \cos\psi_{\rm yr}\,\mathbf{X}_{\rm S} + \sin\psi_{\rm yr}\,\mathbf{Y}_{\rm S} \\ &= \cos\psi_{\rm yr}\,\mathbf{X}_{\rm Eq} + \sin\psi_{\rm yr}\cos\psi_{\oplus}\,\mathbf{Y}_{\rm Eq} - \sin\psi_{\rm yr}\sin\psi_{\oplus}\,\mathbf{Z}_{\rm Eq}\,, \end{aligned} \tag{A7}$$

and the vector perpendicular to the (purple) $\mathbf{Z}_{\rm E} - \mathbf{X}_{\rm E} - \mathbf{r}_{\rm yr}$ plane (i.e., paralle to the $\mathbf{Y}_{\rm E}$–axis) can be obtained by

$$\begin{aligned} \mathbf{Z}_{\rm E}\times\mathbf{r}_{\rm yr} &= \mathbf{Z}_{\rm Eq}\times\Big(\cos\psi_{\rm yr}\,\mathbf{X}_{\rm Eq} + \sin\psi_{\rm yr}\cos\psi_{\oplus}\,\mathbf{Y}_{\rm Eq} - \sin\psi_{\rm yr}\sin\psi_{\oplus}\,\mathbf{Z}_{\rm Eq}\Big) \\ &= \cos\psi_{\rm yr}\,\mathbf{Y}_{\rm Eq} - \sin\psi_{\rm yr}\cos\psi_{\oplus}\,\mathbf{X}_{\rm Eq}\,. \end{aligned} \tag{A8}$$

Here the angle $\psi_{\rm yr}$ can be estimated by the measuring time t of one WIMP event as

$$\psi_{\rm yr}(t) \equiv \frac{2\pi}{365}\Big[\,(t - t_{\rm PM}) - 79.0\Big]\,. \tag{A9}$$

Then the vector perpendicular to the $\mathbf{Y}_{\rm E} - \mathbf{Z}_{\rm E}$ plane (i.e., paralle to the $\mathbf{X}_{\rm E}$–axis) can be given by

$$\begin{aligned} \Big(\mathbf{Z}_{\rm E}\times\mathbf{r}_{\rm yr}\Big)\times\mathbf{Z}_{\rm E} &= \Big(\cos\psi_{\rm yr}\,\mathbf{Y}_{\rm Eq} - \sin\psi_{\rm yr}\cos\psi_{\oplus}\,\mathbf{X}_{\rm Eq}\Big)\times\mathbf{Z}_{\rm Eq} \\ &= \cos\psi_{\rm yr}\,\mathbf{X}_{\rm Eq} + \sin\psi_{\rm yr}\cos\psi_{\oplus}\,\mathbf{Y}_{\rm Eq}\,, \end{aligned} \tag{A10}$$

and its length can thus be obtained as

$$\Big|\Big(\mathbf{Z}_{\rm E}\times\mathbf{r}_{\rm yr}\Big)\times\mathbf{Z}_{\rm E}\Big| = \sqrt{\cos^2\psi_{\rm yr} + \sin^2\psi_{\rm yr}\cos^2\psi_{\oplus}}\,. \tag{A11}$$

Hence, the unit vector $\mathbf{X}_{\rm E}$ of the Earth coordinate system can be expressed as

$$\begin{aligned} \mathbf{X}_{\rm E} &= \frac{(\mathbf{Z}_{\rm E}\times\mathbf{r}_{\rm yr})\times\mathbf{Z}_{\rm E}}{|(\mathbf{Z}_{\rm E}\times\mathbf{r}_{\rm yr})\times\mathbf{Z}_{\rm E}|} \\ &= \frac{\cos\psi_{\rm yr}\,\mathbf{X}_{\rm Eq} + \sin\psi_{\rm yr}\cos\psi_{\oplus}\,\mathbf{Y}_{\rm Eq}}{\sqrt{\cos^2\psi_{\rm yr} + \sin^2\psi_{\rm yr}\cos^2\psi_{\oplus}}} \\ &= \gamma\cos\psi_{\rm yr}\,\mathbf{X}_{\rm Eq} + \gamma\sin\psi_{\rm yr}\cos\psi_{\oplus}\,\mathbf{Y}_{\rm Eq}\,, \end{aligned} \tag{A12a}$$

and thus

$$\begin{aligned} \mathbf{Y}_{\rm E} &= \mathbf{Z}_{\rm E}\times\mathbf{X}_{\rm E} \\ &= \mathbf{Z}_{\rm Eq}\times\Big(\gamma\cos\psi_{\rm yr}\,\mathbf{X}_{\rm Eq} + \gamma\sin\psi_{\rm yr}\cos\psi_{\oplus}\,\mathbf{Y}_{\rm Eq}\Big) \\ &= \gamma\cos\psi_{\rm yr}\,\mathbf{Y}_{\rm Eq} - \gamma\sin\psi_{\rm yr}\cos\psi_{\oplus}\,\mathbf{X}_{\rm Eq}\,, \end{aligned} \tag{A12b}$$

where we define

$$\gamma \equiv \frac{1}{\sqrt{\cos^2\psi_{\rm yr} + \sin^2\psi_{\rm yr}\,\cos^2\psi_{\oplus}}}\,. \tag{A13}$$

Therefore, the transformation matrix from the Equatorial to the Earth coordinate system can be given by

$$\mathbf{M}_{\rm Eq\to E}(t) = \begin{bmatrix} \gamma\cos\psi_{\rm yr} & \gamma\sin\psi_{\rm yr}\,\cos\psi_{\oplus} & 0 \\ -\gamma\sin\psi_{\rm yr}\,\cos\psi_{\oplus} & \gamma\cos\psi_{\rm yr} & 0 \\ 0 & 0 & 1 \end{bmatrix}, \tag{A14a}$$

and, conversely,

$$\mathbf{M}_{\rm E\to Eq}(t) = \mathbf{M}^{\rm T}_{\rm Eq\to E}(t) = \begin{bmatrix} \gamma\cos\psi_{\rm yr} & -\gamma\sin\psi_{\rm yr}\,\cos\psi_{\oplus} & 0 \\ \gamma\sin\psi_{\rm yr}\,\cos\psi_{\oplus} & \gamma\cos\psi_{\rm yr} & 0 \\ 0 & 0 & 1 \end{bmatrix}. \tag{A14b}$$

Finally, by combining the matrices given in Eqs. (A14a) and (A6a), the transformation matrix from the Ecliptic to the Earth coordinate system can be obtained by

$$\begin{aligned} \mathbf{M}_{\rm S\to E}(t) &= \mathbf{M}_{\rm Eq\to E}(t)\,\mathbf{M}_{\rm S\to Eq} \\ &= \begin{bmatrix} \gamma\cos\psi_{\rm yr} & \gamma\sin\psi_{\rm yr}\,\cos^2\psi_{\oplus} & \gamma\sin\psi_{\rm yr}\,\sin\psi_{\oplus}\,\cos\psi_{\oplus} \\ -\gamma\sin\psi_{\rm yr}\,\cos\psi_{\oplus} & \gamma\cos\psi_{\rm yr}\,\cos\psi_{\oplus} & \gamma\cos\psi_{\rm yr}\,\sin\psi_{\oplus} \\ 0 & -\sin\psi_{\oplus} & \cos\psi_{\oplus} \end{bmatrix}, \end{aligned} \tag{A15a}$$

and, conversely,

$$\mathbf{M}_{\rm E\to S}(t) = \mathbf{M}^{\rm T}_{\rm S\to E}(t) = \begin{bmatrix} \gamma\cos\psi_{\rm yr} & -\gamma\sin\psi_{\rm yr}\,\cos\psi_{\oplus} & 0 \\ \gamma\sin\psi_{\rm yr}\,\cos^2\psi_{\oplus} & \gamma\cos\psi_{\rm yr}\,\cos\psi_{\oplus} & -\sin\psi_{\oplus} \\ \gamma\sin\psi_{\rm yr}\,\sin\psi_{\oplus}\,\cos\psi_{\oplus} & \gamma\cos\psi_{\rm yr}\,\sin\psi_{\oplus} & \cos\psi_{\oplus} \end{bmatrix}. \tag{A15b}$$

A.2.3 Velocity of the Earth in the Ecliptic coordinate system

The orbital velocity of the Earth's rotation around the Sun in the Ecliptic coordinate system can be expresses as

$$\mathbf{v}_{\oplus,\rm S}(t) = v_{\oplus,\rm S}\Big(-\sin\psi_{\rm yr}(t)\,\mathbf{X}_{\rm S} + \cos\psi_{\rm yr}(t)\,\mathbf{Y}_{\rm S}\Big) = v_{\oplus,\rm S}\begin{bmatrix} -\sin\psi_{\rm yr}(t) \\ \cos\psi_{\rm yr}(t) \\ 0 \end{bmatrix}_{\rm S}, \tag{A16}$$

where the Earth's orbital speed can be estimated by [64]

$$v_{\oplus,\rm S} = \frac{2\pi\times 1.495978707\times 10^8\ \text{km}}{3.15569252\times 10^7\ \text{s}} \simeq 29.79\ \text{km/s}\,. \tag{A17}$$

Note that the Earth's orbit around the Sun has been assumed here to be perfectly circular on the Ecliptic plane and the orbital speed is thus a constant.

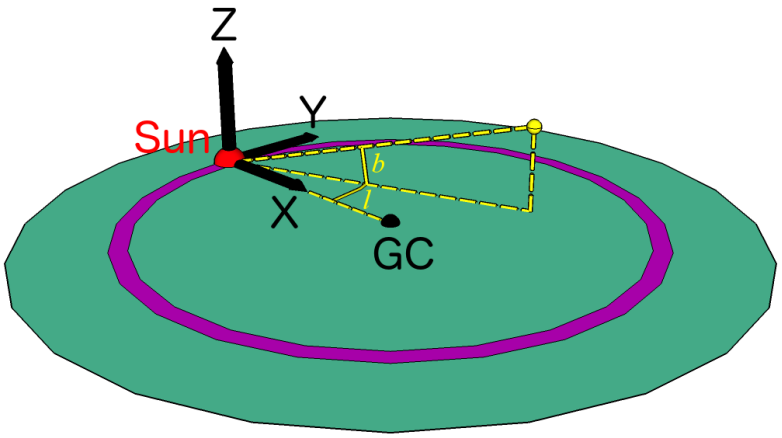

Figure A4: The sketch of the astronomical definitions of the (black) Galactic coordinate system in both of the Cartesian and the spherical coordinates with the origin located at the center of the Sun (not the Galactic Center). The primary direction (the $\mathbf{X}_{\rm G}$–axis) points from the Solar center to the approximate center of the our Galaxy, the $\mathbf{Z}_{\rm G}$–axis points to the Galactic North Pole, and the $\mathbf{Y}_{\rm G}$–axis is then defined as usual by the right–handed convention [62]. On the other hand, the Galactic longitude (l) is measured from the $\mathbf{X}_{\rm G}$–axis on the Galactic plane, while the Galactic latitude (b) measures the angle of the object above or below the approximate Galactic plane [62].

A.3 Definition of the Galactic coordinate system

Finally, we come to define the Galactic coordinate system. The Earth's velocity relative to the Dark Matter halo in the Ecliptic and the Equatorial coordinate systems and its annual modulation in four normal and four advanced seasons given in Table 2 will also be discussed here in detail.

A.3.1 Conventional definition

In Fig. A4, we sketch the astronomical definitions of the Galactic coordinate system in both of the Cartesian and the spherical coordinates with the origin located at the center of the Sun (not the Galactic Center). The primary direction (the $\mathbf{X}_{\rm G}$–axis) points from the Solar center to the approximate center of the our Galaxy, the $\mathbf{Z}_{\rm G}$–axis points to the Galactic North Pole, and the $\mathbf{Y}_{\rm G}$–axis is then defined as usual by the right–handed convention [62]. On the other hand, the Galactic longitude (l) is measured from the $\mathbf{X}_{\rm G}$–axis on the Galactic plane, while the Galactic latitude (b) measures the angle of the object above or below the approximate Galactic plane [62].

A.3.2 Our definition

Our definition of the Galactic coordinate system is described in Sec. 2.1.1 and sketched in Fig. 2. Then, according to Ref. [62], the direction of the Galactic Center in the Equatorial coordinate system can be expressed by

$$\mathbf{X}_{\rm G,Eq} = \left[\cos\theta_{\rm GC,Eq}\cos\phi_{\rm GC,Eq} \qquad \cos\theta_{\rm GC,Eq}\sin\phi_{\rm GC,Eq} \qquad \sin\theta_{\rm GC,Eq} \right]_{\rm Eq}$$

$$\cong \left[\begin{array}{ccc} 0.05495 & 0.87340 & -0.48389 \end{array} \right]_{\rm Eq} , \tag{A18}$$

where we have adopted the values provided by Ref. [62][18]

$$\phi_{\rm GC,Eq} = 5^{\rm h}45.6^{\rm m} = 86.40^\circ , \tag{A19a}$$

and

$$\theta_{\rm GC,Eq} = -28.94^\circ , \tag{A19b}$$

as the right ascension and the declination of the Galactic Center in the Equatorial coordinate system (from the $\mathbf{X}_{\rm Eq}(= \mathbf{X}_{\rm S})$–axis and the Earth's/celestial Equator ($\mathbf{X}_{\rm Eq} - \mathbf{Y}_{\rm Eq}$) plane), respectively. Meanwhile, the direction of the Galactic North Pole in our Equatorial coordinate system can also be given as [62]

$$\begin{aligned} \mathbf{Z}_{\rm G,Eq} &= \left[\begin{array}{ccc} \cos\theta_{\rm GNP,Eq}\cos\phi_{\rm GNP,Eq} & \cos\theta_{\rm GNP,Eq}\sin\phi_{\rm GNP,Eq} & \sin\theta_{\rm GNP,Eq} \end{array} \right]_{\rm Eq} \\ &\cong \left[\begin{array}{ccc} 0.86769 & 0.19793 & 0.45601 \end{array} \right]_{\rm Eq} , \end{aligned} \tag{A20}$$

where we have

$$\phi_{\rm GNP,Eq} = 51.4^{\rm m} = 12.85^\circ , \tag{A21a}$$

and

$$\theta_{\rm GNP,Eq} = 27.13^\circ , \tag{A21b}$$

as the right ascension and the declination of the Galactic North Pole in the Equatorial coordinate system, respectively. By combining Eqs. (A18) and (A20), the $\mathbf{Y}_{\rm G}$–axis of the Galactic coordinate system in the Equatorial coordinate system can be calculated by

$$\begin{aligned} \mathbf{Y}_{\rm G,Eq} &= \mathbf{Z}_{\rm G,Eq} \times \mathbf{X}_{\rm G,Eq} \\ &= \left[\begin{array}{c} \cos\theta_{\rm GNP,Eq}\sin\phi_{\rm GNP,Eq}\sin\theta_{\rm GC,Eq} - \sin\theta_{\rm GNP,Eq}\cos\theta_{\rm GC,Eq}\sin\phi_{\rm GC,Eq} \\ \sin\theta_{\rm GNP,Eq}\cos\theta_{\rm GC,Eq}\cos\phi_{\rm GC,Eq} - \cos\theta_{\rm GNP,Eq}\cos\phi_{\rm GNP,Eq}\sin\theta_{\rm GC,Eq} \\ \cos\theta_{\rm GNP,Eq}\cos\theta_{\rm GC,Eq}\left(\cos\phi_{\rm GNP,Eq}\sin\phi_{\rm GC,Eq} - \sin\phi_{\rm GNP,Eq}\cos\phi_{\rm GC,Eq}\right) \end{array} \right]^{\rm T}_{\rm Eq} \\ &\cong \left[\begin{array}{ccc} -0.49406 & 0.44492 & 0.74696 \end{array} \right]_{\rm Eq} . \end{aligned} \tag{A22}$$

Then the transformation matrix from the Equatorial to the Galactic coordinate system can be given by

$$\mathbf{M}_{\rm Eq\to G} = \left[\begin{array}{c} \mathbf{X}_{\rm G,Eq} \\ \mathbf{Y}_{\rm G,Eq} \\ \mathbf{Z}_{\rm G,Eq} \end{array} \right] = \left[\begin{array}{ccc} 0.05495 & 0.87340 & -0.48389 \\ -0.49406 & 0.44492 & 0.74696 \\ 0.86769 & 0.19793 & 0.45601 \end{array} \right] , \tag{A23a}$$

[18] Remind that, in the Ecliptic and the Equatorial coordinate systems defined in Sec. 2.1.2, the common $\mathbf{X}_{\rm S}/\mathbf{X}_{\rm Eq}$–axis points from the center of the Sun to that of the Earth, which is opposite to the $\mathbf{X}$ direction defined conventionally. Hence, the right ascensions of the Galactic Center and the Galactic North Pole in the Equatorial and the Ecliptic coordinate systems adopted in this section as well as those calculated later would differ from the conventional values by $12^{\rm h} = 180^\circ$.

and, conversely, we have

$$\mathbf{M}_{\mathrm{G}\to\mathrm{Eq}} = \mathbf{M}^{\mathrm{T}}_{\mathrm{Eq}\to\mathrm{G}} = \begin{bmatrix} 0.05495 & -0.49406 & 0.86769 \\ 0.87340 & 0.44492 & 0.19793 \\ -0.48389 & 0.74696 & 0.45601 \end{bmatrix} . \tag{A23b}$$

Furthermore, by using the transformation matrices between the Equatorial and the Ecliptic coordinate systems in Eqs. (A6b) and (A6a), the transformation matrices between the Ecliptic and the Galactic coordinate systems can be given by

$$\mathbf{M}_{\mathrm{G}\to\mathrm{S}} = \mathbf{M}_{\mathrm{Eq}\to\mathrm{S}}\mathbf{M}_{\mathrm{G}\to\mathrm{Eq}} = \begin{bmatrix} 0.05495 & -0.49406 & 0.86769 \\ 0.99374 & 0.11168 & 0.00055 \\ -0.09723 & 0.86223 & 0.49711 \end{bmatrix} , \tag{A24a}$$

and

$$\mathbf{M}_{\mathrm{S}\to\mathrm{G}} = \mathbf{M}^{\mathrm{T}}_{\mathrm{G}\to\mathrm{S}} = \begin{bmatrix} 0.05495 & 0.99374 & -0.09723 \\ -0.49406 & 0.11168 & 0.86223 \\ 0.86769 & 0.00055 & 0.49711 \end{bmatrix} . \tag{A24b}$$

Finally, from the matrix $\mathbf{M}_{\mathrm{G}\to\mathrm{S}}$ given in Eq. (A24a), one can obtain the $\mathbf{X}_{\mathrm{G}}$– and $\mathbf{Z}_{\mathrm{G}}$–axes in the Ecliptic coordinate system as

$$\mathbf{X}_{\mathrm{G,S}} = \mathbf{M}_{\mathrm{G}\to\mathrm{S}} \begin{bmatrix} 1 \\ 0 \\ 0 \end{bmatrix}_{\mathrm{S}} = \begin{bmatrix} 0.05495 \\ 0.99374 \\ -0.09723 \end{bmatrix}_{\mathrm{S}} , \tag{A25}$$

and

$$\mathbf{Z}_{\mathrm{G,S}} = \mathbf{M}_{\mathrm{G}\to\mathrm{S}} \begin{bmatrix} 0 \\ 0 \\ 1 \end{bmatrix}_{\mathrm{S}} = \begin{bmatrix} 0.86769 \\ 0.00055 \\ 0.49711 \end{bmatrix}_{\mathrm{S}} . \tag{A26}$$

These give in turn the right ascensions and the declinations of the Galactic Center and the Galactic North Pole in the Ecliptic coordinate system as

$$\phi_{\mathrm{GC,S}} = 86.84^{\circ} = 5.79^{\mathrm{h}} , \tag{A27a}$$

$$\theta_{\mathrm{GC,S}} = -5.58^{\circ} , \tag{A27b}$$

and

$$\phi_{\mathrm{GNP,S}} = 0.036^{\circ} = 2.17^{\mathrm{m}} , \tag{A28a}$$

$$\theta_{\mathrm{GNP,S}} = 29.81^{\circ} , \tag{A28b}$$

respectively.

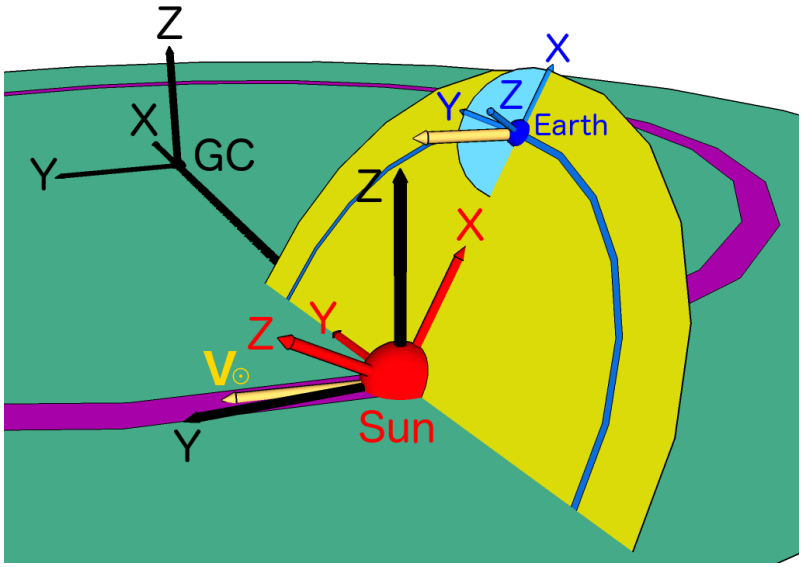

Figure A5: The same as in Fig. 3(b), except that the additional (golden) arrows here indicate the direction of the movement of the Solar system around the Galactic center. Note that the moving direction of the Solar system is not parallel to, but only approximately along the $\mathbf{Y}_{\rm G}$–axis (with an included angle of $8.87^\circ = 35.48^{\rm m}$), nor on the (approximate) $\mathbf{X}_{\rm G} - \mathbf{Y}_{\rm G}$ (Galactic) plane (0.60° above).

A.3.3 Direction of the movement of the Solar system around the Galactic center

In Fig. A5, we add the (golden) arrow to indicate the direction of the movement of the Solar system around the Galactic center (cf. Fig. 3(b)). The Galactic movement of the Solar system pointing currently towards the CYGNUS constellation can be given in the Equatorial coordinate system as [63]

$$\mathbf{v}_{\odot,\rm Eq} = v_{\odot,\rm G} \begin{bmatrix} \cos\theta_{\rm Cyg,Eq}\cos\phi_{\rm Cyg,Eq} \\ \cos\theta_{\rm Cyg,Eq}\sin\phi_{\rm Cyg,Eq} \\ \sin\theta_{\rm Cyg,Eq} \end{bmatrix}_{\rm Eq} = v_{\odot,\rm G} \begin{bmatrix} -0.47069 \\ 0.57508 \\ 0.66913 \end{bmatrix}_{\rm Eq} \cong \begin{bmatrix} -103.55\ \text{km/s} \\ 126.52\ \text{km/s} \\ 147.21\ \text{km/s} \end{bmatrix}_{\rm Eq} . \tag{A29}$$

Here we have used

$$v_{\odot,\rm G} \simeq 220\ \text{km/s}\,, \tag{A30}$$

and the right ascension and the declination of the direction of the CYGNUS constellation in the Equatorial coordinate system are [63]

$$\phi_{\rm Cyg,Eq} = 8.62^{\rm h} = 129.30^\circ\,, \tag{A31a}$$

and

$$\theta_{\rm Cyg,Eq} = 42^\circ\,. \tag{A31b}$$

Moreover, by using the transformation matrices $\mathbf{M}_{\rm Eq\to S}$ and $\mathbf{M}_{\rm Eq\to G}$ given in Eqs. (A6b) and (A23a), the moving direction of the Solar system in the Ecliptic and the Galactic coordinate

systems can be obtained as

$$\begin{aligned}
\mathbf{v}_{\odot,\mathrm{S}} &= \mathbf{M}_{\mathrm{Eq}\to\mathrm{S}}\,\mathbf{v}_{\odot,\mathrm{Eq}} \\
&= v_{\odot,\mathrm{G}} \begin{bmatrix} \cos\theta_{\mathrm{Cyg,Eq}}\cos\phi_{\mathrm{Cyg,Eq}} \\ \cos\psi_{\oplus}\cos\theta_{\mathrm{Cyg,Eq}}\sin\phi_{\mathrm{Cyg,Eq}} - \sin\psi_{\oplus}\sin\theta_{\mathrm{Cyg,Eq}} \\ \sin\psi_{\oplus}\cos\theta_{\mathrm{Cyg,Eq}}\sin\phi_{\mathrm{Cyg,Eq}} + \cos\psi_{\oplus}\sin\theta_{\mathrm{Cyg,Eq}} \end{bmatrix}_{\mathrm{S}} \\
&= v_{\odot,\mathrm{G}} \begin{bmatrix} -0.47069 \\ 0.26203 \\ 0.84249 \end{bmatrix}_{\mathrm{S}} \\
&\cong \begin{bmatrix} -103.55\ \mathrm{km/s} \\ 57.65\ \mathrm{km/s} \\ 185.35\ \mathrm{km/s} \end{bmatrix}_{\mathrm{S}} ,
\end{aligned} \tag{A32}$$

and

$$\mathbf{v}_{\odot,\mathrm{G}} = \mathbf{M}_{\mathrm{Eq}\to\mathrm{G}}\,\mathbf{v}_{\odot,\mathrm{Eq}} = v_{\odot,\mathrm{G}} \begin{bmatrix} 0.15262 \\ 0.98823 \\ 0.01054 \end{bmatrix}_{\mathrm{G}} \cong \begin{bmatrix} 33.58\ \mathrm{km/s} \\ 217.41\ \mathrm{km/s} \\ 2.32\ \mathrm{km/s} \end{bmatrix}_{\mathrm{G}} . \tag{A33}$$

These give in turn the right ascension and the declination of the moving direction of the Solar system in the Ecliptic coordinate system as

$$\phi_{\mathrm{Cyg,S}} = 150.90^{\circ} = 10.06^{\mathrm{h}} , \tag{A34a}$$

$$\theta_{\mathrm{Cyg,S}} = 57.40^{\circ} . \tag{A34b}$$

And, in the Galactic coordinate system, one has

$$\phi_{\mathrm{Cyg,G}} = 81.22^{\circ} = 5.41^{\mathrm{h}} , \tag{A35a}$$

$$\theta_{\mathrm{Cyg,G}} = 0.60^{\circ} . \tag{A35b}$$

A.3.4 Annual modulation of the Earth's velocity in the Ecliptic coordinate system

In this and the next subsections, we discuss the annual modulation of the Earth's velocity relative to the Dark Matter halo in the Ecliptic and the Equatorial coordinate systems separately. Remind that our calculations are based on two assumptions. First, the Earth's orbit around the Sun is perfectly circular on the Ecliptic plane and the orbital speed is thus a constant. Second, the date of the vernal equinox is fixed exactly at the end of the 79th day (the May 20th) of a 365-day year and the few extra hours in an actual Solar year has been neglected.

We begin with four normal seasons, in which the orbital velocity of the Earth's rotation around the Sun in the Ecliptic coordinate system on the central date of each season is along the $\mathbf{X}_{\mathrm{S}}$– or the $\mathbf{Y}_{\mathrm{S}}$–axis, corresponding to the Earth's positions shown in Fig. 9(a). By setting $\psi_{\mathrm{yr}} = 0,\ \pi/2,\ \pi$, and $3\pi/2$, or, equivalently, $t = 79.0$ (the *beginning* of the *21st* of March),

170.25 (June 20th), 261.50 (September 19th), and 352.75 day (December 19th), respectively, into the expression for the Earth's orbital velocity around the Sun given in Eq. (A16), we have the Earth's velocities in four normal seasons in the Ecliptic coordinate system as

$$\mathbf{v}_{\oplus,\mathrm{S},79.00} = v_{\oplus,\mathrm{S}}\mathbf{Y}_{\mathrm{S}}\,, \tag{A36a}$$

$$\mathbf{v}_{\oplus,\mathrm{S},170.25} = -v_{\oplus,\mathrm{S}}\mathbf{X}_{\mathrm{S}}\,, \tag{A36b}$$

$$\mathbf{v}_{\oplus,\mathrm{S},261.50} = -v_{\oplus,\mathrm{S}}\mathbf{Y}_{\mathrm{S}}\,, \tag{A36c}$$

and

$$\mathbf{v}_{\oplus,\mathrm{S},352.75} = v_{\oplus,\mathrm{S}}\mathbf{X}_{\mathrm{S}}\,, \tag{A36d}$$

respectively. By combining with the velocity of the Solar system given in Eq. (A32) and taking the Earth's orbital speed given in Eq. (A17), one can obtain the Earth's velocities relative to the Dark Matter halo in four normal seasons in the Ecliptic coordinate system as

$$\mathbf{v}_{\oplus\chi,\mathrm{S},79.00} = \mathbf{v}_{\odot,\mathrm{S}} + \mathbf{v}_{\oplus,\mathrm{S},79.00} = \begin{bmatrix} -103.55\ \mathrm{km/s} \\ 87.43\ \mathrm{km/s} \\ 185.35\ \mathrm{km/s} \end{bmatrix}_{\mathrm{S}}\,, \tag{A37a}$$

$$\mathbf{v}_{\oplus\chi,\mathrm{S},170.25} = \mathbf{v}_{\odot,\mathrm{S}} + \mathbf{v}_{\oplus,\mathrm{S},170.25} = \begin{bmatrix} -133.34\ \mathrm{km/s} \\ 57.65\ \mathrm{km/s} \\ 185.35\ \mathrm{km/s} \end{bmatrix}_{\mathrm{S}}\,, \tag{A37b}$$

$$\mathbf{v}_{\oplus\chi,\mathrm{S},261.50} = \mathbf{v}_{\odot,\mathrm{S}} + \mathbf{v}_{\oplus,\mathrm{S},261.50} = \begin{bmatrix} -103.55\ \mathrm{km/s} \\ 27.86\ \mathrm{km/s} \\ 185.35\ \mathrm{km/s} \end{bmatrix}_{\mathrm{S}}\,, \tag{A37c}$$

and

$$\mathbf{v}_{\oplus\chi,\mathrm{S},352.75} = \mathbf{v}_{\odot,\mathrm{S}} + \mathbf{v}_{\oplus,\mathrm{S},352.75} = \begin{bmatrix} -73.77\ \mathrm{km/s} \\ 57.65\ \mathrm{km/s} \\ 185.35\ \mathrm{km/s} \end{bmatrix}_{\mathrm{S}}\,, \tag{A37d}$$

respectively.

On the other hand, as shown in Fig. 9(b), the Earth's velocity relative to the Dark Matter halo should be maximal (minimal), once the Earth's velocity is (anti–)parallel to the projection of the moving direction of the Solar system on the Ecliptic plane. This requires that, from Eq. (A34a),

$$\psi_{\mathrm{yr}} = 60.90^{\circ} = 0.3383\pi = 1.0628\,, \tag{A38}$$

or, equivalently,

$$t_{\rm max} = 140.74 \text{ day}\,, \tag{A39}$$

i.e., around the 21st of May. Then, by setting $\psi_{\rm yr} = 1.0628$, 4.2044, -0.5080, and 2.6336 (corresponding to the Earth's positions in four advanced seasons shown in Fig. 9(b)), or, equivalently, $t = 140.74$ (May 21st), 323.24 (November 20th), 49.49 (February 19th), and 231.99 day (August 20th), respectively, into the expression (A16), we have the Earth's velocities as

$$\mathbf{v}_{\oplus,{\rm S},140.74} = v_{\oplus,{\rm S}} \left[\begin{array}{c} -0.874 \\ 0.486 \\ 0 \end{array}\right]_{\rm S} = \left[\begin{array}{c} -26.02 \text{ km/s} \\ 14.49 \text{ km/s} \\ 0 \end{array}\right]_{\rm S}\,, \tag{A40a}$$

$$\mathbf{v}_{\oplus,{\rm S},323.24} = v_{\oplus,{\rm S}} \left[\begin{array}{c} 0.874 \\ -0.486 \\ 0 \end{array}\right]_{\rm S} = \left[\begin{array}{c} 26.02 \text{ km/s} \\ -14.49 \text{ km/s} \\ 0 \end{array}\right]_{\rm S}\,, \tag{A40b}$$

$$\mathbf{v}_{\oplus,{\rm S},49.49} = v_{\oplus,{\rm S}} \left[\begin{array}{c} 0.486 \\ 0.874 \\ 0 \end{array}\right]_{\rm S} = \left[\begin{array}{c} 14.49 \text{ km/s} \\ 26.02 \text{ km/s} \\ 0 \end{array}\right]_{\rm S}\,, \tag{A40c}$$

and

$$\mathbf{v}_{\oplus,{\rm S},231.99} = v_{\oplus,{\rm S}} \left[\begin{array}{c} -0.486 \\ -0.874 \\ 0 \end{array}\right]_{\rm S} = \left[\begin{array}{c} -14.49 \text{ km/s} \\ -26.02 \text{ km/s} \\ 0 \end{array}\right]_{\rm S}\,, \tag{A40d}$$

respectively. Then the maximal, the minimal and the middle values of the Earth's velocities relative to the Dark Matter halo in four advanced seasons can be obtained as

$$\mathbf{v}_{\oplus\chi,{\rm S},140.74} = \mathbf{v}_{\odot,{\rm S}} + \mathbf{v}_{\oplus,{\rm S},140.74} = \left[\begin{array}{c} -129.58 \text{ km/s} \\ 72.14 \text{ km/s} \\ 185.35 \text{ km/s} \end{array}\right]_{\rm S}\,, \tag{A41a}$$

$$\mathbf{v}_{\oplus\chi,{\rm S},323.24} = \mathbf{v}_{\odot,{\rm S}} + \mathbf{v}_{\oplus,{\rm S},323.24} = \left[\begin{array}{c} -77.53 \text{ km/s} \\ 43.16 \text{ km/s} \\ 185.35 \text{ km/s} \end{array}\right]_{\rm S}\,, \tag{A41b}$$

$$\mathbf{v}_{\oplus\chi,{\rm S},49.49} = \mathbf{v}_{\odot,{\rm S}} + \mathbf{v}_{\oplus,{\rm S},49.49} = \left[\begin{array}{c} -89.06 \text{ km/s} \\ 83.67 \text{ km/s} \\ 185.35 \text{ km/s} \end{array}\right]_{\rm S}\,, \tag{A41c}$$

Date (day)	Magnitude $v_{\oplus\chi}$ (km/s)	Right ascension $\phi_{\chi,\mathrm{S}}$	Declination $\theta_{\chi,\mathrm{S}}$
79.0	229.61	$139.82^\circ = 9.32^\mathrm{h}$	53.83°
170.25	235.49	$156.62^\circ = 10.44^\mathrm{h}$	51.91°
261.50	214.13	$164.94^\circ = 11.00^\mathrm{h}$	59.95°
352.75	207.65	$141.99^\circ = 9.47^\mathrm{h}$	63.20°
49.49	222.01	$136.79^\circ = 9.12^\mathrm{h}$	56.60°
140.74	237.38	$150.90^\circ = 10.06^\mathrm{h}$	51.34°
231.99	222.01	$165.00^\circ = 11.00^\mathrm{h}$	56.60°
323.24	205.49	$150.90^\circ = 10.06^\mathrm{h}$	64.42°

Table A1: The list of the magnitudes, the right ascensions and the declinations of the Earth's velocity relative to the Dark Matter halo in four normal and four advanced seasons in the Ecliptic coordinate system.

and

$$\mathbf{v}_{\oplus\chi,\mathrm{S},231.99} = \mathbf{v}_{\odot,\mathrm{S}} + \mathbf{v}_{\oplus,\mathrm{S},231.99} = \begin{bmatrix} -118.04\ \mathrm{km/s} \\ 31.62\ \mathrm{km/s} \\ 185.35\ \mathrm{km/s} \end{bmatrix}_\mathrm{S} , \tag{A41d}$$

respectively. One can thus estimate the magnitudes and the directions (the right ascensions and the declinations) of the Earth's velocity relative to the Dark Matter halo in four normal and four advanced seasons straightforwardly, which we summarize in Table A1 for readers' reference.

Furthermore, one can in general have that

$$\begin{aligned} \mathbf{v}_{\oplus\chi,\mathrm{S}}(t) &= \mathbf{v}_{\odot,\mathrm{S}} + \mathbf{v}_{\oplus,\mathrm{S}}(t) \\ &= v_{\odot,\mathrm{G}} \begin{bmatrix} \cos\theta_{\mathrm{Cyg,Eq}}\cos\phi_{\mathrm{Cyg,Eq}} - \left(\dfrac{v_{\oplus,\mathrm{S}}}{v_{\odot,\mathrm{G}}}\right)\sin\psi_\mathrm{yr} \\ \cos\psi_\oplus\cos\theta_{\mathrm{Cyg,Eq}}\sin\phi_{\mathrm{Cyg,Eq}} - \sin\psi_\oplus\sin\theta_{\mathrm{Cyg,Eq}} + \left(\dfrac{v_{\oplus,\mathrm{S}}}{v_{\odot,\mathrm{G}}}\right)\cos\psi_\mathrm{yr} \\ \sin\psi_\oplus\cos\theta_{\mathrm{Cyg,Eq}}\sin\phi_{\mathrm{Cyg,Eq}} + \cos\psi_\oplus\sin\theta_{\mathrm{Cyg,Eq}} \end{bmatrix}_\mathrm{S} \\ &= v_{\odot,\mathrm{G}} \begin{bmatrix} -0.47069 - \left(\dfrac{v_{\oplus,\mathrm{S}}}{v_{\odot,\mathrm{G}}}\right)\sin\psi_\mathrm{yr} \\ 0.26203 + \left(\dfrac{v_{\oplus,\mathrm{S}}}{v_{\odot,\mathrm{G}}}\right)\cos\psi_\mathrm{yr} \\ 0.84249 \end{bmatrix}_\mathrm{S} . \end{aligned} \tag{A42}$$

Hence, we can get that

$$v_{\oplus\chi}(t) = v_{\odot,\mathrm{G}}\left[1 + \left(\frac{v_{\oplus,\mathrm{S}}}{v_{\odot,\mathrm{G}}}\right)^2 + 2\left(\frac{v_{\oplus,\mathrm{S}}}{v_{\odot,\mathrm{G}}}\right)\left(0.47069\sin\psi_\mathrm{yr} + 0.26203\cos\psi_\mathrm{yr}\right)\right]^{1/2}$$

$$= v_{\odot,\mathrm{G}} \left[\alpha_{v,0} + \alpha_{v,1} \cos\left(\frac{2\pi(t - t_{\max})}{1\ \mathrm{yr}} \right) + \alpha_{v,2} \cos\left(\frac{2 \cdot 2\pi(t - t_{\max})}{1\ \mathrm{yr}} \right) + \cdots \right] . \quad \text{(A43)}$$

Here, in the last line, we expand $v_{\oplus\chi}(t)$ by the Fourier cosine series around the date of the maximal Earth's relative velocity $t_{\max} = 140.74$ day. By some numerical calculations, one can find easily that

$$\alpha_{v,0} = 1.0078\,, \quad \text{(A44a)}$$

$$\alpha_{v,1} = 0.0724\,, \quad \text{(A44b)}$$

and

$$\alpha_{v,2} = -0.0013\,. \quad \text{(A44c)}$$

Hence, the time–dependent Earth's speed relative to the Dark Matter halo can be expressed as

$$v_{\oplus\chi}(t) = v_{\odot,\mathrm{G}} \left[1.0078 + 0.0724 \cos\left(\frac{2\pi(t - t_{\max})}{1\ \mathrm{yr}} \right) - 0.0013 \cos\left(\frac{2 \cdot 2\pi(t - t_{\max})}{1\ \mathrm{yr}} \right) \right] . \quad \text{(A45)}$$

In Figs. A6, we show the fitted $v_{\oplus\chi}(t)$ of the order of 1 (upper) and 2 (below), respectively.

A.3.5 Annual modulation of the Earth's velocity in the Equatorial coordinate system

First, by using the transformation matrix from the Ecliptic to the Equatorial coordinate system $\mathbf{M}_{\mathrm{S}\to\mathrm{Eq}}$ given in Eq. (A6a), the Earth's velocities relative to the Dark Matter halo in four normal seasons in the Equatorial coordinate system can be calculated directly as

$$\mathbf{v}_{\oplus\chi,\mathrm{Eq},79.00} = \mathbf{M}_{\mathrm{S}\to\mathrm{Eq}}\, \mathbf{v}_{\oplus\chi,\mathrm{S},79.00} = \begin{bmatrix} -103.55\ \mathrm{km/s} \\ 153.85\ \mathrm{km/s} \\ 135.38\ \mathrm{km/s} \end{bmatrix}_{\mathrm{Eq}} , \quad \text{(A46a)}$$

$$\mathbf{v}_{\oplus\chi,\mathrm{Eq},170.25} = \mathbf{M}_{\mathrm{S}\to\mathrm{Eq}}\, \mathbf{v}_{\oplus\chi,\mathrm{S},170.25} = \begin{bmatrix} -133.34\ \mathrm{km/s} \\ 126.52\ \mathrm{km/s} \\ 147.21\ \mathrm{km/s} \end{bmatrix}_{\mathrm{Eq}} , \quad \text{(A46b)}$$

$$\mathbf{v}_{\oplus\chi,\mathrm{Eq},261.50} = \mathbf{M}_{\mathrm{S}\to\mathrm{Eq}}\, \mathbf{v}_{\oplus\chi,\mathrm{S},261.50} = \begin{bmatrix} -103.55\ \mathrm{km/s} \\ 99.18\ \mathrm{km/s} \\ 159.04\ \mathrm{km/s} \end{bmatrix}_{\mathrm{Eq}} , \quad \text{(A46c)}$$

and

$$\mathbf{v}_{\oplus\chi,\mathrm{Eq},352.75} = \mathbf{M}_{\mathrm{S}\to\mathrm{Eq}}\, \mathbf{v}_{\oplus\chi,\mathrm{S},352.75} = \begin{bmatrix} -73.77\ \mathrm{km/s} \\ 126.52\ \mathrm{km/s} \\ 147.21\ \mathrm{km/s} \end{bmatrix}_{\mathrm{Eq}} , \quad \text{(A46d)}$$

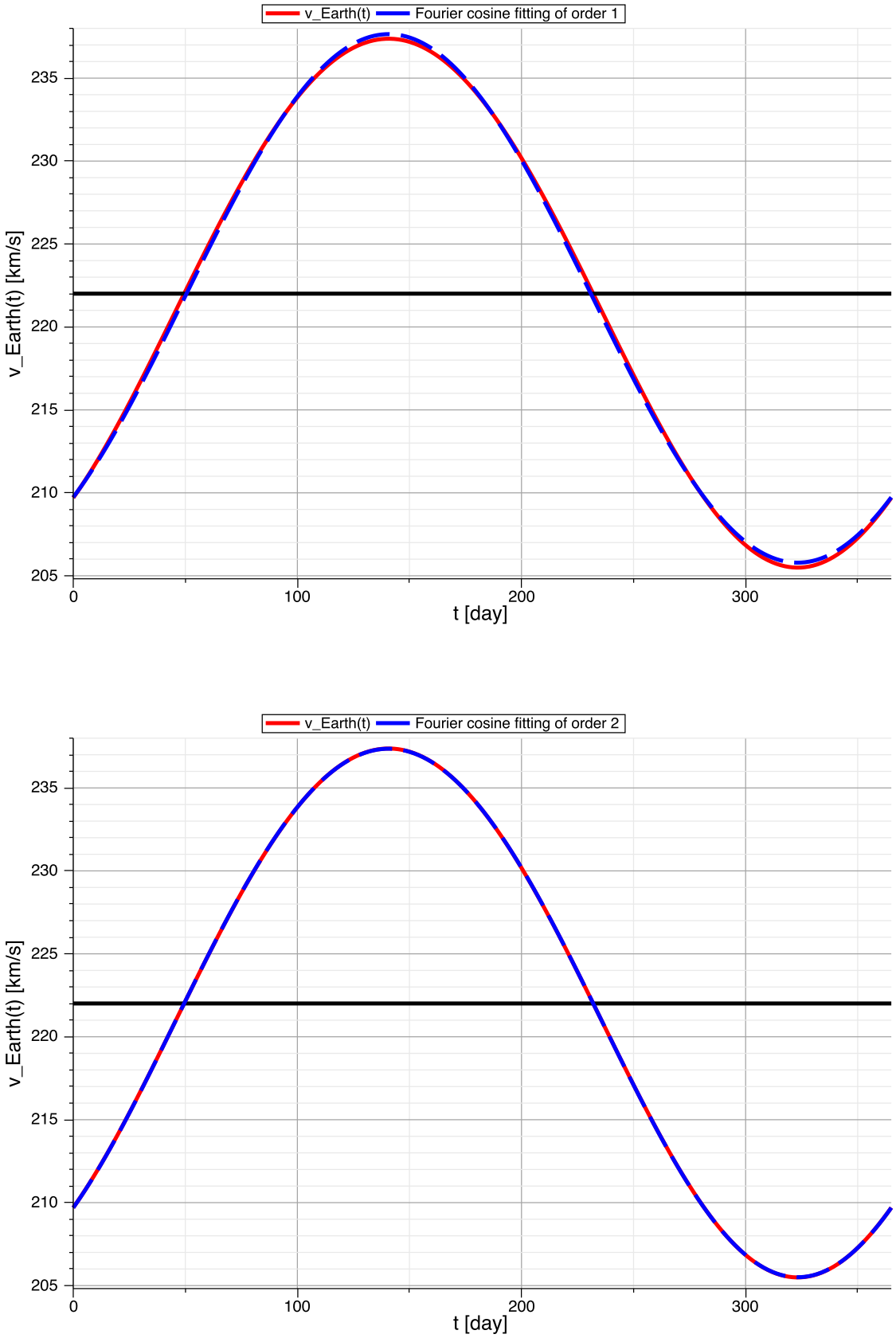

Figure A6: Fourier cosine fitting of the time–dependent Earth's speed relative to the Dark Matter halo $v_{\oplus\chi}(t)$ of the order of 1 (upper) and 2 (below), respectively. The date of the maximal Earth's relative velocity is $t_{\max} = 140.74$ day.

Date (day)	Magnitude $v_{\oplus\chi}$ (km/s)	Right ascension $\phi_{\chi,\mathrm{Eq}}$	Declination $\theta_{\chi,\mathrm{Eq}}$
79.0	229.61	$123.94^\circ = 8.26^\mathrm{h}$	36.13°
170.25	235.49	$136.50^\circ = 9.10^\mathrm{h}$	38.69°
261.50	214.13	$136.24^\circ = 9.08^\mathrm{h}$	47.96°
352.75	207.65	$120.24^\circ = 8.01^\mathrm{h}$	45.15°
49.49	222.01	$120.63^\circ = 8.04^\mathrm{h}$	38.06°
140.74	237.38	$132.82^\circ = 8.85^\mathrm{h}$	36.58°
231.99	222.01	$138.99^\circ = 9.27^\mathrm{h}$	45.21°
323.24	205.49	$124.40^\circ = 8.29^\mathrm{h}$	48.11°

Table A2: The list of the magnitudes, the right ascensions and the declinations of the Earth's velocity relative to the Dark Matter halo in four normal and four advanced seasons in the Equatorial coordinate system.

respectively. Similarly, for four advanced seasons, one has

$$\mathbf{v}_{\oplus\chi,\mathrm{Eq},140.74} = \mathbf{M}_{\mathrm{S}\to\mathrm{Eq}}\,\mathbf{v}_{\oplus\chi,\mathrm{S},140.74} = \left[\begin{array}{c} -129.58\ \mathrm{km/s} \\ 139.81\ \mathrm{km/s} \\ 141.45\ \mathrm{km/s} \end{array}\right]_{\mathrm{Eq}}, \tag{A47a}$$

$$\mathbf{v}_{\oplus\chi,\mathrm{Eq},323.24} = \mathbf{M}_{\mathrm{S}\to\mathrm{Eq}}\,\mathbf{v}_{\oplus\chi,\mathrm{S},323.24} = \left[\begin{array}{c} -77.53\ \mathrm{km/s} \\ 113.22\ \mathrm{km/s} \\ 152.96\ \mathrm{km/s} \end{array}\right]_{\mathrm{Eq}}, \tag{A47b}$$

$$\mathbf{v}_{\oplus\chi,\mathrm{Eq},49.49} = \mathbf{M}_{\mathrm{S}\to\mathrm{Eq}}\,\mathbf{v}_{\oplus\chi,\mathrm{S},49.49} = \left[\begin{array}{c} -89.06\ \mathrm{km/s} \\ 150.40\ \mathrm{km/s} \\ 136.87\ \mathrm{km/s} \end{array}\right]_{\mathrm{Eq}}, \tag{A47c}$$

and

$$\mathbf{v}_{\oplus\chi,\mathrm{Eq},231.99} = \mathbf{M}_{\mathrm{S}\to\mathrm{Eq}}\,\mathbf{v}_{\oplus\chi,\mathrm{S},231.99} = \left[\begin{array}{c} -118.04\ \mathrm{km/s} \\ 102.63\ \mathrm{km/s} \\ 157.54\ \mathrm{km/s} \end{array}\right]_{\mathrm{Eq}}, \tag{A47d}$$

respectively. Then we can obtain the directions (the right ascensions and the declinations) of the Earth's velocity relative to the Dark Matter halo in four normal and four advanced seasons in the Equatorial coordinate system (i.e., the blue–yellow points shown in Figs. 14 and 37 as well as in Figs. 15 and 38) summarized in Table A2 for readers' reference.

A.3.6 Dates considered for demonstrating the diurnal modulation of the angular WIMP velocity distribution

At the end of this section, we calculate the dates considered for demonstrating the diurnal modulation of the angular WIMP velocity distribution shown in Sec. 3.5.1 and Appendix B.

From Fig. A3 and Eq. (A12a), one can have

$$\begin{aligned}\mathbf{X}_{\rm E} &= \cos\psi_{\rm PM}\,\mathbf{X}_{\rm Eq} + \sin\psi_{\rm PM}\,\mathbf{Y}_{\rm Eq} \\ &= \gamma\cos\psi_{\rm yr}\,\mathbf{X}_{\rm Eq} + \gamma\sin\psi_{\rm yr}\cos\psi_{\oplus}\,\mathbf{Y}_{\rm Eq}\,. \end{aligned} \tag{A48}$$

Then, by taking $\psi_{\rm PM} = \phi_{\rm Cyg,Eq} = 129.30^\circ$ given in Eq. (A31a), the specified angle $\psi_{\rm yr}$ can be solved directly as

$$\psi_{\rm yr} = \tan^{-1}\left(\frac{\tan\psi_{\rm PM}}{\cos\psi_{\oplus}}\right) = 126.9^\circ\,. \tag{A49}$$

This means in turn that the date on which the WIMP wind points straightly to the Prime Meridian in the night is[19]

$$126.9^\circ\left(\frac{365\ {\rm day}}{360^\circ}\right) + 79.0\ {\rm day} = 207.66\ {\rm day}\,. \tag{A50}$$

And the date on which the WIMP wind points straightly to the Prime Meridian in the day is 25.16 day.

B Angular distributions of the 3-D WIMP velocity observed at the known underground laboratories

For readers' reference, we summarize in this section the angular distributions of the 3-D WIMP velocity in two laboratory–dependent (horizontal and laboratory) coordinate systems at the locations of several underground laboratories. Due to their geographical advantages, two under–constructed laboratories have also been considered: the Agua Negra Deep Experiment Site (ANDES) on the border between Argentina and Chile as the second underground laboratory in the Southern Hemisphere and the Callio Laboratory located at the Pyhäsalmi Mine in Finnland, which will be the northernmost (close to the Arctic Circle) underground laboratory in the future (the Boulby Laboratory is so far the northernmost one).

For each laboratory, we provide the following figures:

- the angular distributions of the 3-D WIMP velocity in the horizontal coordinate system in one entire year and in the 60-day observation periods of four advanced seasons on the central date of 49.49 day, 140.74 day, 231.99 day, and 323.24 day, respectively;
- the angular distributions of the 3-D WIMP velocity in the laboratory coordinate system in one entire year and in the 60-day observation periods of four advanced seasons;
- the angular distributions of the 3-D WIMP velocity in the laboratory coordinate system in four 4-hour daily shifts in two 60-day observation periods with the central dates of 207.66 day and 25.16 (= 390.16) day.

[19] Remind that these dates are only pure theoretical estimations under some simplified assumptions. It is obviously that the Prime Meridian should be in the day (night) on the 207.66 (25.16) day, respectively.

Remind that, firstly, 50 and 500 total WIMP events on average in (one daily shift of) one observation period (365 days/year, 60 days/season, or 4 hours/shift $\times$ 60 days) have been simulated. Secondly, in the simulations of the diurnal modulation of the angular WIMP velocity distribution presented here, we have re–calculated the local time of each simulated event of the considered laboratory from the generated measuring UTC time. Moreover, by comparing the angular distribution patterns observed at different laboratories, it can be found that, with $\mathcal{O}(500)$ total WIMP events and a higher analysis resolution, we might even be able to demonstrate a more detailed latitude–dependent distribution pattern.

For the identification of the annual modulation of the angular distribution pattern with real experimental data in the future, as the first confirmation of the directionality of the WIMP wind, we also summarize the directions of the simulated 3-D WIMP velocity with the highest event numbers ($>$ 4 times of the all–sky average value) in the *horizontal* coordinate system in one entire year and in four advanced seasons in one table for each laboratory. Note that in these tables we mark the ranges with a double–underline to indicate that, with $\mathcal{O}(500)$ total WIMP events and a higher analysis resolution, some extra bins would exceed the high–WIMP–flux areas identified with only $\mathcal{O}(50)$ total events and a lower resolution.

B.1 Agua Negra Deep Experiment Site (ANDES)

Central date (observation period) (day)	Most–event directions	
	50 events	500 events
0 – 365	—	—
49.49 (19.49 – 79.49)	0° – 60°N 120°W – 60°W	0° – 60°N, 120°W – 60°W 60°N – 75°N, 120°E – 180°
140.74 (110.74 – 170.74)	0° – 60°N 60°E – 180°	0° – 60°N 60°E – 150°E
231.99 (201.99 – 261.99)	30°S – 30°N 60°E – 180°	30°S – 30°N 90°E – 150°W
323.24 (293.24 – 353.24)	30°S – 60°N 180° – 120°W	45°S – 60°N 180° – 120°W

Table A3: The summary of the directions of the simulated 3-D WIMP velocity with the highest event numbers ($>$ 4 times of the all–sky average value) in the horizontal coordinate system in one entire year and four advanced seasons at the location of the ANDES laboratory (30.19°S, 69.82°W). 50 and 500 total events on average in each observation period of 60 days have been simulated.

Remark: in Fig. A8(b) one can find that, with $\mathcal{O}(500)$ total WIMP events and a higher analysis resolution, a second high–WIMP–flux bin ("hot–point") from 60°N to 75°N and 120°E to 180° in the angular distribution pattern in the horizontal coordinate system would be observed at the ANDES laboratory.

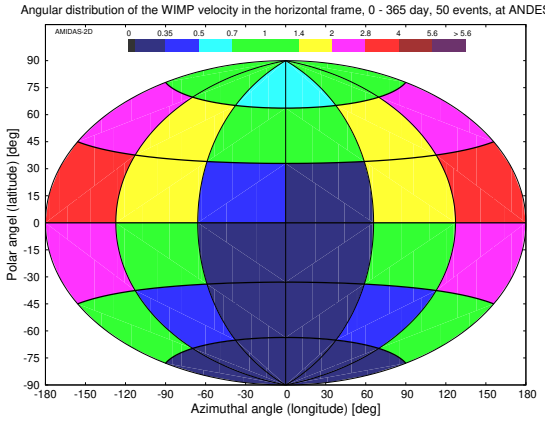

(a) 0 – 365 day

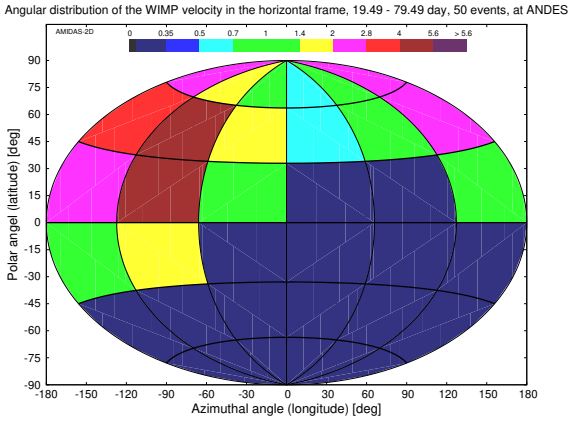

(b) 19.49 – 79.49 day

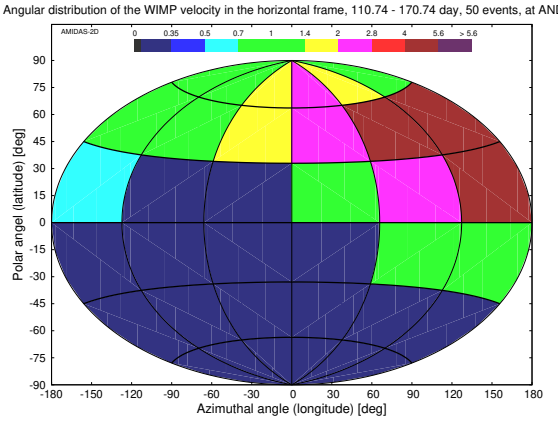

(c) 110.74 – 170.74 day

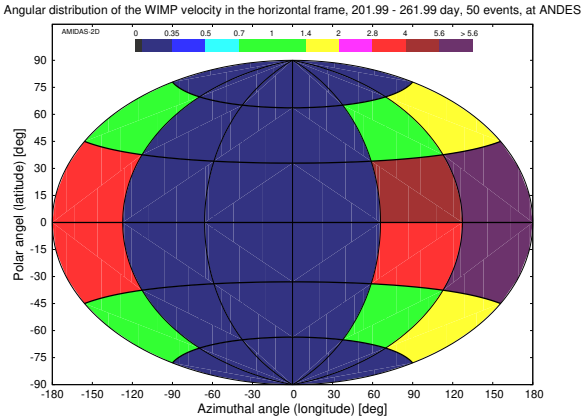

(d) 201.99 – 261.99 day

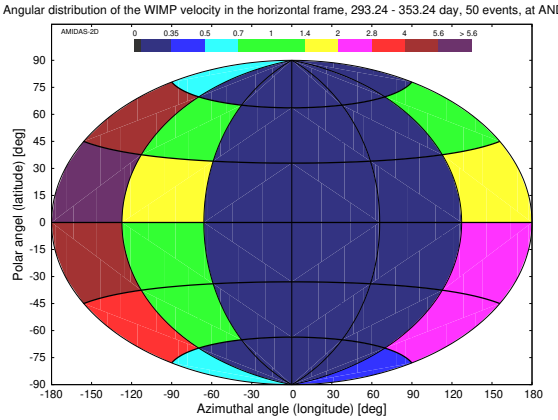

(e) 293.24 – 353.24 day

Figure A7: The angular distributions of the 3-D WIMP velocity in the horizontal coordinate system at the location of the ANDES laboratory (30.19°S, 69.82°W). 50 total events on average in one entire year (a) and in each 60-day observation period of four advanced seasons (b – e) have been simulated.

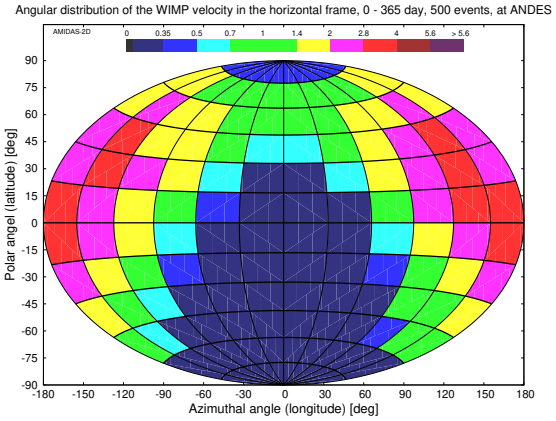

(a) 0 – 365 day

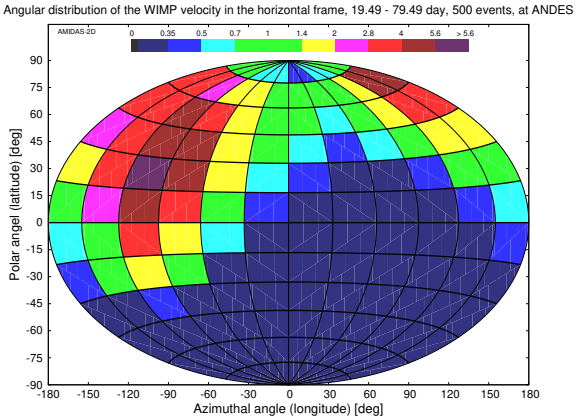

(b) 19.49 – 79.49 day

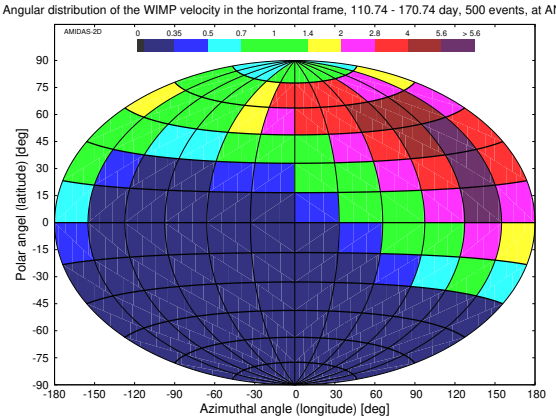

(c) 110.74 – 170.74 day

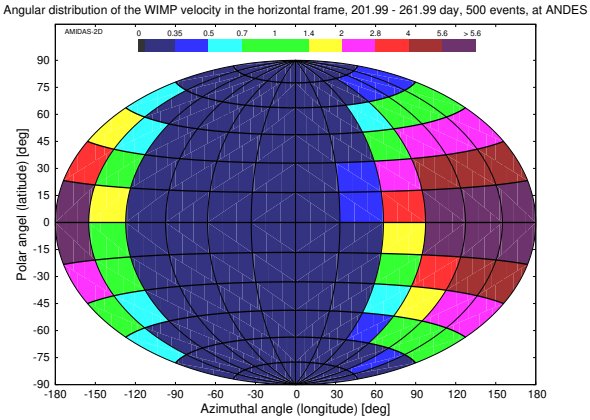

(d) 201.99 – 261.99 day

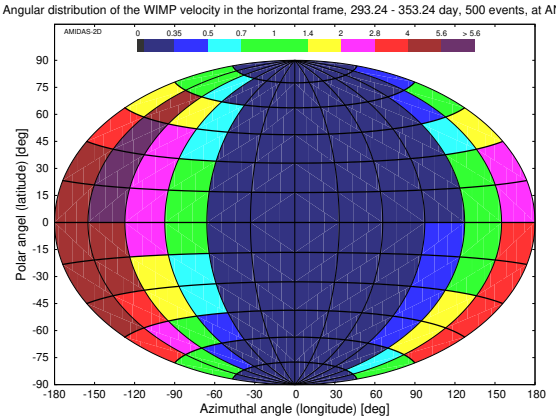

(e) 293.24 – 353.24 day

Figure A8: As in Figs. A7, except that 500 total events on average in one entire year (a) and in each 60-day observation period of four advanced seasons (b – e) have been simulated.

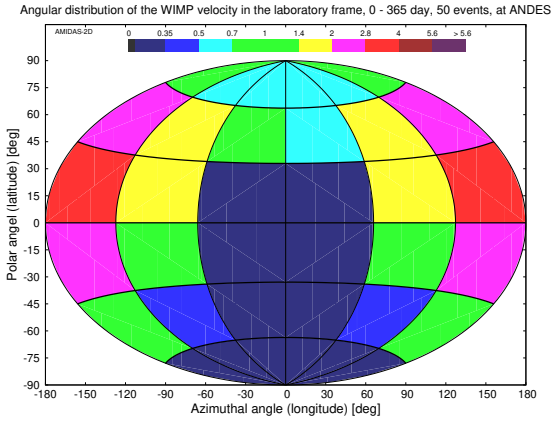

(a) 0 – 365 day

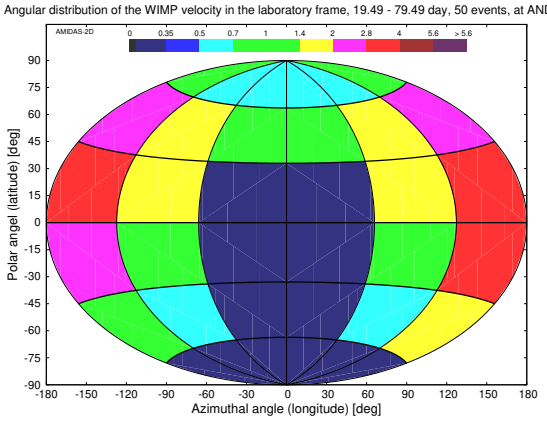

(b) 19.49 – 79.49 day

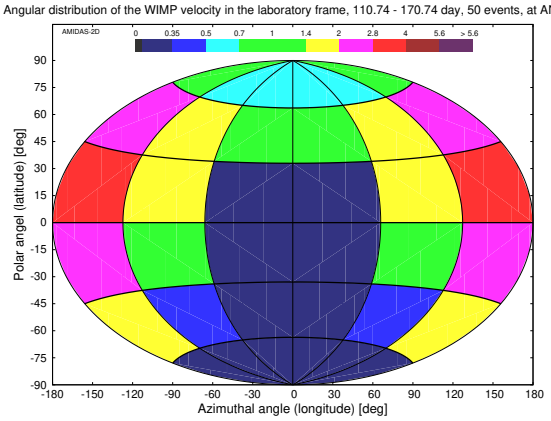

(c) 110.74 – 170.74 day

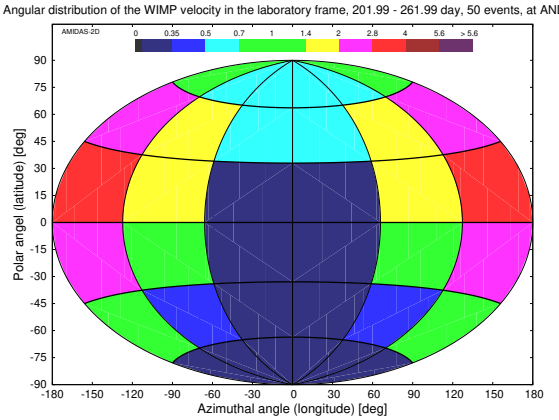

(d) 201.99 – 261.99 day

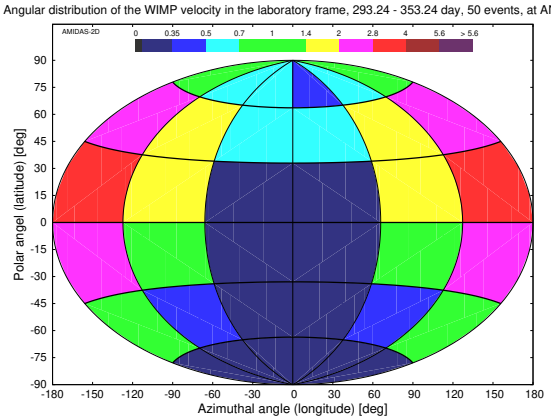

(e) 293.24 – 353.24 day

Figure A9: The angular distributions of the 3-D WIMP velocity transformed from events shown in Fig. A7 to the laboratory coordinate system at the location of the ANDES laboratory. All simulation setup and notations are the same as in Fig. A7.

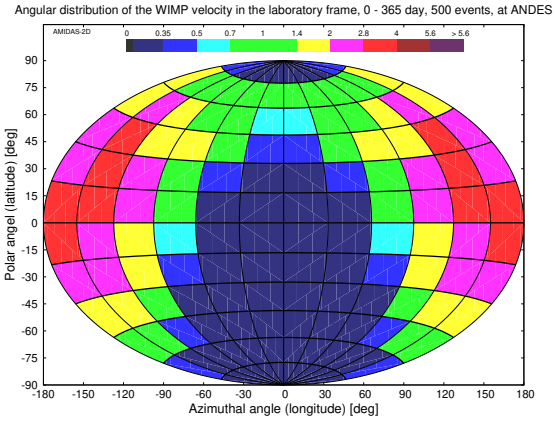

(a) 0 – 365 day

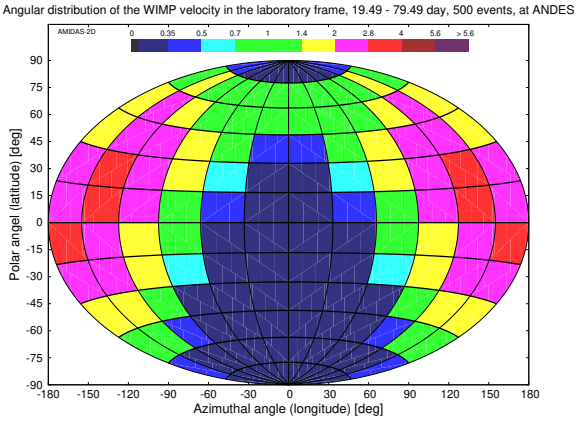

(b) 19.49 – 79.49 day

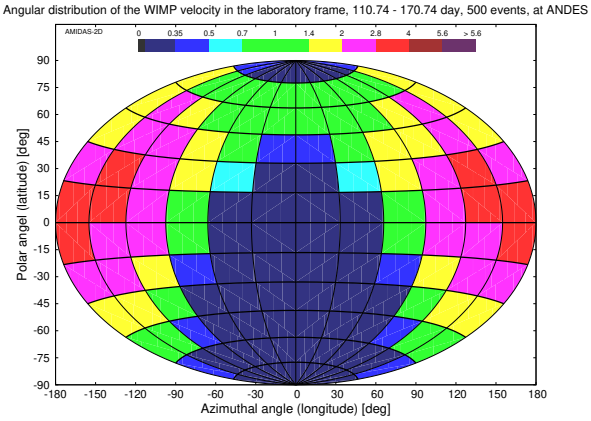

(c) 110.74 – 170.74 day

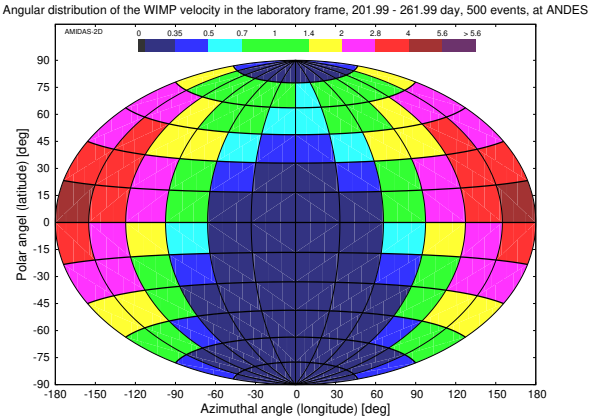

(d) 201.99 – 261.99 day

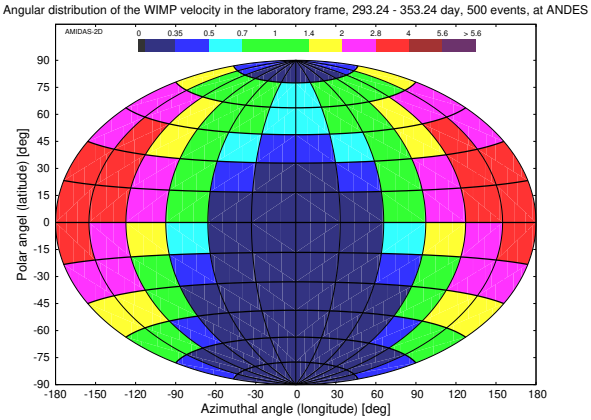

(e) 293.24 – 353.24 day

Figure A10: As in Figs. A9, except that 500 total events on average in one entire year (a) and in each 60-day observation period of four advanced seasons (b – e) have been simulated.

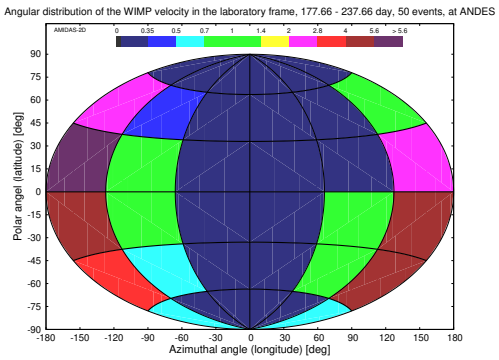

(a) 177.66 – 237.66 day, 22 – 2 hour

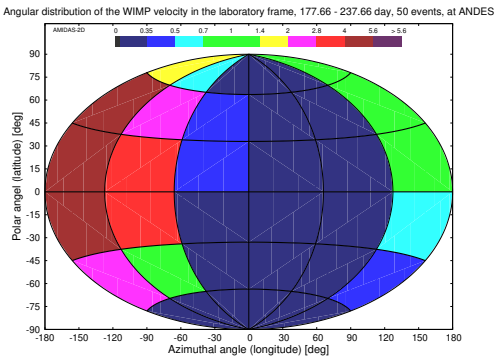

(b) 177.66 – 237.66 day, 4 – 8 hour

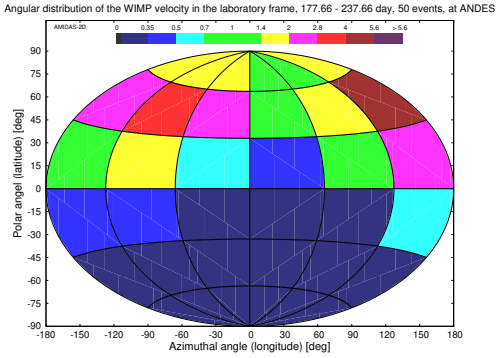

(c) 177.66 – 237.66 day, 10 – 14 hour

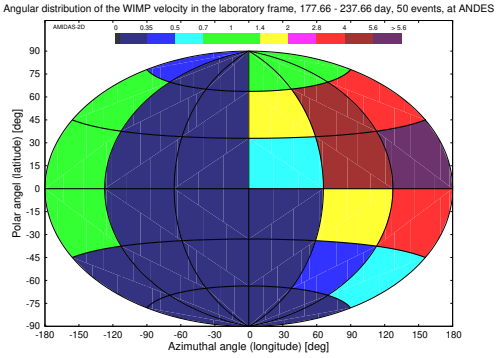

(d) 177.66 – 237.66 day, 16 – 20 hour

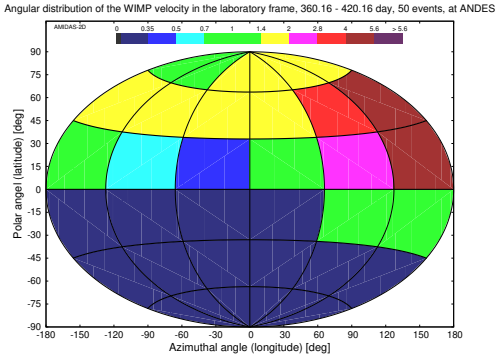

(e) 360.16 – 420.16 day, 22 – 2 hour

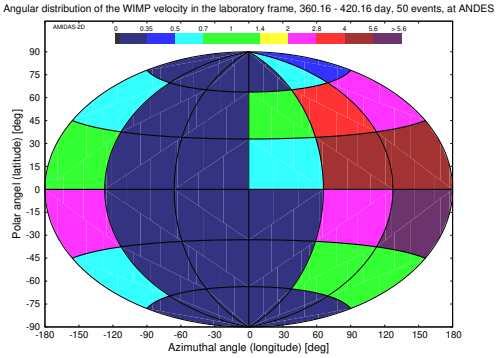

(f) 360.16 – 420.16 day, 4 – 8 hour

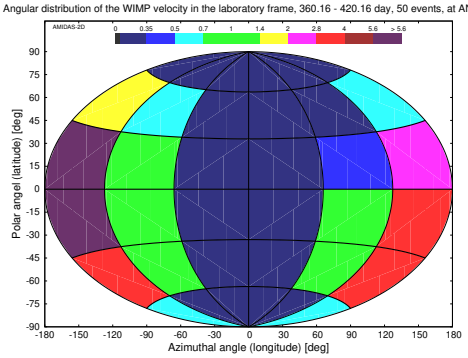

(g) 360.16 – 420.16 day, 10 – 14 hour

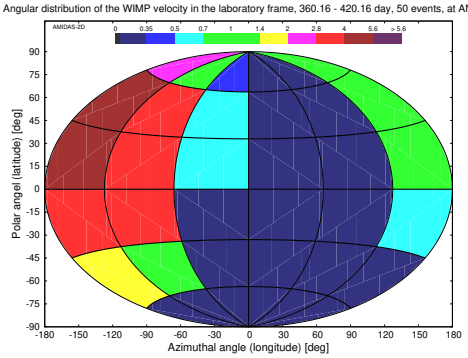

(h) 360.16 – 420.16 day, 16 – 20 hour

Figure A11: The angular distributions of the 3-D WIMP velocity observed at the location of the ANDES laboratory. 50 total events on average in each 4-hour daily shift in the 60-day observation periods of 177.66 – 237.66 day (a – d) and 360.16 – 420.16 (= 55.16) day (e – h) have been simulated.

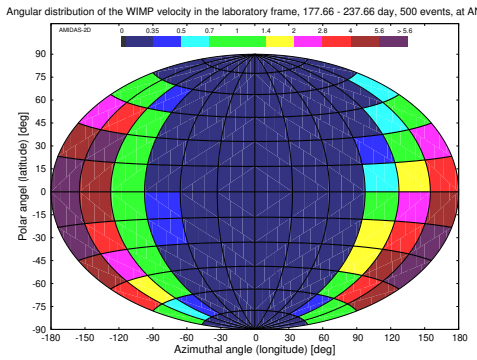

(a) 177.66 – 237.66 day, 22 – 2 hour

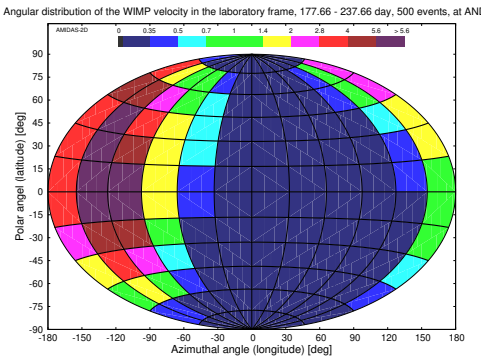

(b) 177.66 – 237.66 day, 4 – 8 hour

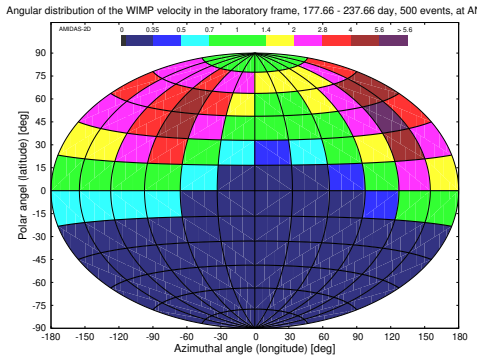

(c) 177.66 – 237.66 day, 10 – 14 hour

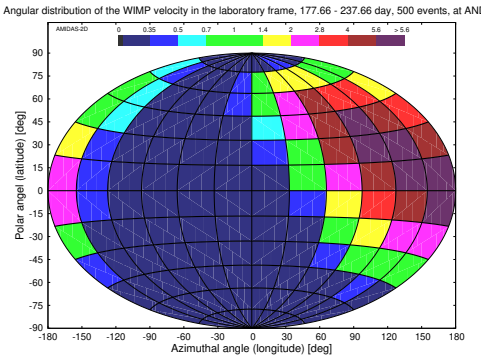

(d) 177.66 – 237.66 day, 16 – 20 hour

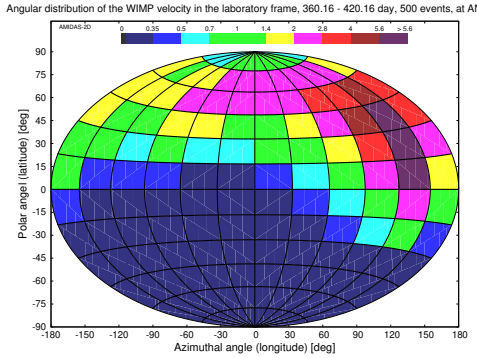

(e) 360.16 – 420.16 day, 22 – 2 hour

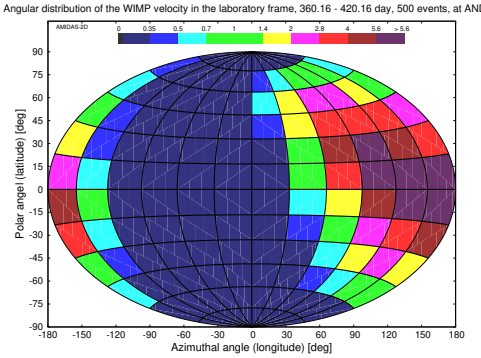

(f) 360.16 – 420.16 day, 4 – 8 hour

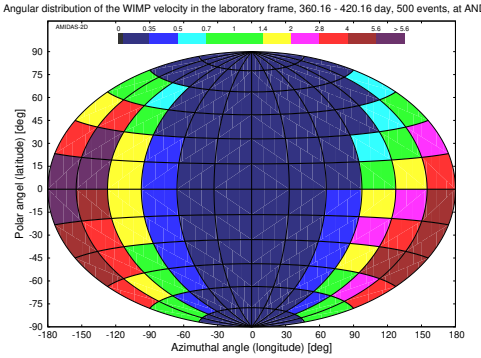

(g) 360.16 – 420.16 day, 10 – 14 hour

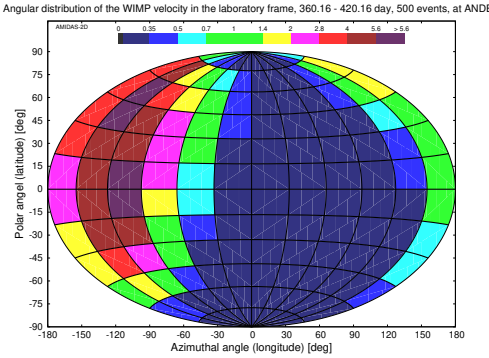

(h) 360.16 – 420.16 day, 16 – 20 hour

Figure A12: As in Figs. A11, except that 500 total events on average in each 4-hour daily shift in the 60-day observation periods have been simulated.

B.2 Boulby Laboratory

Central date (observation period) (day)	Most–event directions	
	50 events	500 events
0 – 365	—	—
49.49 (19.49 – 79.49)	30°S – 30°N 120°E – 180°	$\underline{\underline{45°S}}$ – 30°N $\underline{\underline{90°E}}$ – $\underline{\underline{150°W}}$
140.74 (110.74 – 170.74)	60°S – 0° 60°E – 120°E	60°S – $\underline{\underline{15°N}}$ 60°E – $\underline{\underline{150°E}}$
231.99 (201.99 – 261.99)	60°S – 30°S 180° – 120°W + 0° – 60°E	60°S – 30°S 150°W – $\underline{\underline{90°W}}$ + $\underline{\underline{30°W}}$ – 60°E
323.24 (293.24 – 353.24)	30°S – 0° 180° – 60°W	$\underline{\underline{45°S}}$ – 0° $\underline{\underline{150°E}}$ – 60°W

Table A4: The summary of the directions of the simulated 3-D WIMP velocity with the highest event numbers ($>$ 4 times of the all–sky average value) in the horizontal coordinate system in one entire year and four advanced seasons at the location of the Boulby laboratory (54.55°N, 0.82°W). 50 and 500 total events on average in each observation period of 60 days have been simulated.

Remark: Fig. A13(d) shows that, with only $\mathcal{O}(50)$ total WIMP events, one could already observe two separate high–WIMP–flux bins in the angular distribution pattern in the horizontal coordinate system of the Boulby laboratory; with $\mathcal{O}(500)$ total events and a higher analysis resolution, these two hot–points could be identified more clearly (see Fig. A14(d)).

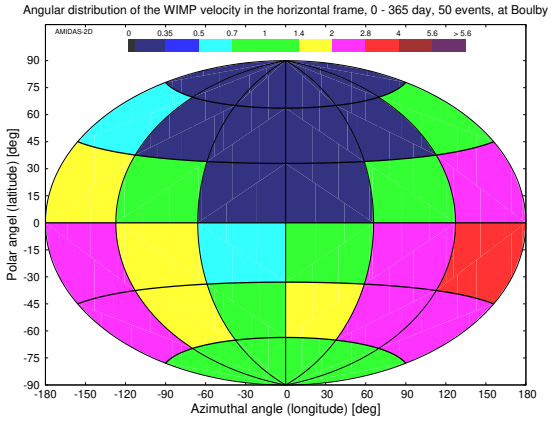

(a) 0 – 365 day

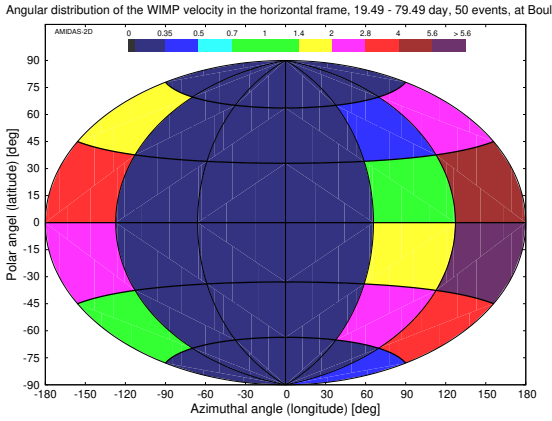

(b) 19.49 – 79.49 day

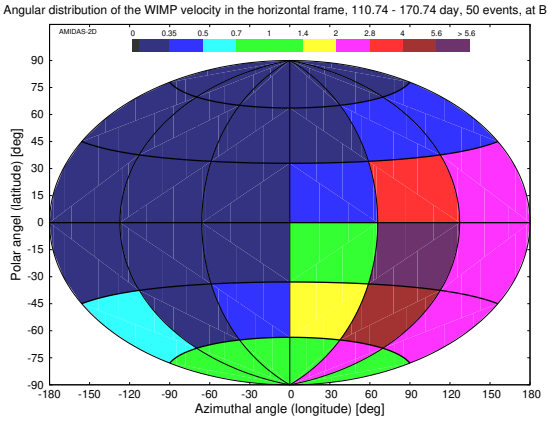

(c) 110.74 – 170.74 day

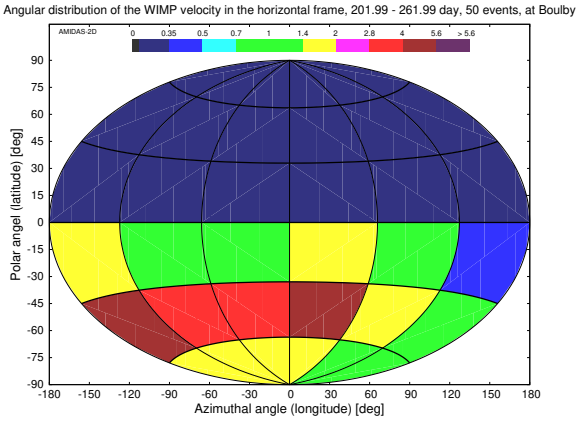

(d) 201.99 – 261.99 day

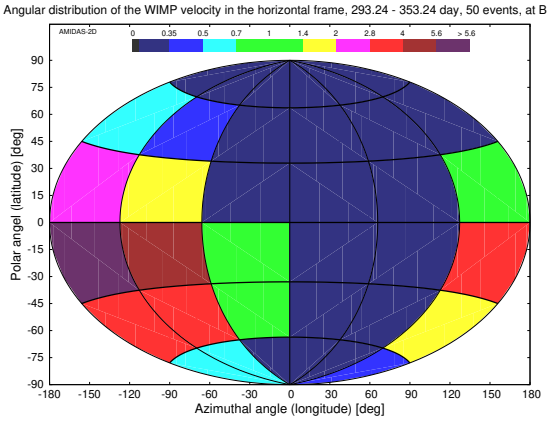

(e) 293.24 – 353.24 day

Figure A13: The angular distributions of the 3-D WIMP velocity in the horizontal coordinate system at the location of the Boulby laboratory (54.55°N, 0.82°W). 50 total events on average in one entire year (a) and in each 60-day observation period of four advanced seasons (b – e) have been simulated.

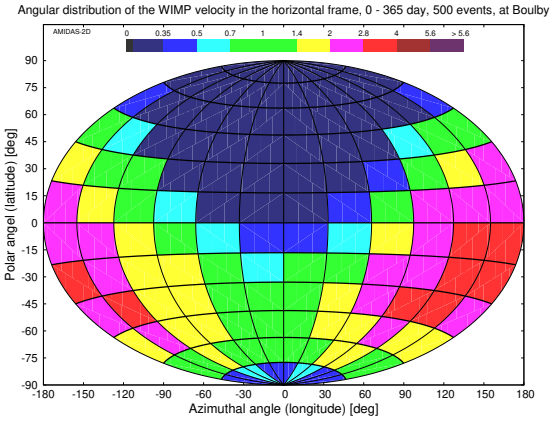

(a) 0 – 365 day

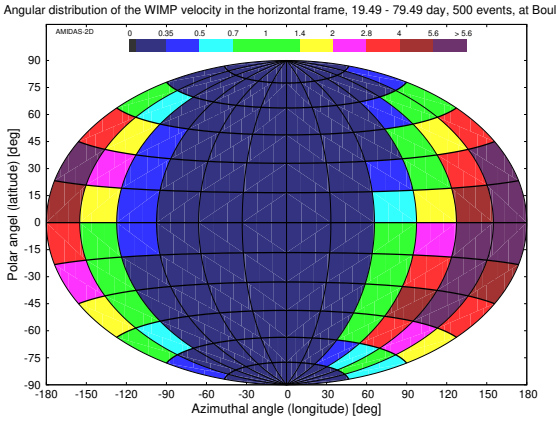

(b) 19.49 – 79.49 day

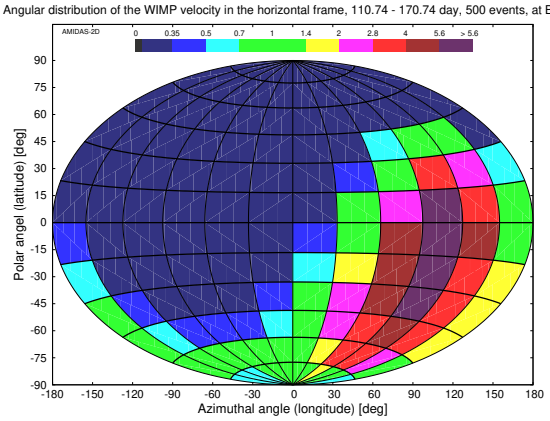

(c) 110.74 – 170.74 day

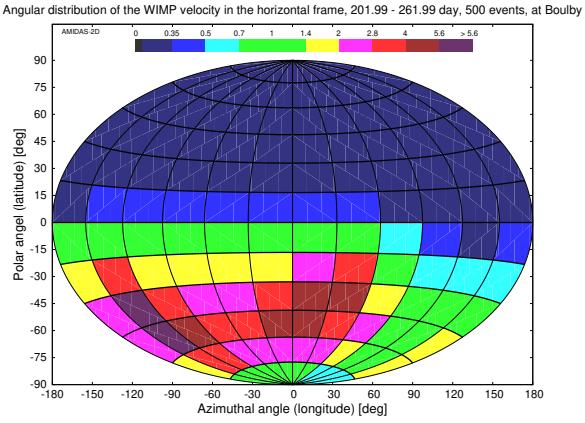

(d) 201.99 – 261.99 day

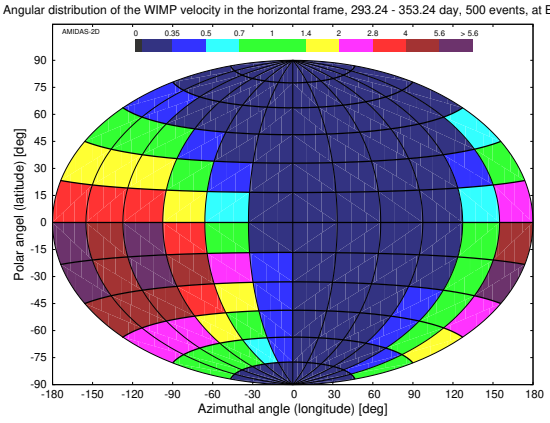

(e) 293.24 – 353.24 day

Figure A14: As in Figs. A13, except that 500 total events on average in one entire year (a) and in each 60-day observation period of four advanced seasons (b – e) have been simulated.

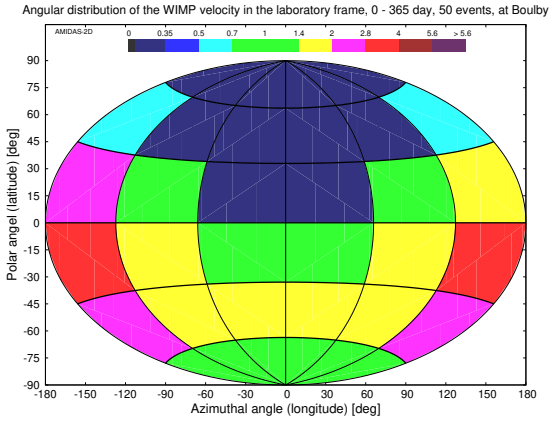

(a) 0 – 365 day

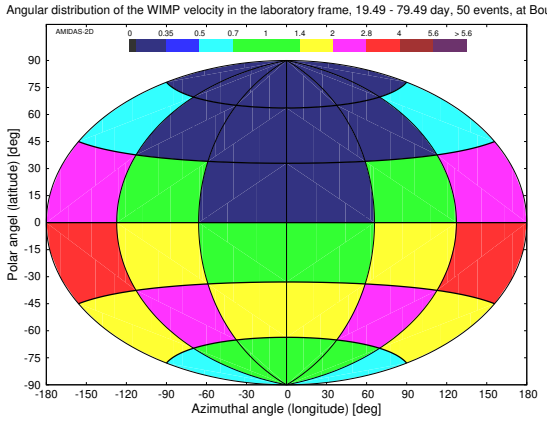

(b) 19.49 – 79.49 day

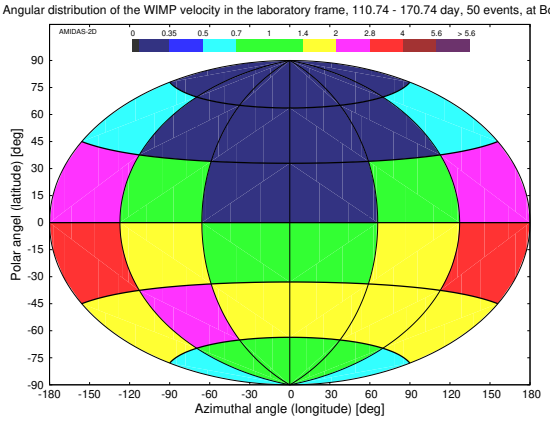

(c) 110.74 – 170.74 day

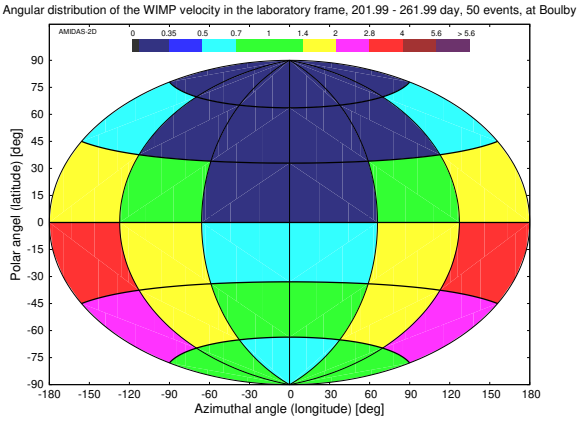

(d) 201.99 – 261.99 day

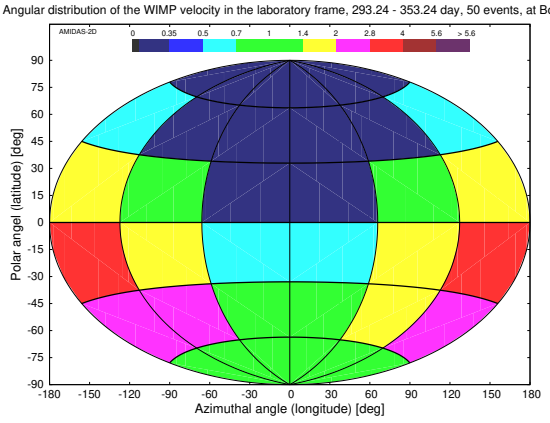

(e) 293.24 – 353.24 day

Figure A15: The angular distributions of the 3-D WIMP velocity transformed from events shown in Fig. A13 to the laboratory coordinate system at the location of the Boulby laboratory. All simulation setup and notations are the same as in Fig. A13.

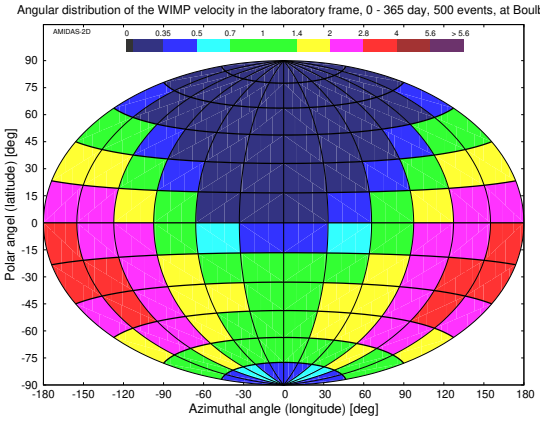

(a) 0 – 365 day

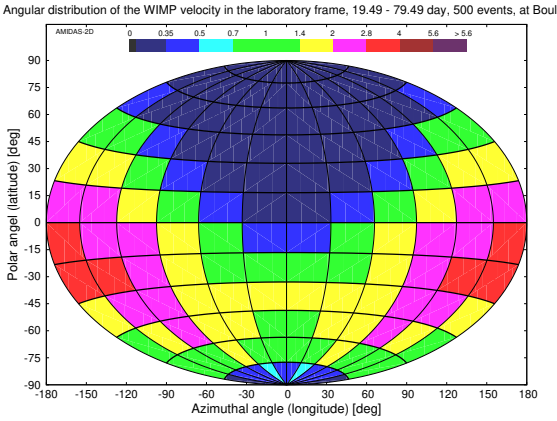

(b) 19.49 – 79.49 day

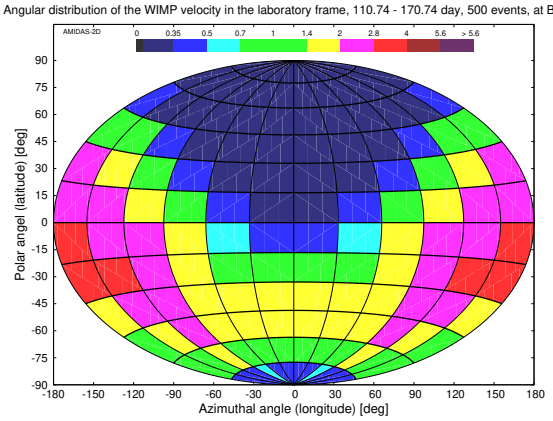

(c) 110.74 – 170.74 day

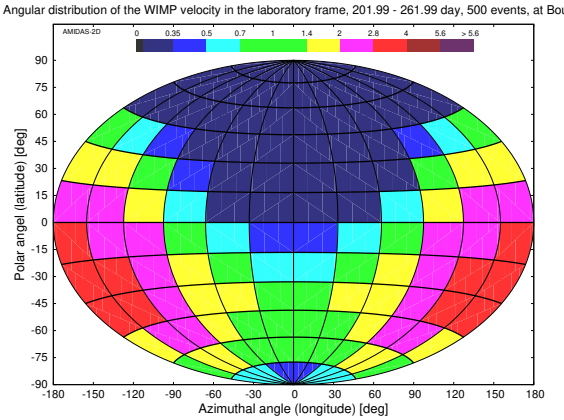

(d) 201.99 – 261.99 day

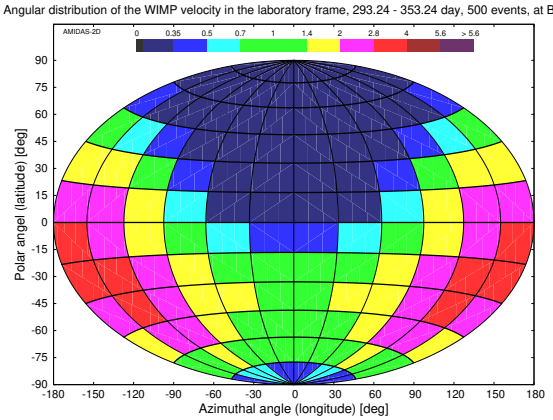

(e) 293.24 – 353.24 day

Figure A16: As in Figs. A15, except that 500 total events on average in one entire year (a) and in each 60-day observation period of four advanced seasons (b – e) have been simulated.

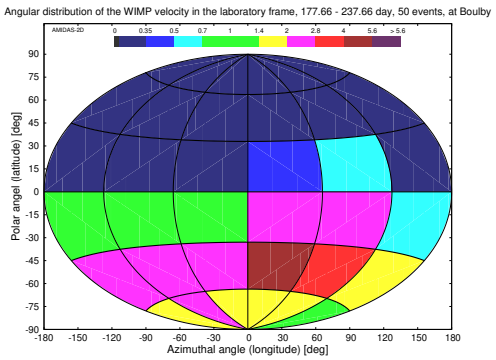

(a) 177.66 – 237.66 day, 22 – 2 hour

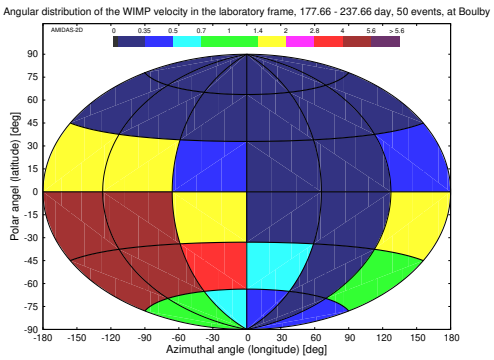

(b) 177.66 – 237.66 day, 4 – 8 hour

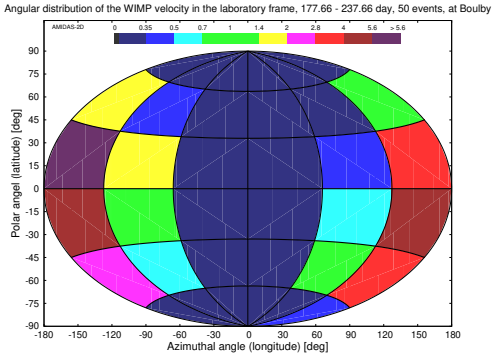

(c) 177.66 – 237.66 day, 10 – 14 hour

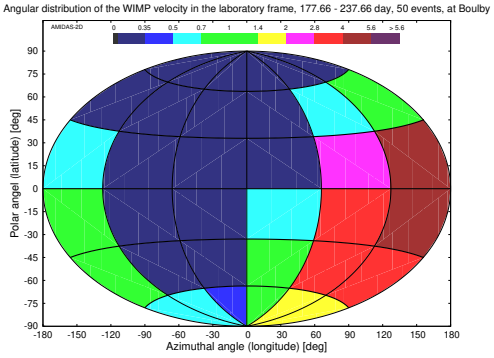

(d) 177.66 – 237.66 day, 16 – 20 hour

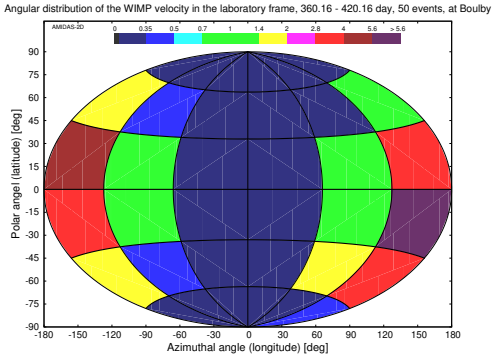

(e) 360.16 – 420.16 day, 22 – 2 hour

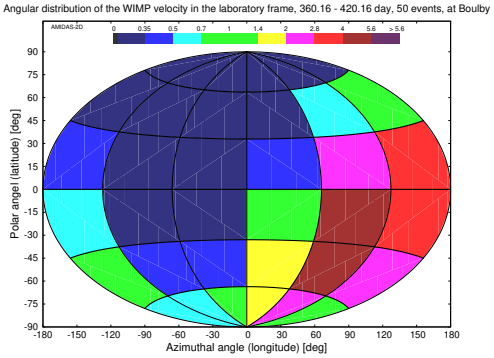

(f) 360.16 – 420.16 day, 4 – 8 hour

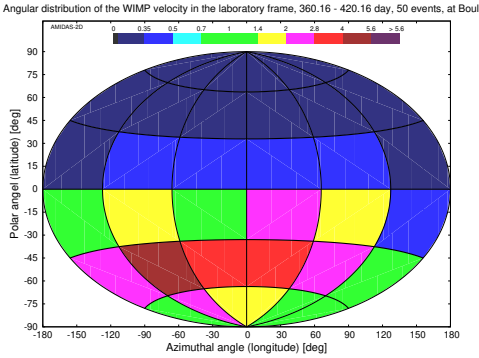

(g) 360.16 – 420.16 day, 10 – 14 hour

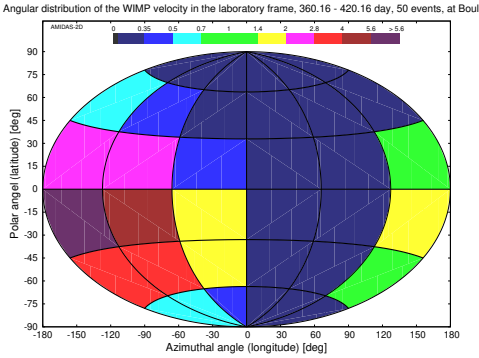

(h) 360.16 – 420.16 day, 16 – 20 hour

Figure A17: The angular distributions of the 3-D WIMP velocity observed at the location of the Boulby laboratory. 50 total events on average in each 4-hour daily shift in the 60-day observation periods of 177.66 – 237.66 day (a – d) and 360.16 – 420.16 (= 55.16) day (e – h) have been simulated.

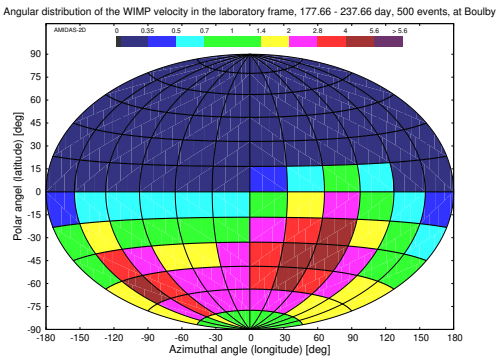

(a) 177.66 – 237.66 day, 22 – 2 hour

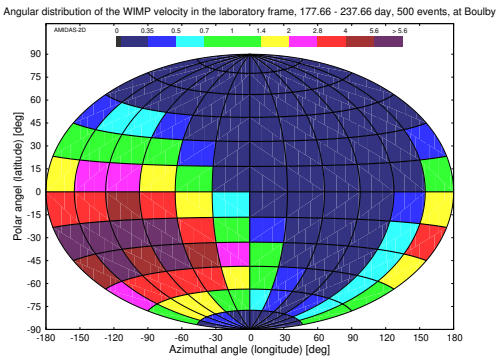

(b) 177.66 – 237.66 day, 4 – 8 hour

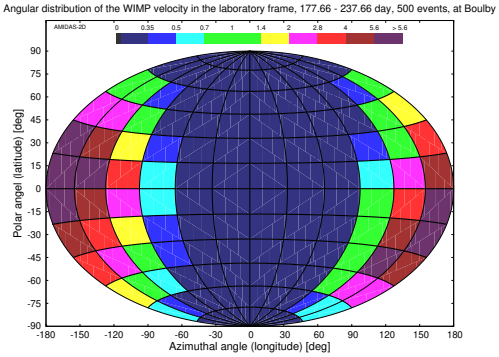

(c) 177.66 – 237.66 day, 10 – 14 hour

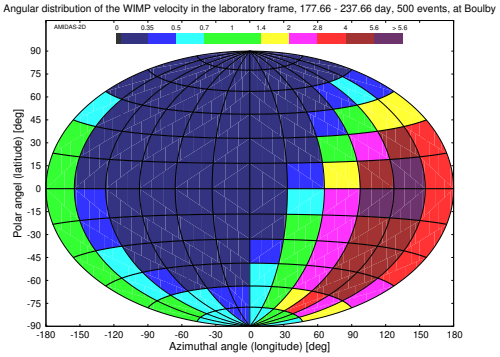

(d) 177.66 – 237.66 day, 16 – 20 hour

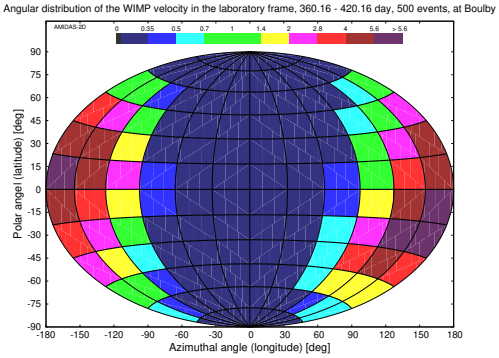

(e) 360.16 – 420.16 day, 22 – 2 hour

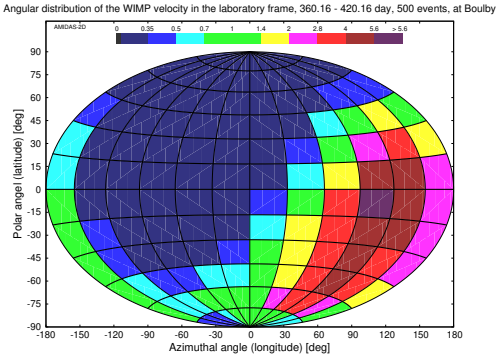

(f) 360.16 – 420.16 day, 4 – 8 hour

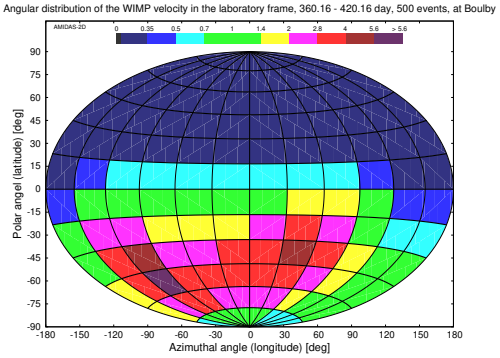

(g) 360.16 – 420.16 day, 10 – 14 hour

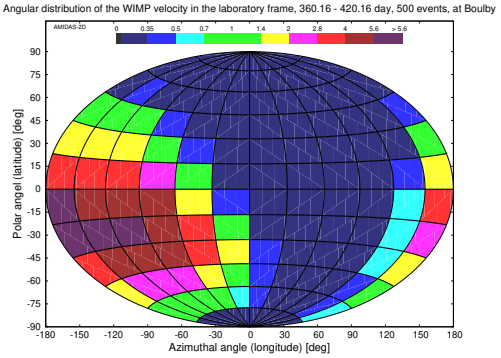

(h) 360.16 – 420.16 day, 16 – 20 hour

Figure A18: As in Figs. A17, except that 500 total events on average in each 4-hour daily shift in the 60-day observation periods have been simulated.

B.3 Callio Laboratory

Central date (observation period) (day)	Most–event directions	
	50 events	500 events
0 – 365	—	—
49.49 (19.49 – 79.49)	60°S – 30°N 60°E – 180°	60°S – 30°N 60°E – 180°
140.74 (110.74 – 170.74)	60°S – 0° 60°E – 120°E	60°S – 0° 30°E – 120°E
231.99 (201.99 – 261.99)	60°S – 30°S 180° – 0° (western)	60°S – 30°S, 150°W – 90°W 60°S – 15°S, 60°W – 30°E
323.24 (293.24 – 353.24)	30°S – 0° 120°E – 60°W	45°S – 15°N 150°E – 90°W

Table A5: The summary of the directions of the simulated 3-D WIMP velocity with the highest event numbers ($>$ 4 times of the all–sky average value) in the horizontal coordinate system in one entire year and four advanced seasons at the location of the Callio laboratory (63.66°N, 26.04°E). 50 and 500 total events on average in each observation period of 60 days have been simulated.

Remark: By comparing Fig. A20(d) with Fig. A19(d), one can find that, with $\mathcal{O}(500)$ total WIMP events and a higher analysis resolution, the high–WIMP–flux bins in the angular distribution pattern in the horizontal coordinate system of the Callio laboratory could be distinguished into two separate areas.

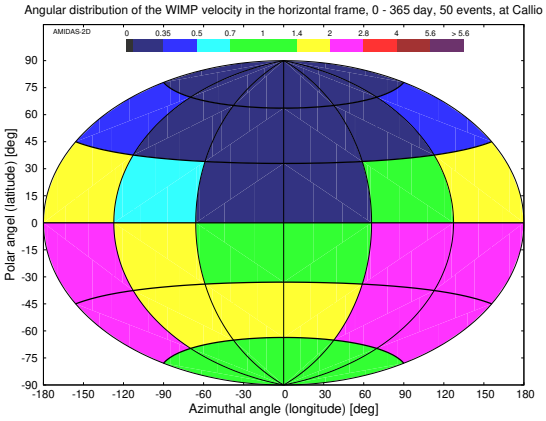

(a) 0 – 365 day

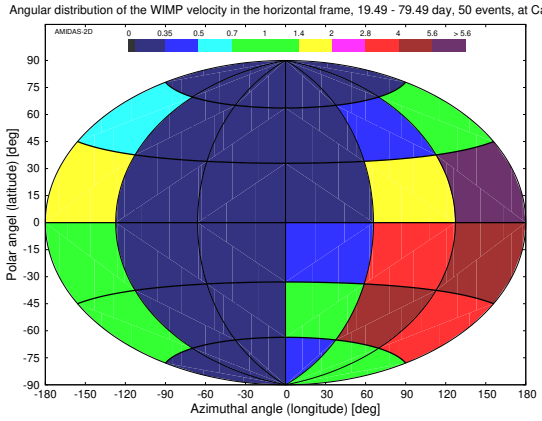

(b) 19.49 – 79.49 day

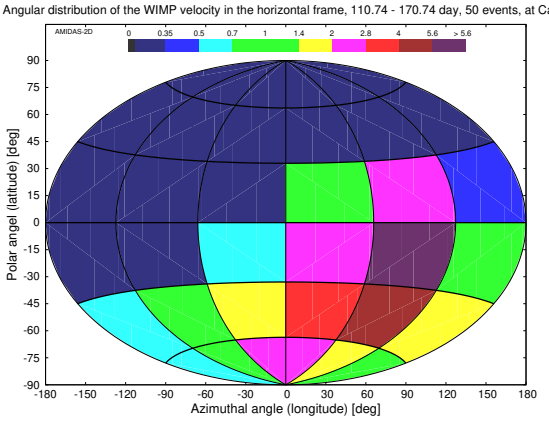

(c) 110.74 – 170.74 day

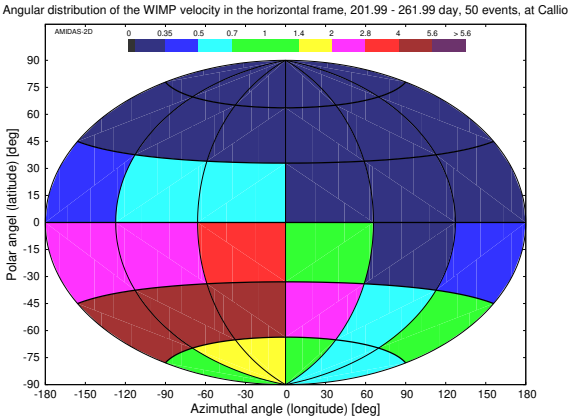

(d) 201.99 – 261.99 day

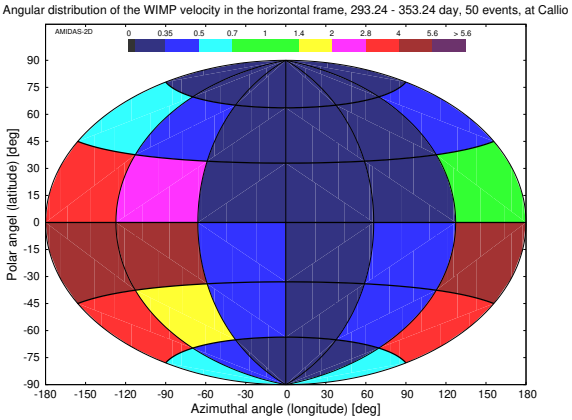

(e) 293.24 – 353.24 day

Figure A19: The angular distributions of the 3-D WIMP velocity in the horizontal coordinate system at the location of the Callio laboratory (63.66°N, 26.04°E). 50 total events on average in one entire year (a) and in each 60-day observation period of four advanced seasons (b – e) have been simulated.

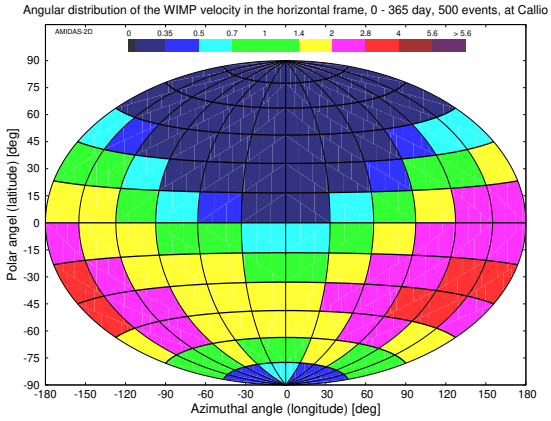

(a) 0 – 365 day

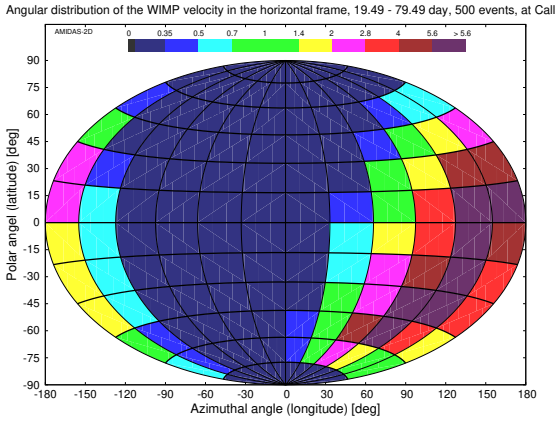

(b) 19.49 – 79.49 day

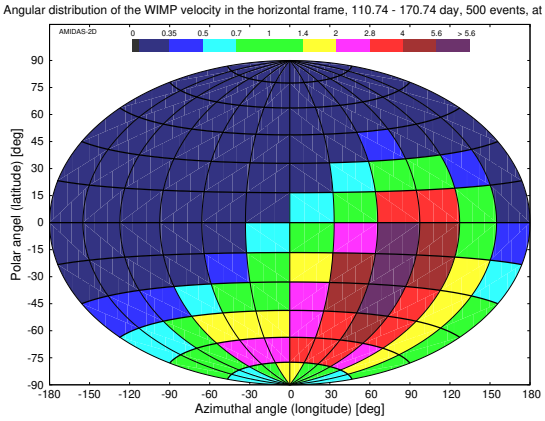

(c) 110.74 – 170.74 day

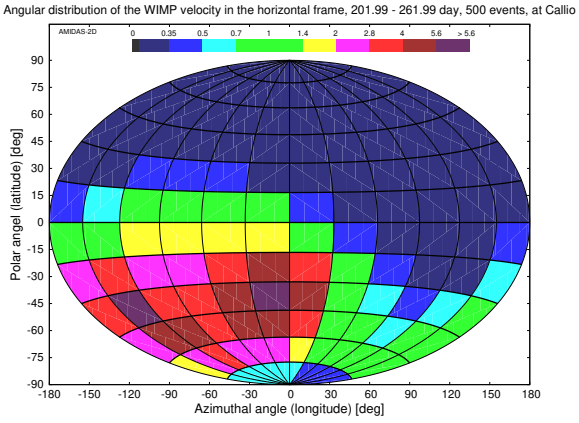

(d) 201.99 – 261.99 day

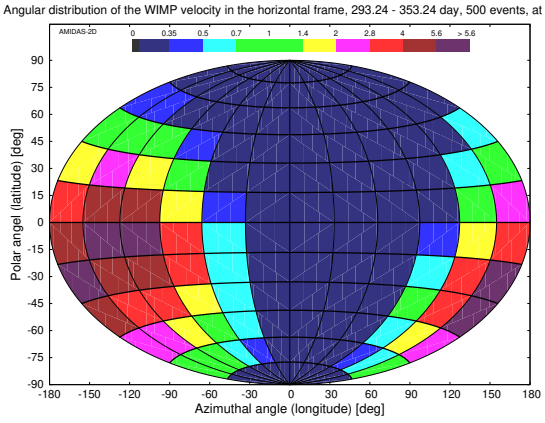

(e) 293.24 – 353.24 day

Figure A20: As in Figs. A19, except that 500 total events on average in one entire year (a) and in each 60-day observation period of four advanced seasons (b – e) have been simulated.

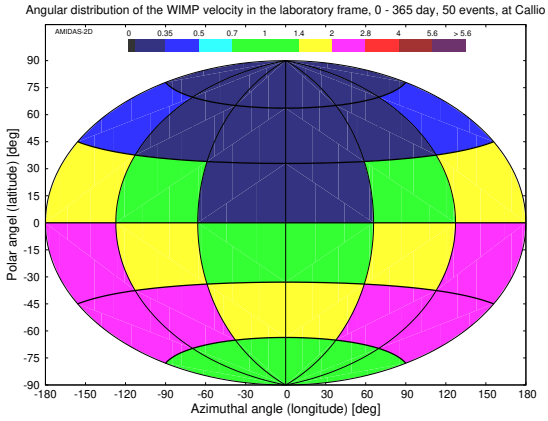

(a) 0 – 365 day

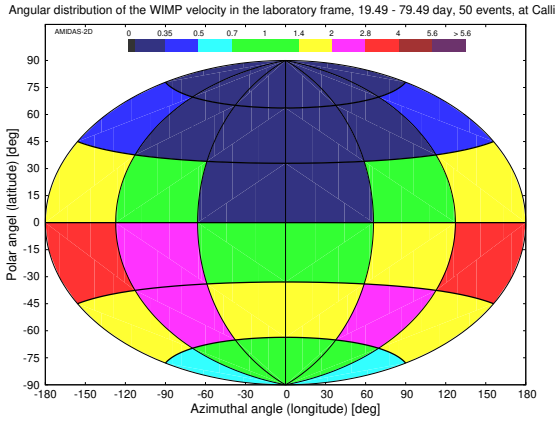

(b) 19.49 – 79.49 day

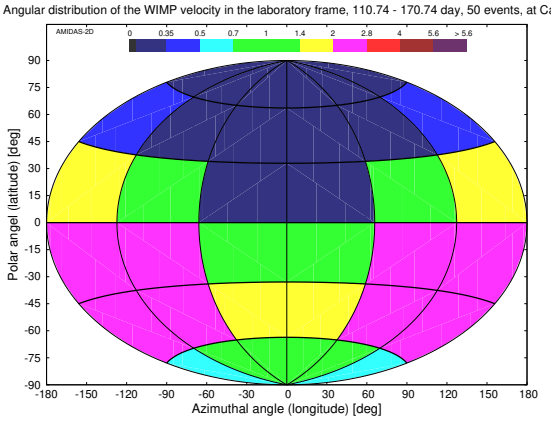

(c) 110.74 – 170.74 day

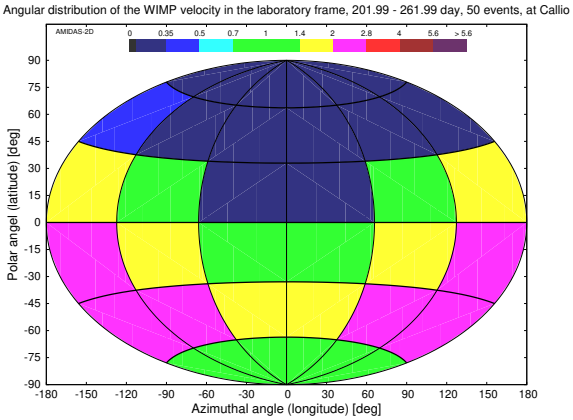

(d) 201.99 – 261.99 day

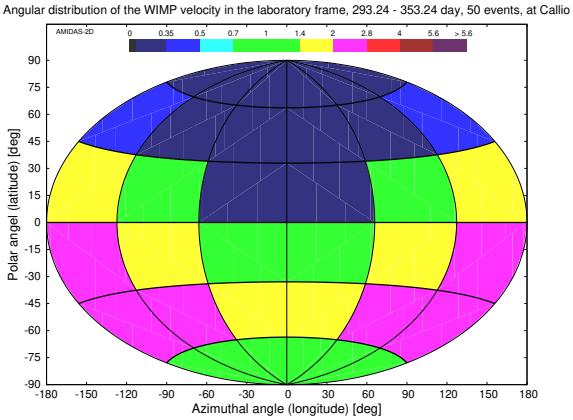

(e) 293.24 – 353.24 day

Figure A21: The angular distributions of the 3-D WIMP velocity transformed from events shown in Fig. A19 to the laboratory coordinate system at the location of the Callio laboratory. All simulation setup and notations are the same as in Fig. A19.

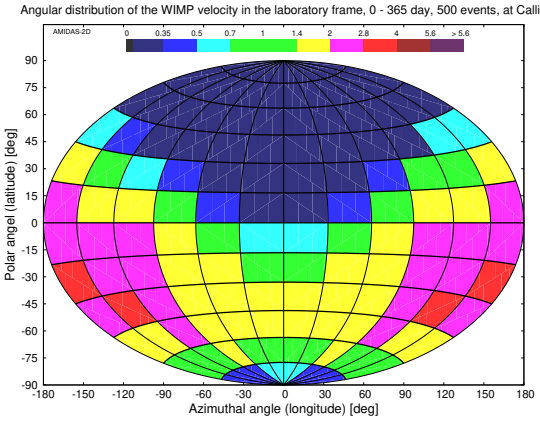

(a) 0 – 365 day

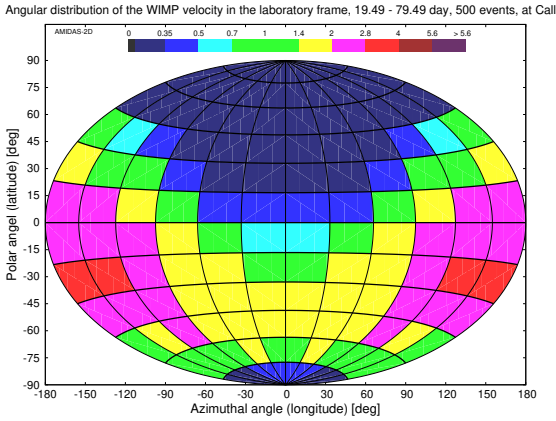

(b) 19.49 – 79.49 day

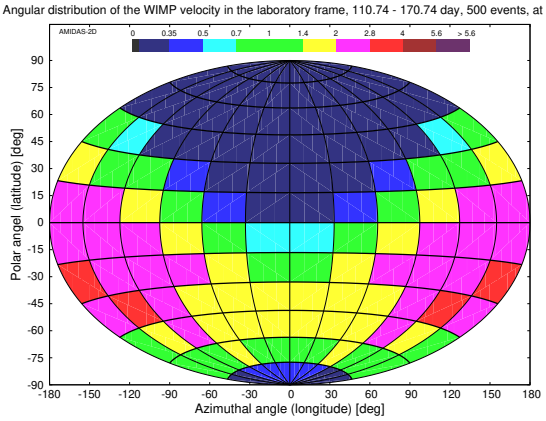

(c) 110.74 – 170.74 day

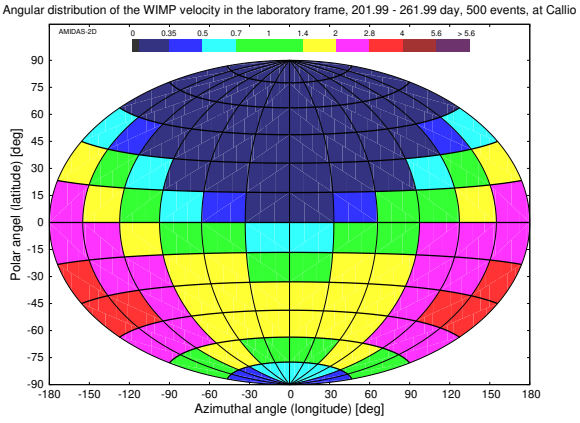

(d) 201.99 – 261.99 day

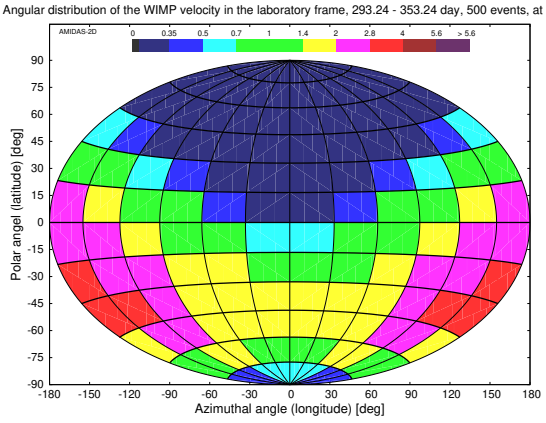

(e) 293.24 – 353.24 day

Figure A22: As in Figs. A21, except that 500 total events on average in one entire year (a) and in each 60-day observation period of four advanced seasons (b – e) have been simulated.

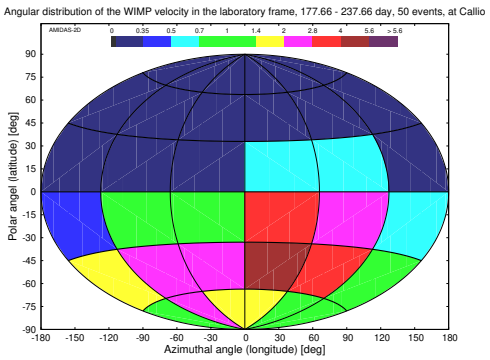

(a) 177.66 – 237.66 day, 22 – 2 hour

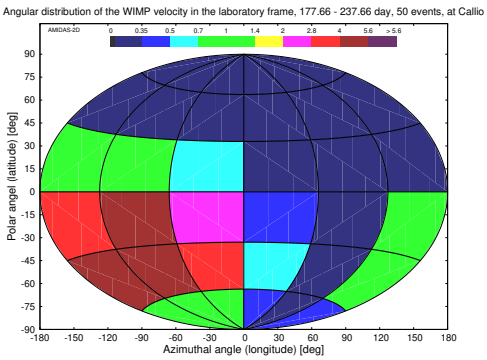

(b) 177.66 – 237.66 day, 4 – 8 hour

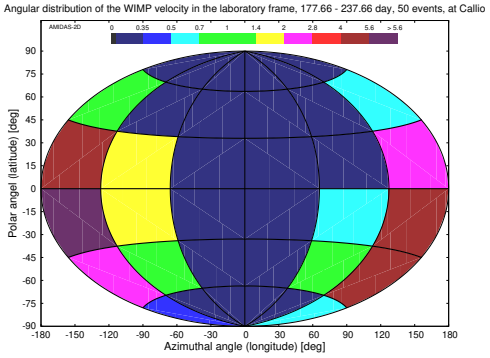

(c) 177.66 – 237.66 day, 10 – 14 hour

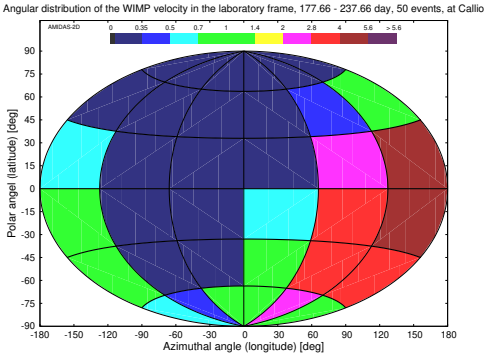

(d) 177.66 – 237.66 day, 16 – 20 hour

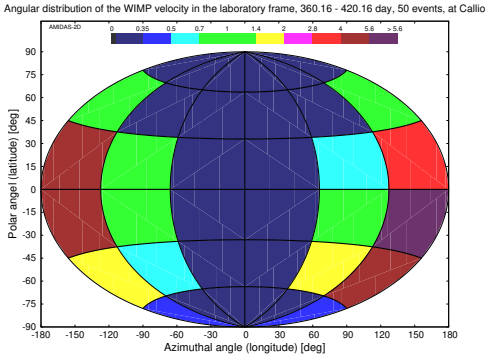

(e) 360.16 – 420.16 day, 22 – 2 hour

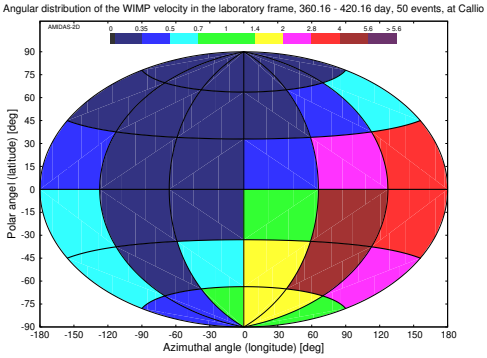

(f) 360.16 – 420.16 day, 4 – 8 hour

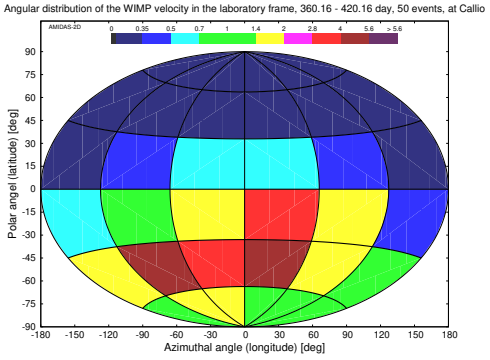

(g) 360.16 – 420.16 day, 10 – 14 hour

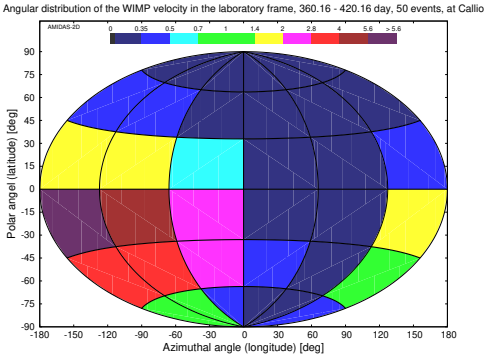

(h) 360.16 – 420.16 day, 16 – 20 hour

Figure A23: The angular distributions of the 3-D WIMP velocity observed at the location of the Callio laboratory. 50 total events on average in each 4-hour daily shift in the 60-day observation periods of 177.66 – 237.66 day (a – d) and 360.16 – 420.16 (= 55.16) day (e – h) have been simulated.

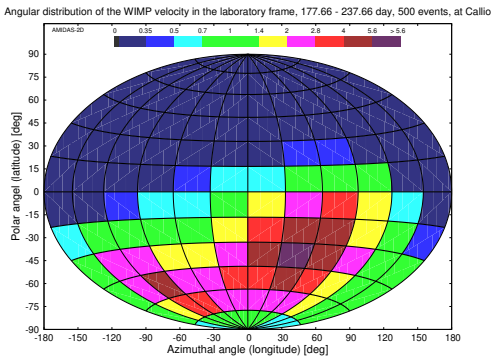

(a) 177.66 – 237.66 day, 22 – 2 hour

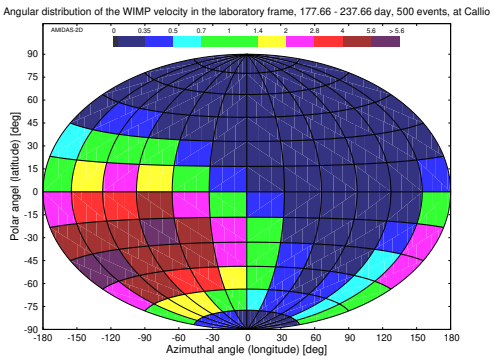

(b) 177.66 – 237.66 day, 4 – 8 hour

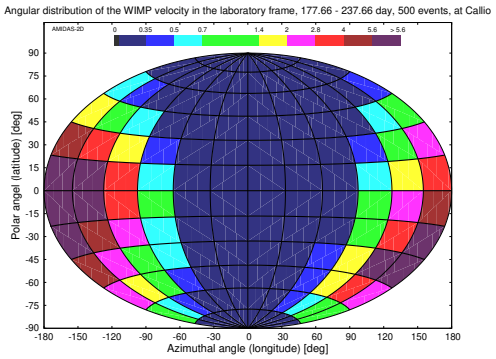

(c) 177.66 – 237.66 day, 10 – 14 hour

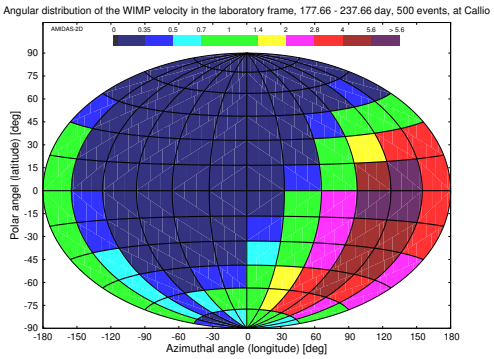

(d) 177.66 – 237.66 day, 16 – 20 hour

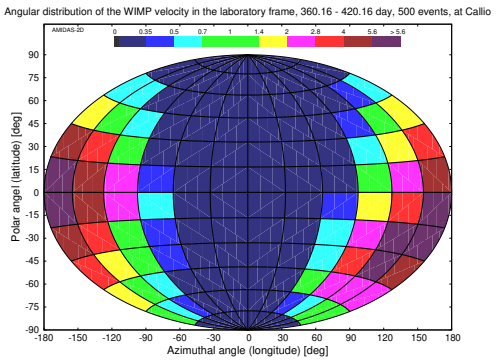

(e) 360.16 – 420.16 day, 22 – 2 hour

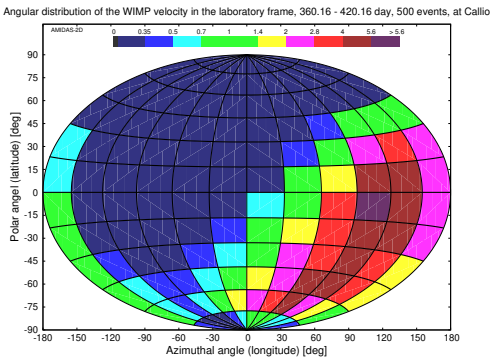

(f) 360.16 – 420.16 day, 4 – 8 hour

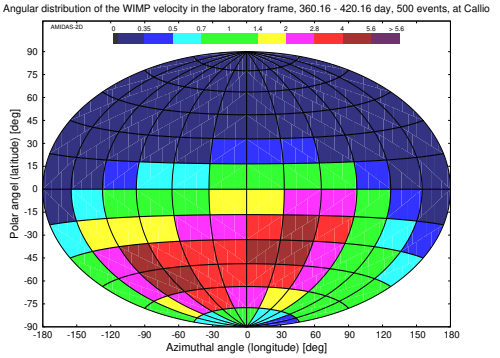

(g) 360.16 – 420.16 day, 10 – 14 hour

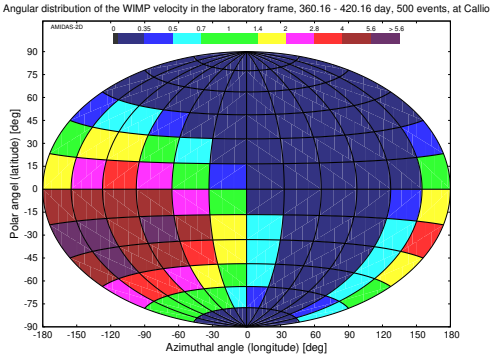

(h) 360.16 – 420.16 day, 16 – 20 hour

Figure A24: As in Figs. A23, except that 500 total events on average in each 4-hour daily shift in the 60-day observation periods have been simulated.

B.4 China Jinping Underground Laboratory (CJPL)

Central date (observation period) (day)	Most–event directions	
	50 events	500 events
0 – 365	—	—
49.49 (19.49 – 79.49)	60°S – 0° 60°E – 120°E	75°S – 15°N 60°E – 150°W
140.74 (110.74 – 170.74)	60°S – 0° 180° – 120°W	60°S – 0° 150°W – 90°W
231.99 (201.99 – 261.99)	30°S – 30°N 180° – 60°W	30°S – 30°N 150°E – 90°W
323.24 (293.24 – 353.24)	30°S – 30°N 120°E – 180°	45°S – 45°N 120°E – 150°W

Table A6: The summary of the directions of the simulated 3-D WIMP velocity with the highest event numbers ($>$ 4 times of the all–sky average value) in the horizontal coordinate system in one entire year and four advanced seasons at the location of the CJPL laboratory (28.15°N, 101.71°E). 50 and 500 total events on average in each observation period of 60 days have been simulated.

Remark: Fig. A26(b) shows that, with $\mathcal{O}(500)$ total WIMP events and a higher analysis resolution, the high–WIMP–flux bins in the angular distribution pattern in the horizontal coordinate system of the CJPL laboratory could spread towards the southeast pretty widely.

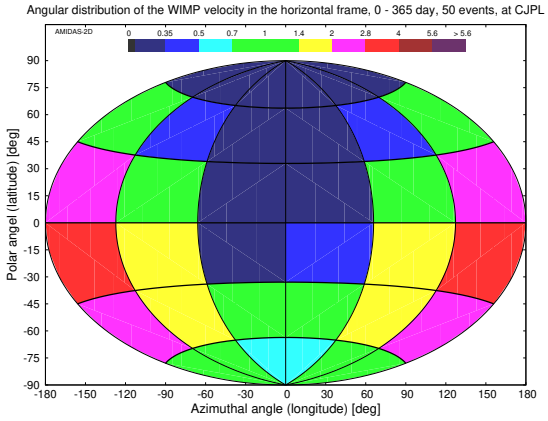

(a) 0 – 365 day

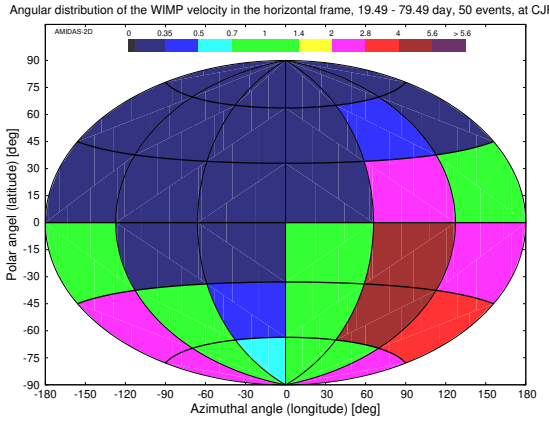

(b) 19.49 – 79.49 day

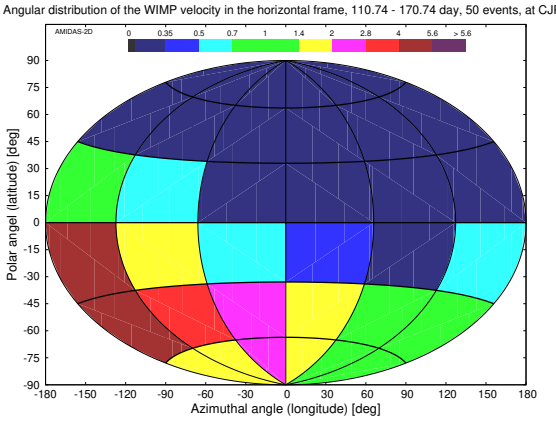

(c) 110.74 – 170.74 day

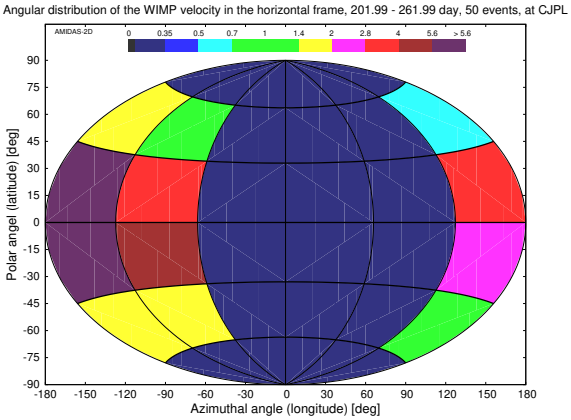

(d) 201.99 – 261.99 day

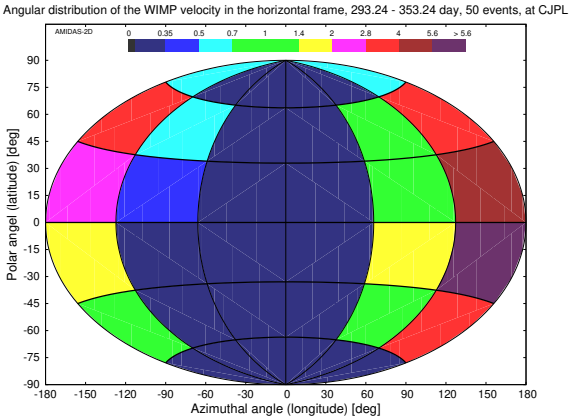

(e) 293.24 – 353.24 day

Figure A25: The angular distributions of the 3-D WIMP velocity in the horizontal coordinate system at the location of the CJPL laboratory (28.15°N, 101.71°E). 50 total events on average in one entire year (a) and in each 60-day observation period of four advanced seasons (b – e) have been simulated.

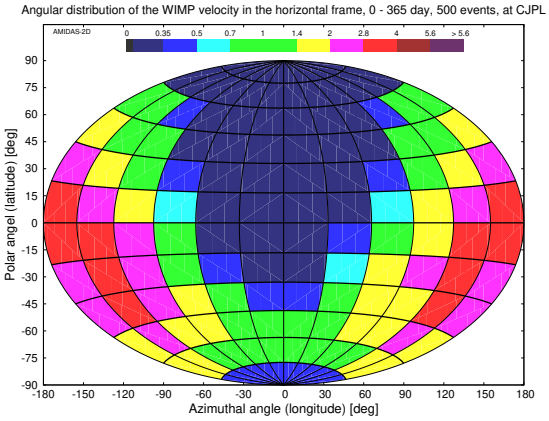

(a) 0 – 365 day

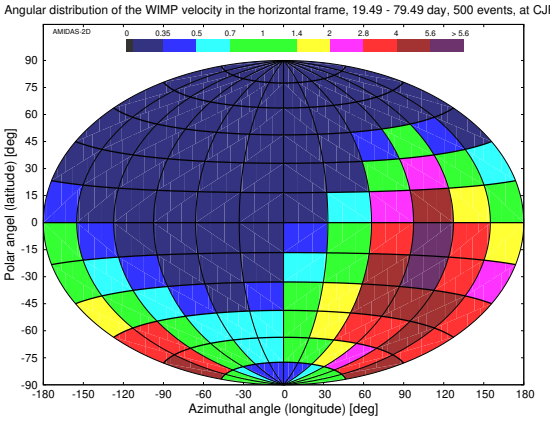

(b) 19.49 – 79.49 day

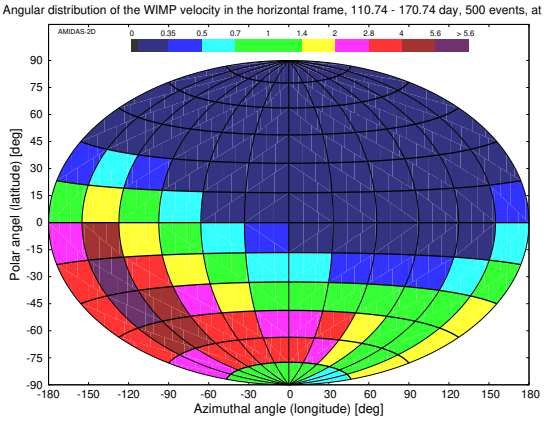

(c) 110.74 – 170.74 day

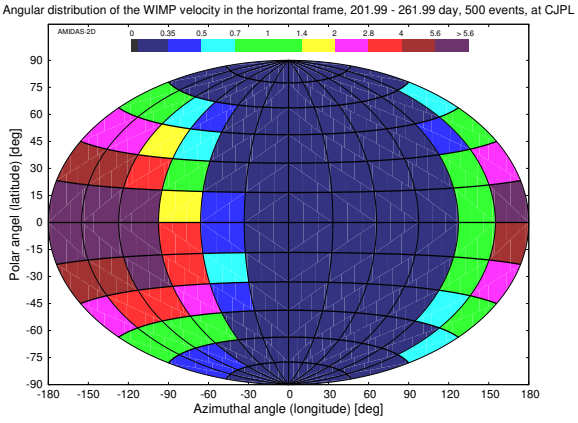

(d) 201.99 – 261.99 day

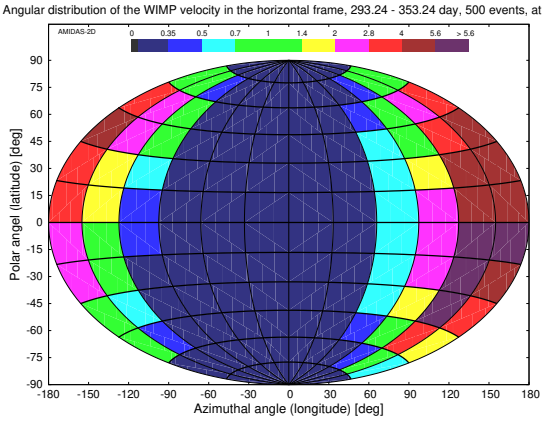

(e) 293.24 – 353.24 day

Figure A26: As in Figs. A25, except that 500 total events on average in one entire year (a) and in each 60-day observation period of four advanced seasons (b – e) have been simulated.

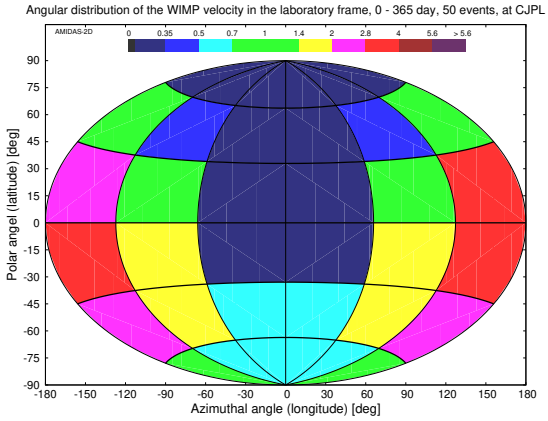

(a) 0 – 365 day

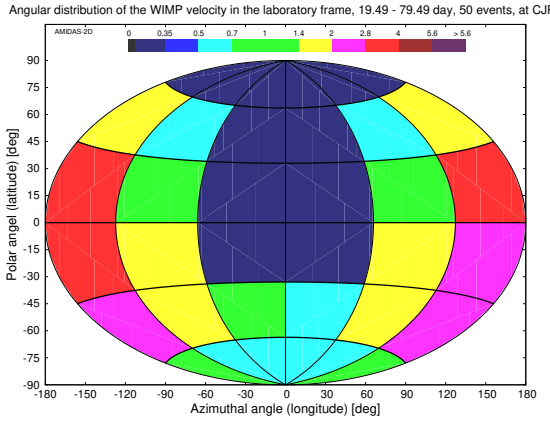

(b) 19.49 – 79.49 day

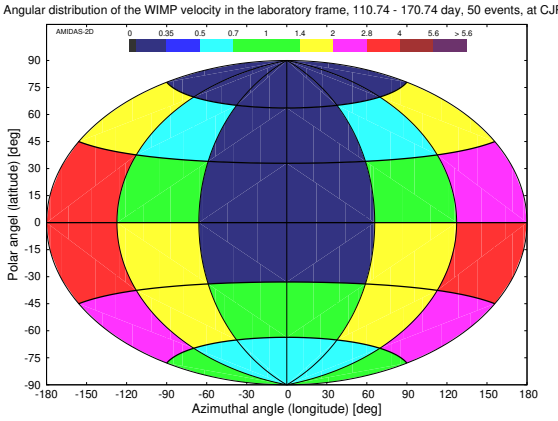

(c) 110.74 – 170.74 day

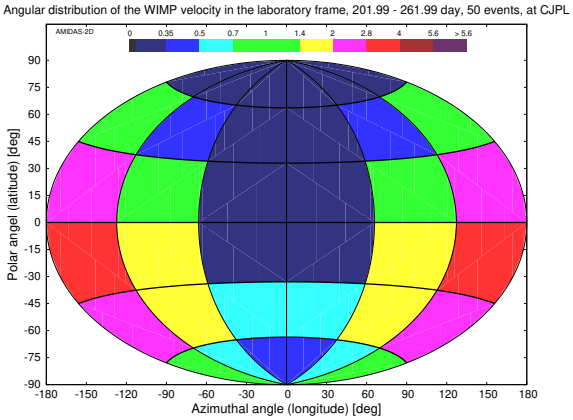

(d) 201.99 – 261.99 day

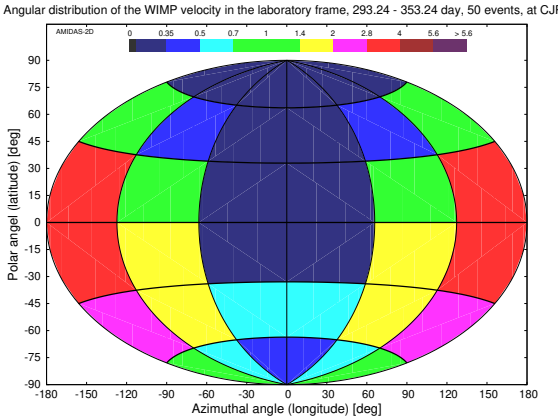

(e) 293.24 – 353.24 day

Figure A27: The angular distributions of the 3-D WIMP velocity transformed from events shown in Fig. A25 to the laboratory coordinate system at the location of the CJPL laboratory. All simulation setup and notations are the same as in Fig. A25.

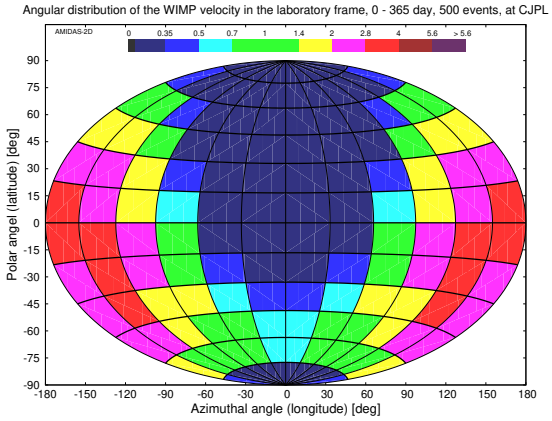

(a) 0 – 365 day

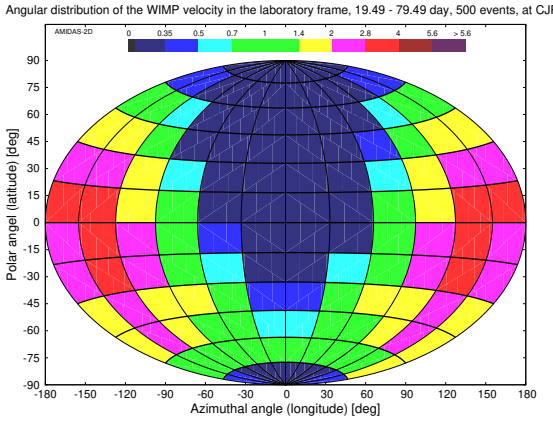

(b) 19.49 – 79.49 day

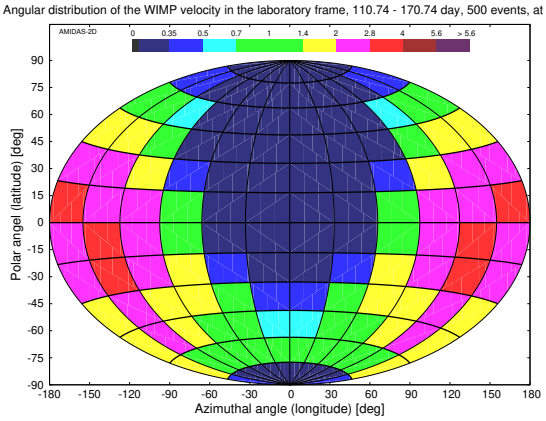

(c) 110.74 – 170.74 day

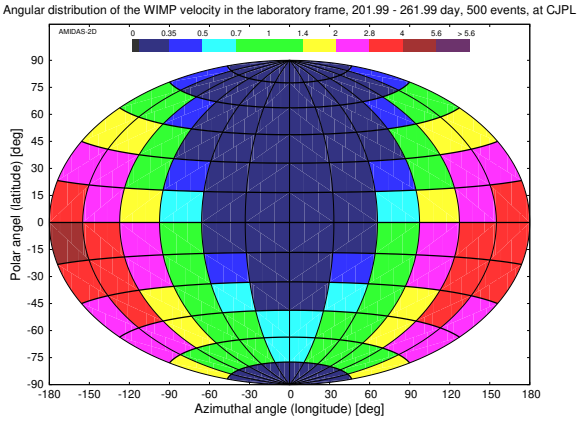

(d) 201.99 – 261.99 day

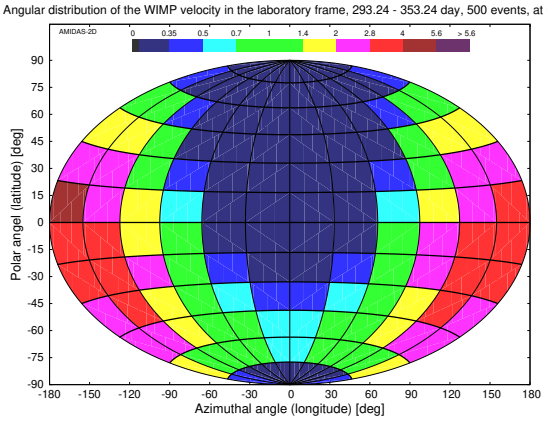

(e) 293.24 – 353.24 day

Figure A28: As in Figs. A27, except that 500 total events on average in one entire year (a) and in each 60-day observation period of four advanced seasons (b – e) have been simulated.

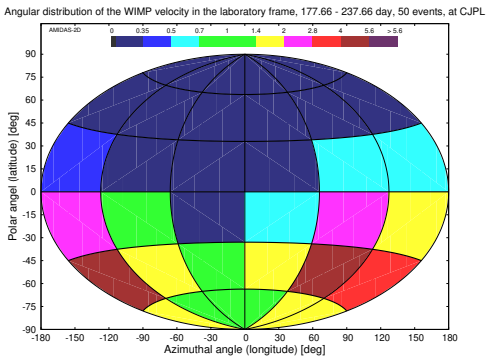

(a) 177.66 – 237.66 day, 22 – 2 hour

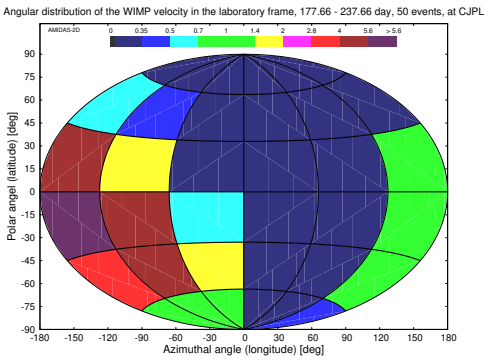

(b) 177.66 – 237.66 day, 4 – 8 hour

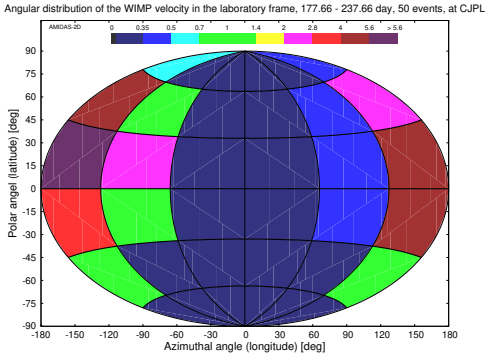

(c) 177.66 – 237.66 day, 10 – 14 hour

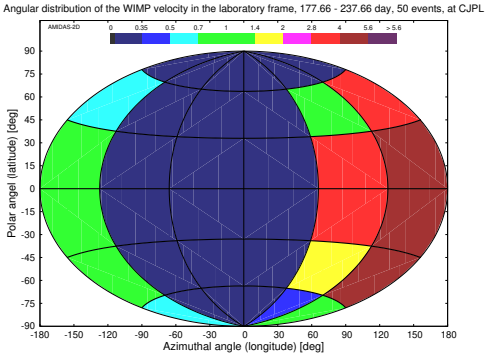

(d) 177.66 – 237.66 day, 16 – 20 hour

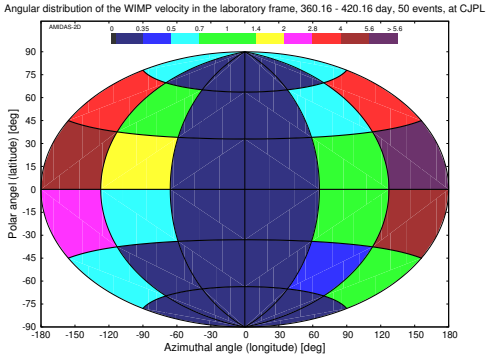

(e) 360.16 – 420.16 day, 22 – 2 hour

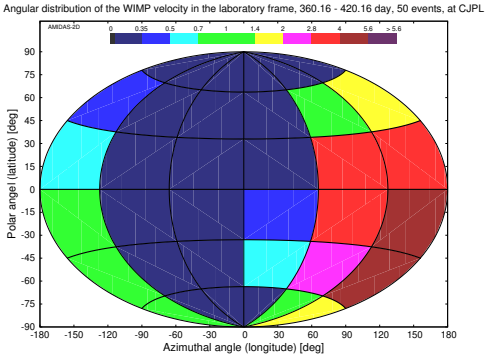

(f) 360.16 – 420.16 day, 4 – 8 hour

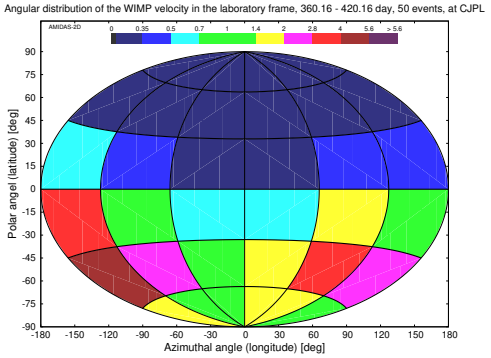

(g) 360.16 – 420.16 day, 10 – 14 hour

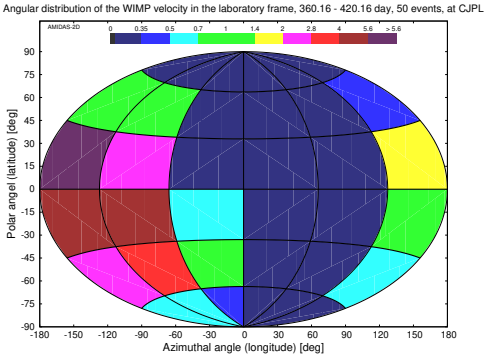

(h) 360.16 – 420.16 day, 16 – 20 hour

Figure A29: The angular distributions of the 3-D WIMP velocity observed at the location of the CJPL laboratory. 50 total events on average in each 4-hour daily shift in the 60-day observation periods of 177.66 – 237.66 day (a – d) and 360.16 – 420.16 (= 55.16) day (e – h) have been simulated.

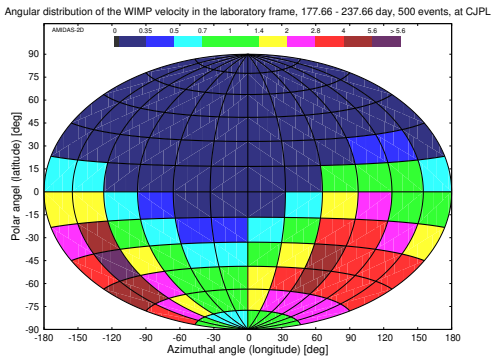

(a) 177.66 – 237.66 day, 22 – 2 hour

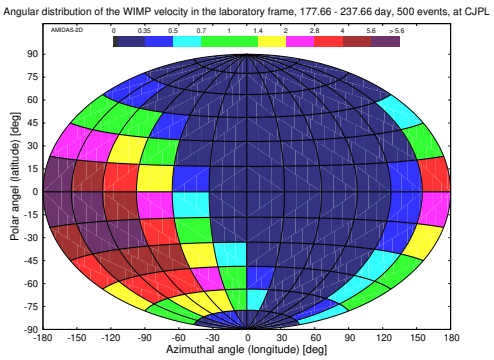

(b) 177.66 – 237.66 day, 4 – 8 hour

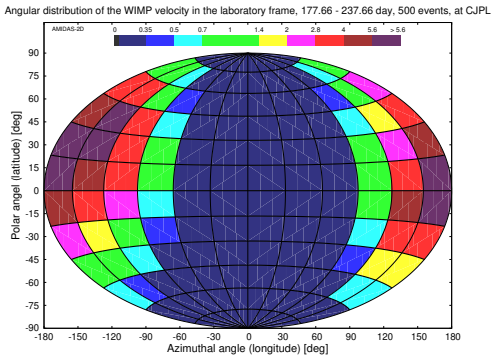

(c) 177.66 – 237.66 day, 10 – 14 hour

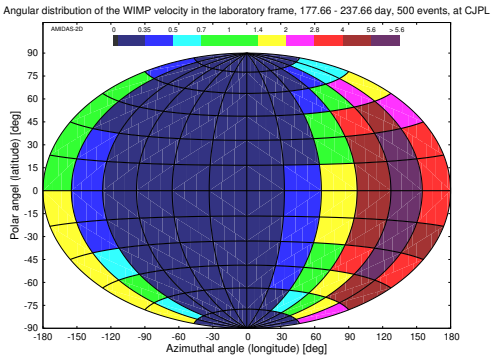

(d) 177.66 – 237.66 day, 16 – 20 hour

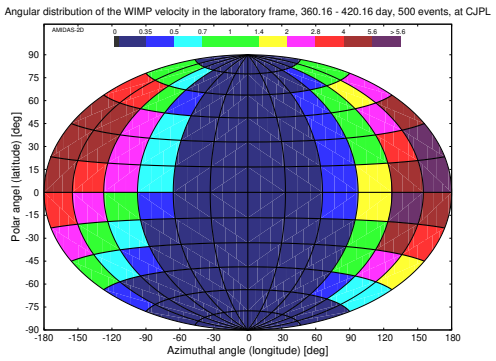

(e) 360.16 – 420.16 day, 22 – 2 hour

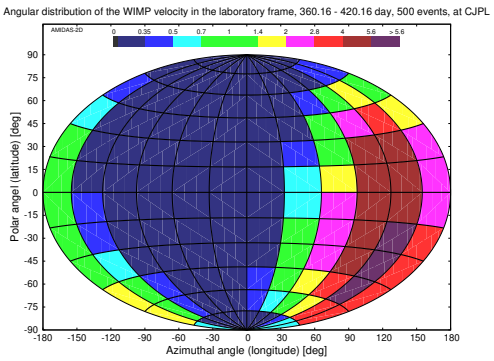

(f) 360.16 – 420.16 day, 4 – 8 hour

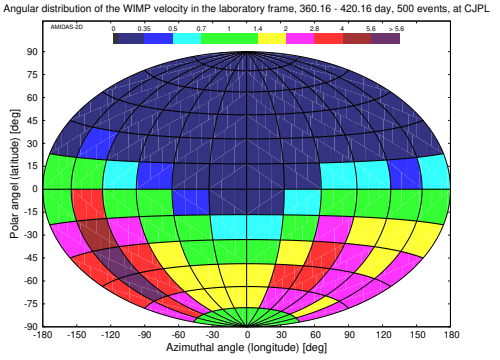

(g) 360.16 – 420.16 day, 10 – 14 hour

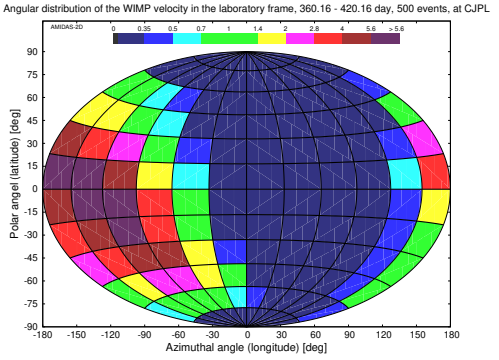

(h) 360.16 – 420.16 day, 16 – 20 hour

Figure A30: As in Figs. A29, except that 500 total events on average in each 4-hour daily shift in the 60-day observation periods have been simulated.

B.5 Deep Underground Science and Engineering Laboratory (DUSEL)

Central date (observation period) (day)	Most–event directions	
	50 events	500 events
0 – 365	—	15°S – 0° 150°E – 150°W
49.49 (19.49 – 79.49)	30°S – 30°N 180° – 60°W	$\underline{\underline{45°S}}$ – 15°N 180° – 60°W
140.74 (110.74 – 170.74)	30°S – 30°N 120°E – 120°W	30°S – $\underline{\underline{45°N}}$ 120°E – 120°W
231.99 (201.99 – 261.99)	60°S – 0° 60°E – 180°	$\underline{\underline{75°S}}$ – $\underline{\underline{30°N}}$ 90°E – 150°E
323.24 (293.24 – 353.24)	60°S – 30°S 180° – 120°W	60°S – $\underline{\underline{15°S}}$ 150°W – 120°W

Table A7: The summary of the directions of the simulated 3-D WIMP velocity with the highest event numbers ($>$ 4 times of the all–sky average value) in the horizontal coordinate system in one entire year and four advanced seasons at the location of the DUSEL laboratory (44.35°N, 103.75°W). 50 and 500 total events on average in each observation period of 60 days have been simulated.

Remark: although due to the Earth's orbital motion around the Sun and thus the horizontal coordinate system rotates daily, by using data recorded in one entire year, the angular distribution of the 3-D WIMP velocity spreads out latitudinally and the anisotropy of the incident direction of Galactic WIMPs of the main direction of the WIMP wind would be in principle averaged out, in Fig. A32(a) one can (unexpectedly) find that, with $\mathcal{O}(500)$ total WIMP events and a higher analysis resolution, clear high–WIMP–flux bins from 15°S to 0° and 150°E to 150°W could be identified in the angular distribution pattern in the horizontal coordinate system of the DUSEL laboratory.

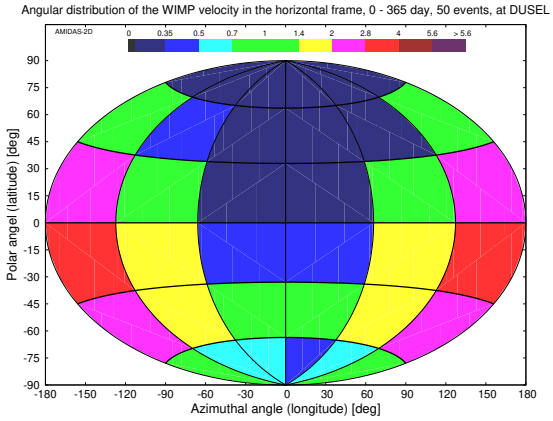

(a) 0 – 365 day

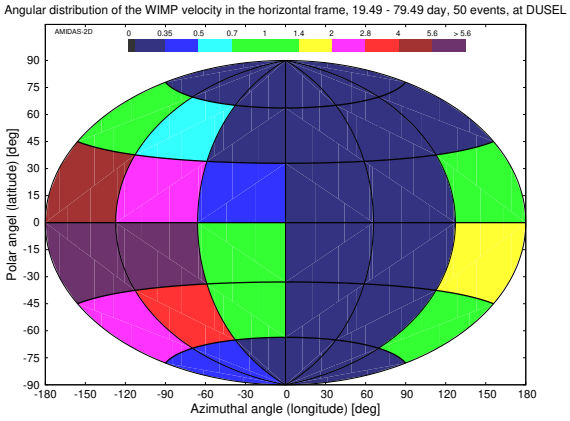

(b) 19.49 – 79.49 day

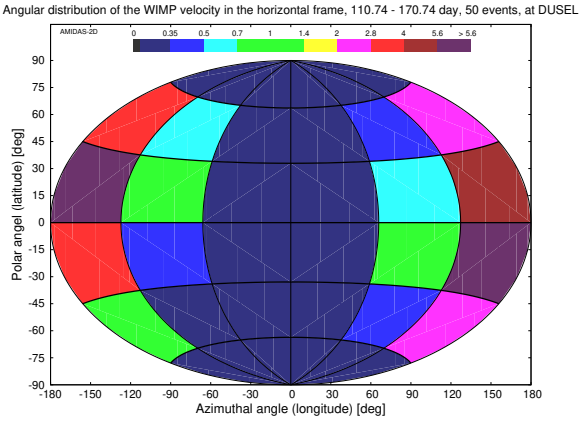

(c) 110.74 – 170.74 day

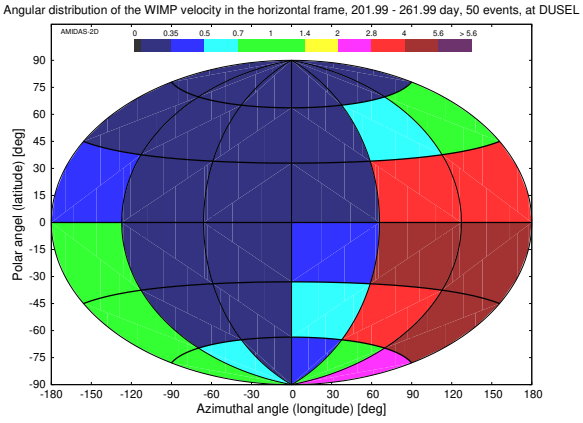

(d) 201.99 – 261.99 day

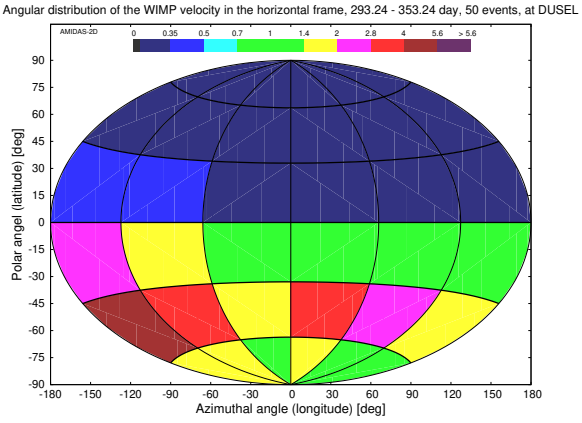

(e) 293.24 – 353.24 day

Figure A31: The angular distributions of the 3-D WIMP velocity in the horizontal coordinate system at the location of the DUSEL laboratory (44.35°N, 103.75°W). 50 total events on average in one entire year (a) and in each 60-day observation period of four advanced seasons (b – e) have been simulated.

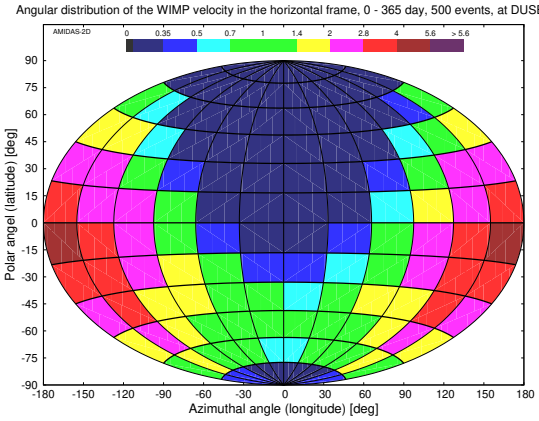

(a) 0 – 365 day

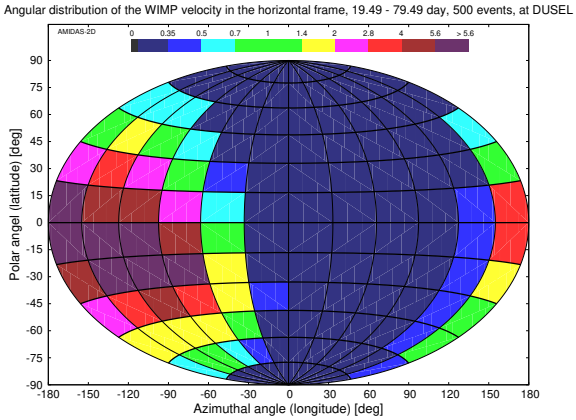

(b) 19.49 – 79.49 day

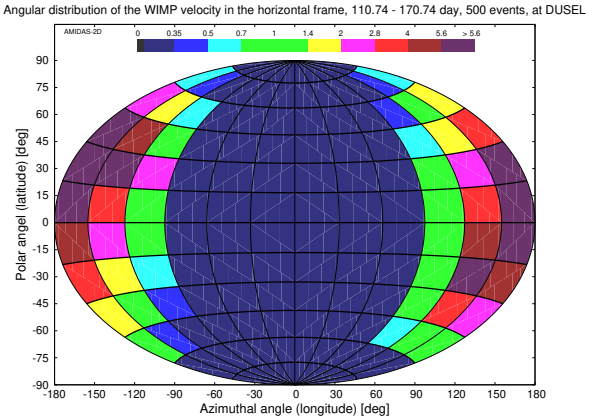

(c) 110.74 – 170.74 day

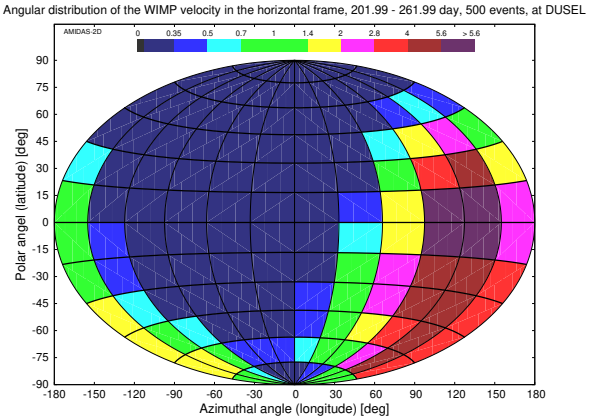

(d) 201.99 – 261.99 day

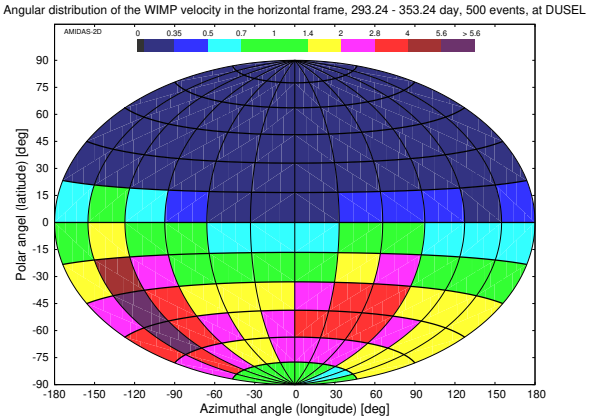

(e) 293.24 – 353.24 day

Figure A32: As in Figs. A31, except that 500 total events on average in one entire year (a) and in each 60-day observation period of four advanced seasons (b – e) have been simulated.

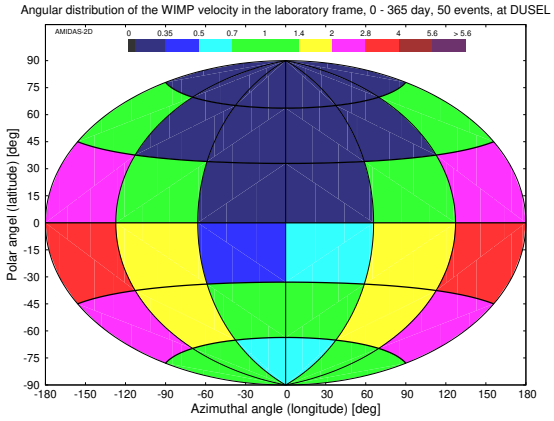

(a) 0 – 365 day

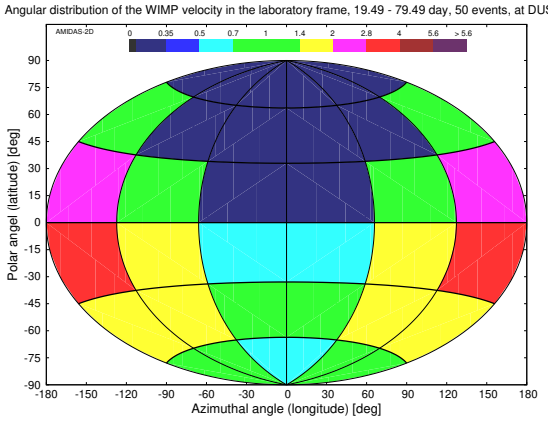

(b) 19.49 – 79.49 day

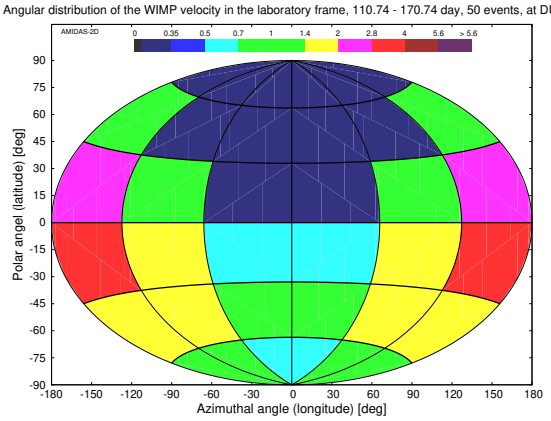

(c) 110.74 – 170.74 day

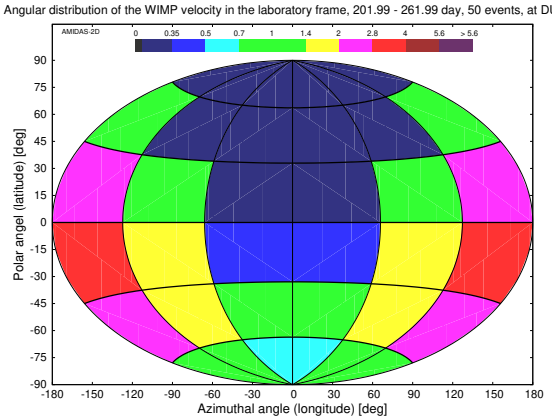

(d) 201.99 – 261.99 day

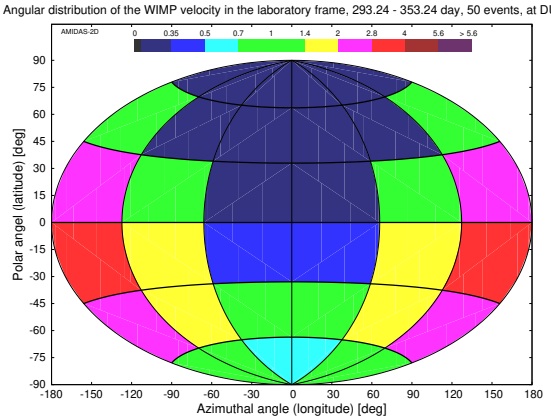

(e) 293.24 – 353.24 day

Figure A33: The angular distributions of the 3-D WIMP velocity transformed from events shown in Fig. A31 to the laboratory coordinate system at the location of the DUSEL laboratory. All simulation setup and notations are the same as in Fig. A31.

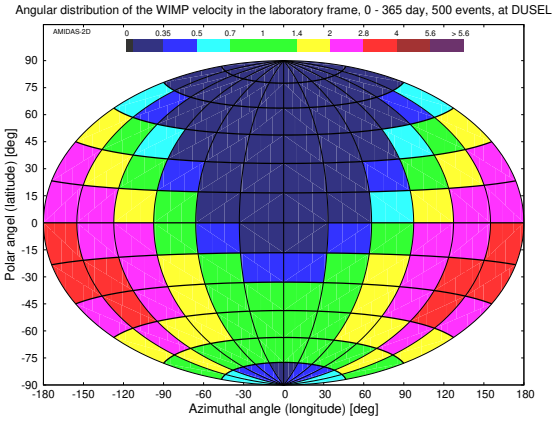

(a) 0 – 365 day

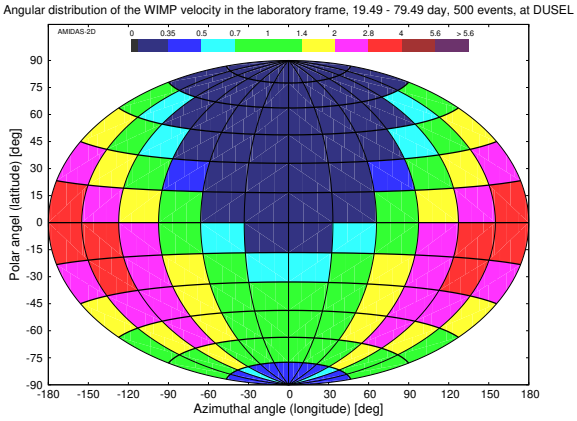

(b) 19.49 – 79.49 day

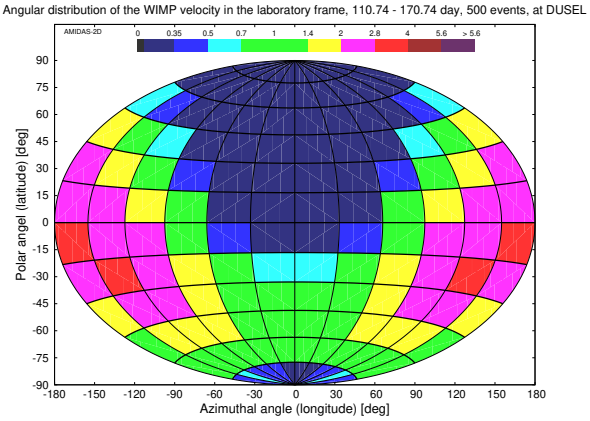

(c) 110.74 – 170.74 day

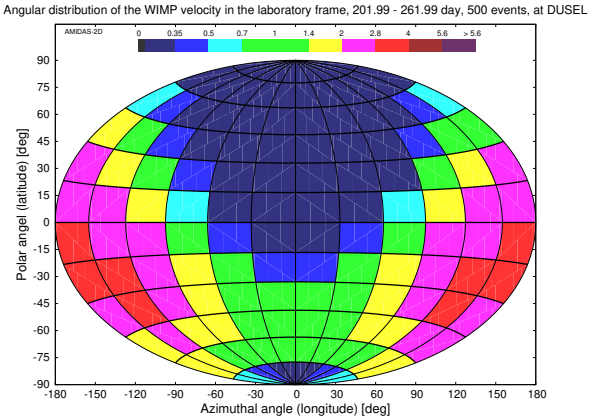

(d) 201.99 – 261.99 day

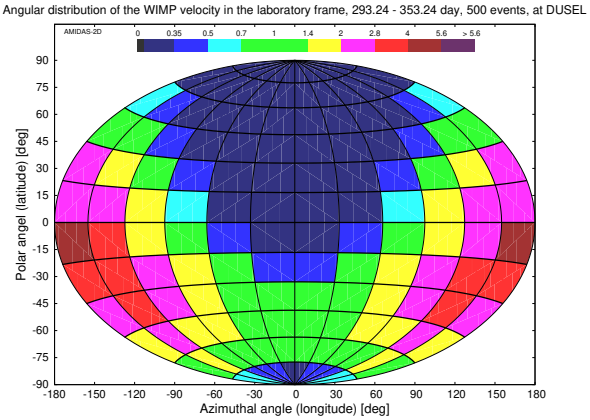

(e) 293.24 – 353.24 day

Figure A34: As in Figs. A33, except that 500 total events on average in one entire year (a) and in each 60-day observation period of four advanced seasons (b – e) have been simulated.

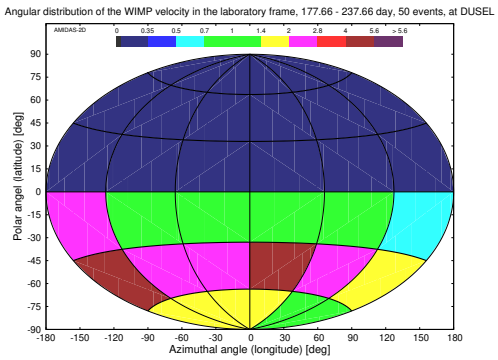

(a) 177.66 – 237.66 day, 22 – 2 hour

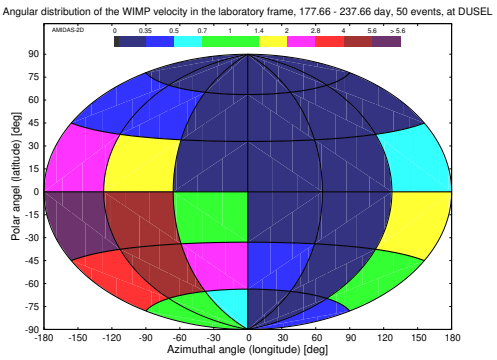

(b) 177.66 – 237.66 day, 4 – 8 hour

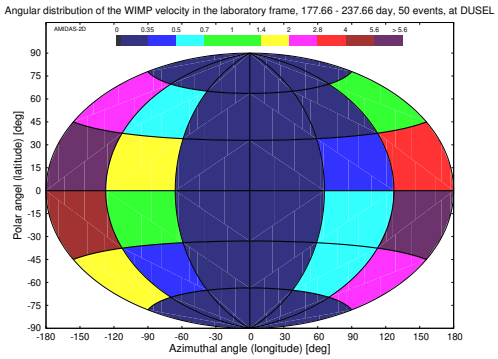

(c) 177.66 – 237.66 day, 10 – 14 hour

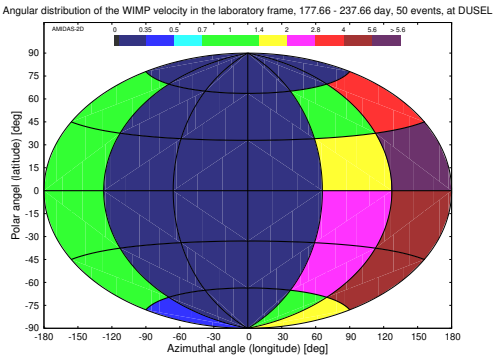

(d) 177.66 – 237.66 day, 16 – 20 hour

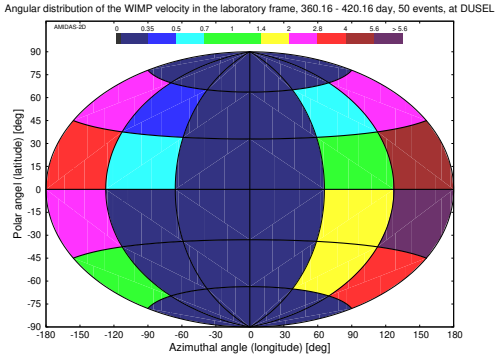

(e) 360.16 – 420.16 day, 22 – 2 hour

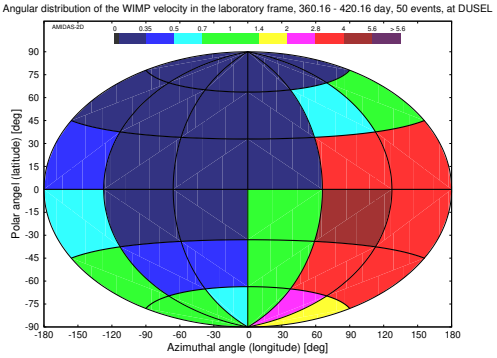

(f) 360.16 – 420.16 day, 4 – 8 hour

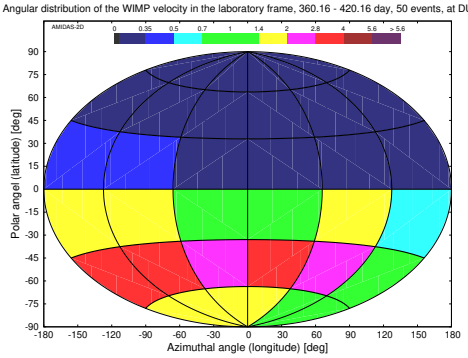

(g) 360.16 – 420.16 day, 10 – 14 hour

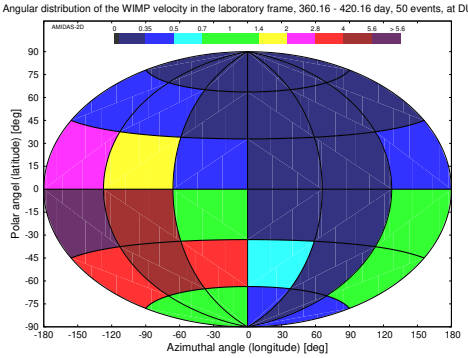

(h) 360.16 – 420.16 day, 16 – 20 hour

Figure A35: The angular distributions of the 3-D WIMP velocity observed at the location of the DUSEL laboratory. 50 total events on average in each 4-hour daily shift in the 60-day observation periods of 177.66 – 237.66 day (a – d) and 360.16 – 420.16 (= 55.16) day (e – h) have been simulated.

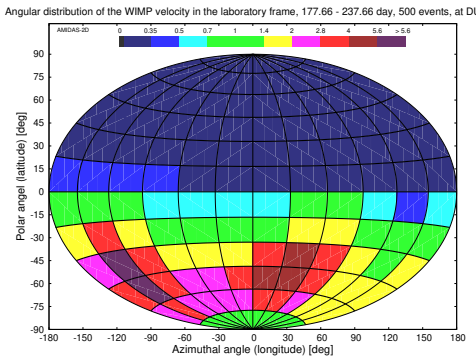

(a) 177.66 – 237.66 day, 22 – 2 hour

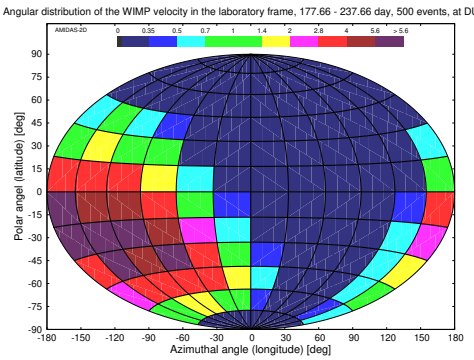

(b) 177.66 – 237.66 day, 4 – 8 hour

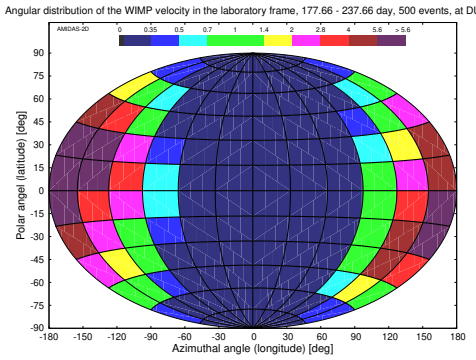

(c) 177.66 – 237.66 day, 10 – 14 hour

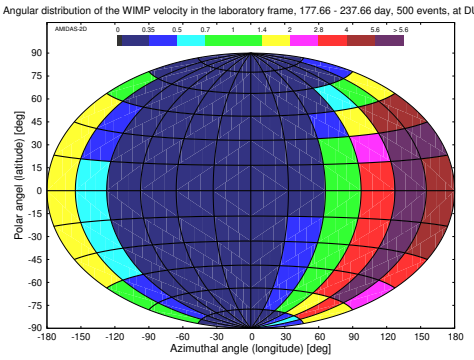

(d) 177.66 – 237.66 day, 16 – 20 hour

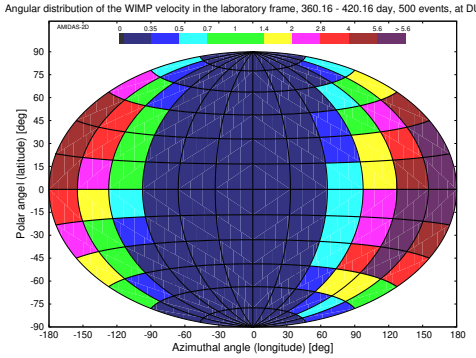

(e) 360.16 – 420.16 day, 22 – 2 hour

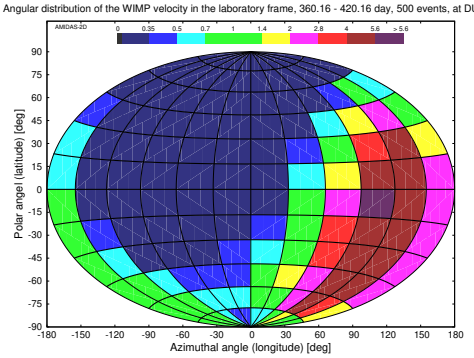

(f) 360.16 – 420.16 day, 4 – 8 hour

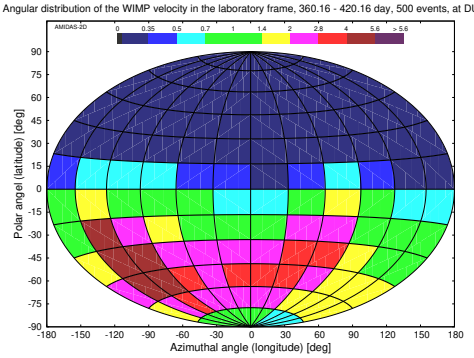

(g) 360.16 – 420.16 day, 10 – 14 hour

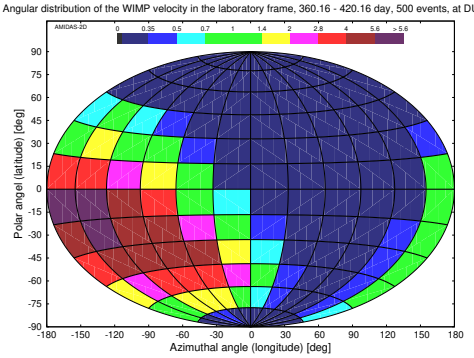

(h) 360.16 – 420.16 day, 16 – 20 hour

Figure A36: As in Figs. A35, except that 500 total events on average in each 4-hour daily shift in the 60-day observation periods have been simulated.

B.6 Kamioka Observatory

Central date (observation period) (day)	Most–event directions	
	50 events	500 events
0 – 365	—	—
49.49 (19.49 – 79.49)	60°S – 30°S 60°E – 120°E	75°S – 30°S, 150°W – 90°W 60°S – 15°S, 30°E – 90°E
140.74 (110.74 – 170.74)	60°S – 0° 180° – 60°W	60°S – 0° 180° – 30°W
231.99 (201.99 – 261.99)	30°S – 30°N 120°E – 120°W	30°S – 30°N 150°E – 90°W
323.24 (293.24 – 353.24)	60°S – 30°N 120°E – 180°	60°S – 45°N 120°E – 180°

Table A8: The summary of the directions of the simulated 3-D WIMP velocity with the highest event numbers ($>$ 4 times of the all–sky average value) in the horizontal coordinate system in one entire year and four advanced seasons at the location of the Kamioka laboratory (36.43°N, 137.31°E). 50 and 500 total events on average in each observation period of 60 days have been simulated.

Remark: as at the ANDES laboratory, in Fig. A38(b) one can find clearly that, with $\mathcal{O}(500)$ total WIMP events and a higher analysis resolution, a second "hot–point" from 75°S to 30°S, and 150°W to 90°W in the angular distribution pattern in the horizontal coordinate system would also be observed at the Kamioka laboratory.

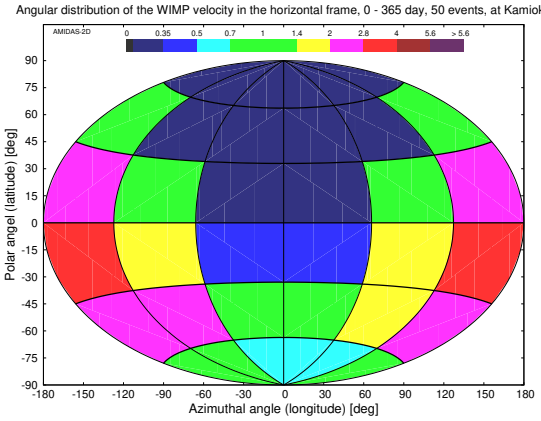

(a) 0 – 365 day

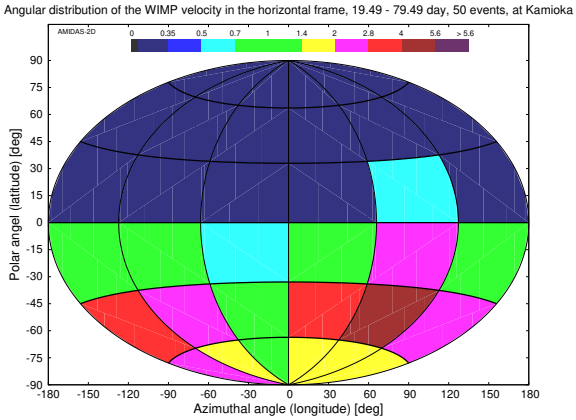

(b) 19.49 – 79.49 day

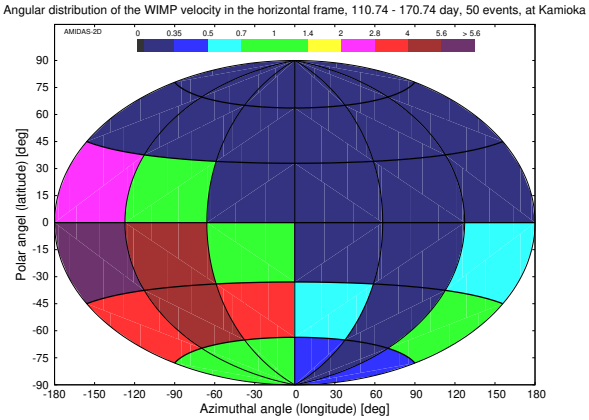

(c) 110.74 – 170.74 day

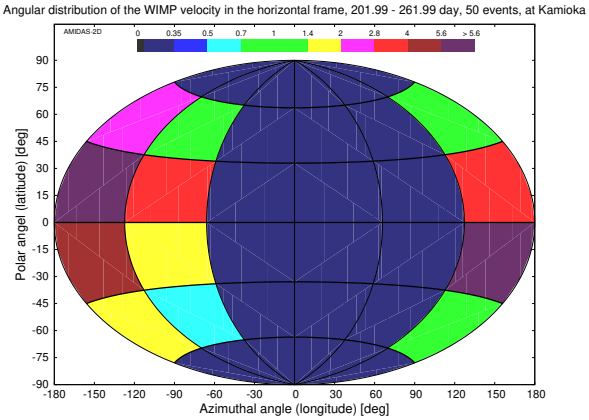

(d) 201.99 – 261.99 day

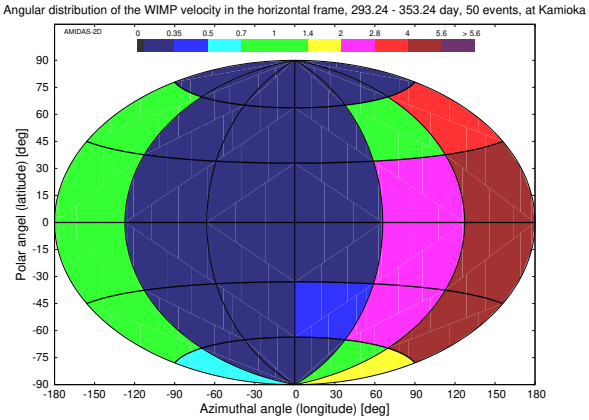

(e) 293.24 – 353.24 day

Figure A37: The angular distributions of the 3-D WIMP velocity in the horizontal coordinate system at the location of the Kamioka laboratory (36.43°N, 137.31°E). 50 total events on average in one entire year (a) and in each 60-day observation period of four advanced seasons (b – e) have been simulated.

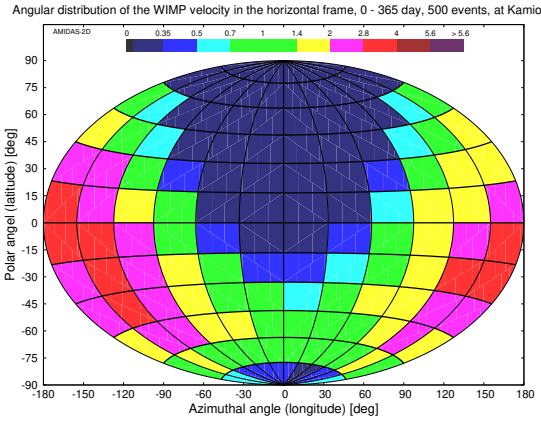

(a) 0 – 365 day

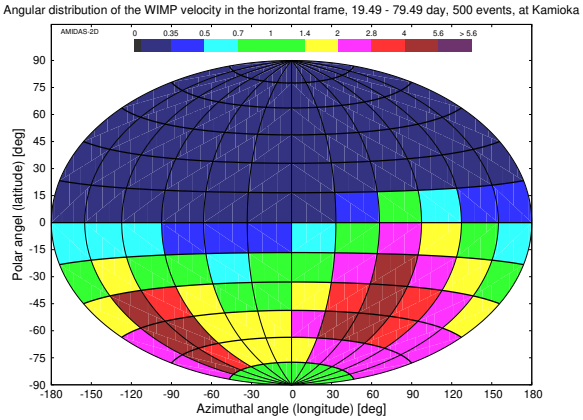

(b) 19.49 – 79.49 day

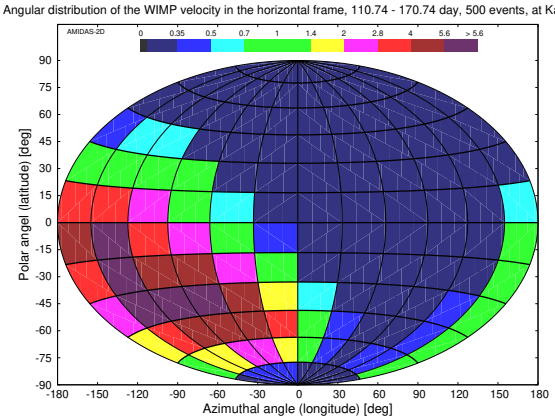

(c) 110.74 – 170.74 day

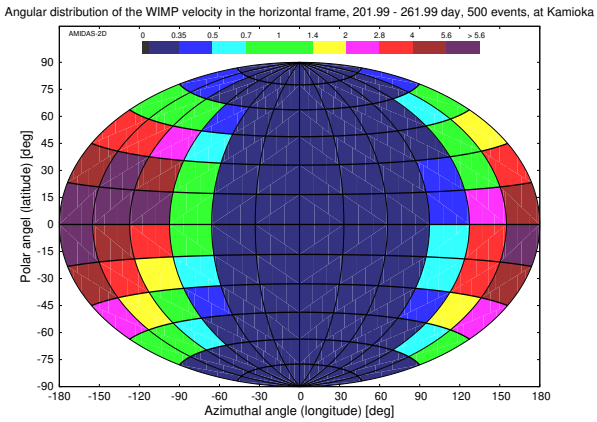

(d) 201.99 – 261.99 day

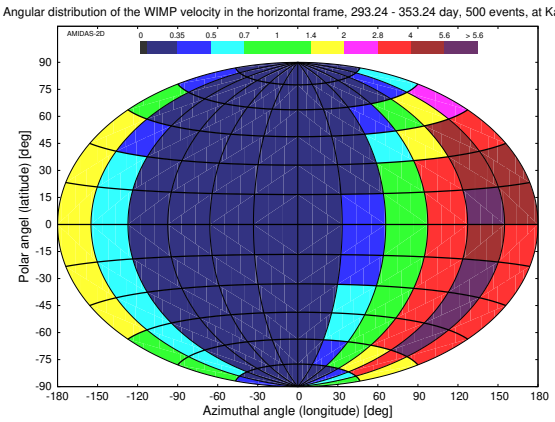

(e) 293.24 – 353.24 day

Figure A38: As in Figs. A37, except that 500 total events on average in one entire year (a) and in each 60-day observation period of four advanced seasons (b – e) have been simulated.

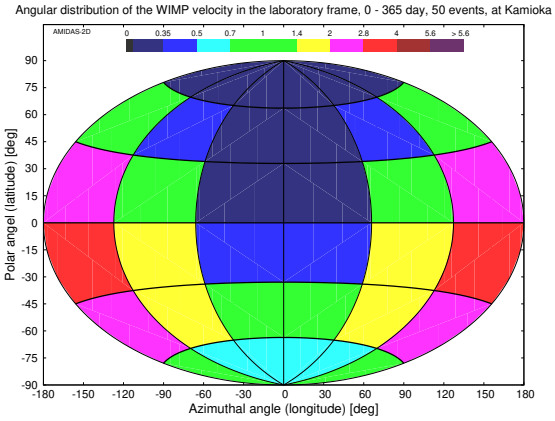

(a) 0 – 365 day

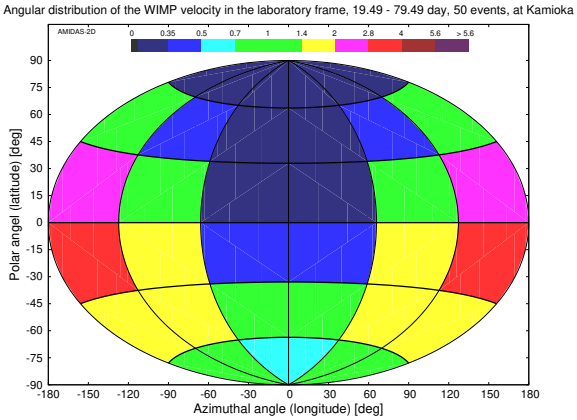

(b) 19.49 – 79.49 day

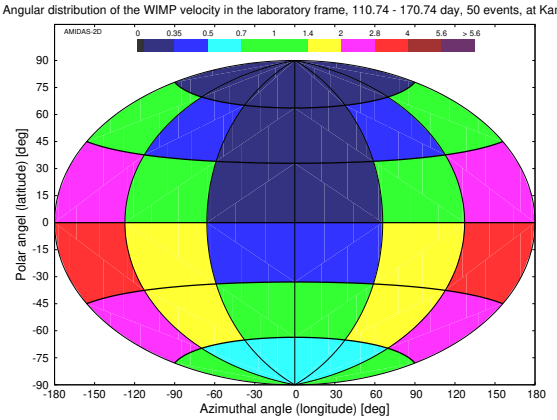

(c) 110.74 – 170.74 day

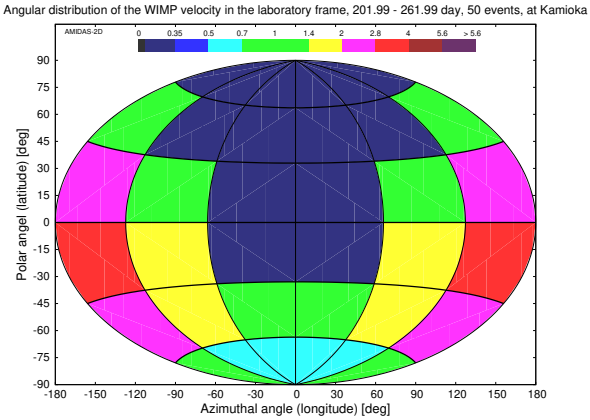

(d) 201.99 – 261.99 day

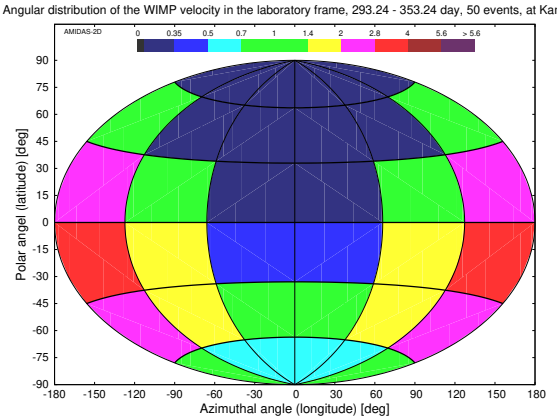

(e) 293.24 – 353.24 day

Figure A39: The angular distributions of the 3-D WIMP velocity transformed from events shown in Fig. A37 to the laboratory coordinate system at the location of the Kamioka laboratory. All simulation setup and notations are the same as in Fig. A37.

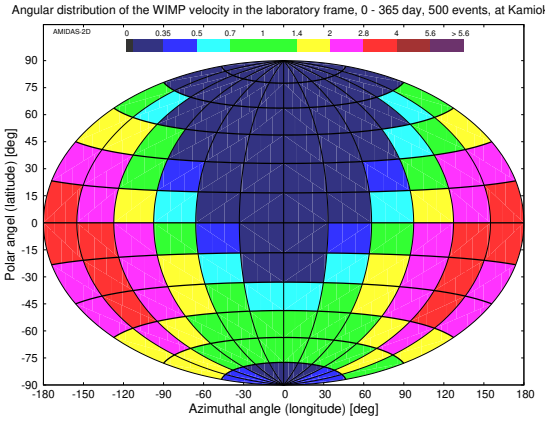

(a) 0 – 365 day

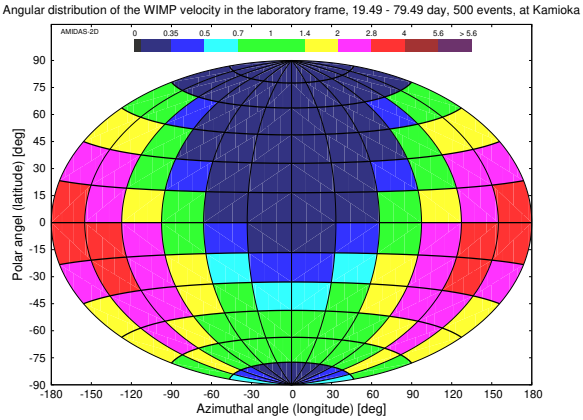

(b) 19.49 – 79.49 day

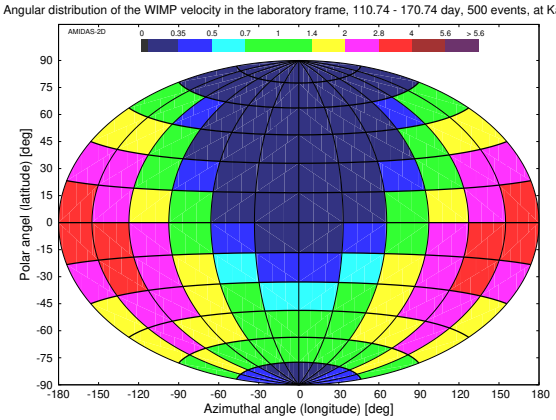

(c) 110.74 – 170.74 day

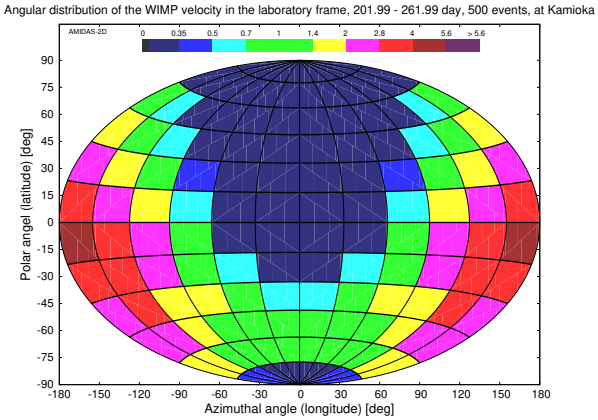

(d) 201.99 – 261.99 day

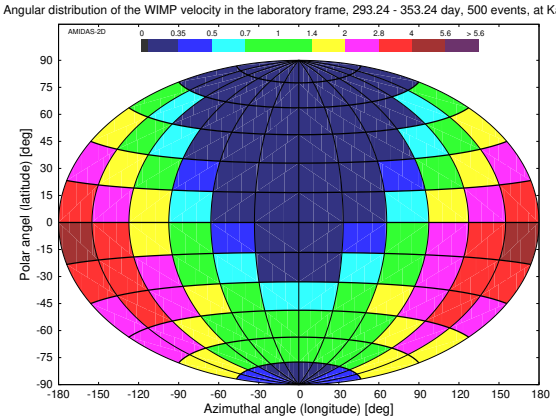

(e) 293.24 – 353.24 day

Figure A40: As in Figs. A39, except that 500 total events on average in one entire year (a) and in each 60-day observation period of four advanced seasons (b – e) have been simulated.

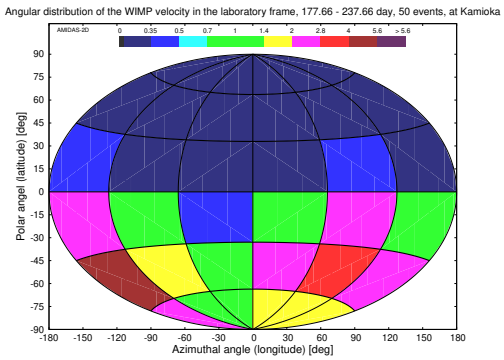

(a) 177.66 – 237.66 day, 22 – 2 hour

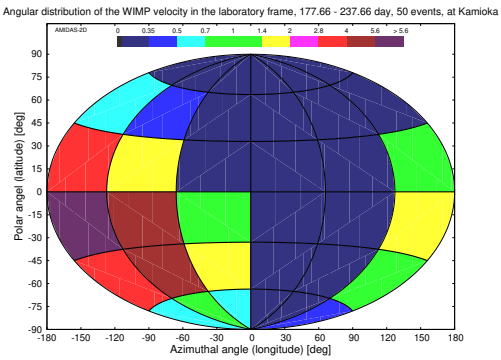

(b) 177.66 – 237.66 day, 4 – 8 hour

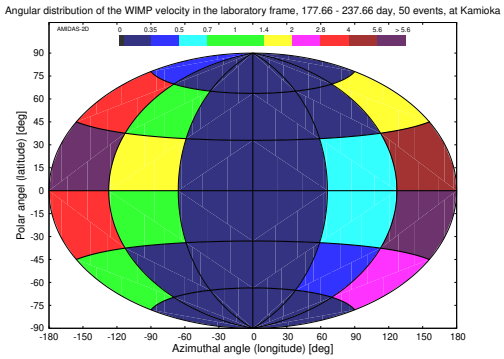

(c) 177.66 – 237.66 day, 10 – 14 hour

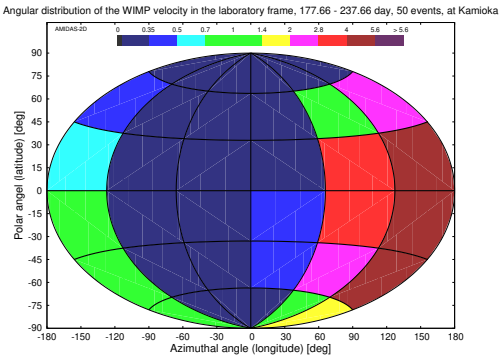

(d) 177.66 – 237.66 day, 16 – 20 hour

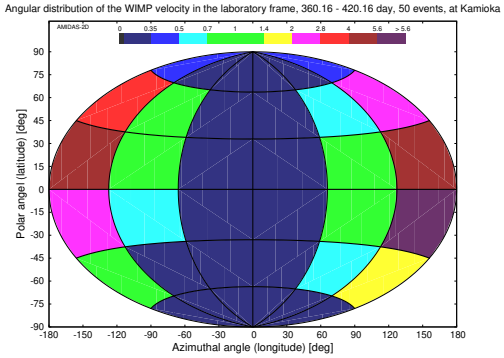

(e) 360.16 – 420.16 day, 22 – 2 hour

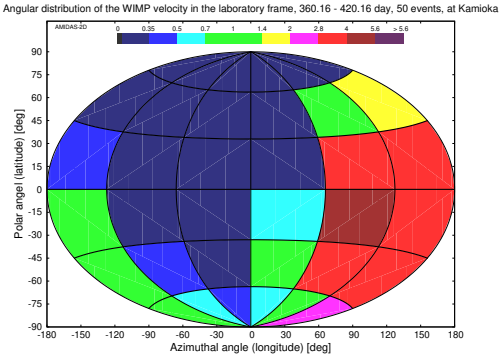

(f) 360.16 – 420.16 day, 4 – 8 hour

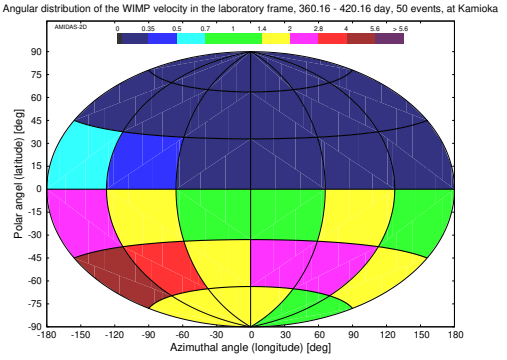

(g) 360.16 – 420.16 day, 10 – 14 hour

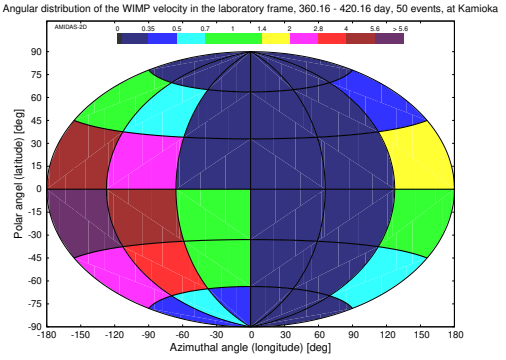

(h) 360.16 – 420.16 day, 16 – 20 hour

Figure A41: The angular distributions of the 3-D WIMP velocity observed at the location of the Kamioka laboratory. 50 total events on average in each 4-hour daily shift in the 60-day observation periods of 177.66 – 237.66 day (a – d) and 360.16 – 420.16 (= 55.16) day (e – h) have been simulated.

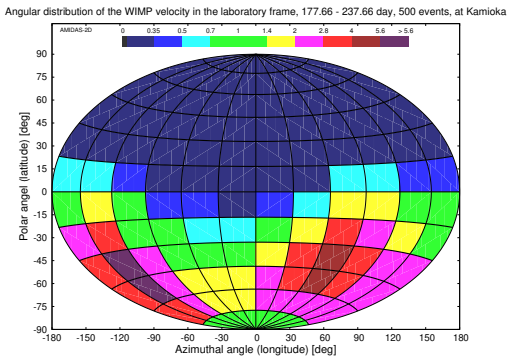

(a) 177.66 – 237.66 day, 22 – 2 hour

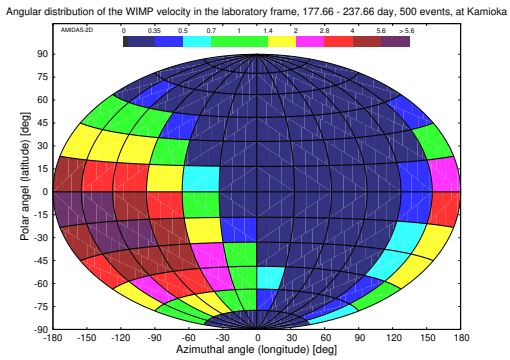

(b) 177.66 – 237.66 day, 4 – 8 hour

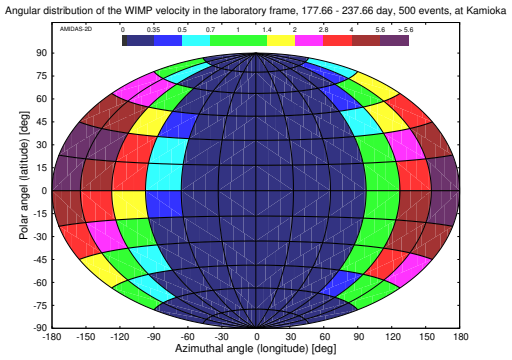

(c) 177.66 – 237.66 day, 10 – 14 hour

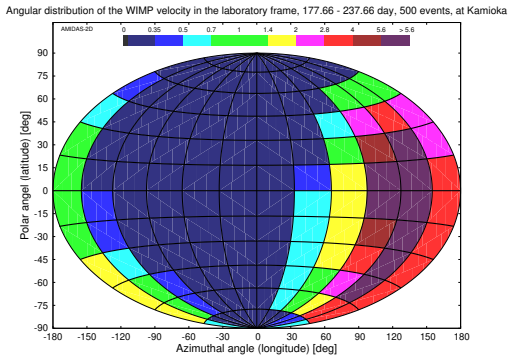

(d) 177.66 – 237.66 day, 16 – 20 hour

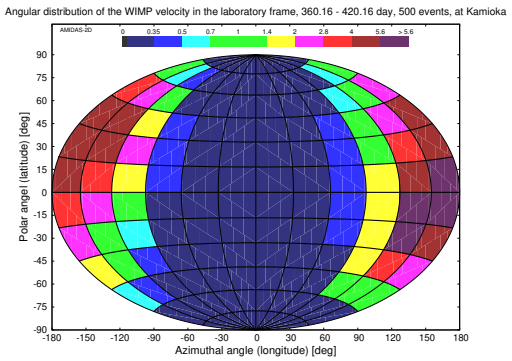

(e) 360.16 – 420.16 day, 22 – 2 hour

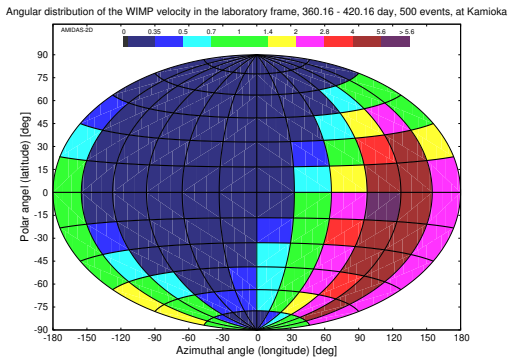

(f) 360.16 – 420.16 day, 4 – 8 hour

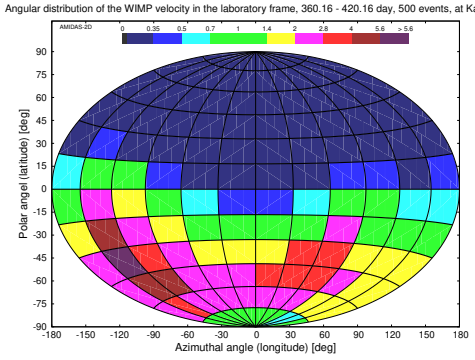

(g) 360.16 – 420.16 day, 10 – 14 hour

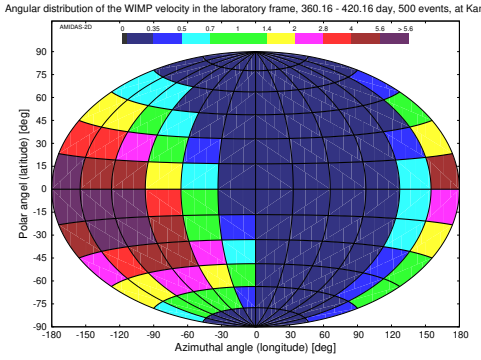

(h) 360.16 – 420.16 day, 16 – 20 hour

Figure A42: As in Figs. A41, except that 500 total events on average in each 4-hour daily shift in the 60-day observation periods have been simulated.

B.7 Laboratori Nazionali del Gran Sasso (LNGS)

Central date (observation period) (day)	Most–event directions	
	50 events	500 events
0 – 365	—	—
49.49 (19.49 – 79.49)	30°S – 30°N 120°E – 180°	45°S – 45°N 90°E – 180°
140.74 (110.74 – 170.74)	60°S – 0° 60°E – 120°E	60°S – 15°N 60°E – 120°E
231.99 (201.99 – 261.99)	60°S – 30°S 180° – 120°W	60°S – 15°S, 150°W – 120°W 60°S – 45°S, 30°W – 30°E
323.24 (293.24 – 353.24)	30°S – 30°N 120°E – 60°W	30°S – 15°N 150°E – 90°W

Table A9: The summary of the directions of the simulated 3-D WIMP velocity with the highest event numbers ($>$ 4 times of the all–sky average value) in the horizontal coordinate system in one entire year and four advanced seasons at the location of the LNGS laboratory (42.45°N, 13.58°E). 50 and 500 total events on average in each observation period of 60 days have been simulated.

Remark: as at the ANDES and the Kamioka laboratories, in Fig. A44(d) one could also find clearly a second "hot–point" from 60°S to 45°S, and 30°W to 30°E in the angular distribution pattern in the horizontal coordinate system of the LNGS laboratory.

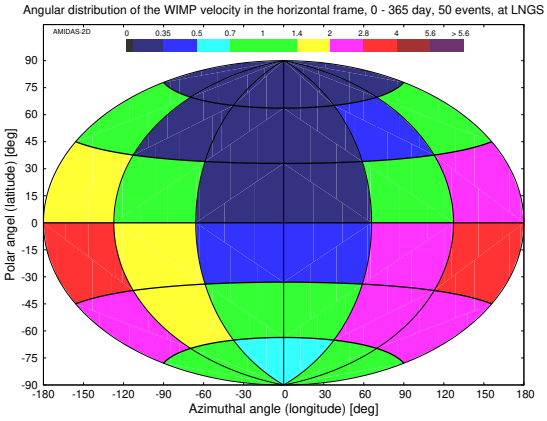

(a) 0 – 365 day

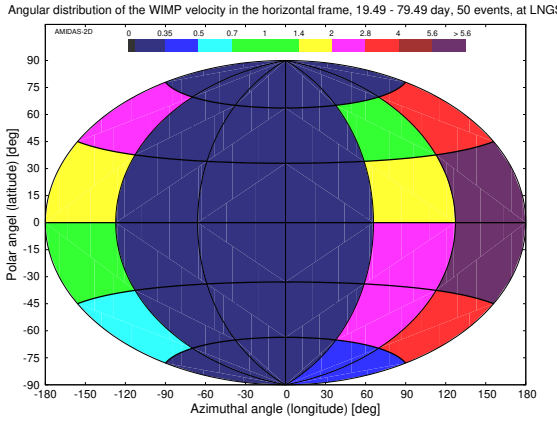

(b) 19.49 – 79.49 day

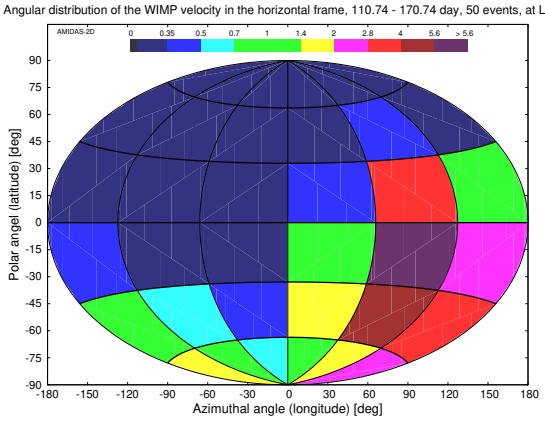

(c) 110.74 – 170.74 day

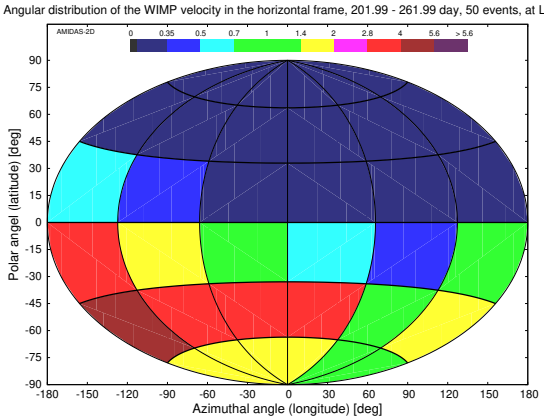

(d) 201.99 – 261.99 day

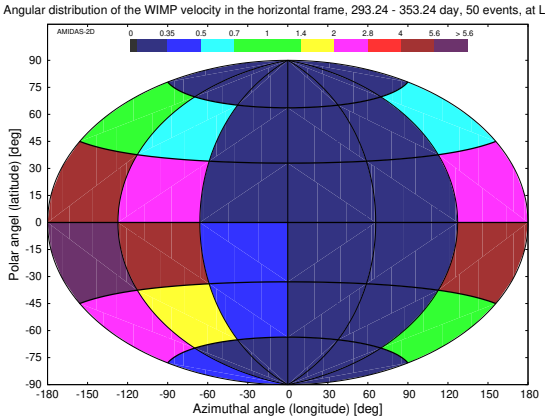

(e) 293.24 – 353.24 day

Figure A43: The angular distributions of the 3-D WIMP velocity in the horizontal coordinate system at the location of the LNGS laboratory (42.45°N, 13.58°E). 50 total events on average in one entire year (a) and in each 60-day observation period of four advanced seasons (b – e) have been simulated.

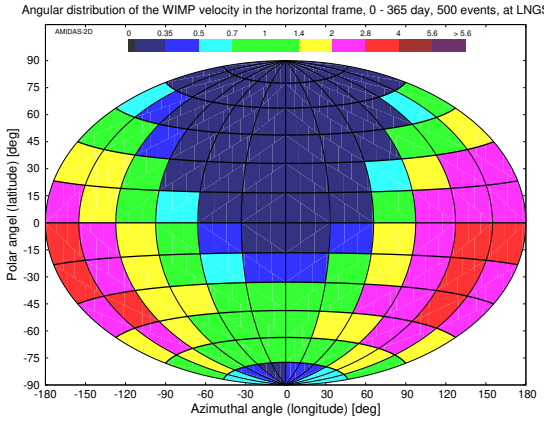

(a) 0 – 365 day

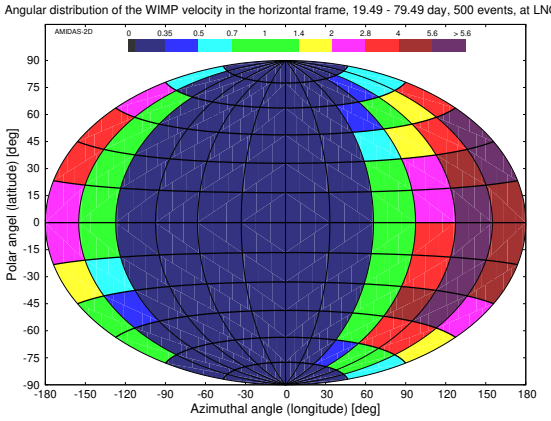

(b) 19.49 – 79.49 day

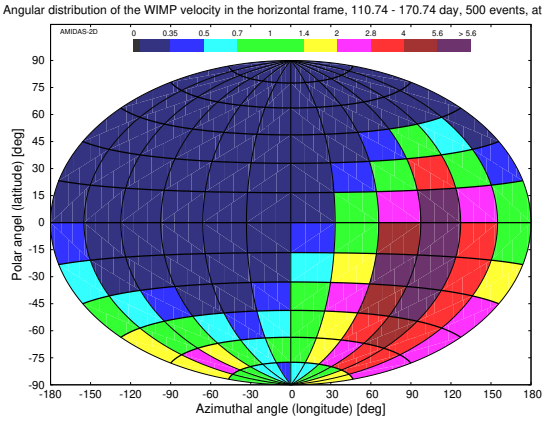

(c) 110.74 – 170.74 day

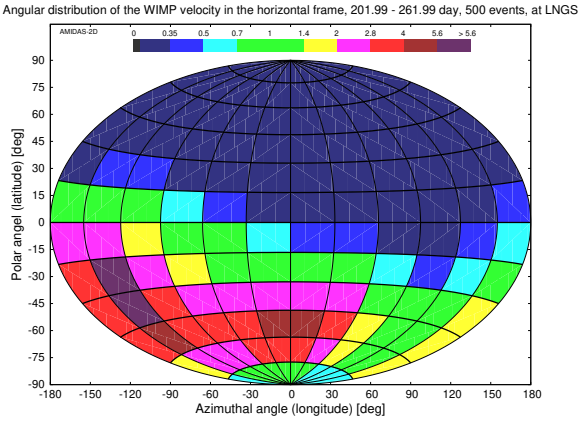

(d) 201.99 – 261.99 day

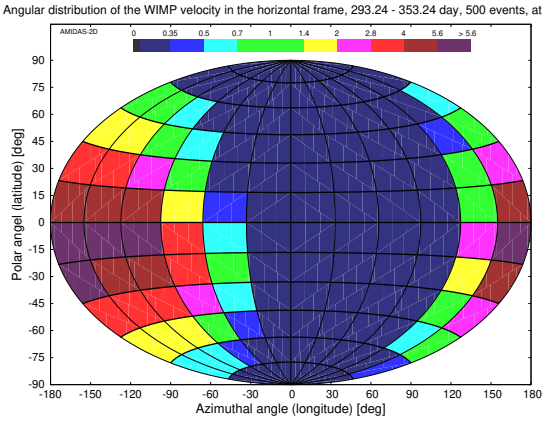

(e) 293.24 – 353.24 day

Figure A44: As in Figs. A43, except that 500 total events on average in one entire year (a) and in each 60-day observation period of four advanced seasons (b – e) have been simulated.

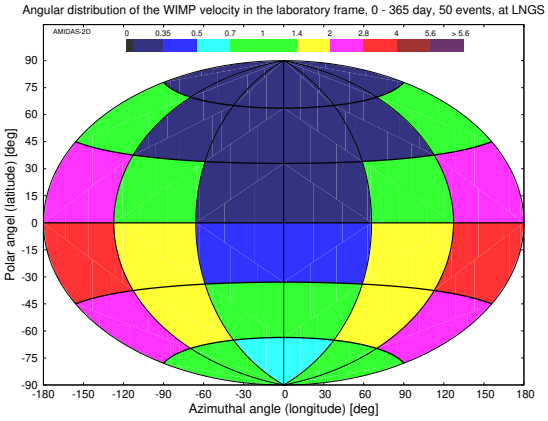

(a) 0 – 365 day

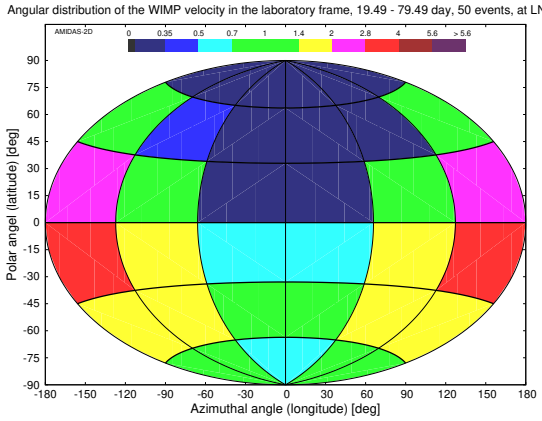

(b) 19.49 – 79.49 day

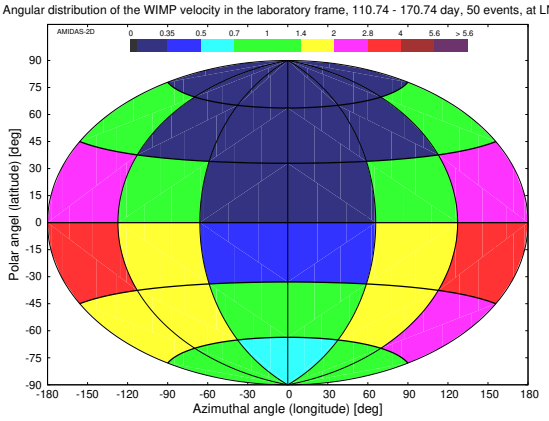

(c) 110.74 – 170.74 day

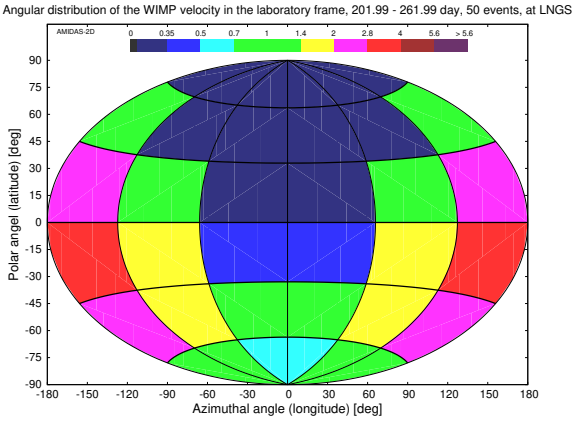

(d) 201.99 – 261.99 day

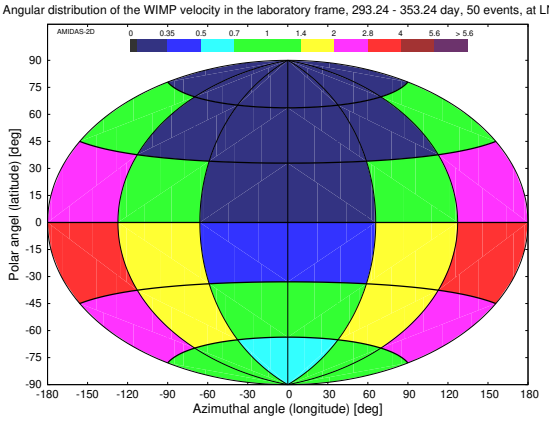

(e) 293.24 – 353.24 day

Figure A45: The angular distributions of the 3-D WIMP velocity transformed from events shown in Fig. A43 to the laboratory coordinate system at the location of the LNGS laboratory. All simulation setup and notations are the same as in Fig. A43.

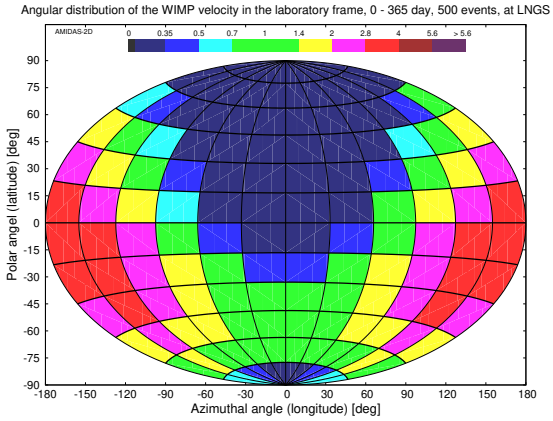

(a) 0 – 365 day

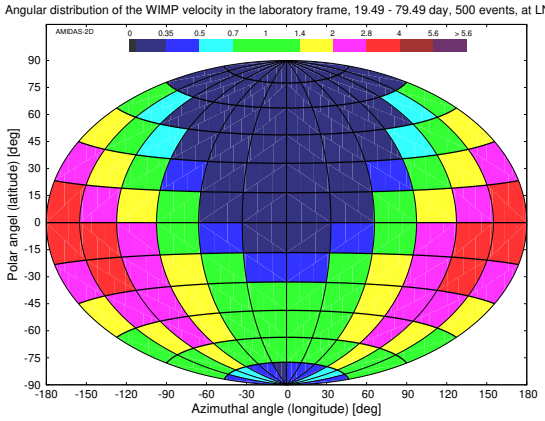

(b) 19.49 – 79.49 day

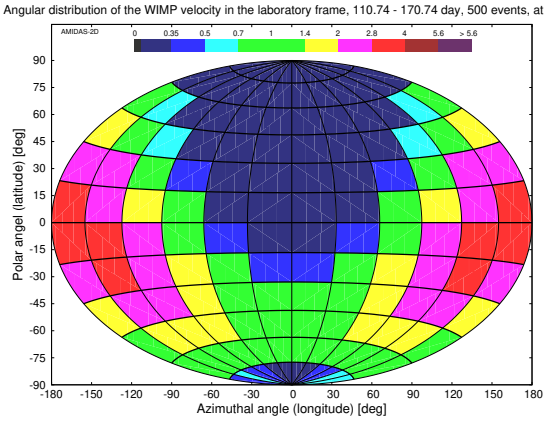

(c) 110.74 – 170.74 day

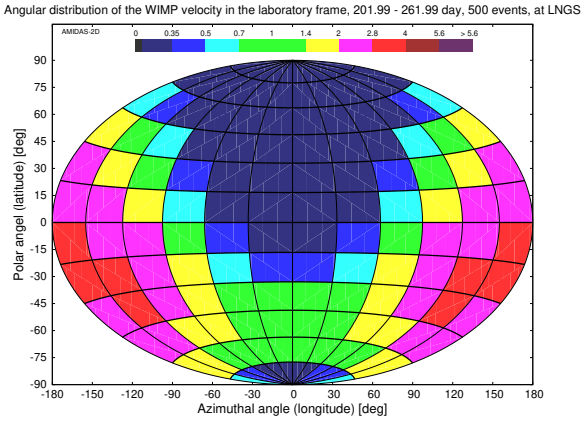

(d) 201.99 – 261.99 day

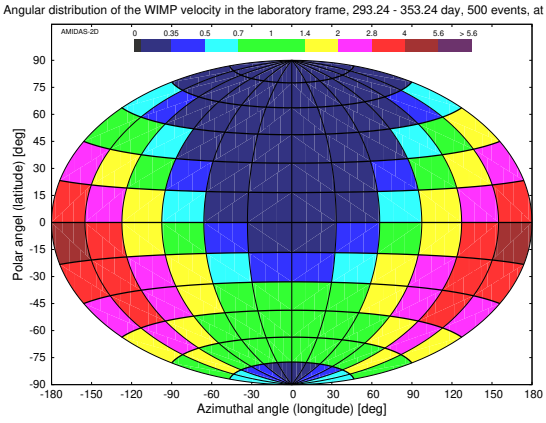

(e) 293.24 – 353.24 day

Figure A46: As in Figs. A45, except that 500 total events on average in one entire year (a) and in each 60-day observation period of four advanced seasons (b – e) have been simulated.

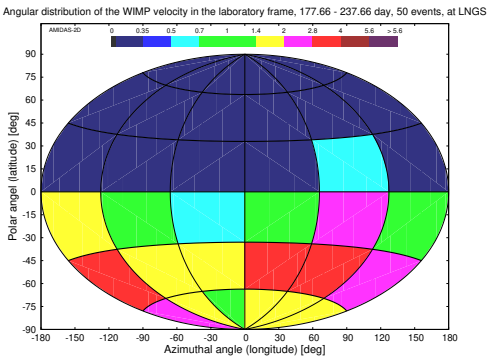

(a) 177.66 – 237.66 day, 22 – 2 hour

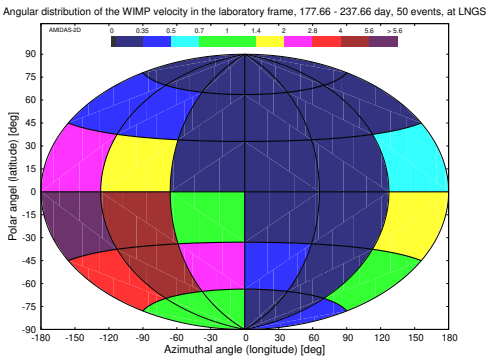

(b) 177.66 – 237.66 day, 4 – 8 hour

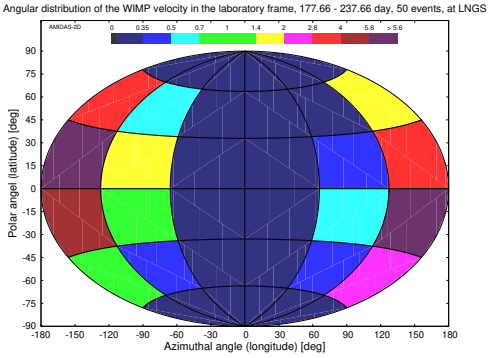

(c) 177.66 – 237.66 day, 10 – 14 hour

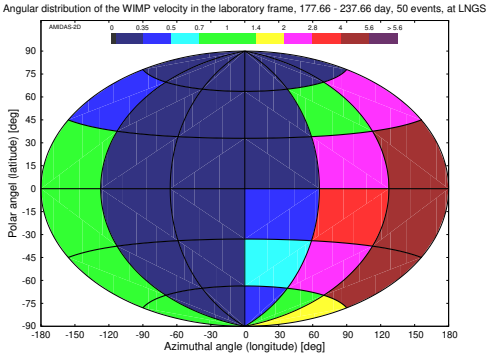

(d) 177.66 – 237.66 day, 16 – 20 hour

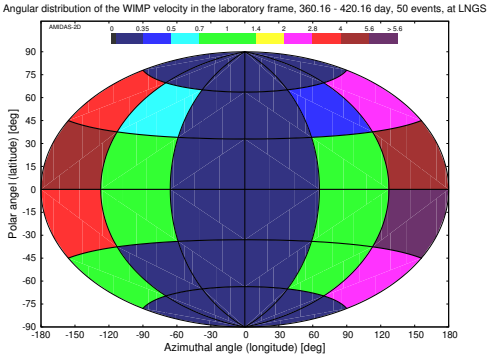

(e) 360.16 – 420.16 day, 22 – 2 hour

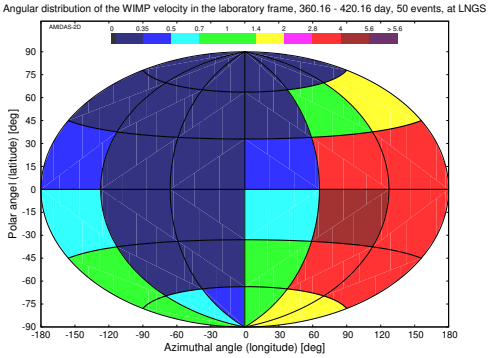

(f) 360.16 – 420.16 day, 4 – 8 hour

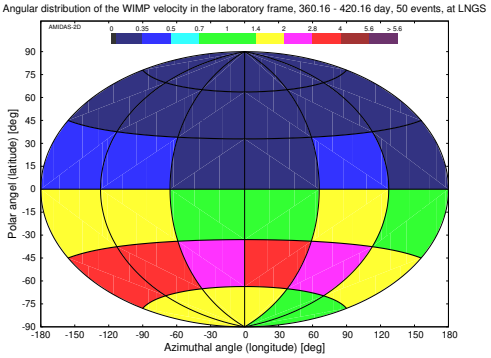

(g) 360.16 – 420.16 day, 10 – 14 hour

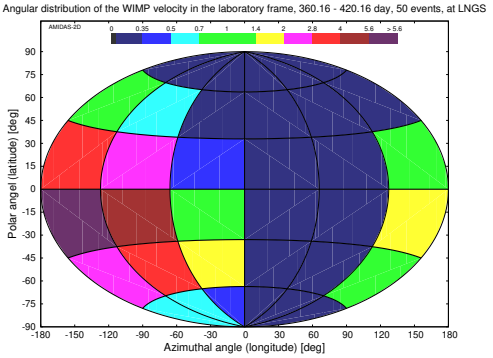

(h) 360.16 – 420.16 day, 16 – 20 hour

Figure A47: The angular distributions of the 3-D WIMP velocity observed at the location of the LNGS laboratory. 50 total events on average in each 4-hour daily shift in the 60-day observation periods of 177.66 – 237.66 day (a – d) and 360.16 – 420.16 (= 55.16) day (e – h) have been simulated.

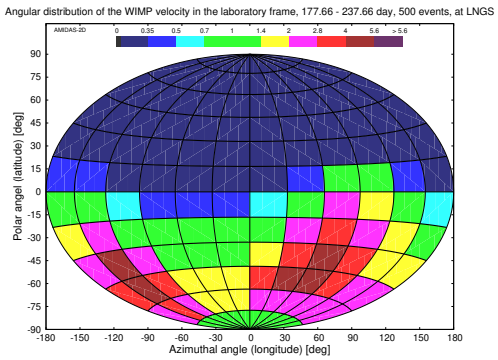

(a) 177.66 – 237.66 day, 22 – 2 hour

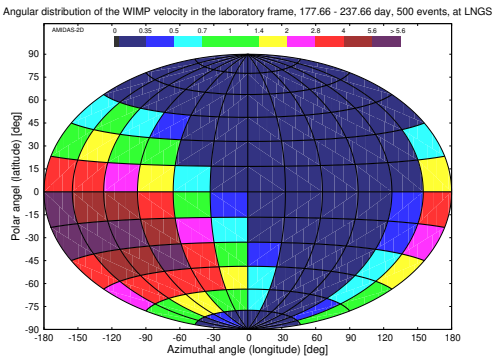

(b) 177.66 – 237.66 day, 4 – 8 hour

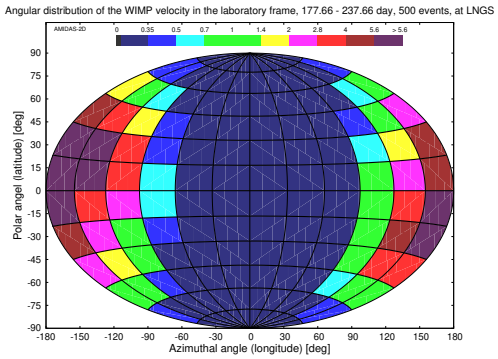

(c) 177.66 – 237.66 day, 10 – 14 hour

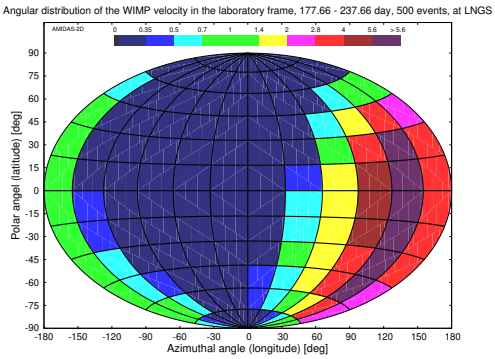

(d) 177.66 – 237.66 day, 16 – 20 hour

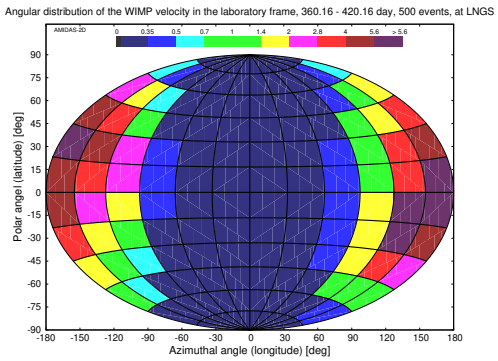

(e) 360.16 – 420.16 day, 22 – 2 hour

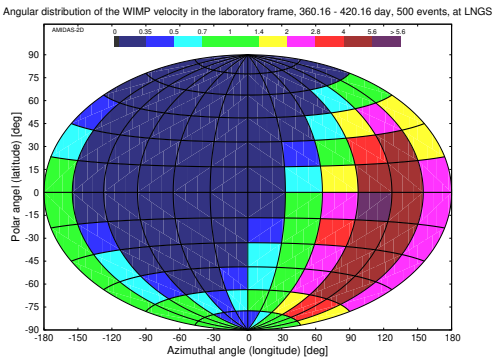

(f) 360.16 – 420.16 day, 4 – 8 hour

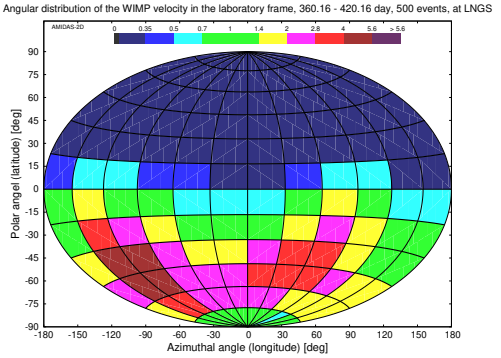

(g) 360.16 – 420.16 day, 10 – 14 hour

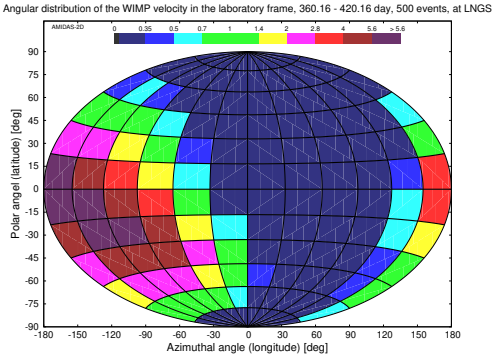

(h) 360.16 – 420.16 day, 16 – 20 hour

Figure A48: As in Figs. A47, except that 500 total events on average in each 4-hour daily shift in the 60-day observation periods have been simulated.

B.8 Laboratoire Souterrain Canfranc (LSC)

Central date (observation period) (day)	Most–event directions	
	50 events	500 events
0 – 365	—	—
49.49 (19.49 – 79.49)	30°S – 30°N 120°E – 180°	45°S – 45°N 120°E – 150°W
140.74 (110.74 – 170.74)	60°S – 0° 60°E – 120°E	60°S – 60°N 90°E – 150°E
231.99 (201.99 – 261.99)	60°S – 30°S 180° – 120°W	60°S – 15°S, 150°W – 120°W 60°S – 45°S, 0° – 60°E
323.24 (293.24 – 353.24)	30°S – 0° 180° – 60°W	45°S – 15°N 150°E – 60°W

Table A10: The summary of the directions of the simulated 3-D WIMP velocity with the highest event numbers ($>$ 4 times of the all–sky average value) in the horizontal coordinate system in one entire year and four advanced seasons at the location of the LSC laboratory (42.81°N, 0.56°W). 50 and 500 total events on average in each observation period of 60 days have been simulated.

Remark: as at the ANDES, the Kamioka, and the LNGS laboratories, in Fig. A50(d) one could also find clearly a second "hot–point" from 60°S to 45°S, and 0° to 60°E in the angular distribution pattern in the horizontal coordinate system of the LSC laboratory.

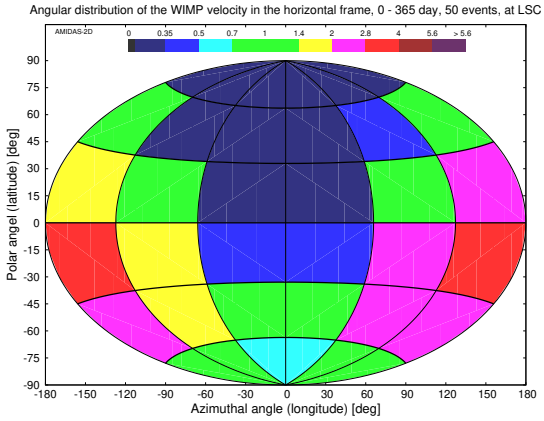

(a) 0 – 365 day

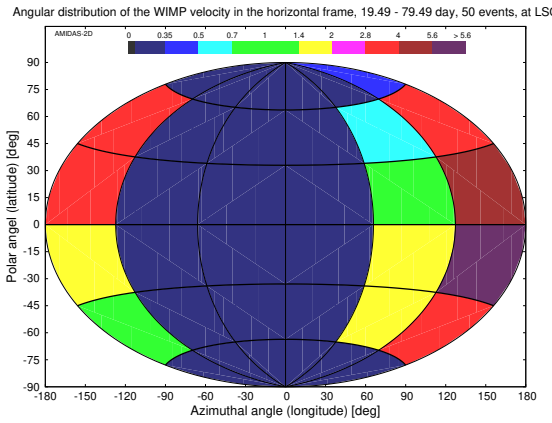

(b) 19.49 – 79.49 day

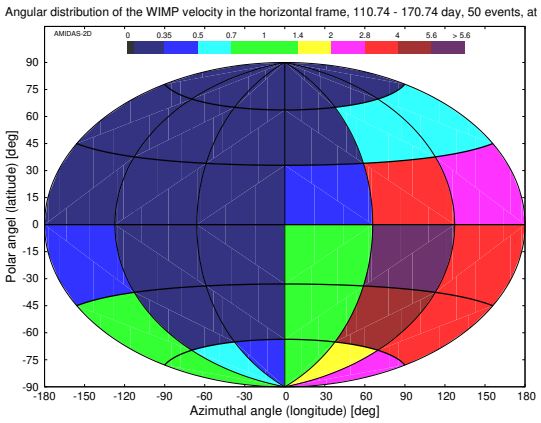

(c) 110.74 – 170.74 day

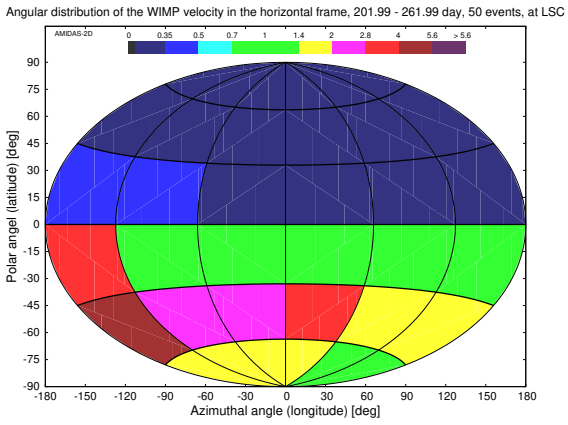

(d) 201.99 – 261.99 day

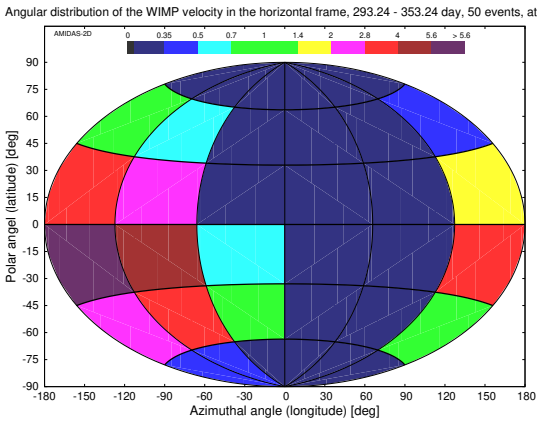

(e) 293.24 – 353.24 day

Figure A49: The angular distributions of the 3-D WIMP velocity in the horizontal coordinate system at the location of the LSC laboratory (42.81°N, 0.56°W). 50 total events on average in one entire year (a) and in each 60-day observation period of four advanced seasons (b – e) have been simulated.

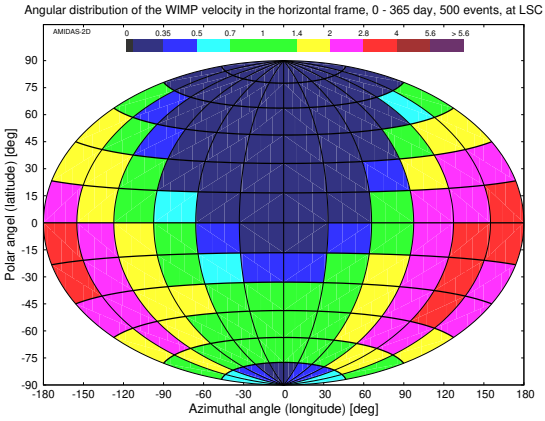

(a) 0 – 365 day

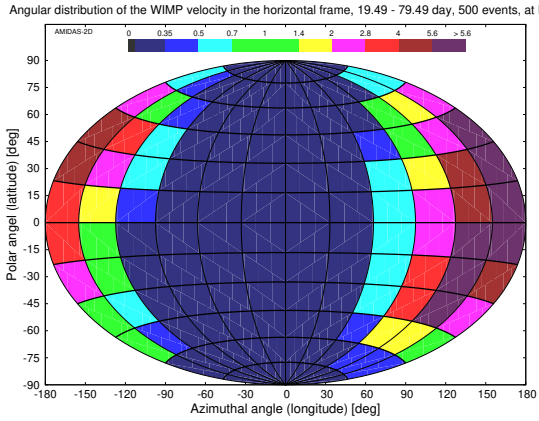

(b) 19.49 – 79.49 day

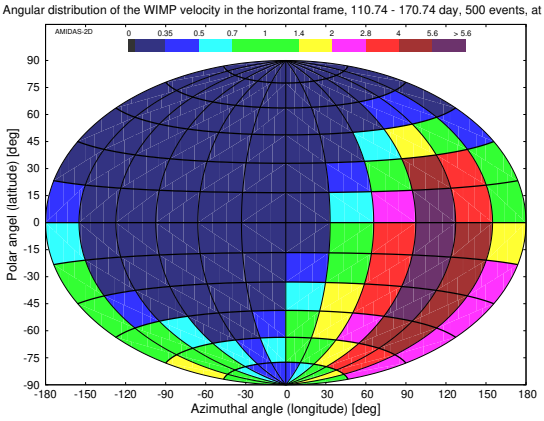

(c) 110.74 – 170.74 day

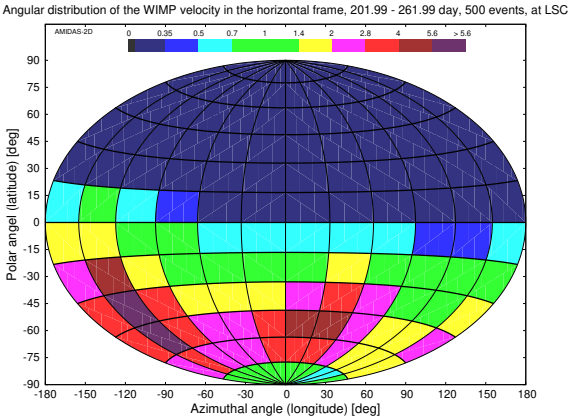

(d) 201.99 – 261.99 day

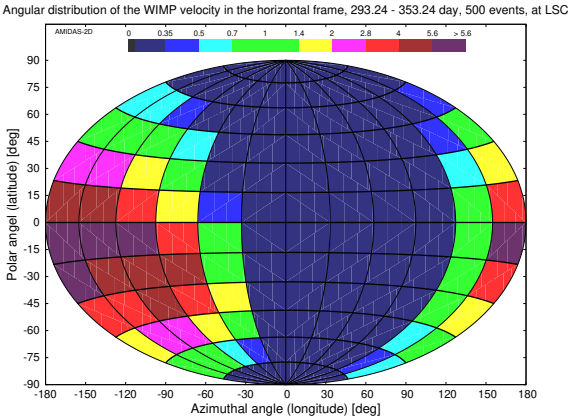

(e) 293.24 – 353.24 day

Figure A50: As in Figs. A49, except that 500 total events on average in one entire year (a) and in each 60-day observation period of four advanced seasons (b – e) have been simulated.

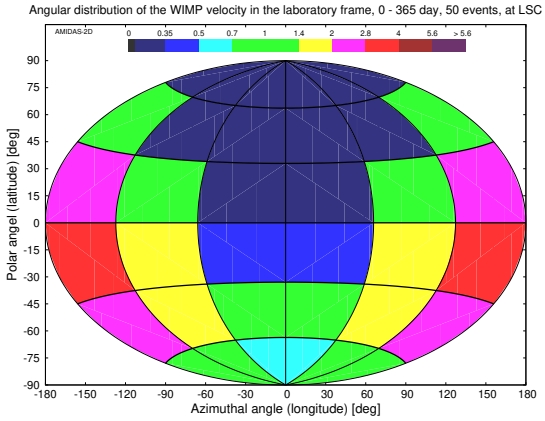

(a) 0 – 365 day

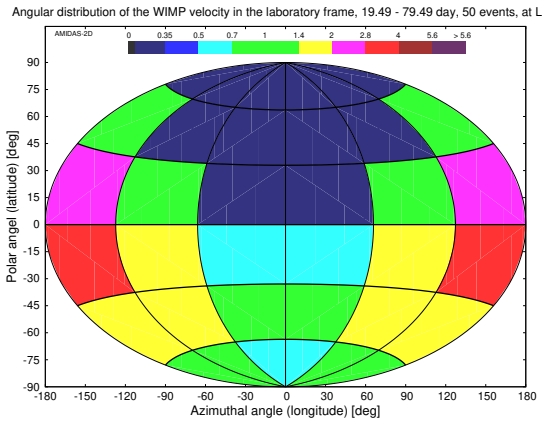

(b) 19.49 – 79.49 day

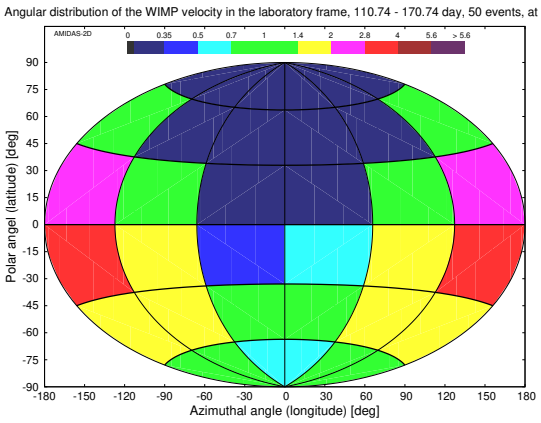

(c) 110.74 – 170.74 day

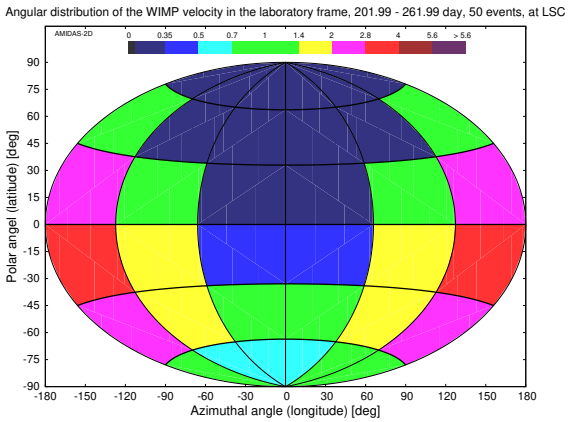

(d) 201.99 – 261.99 day

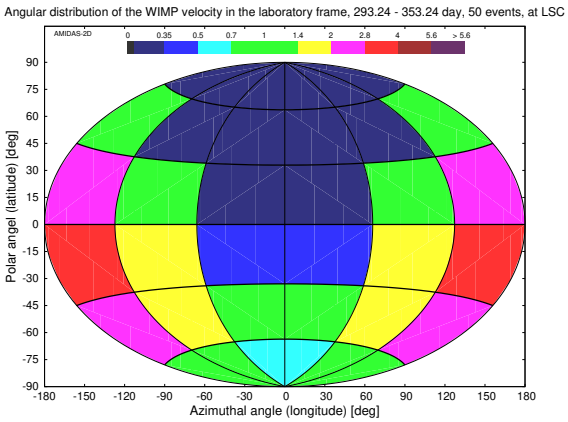

(e) 293.24 – 353.24 day

Figure A51: The angular distributions of the 3-D WIMP velocity transformed from events shown in Fig. A49 to the laboratory coordinate system at the location of the LSC laboratory. All simulation setup and notations are the same as in Fig. A49.

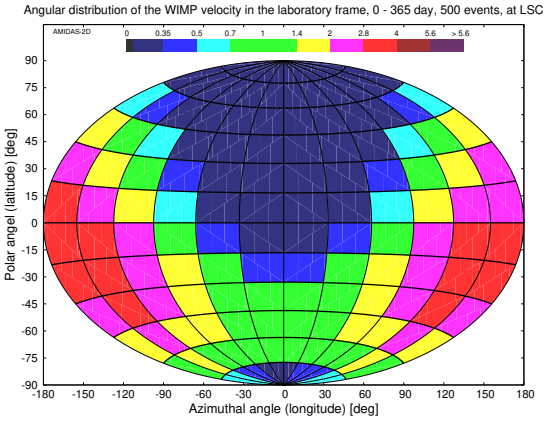

(a) 0 – 365 day

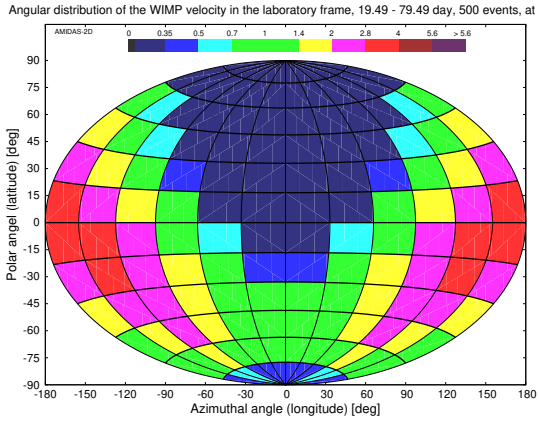

(b) 19.49 – 79.49 day

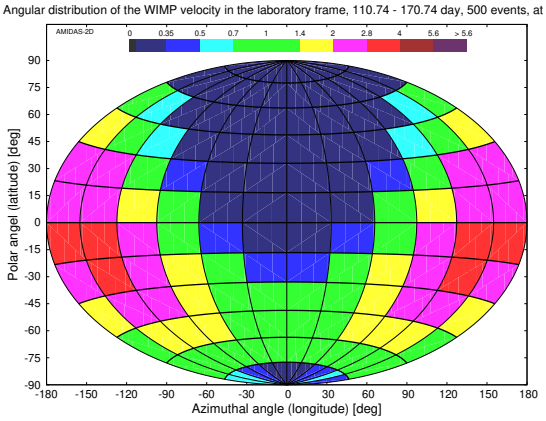

(c) 110.74 – 170.74 day

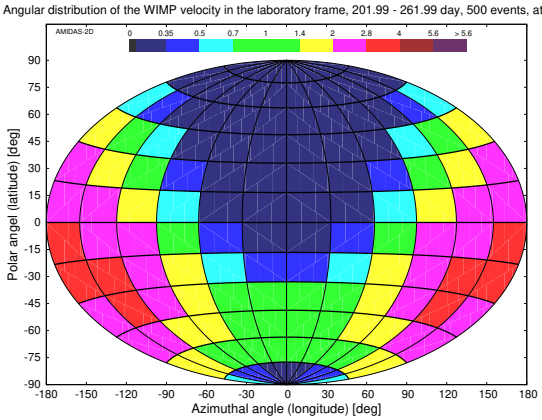

(d) 201.99 – 261.99 day

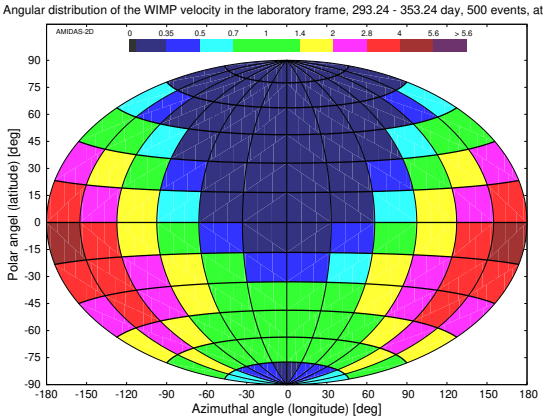

(e) 293.24 – 353.24 day

Figure A52: As in Figs. A51, except that 500 total events on average in one entire year (a) and in each 60-day observation period of four advanced seasons (b – e) have been simulated.

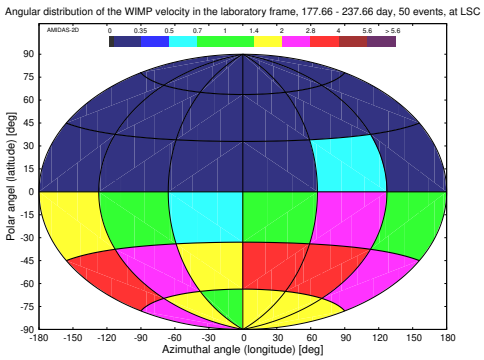

(a) 177.66 – 237.66 day, 22 – 2 hour

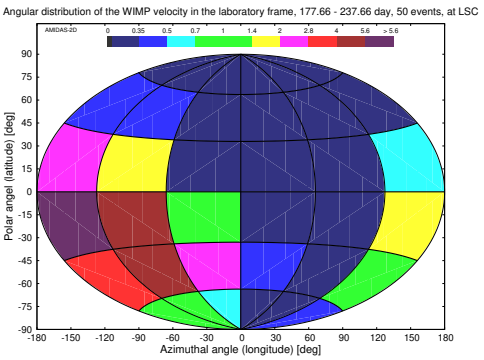

(b) 177.66 – 237.66 day, 4 – 8 hour

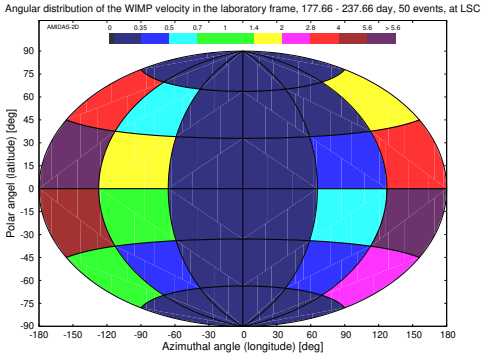

(c) 177.66 – 237.66 day, 10 – 14 hour

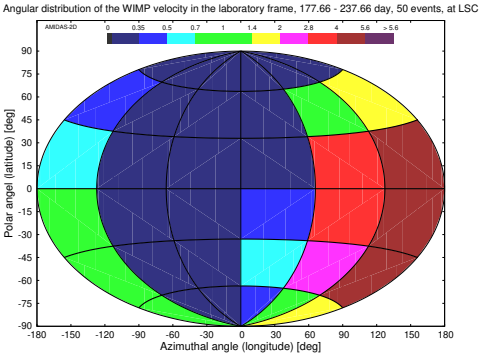

(d) 177.66 – 237.66 day, 16 – 20 hour

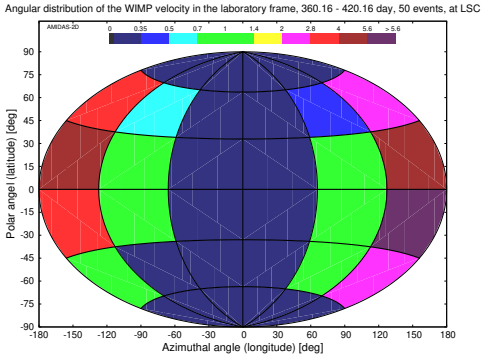

(e) 360.16 – 420.16 day, 22 – 2 hour

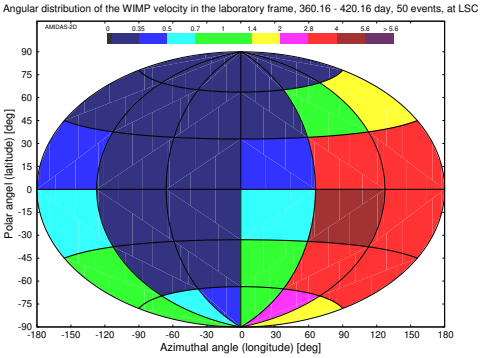

(f) 360.16 – 420.16 day, 4 – 8 hour

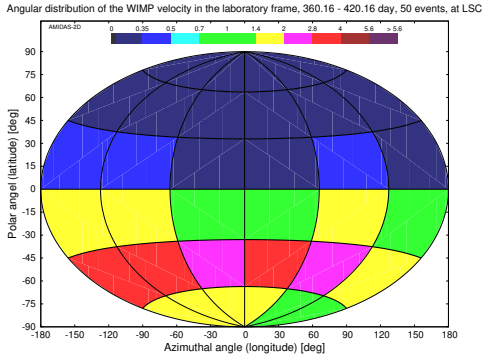

(g) 360.16 – 420.16 day, 10 – 14 hour

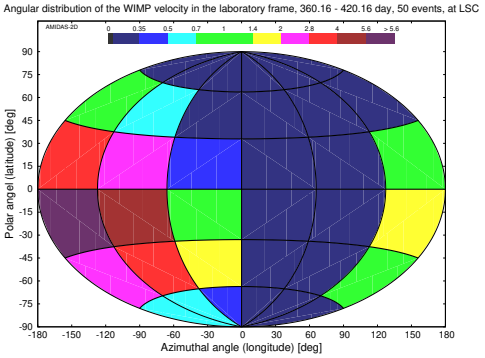

(h) 360.16 – 420.16 day, 16 – 20 hour

Figure A53: The angular distributions of the 3-D WIMP velocity observed at the location of the LSC laboratory. 50 total events on average in each 4-hour daily shift in the 60-day observation periods of 177.66 – 237.66 day (a – d) and 360.16 – 420.16 (= 55.16) day (e – h) have been simulated.

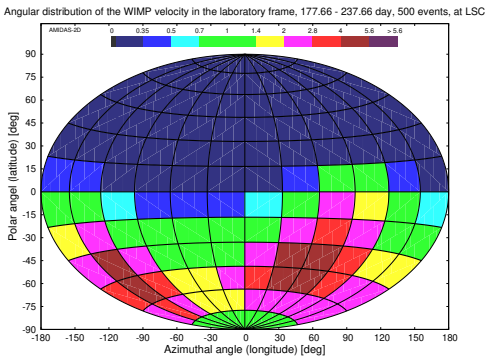

(a) 177.66 – 237.66 day, 22 – 2 hour

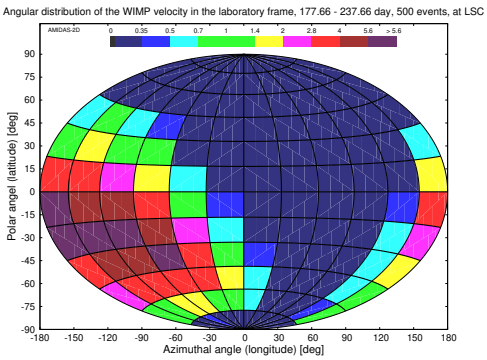

(b) 177.66 – 237.66 day, 4 – 8 hour

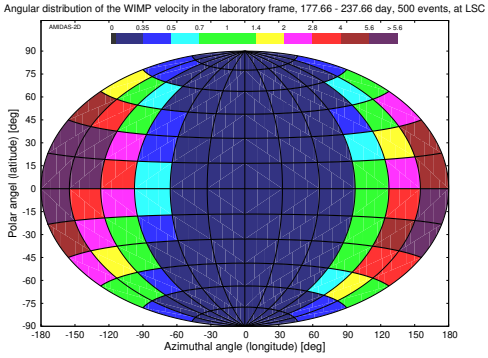

(c) 177.66 – 237.66 day, 10 – 14 hour

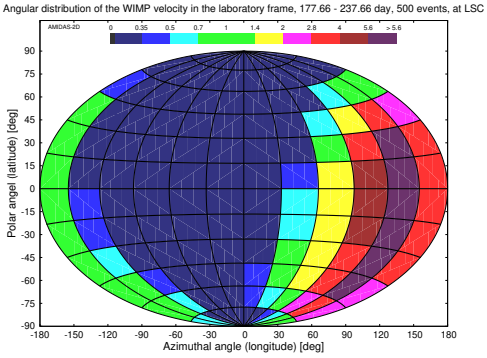

(d) 177.66 – 237.66 day, 16 – 20 hour

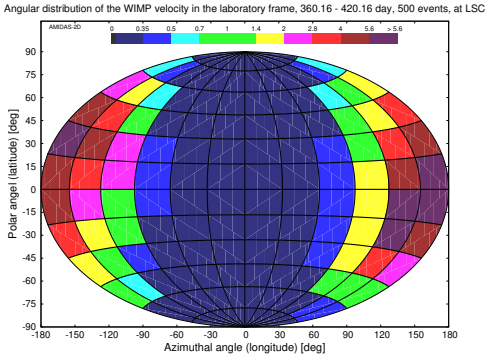

(e) 360.16 – 420.16 day, 22 – 2 hour

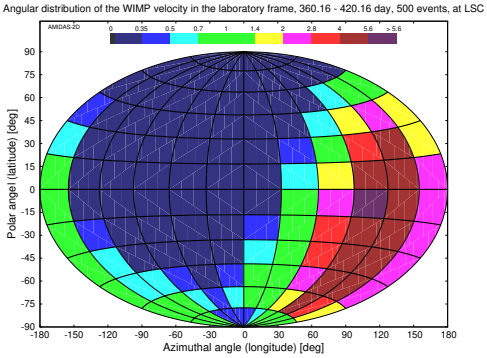

(f) 360.16 – 420.16 day, 4 – 8 hour

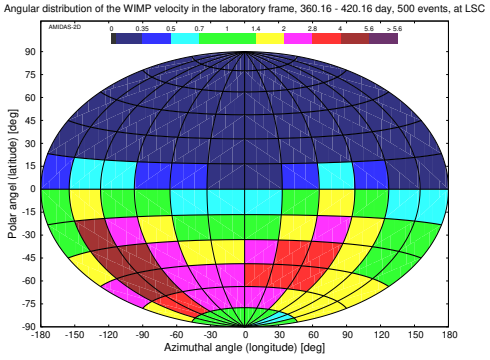

(g) 360.16 – 420.16 day, 10 – 14 hour

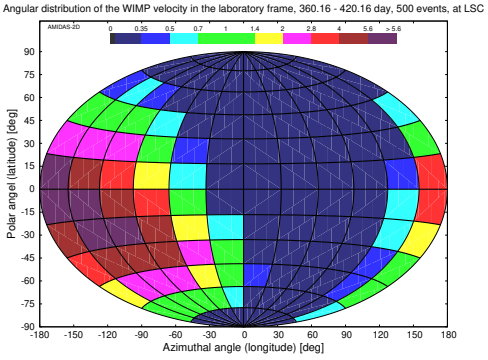

(h) 360.16 – 420.16 day, 16 – 20 hour

Figure A54: As in Figs. A53, except that 500 total events on average in each 4-hour daily shift in the 60-day observation periods have been simulated.

B.9 Laboratoire Souterrain de Modane (LSM)

Central date (observation period) (day)	Most–event directions	
	50 events	500 events
0 – 365	—	—
49.49 (19.49 – 79.49)	30°S – 30°N 120°E – 180°	45°S – 45°N 90°E – 150°W
140.74 (110.74 – 170.74)	60°S – 0° 60°E – 120°E	75°S – 15°N 60°E – 120°E
231.99 (201.99 – 261.99)	60°S – 30°S 180° – 120°W	60°S – 15°S, 150°W – 120°W 60°S – 45°S, 30°W – 30°E
323.24 (293.24 – 353.24)	30°S – 0° 120°E – 60°W	30°S – 15°N 150°E – 60°W

Table A11: The summary of the directions of the simulated 3-D WIMP velocity with the highest event numbers (> 4 times of the all–sky average value) in the horizontal coordinate system in one entire year and four advanced seasons at the location of the LSM laboratory (45.14°N, 6.70°E). 50 and 500 total events on average in each observation period of 60 days have been simulated.

Remark: as at the ANDES, the Kamioka, the LNGS, and the LSC laboratories, in Fig. A56(d) one could also find clearly a second "hot–point" from 60°S to 45°S, and 30°W to 30°E in the angular distribution pattern in the horizontal coordinate system of the LSM laboratory.

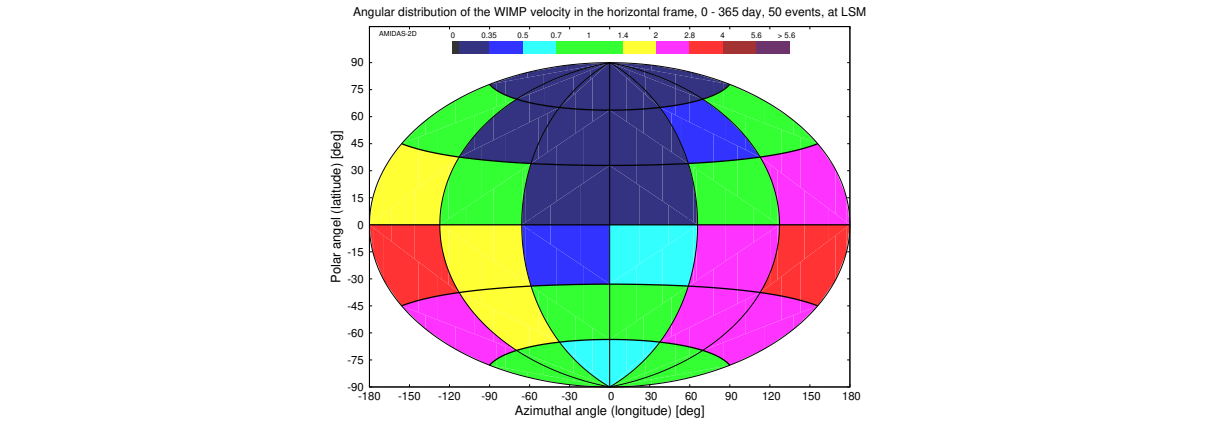

(a) 0 – 365 day

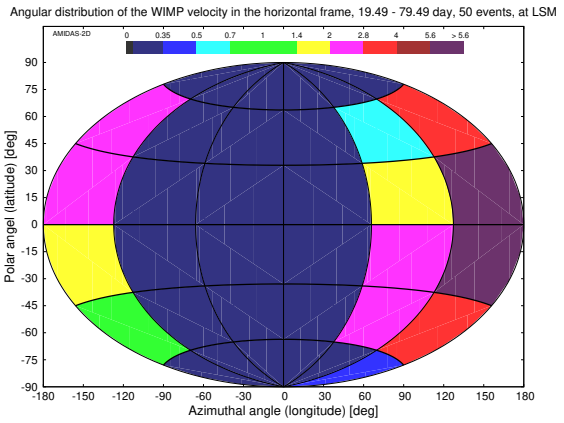

(b) 19.49 – 79.49 day

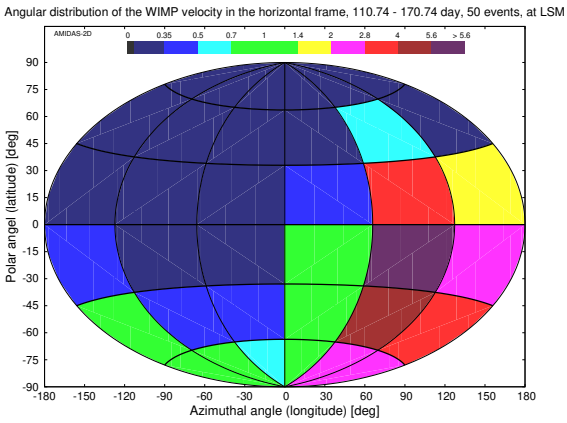

(c) 110.74 – 170.74 day

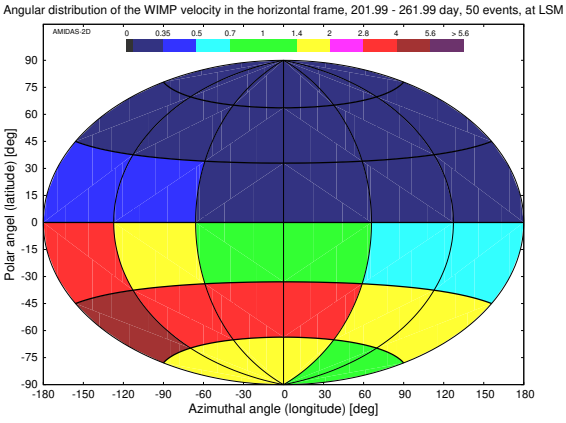

(d) 201.99 – 261.99 day

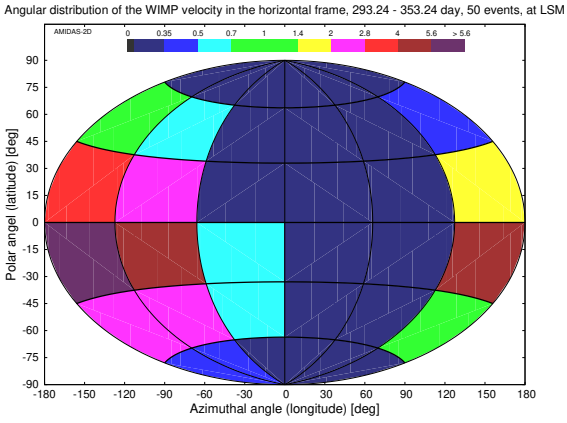

(e) 293.24 – 353.24 day

Figure A55: The angular distributions of the 3-D WIMP velocity in the horizontal coordinate system at the location of the LSM laboratory (45.14°N, 6.70°E). 50 total events on average in one entire year (a) and in each 60-day observation period of four advanced seasons (b – e) have been simulated.

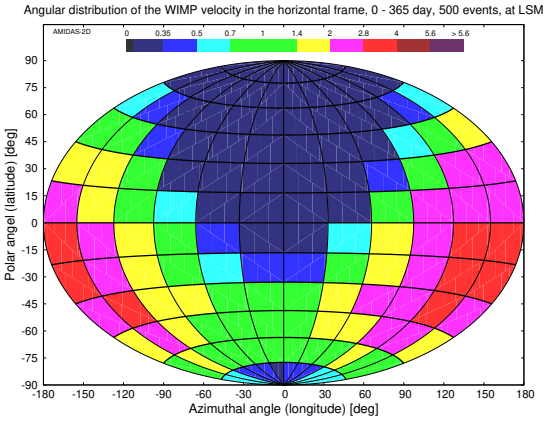

(a) 0 – 365 day

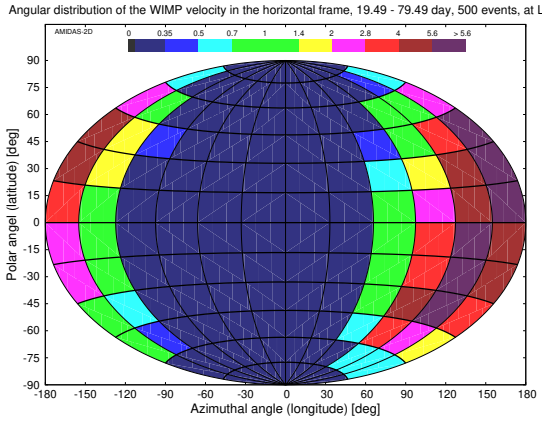

(b) 19.49 – 79.49 day

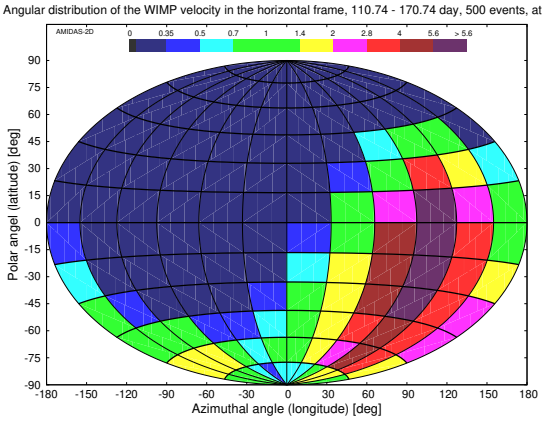

(c) 110.74 – 170.74 day

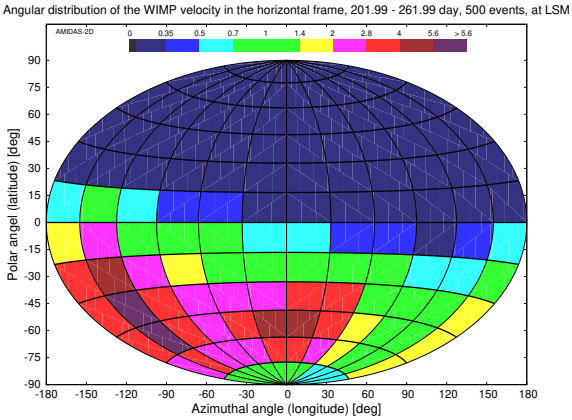

(d) 201.99 – 261.99 day

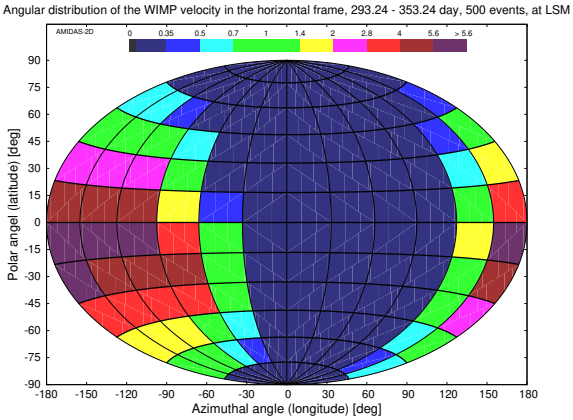

(e) 293.24 – 353.24 day

Figure A56: As in Figs. A55, except that 500 total events on average in one entire year (a) and in each 60-day observation period of four advanced seasons (b – e) have been simulated.

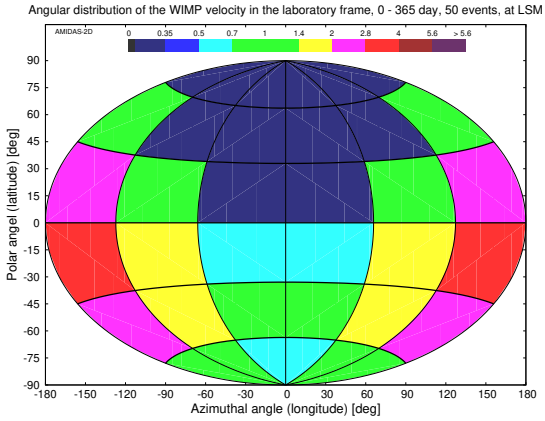

(a) 0 – 365 day

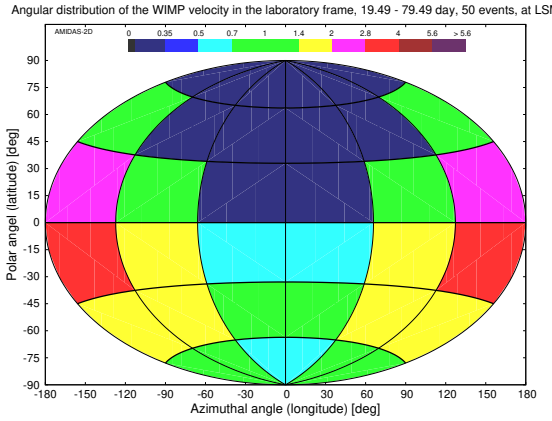

(b) 19.49 – 79.49 day

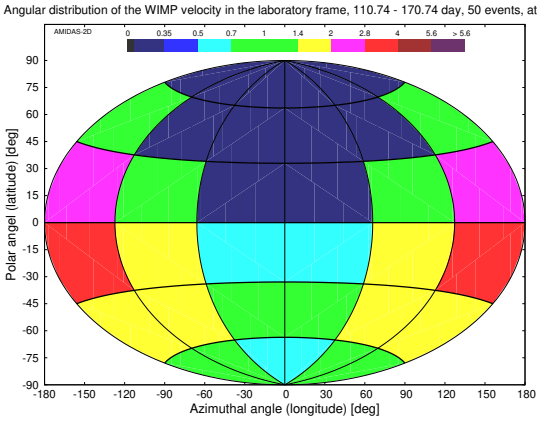

(c) 110.74 – 170.74 day

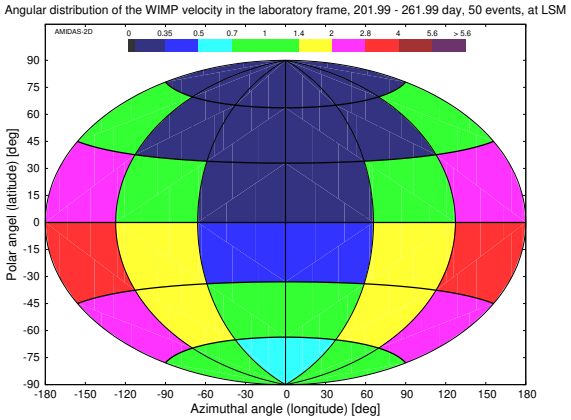

(d) 201.99 – 261.99 day

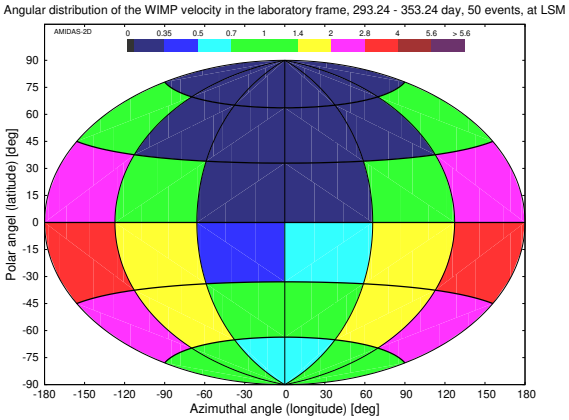

(e) 293.24 – 353.24 day

Figure A57: The angular distributions of the 3-D WIMP velocity transformed from events shown in Fig. A55 to the laboratory coordinate system at the location of the LSM laboratory. All simulation setup and notations are the same as in Fig. A55.

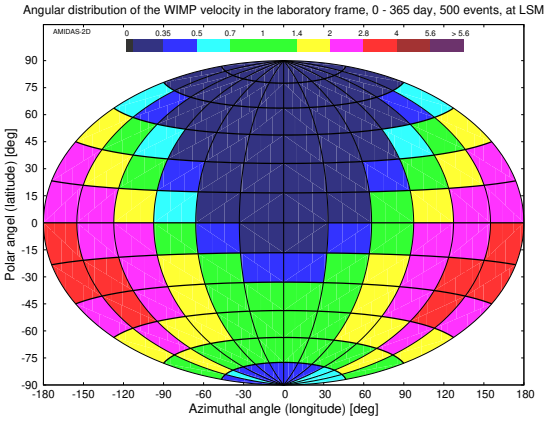

(a) 0 – 365 day

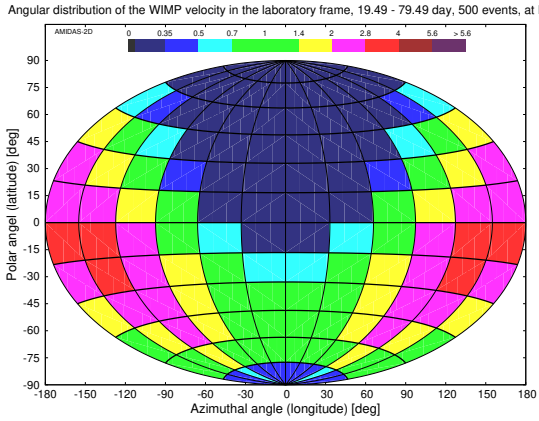

(b) 19.49 – 79.49 day

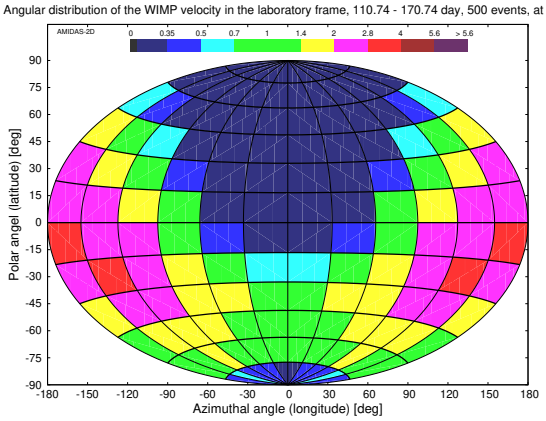

(c) 110.74 – 170.74 day

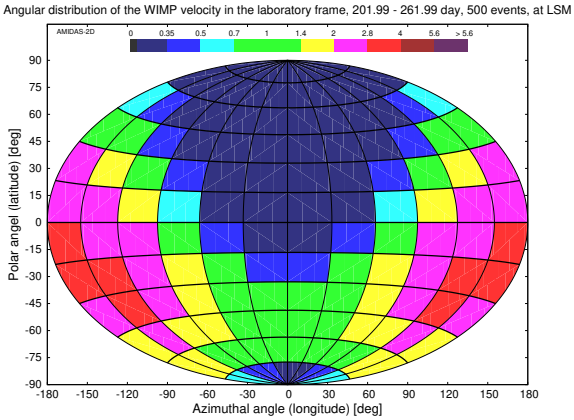

(d) 201.99 – 261.99 day

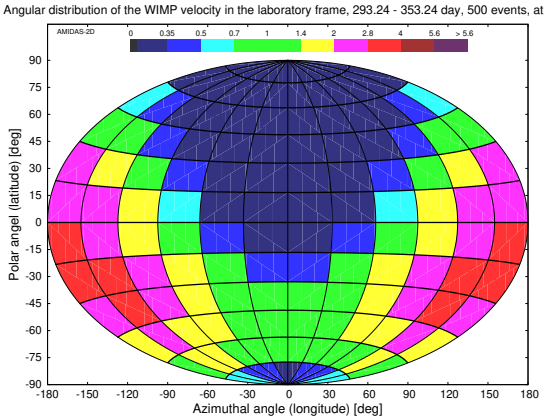

(e) 293.24 – 353.24 day

Figure A58: As in Figs. A57, except that 500 total events on average in one entire year (a) and in each 60-day observation period of four advanced seasons (b – e) have been simulated.

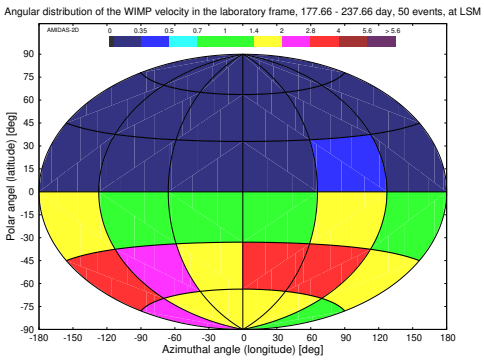

(a) 177.66 – 237.66 day, 22 – 2 hour

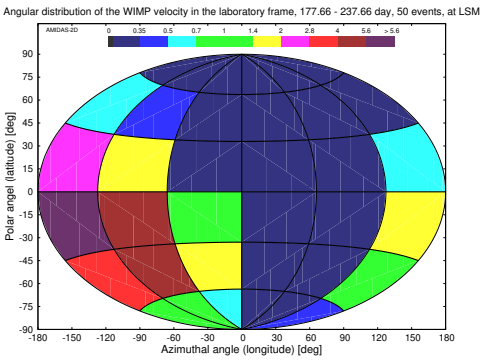

(b) 177.66 – 237.66 day, 4 – 8 hour

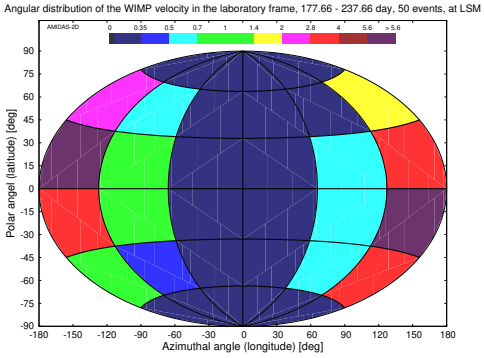

(c) 177.66 – 237.66 day, 10 – 14 hour

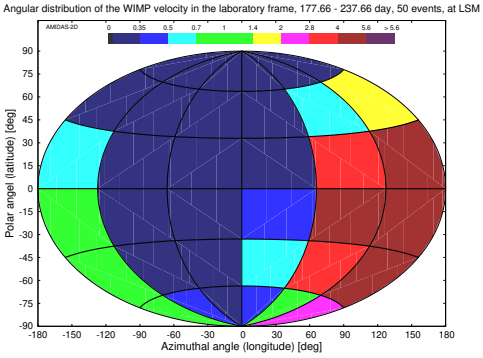

(d) 177.66 – 237.66 day, 16 – 20 hour

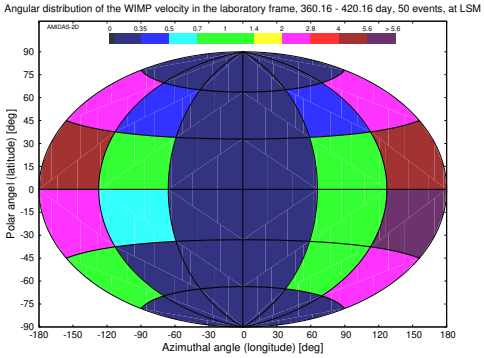

(e) 360.16 – 420.16 day, 22 – 2 hour

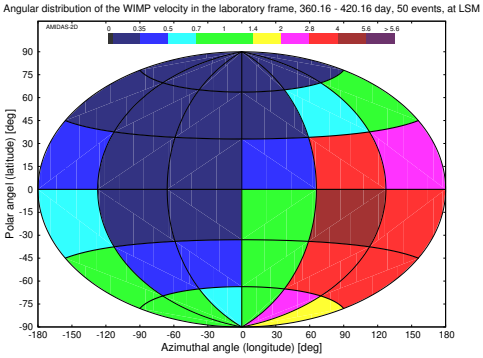

(f) 360.16 – 420.16 day, 4 – 8 hour

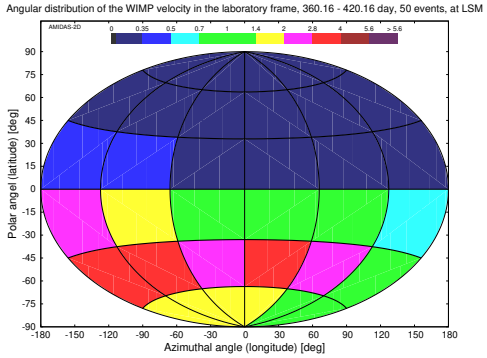

(g) 360.16 – 420.16 day, 10 – 14 hour

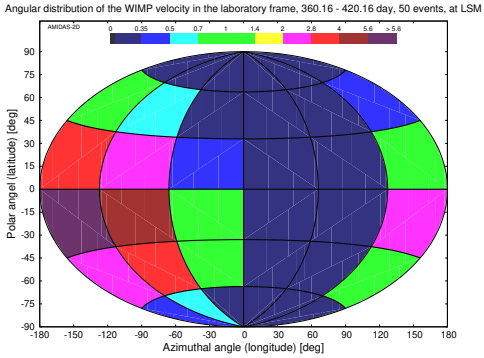

(h) 360.16 – 420.16 day, 16 – 20 hour

Figure A59: The angular distributions of the 3-D WIMP velocity observed at the location of the LSM laboratory. 50 total events on average in each 4-hour daily shift in the 60-day observation periods of 177.66 – 237.66 day (a – d) and 360.16 – 420.16 (= 55.16) day (e – h) have been simulated.

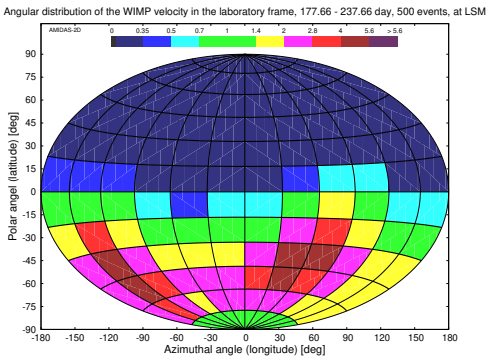

(a) 177.66 – 237.66 day, 22 – 2 hour

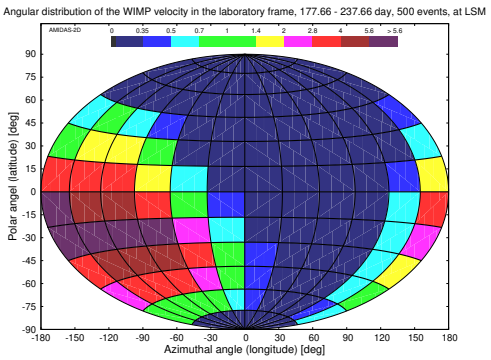

(b) 177.66 – 237.66 day, 4 – 8 hour

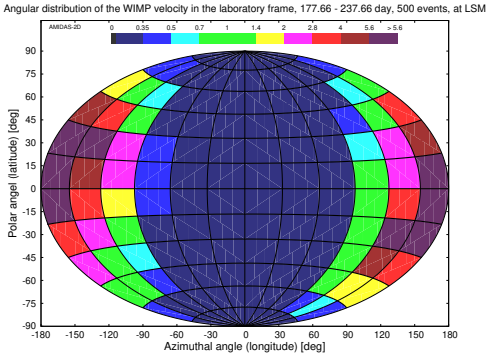

(c) 177.66 – 237.66 day, 10 – 14 hour

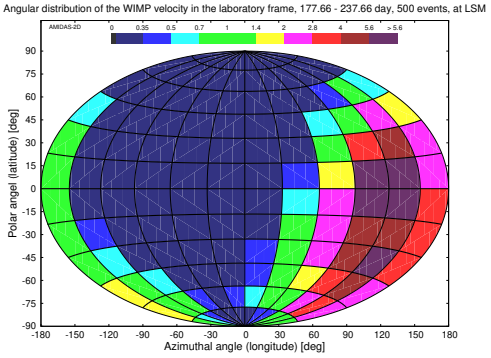

(d) 177.66 – 237.66 day, 16 – 20 hour

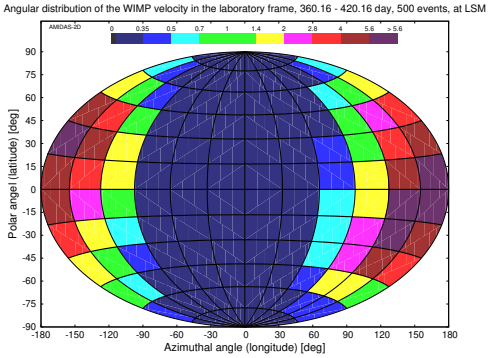

(e) 360.16 – 420.16 day, 22 – 2 hour

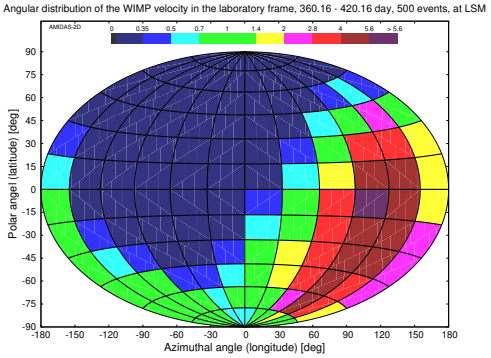

(f) 360.16 – 420.16 day, 4 – 8 hour

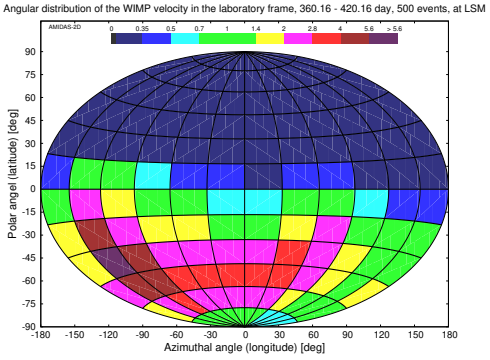

(g) 360.16 – 420.16 day, 10 – 14 hour

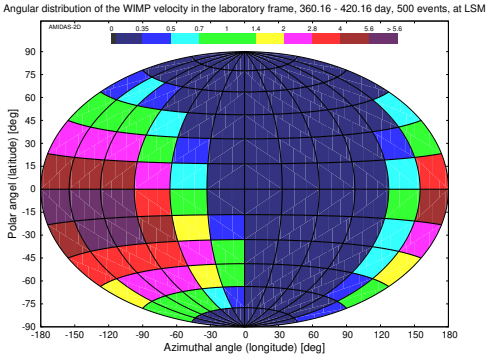

(h) 360.16 – 420.16 day, 16 – 20 hour

Figure A60: As in Figs. A59, except that 500 total events on average in each 4-hour daily shift in the 60-day observation periods have been simulated.

B.10 Sudbury Neutrino Observatory (SNOLAB)

Central date (observation period) (day)	Most–event directions	
	50 events	500 events
0 – 365	—	15°S – 0° 150°E – 150°W
49.49 (19.49 – 79.49)	30°S – 30°N 180° – 60°W	30°S – 15°N 150°E – 90°W
140.74 (110.74 – 170.74)	30°S – 30°N 120°E – 180°	45°S – 45°N 120°E – 150°W
231.99 (201.99 – 261.99)	30°S – 0° 60°E – 120°E	60°S – 15°N 90°E – 150°E
323.24 (293.24 – 353.24)	60°S – 0° 180° – 120°W	60°S – 15°S 150°W – 120°W

Table A12: The summary of the directions of the simulated 3-D WIMP velocity with the highest event numbers ($>$ 4 times of the all–sky average value) in the horizontal coordinate system in one entire year and four advanced seasons at the location of the SNOLAB laboratory (46.47°N, 81.19°W). 50 and 500 total events on average in each observation period of 60 days have been simulated.

Remark: as at the DUSEL laboratory, with $\mathcal{O}(500)$ total WIMP events recorded in one entire year and a higher analysis resolution, in the angular distribution pattern in the horizontal coordinate system of the SNOLAB laboratory shown in Fig. A62(a), clear high–WIMP–flux bins from 15°S to 0° and 150°E to 150°W could be identified.

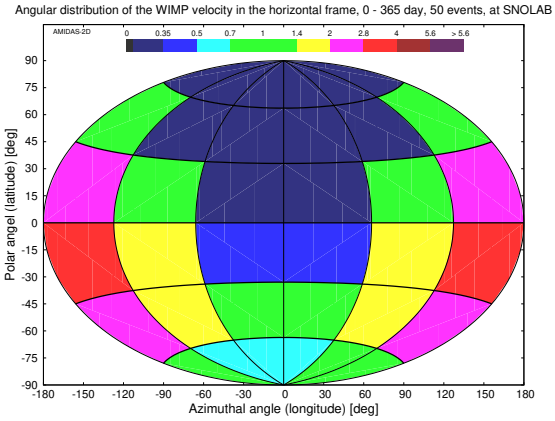

(a) 0 – 365 day

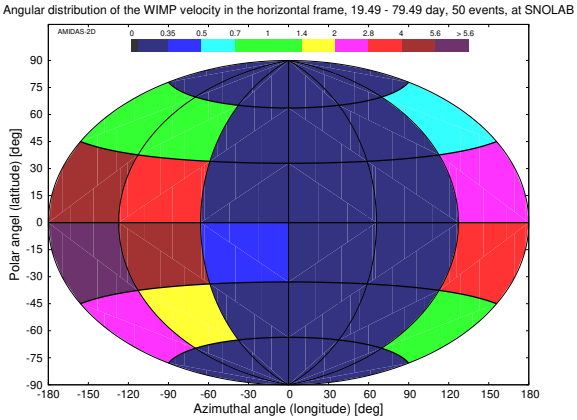

(b) 19.49 – 79.49 day

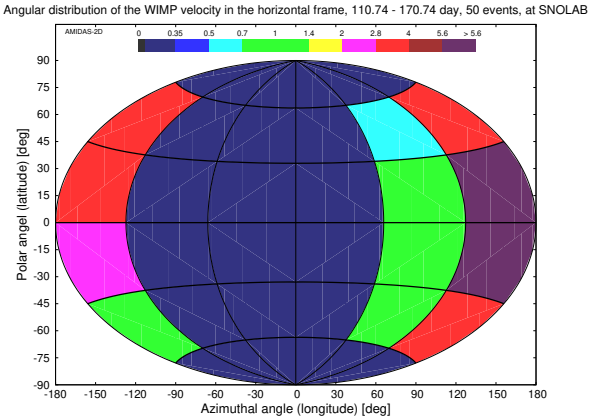

(c) 110.74 – 170.74 day

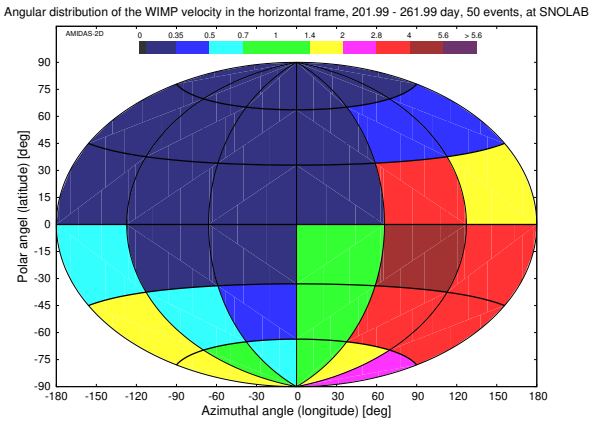

(d) 201.99 – 261.99 day

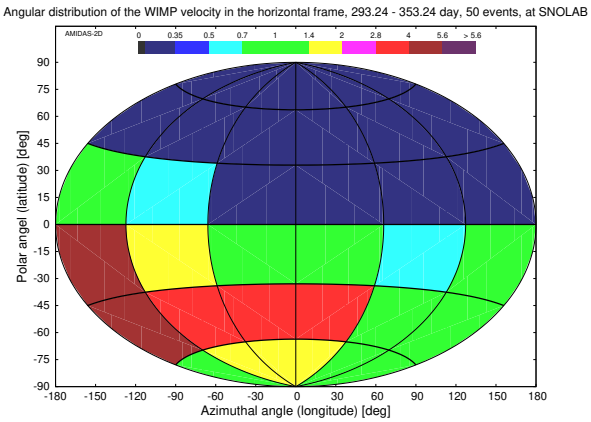

(e) 293.24 – 353.24 day

Figure A61: The angular distributions of the 3-D WIMP velocity in the horizontal coordinate system at the location of the SNOLAB laboratory (46.47°N, 81.19°W). 50 total events on average in one entire year (a) and in each 60-day observation period of four advanced seasons (b – e) have been simulated.

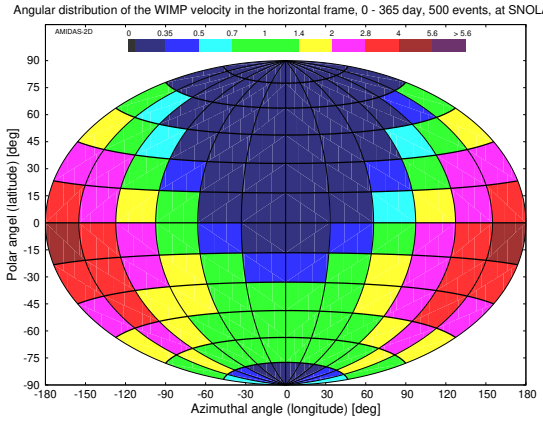

(a) 0 – 365 day

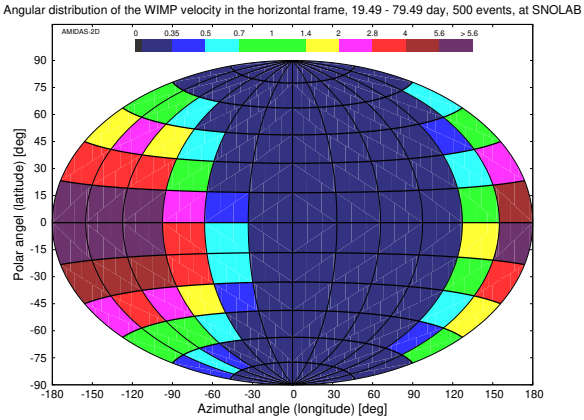

(b) 19.49 – 79.49 day

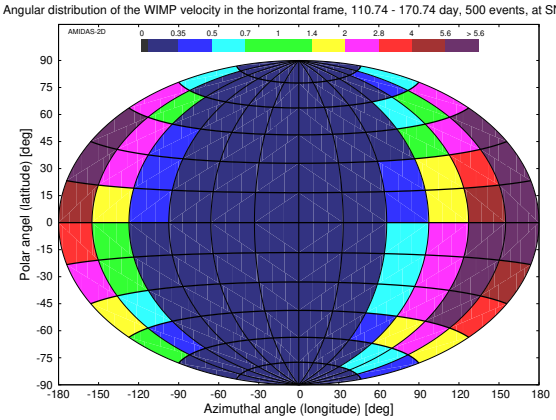

(c) 110.74 – 170.74 day

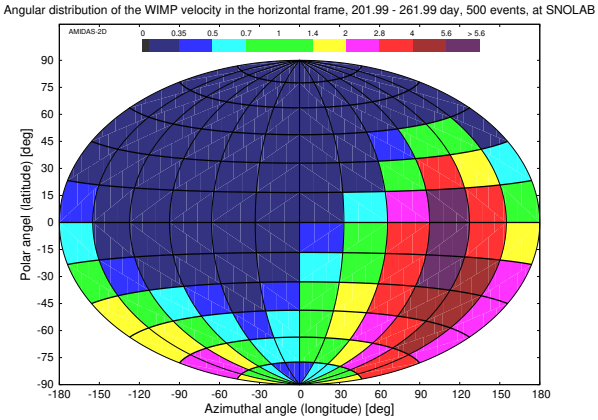

(d) 201.99 – 261.99 day

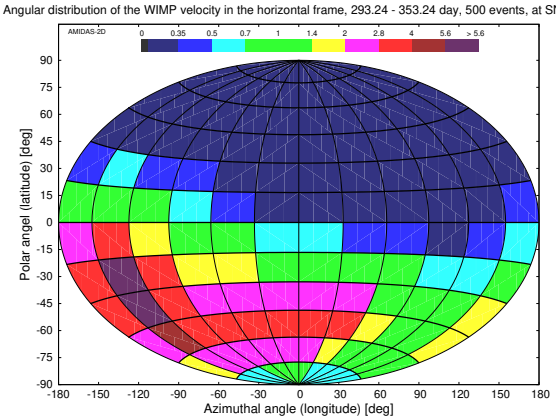

(e) 293.24 – 353.24 day

Figure A62: As in Figs. A61, except that 500 total events on average in one entire year (a) and in each 60-day observation period of four advanced seasons (b – e) have been simulated.

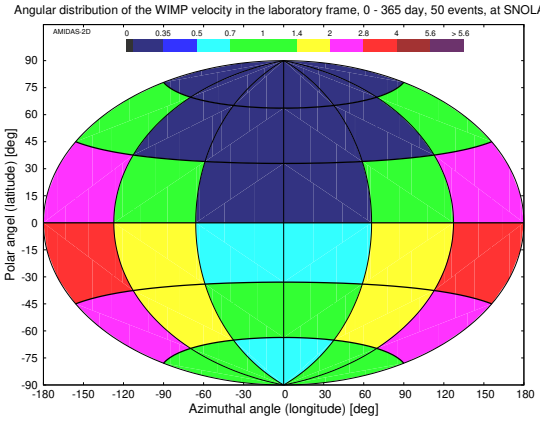

(a) 0 – 365 day

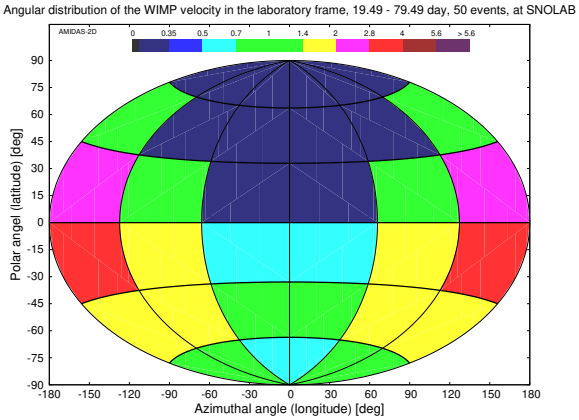

(b) 19.49 – 79.49 day

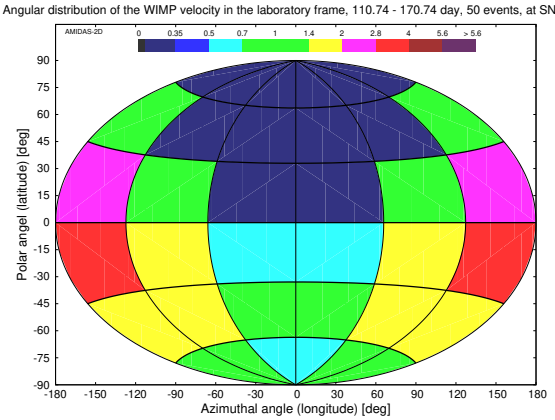

(c) 110.74 – 170.74 day

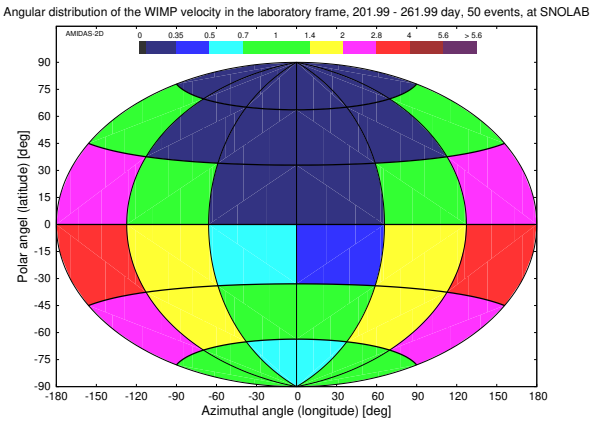

(d) 201.99 – 261.99 day

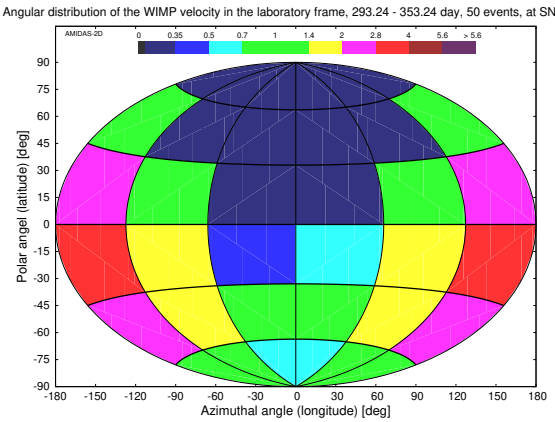

(e) 293.24 – 353.24 day

Figure A63: The angular distributions of the 3-D WIMP velocity transformed from events shown in Fig. A61 to the laboratory coordinate system at the location of the SNOLAB laboratory. All simulation setup and notations are the same as in Fig. A61.

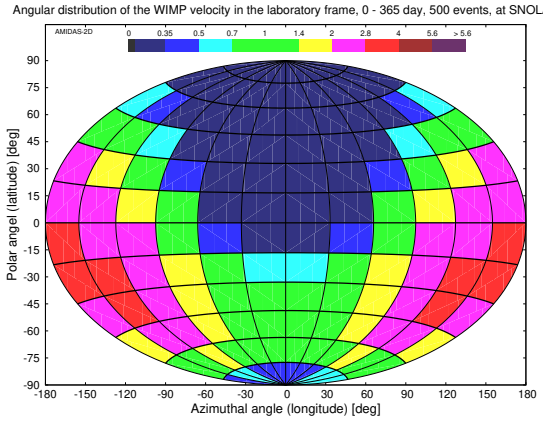

(a) 0 – 365 day

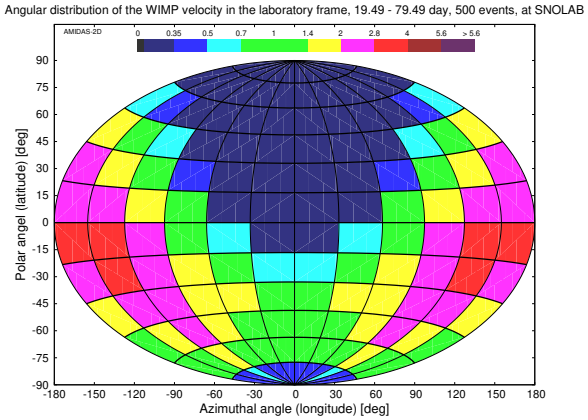

(b) 19.49 – 79.49 day

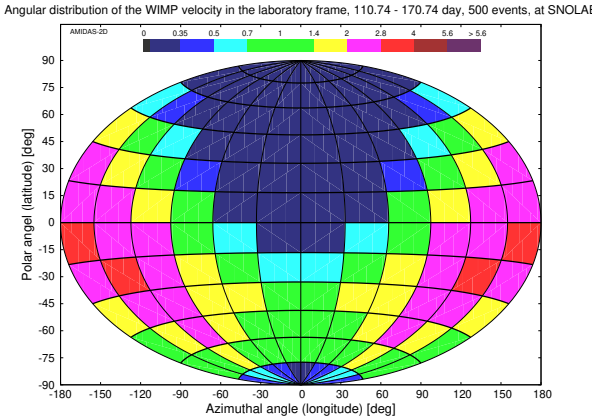

(c) 110.74 – 170.74 day

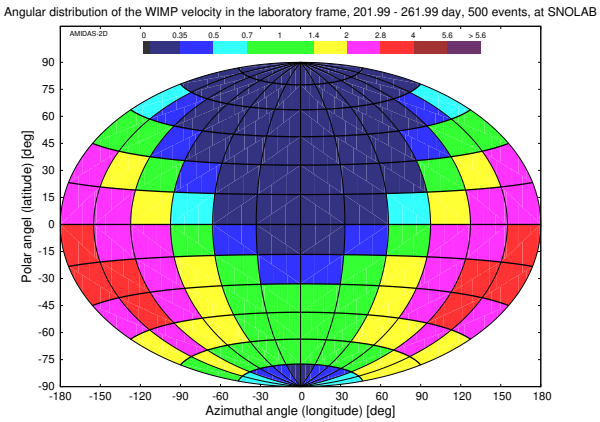

(d) 201.99 – 261.99 day

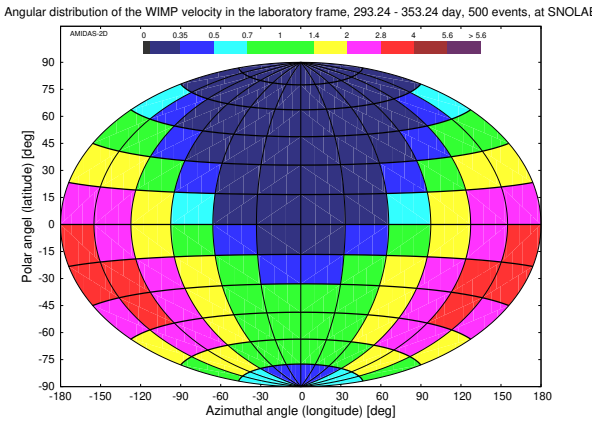

(e) 293.24 – 353.24 day

Figure A64: As in Figs. A63, except that 500 total events on average in one entire year (a) and in each 60-day observation period of four advanced seasons (b – e) have been simulated.

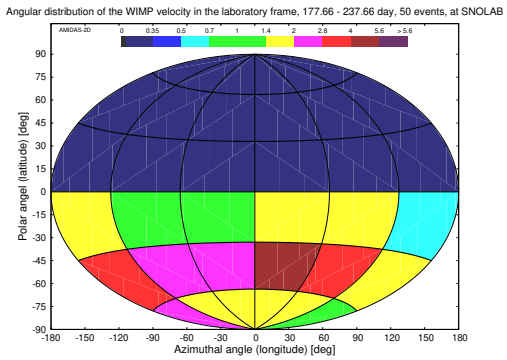

(a) 177.66 – 237.66 day, 22 – 2 hour

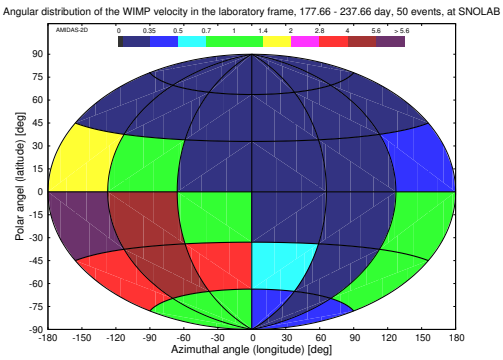

(b) 177.66 – 237.66 day, 4 – 8 hour

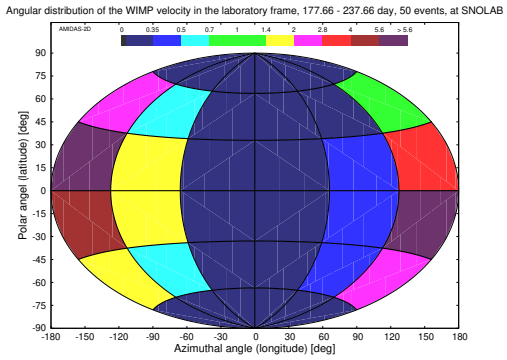

(c) 177.66 – 237.66 day, 10 – 14 hour

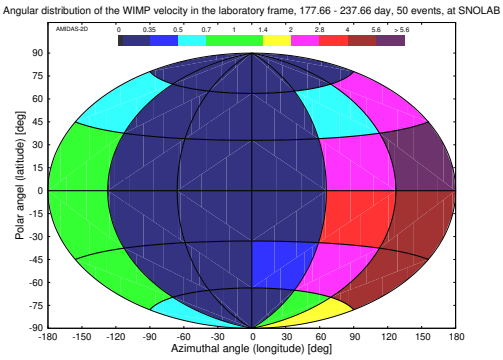

(d) 177.66 – 237.66 day, 16 – 20 hour

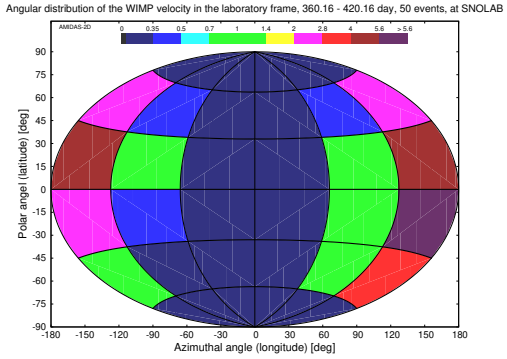

(e) 360.16 – 420.16 day, 22 – 2 hour

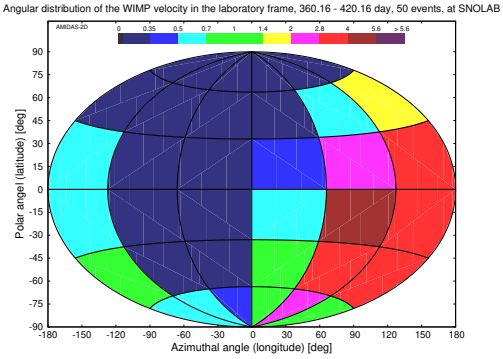

(f) 360.16 – 420.16 day, 4 – 8 hour

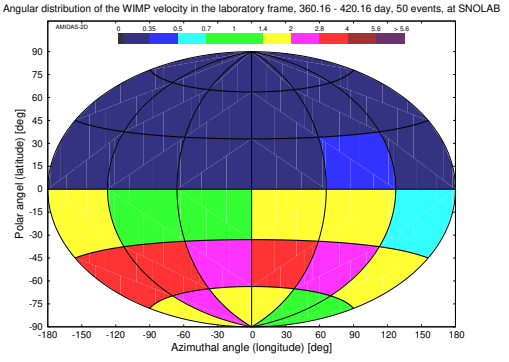

(g) 360.16 – 420.16 day, 10 – 14 hour

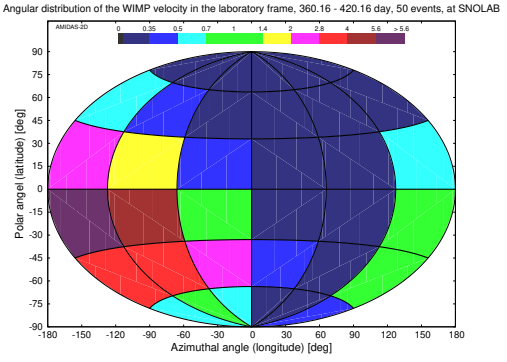

(h) 360.16 – 420.16 day, 16 – 20 hour

Figure A65: The angular distributions of the 3-D WIMP velocity observed at the location of the SNOLAB laboratory. 50 total events on average in each 4-hour daily shift in the 60-day observation periods of 177.66 – 237.66 day (a – d) and 360.16 – 420.16 (= 55.16) day (e – h) have been simulated.

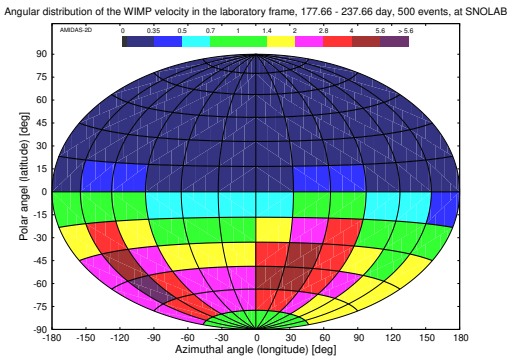

(a) 177.66 – 237.66 day, 22 – 2 hour

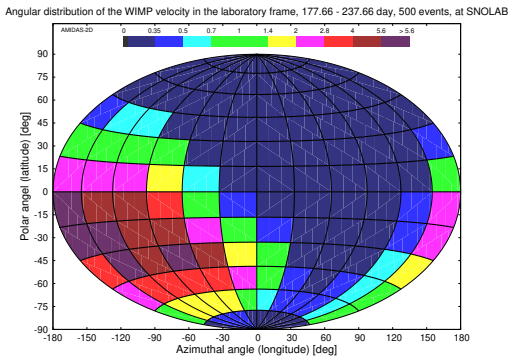

(b) 177.66 – 237.66 day, 4 – 8 hour

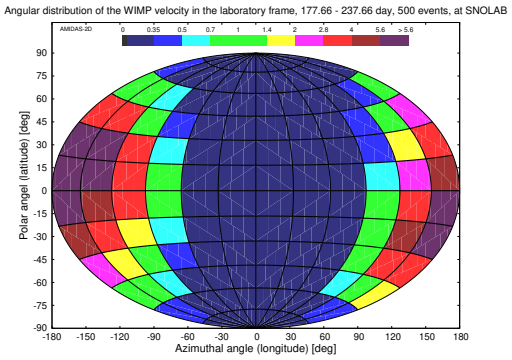

(c) 177.66 – 237.66 day, 10 – 14 hour

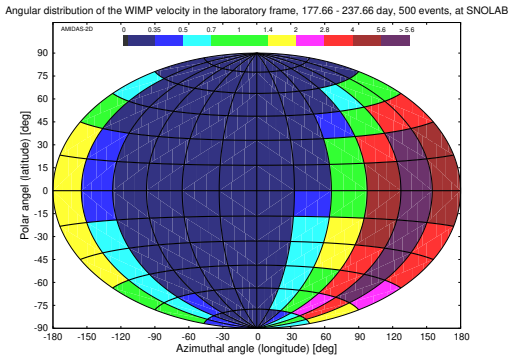

(d) 177.66 – 237.66 day, 16 – 20 hour

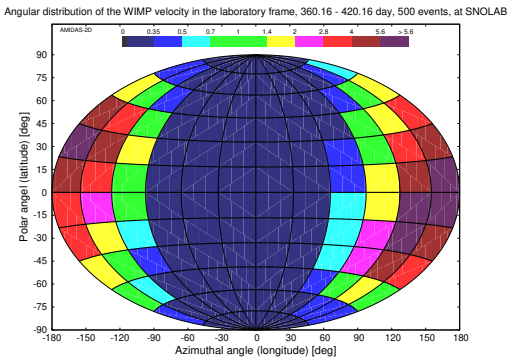

(e) 360.16 – 420.16 day, 22 – 2 hour

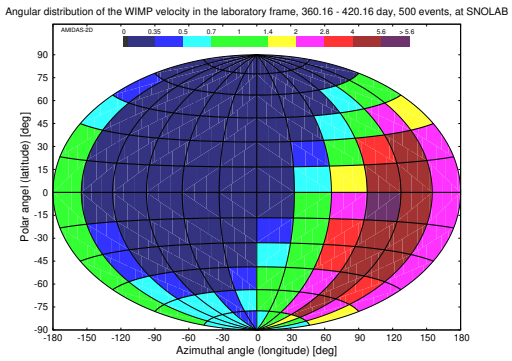

(f) 360.16 – 420.16 day, 4 – 8 hour

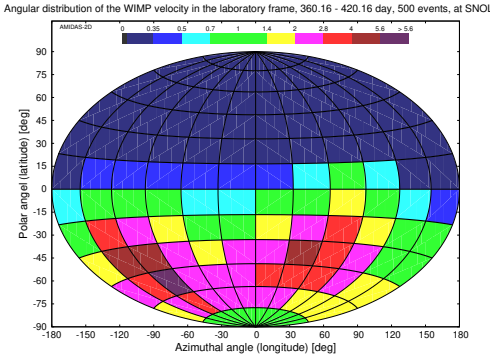

(g) 360.16 – 420.16 day, 10 – 14 hour

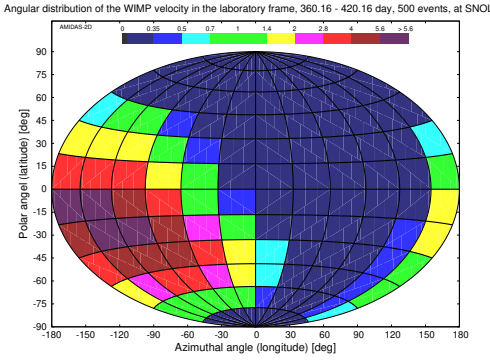

(h) 360.16 – 420.16 day, 16 – 20 hour

Figure A66: As in Figs. A65, except that 500 total events on average in each 4-hour daily shift in the 60-day observation periods have been simulated.

B.11 Stawell Underground Physics Laboratory (SUPL)

Central date (observation period) (day)	Most–event directions	
	50 events	500 events
0 – 365	—	—
49.49 (19.49 – 79.49)	30°S – 30°N 120°E – 120°W	$\underline{\underline{45°S}}$ – 30°N 120°E – 120°W
140.74 (110.74 – 170.74)	30°S – 60°N 180° – 120°W	$\underline{\underline{45°S}}$ – 60°N 150°W – $\underline{\underline{90°W}}$
231.99 (201.99 – 261.99)	30°N – 60°N 120°W – 60°W + 120°E – 180°	$\underline{\underline{15°N}}$ – 60°N, 120°W – 60°W 30°N – 60°N, 120°E – 150°E
323.24 (293.24 – 353.24)	0° – 60°N 60°E – 180°	$\underline{\underline{15°S}}$ – 45°N 60°E – 180°

Table A13: The summary of the directions of the simulated 3-D WIMP velocity with the highest event numbers ($>$ 4 times of the all–sky average value) in the horizontal coordinate system in one entire year and four advanced seasons at the location of the SUPL laboratory (37.07°S, 142.81°E). 50 and 500 total events on average in each observation period of 60 days have been simulated.

Remark: as at the Boulby laboratory, with only $\mathcal{O}(50)$ total WIMP events one could already observe two separate high–WIMP–flux bins in the angular distribution pattern in the horizontal coordinate system of the SUPL laboratory shown in Fig. A67(d); with $\mathcal{O}(500)$ total events and a higher analysis resolution, these two hot–points could be identified more clearly (see Fig. A68(d)).

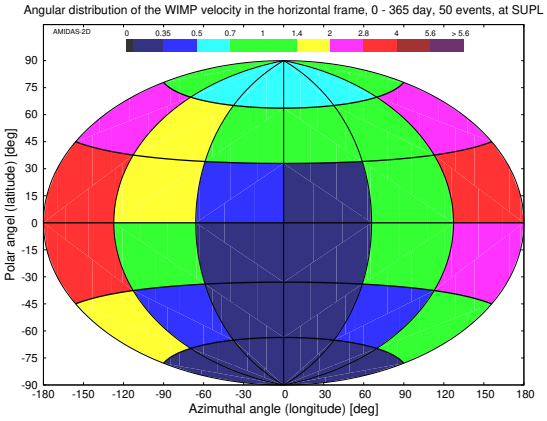

(a) 0 – 365 day

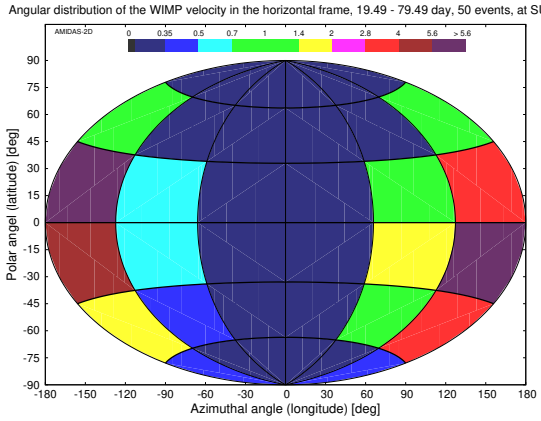

(b) 19.49 – 79.49 day

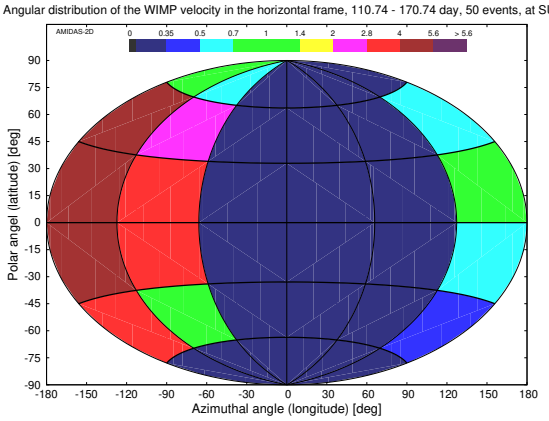

(c) 110.74 – 170.74 day

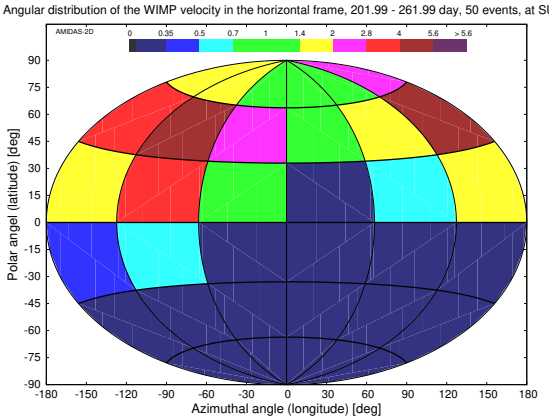

(d) 201.99 – 261.99 day

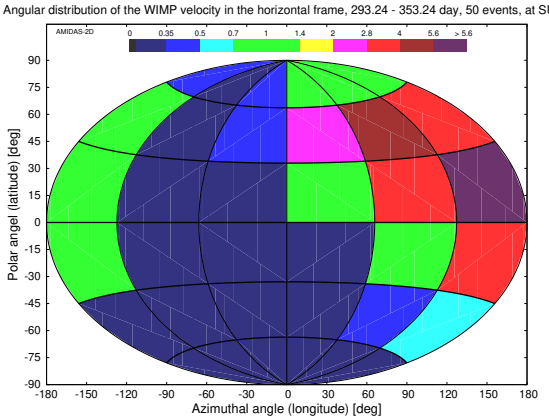

(e) 293.24 – 353.24 day

Figure A67: The angular distributions of the 3-D WIMP velocity in the horizontal coordinate system at the location of the SUPL laboratory (37.07°S, 142.81°E). 50 total events on average in one entire year (a) and in each 60-day observation period of four advanced seasons (b – e) have been simulated.

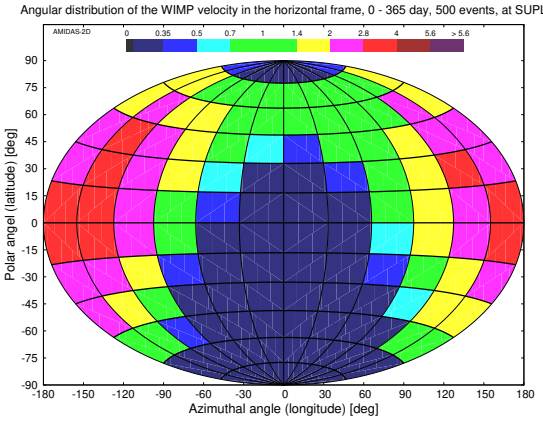

(a) 0 – 365 day

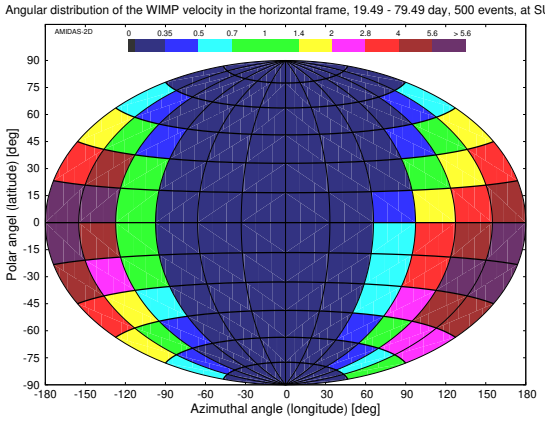

(b) 19.49 – 79.49 day

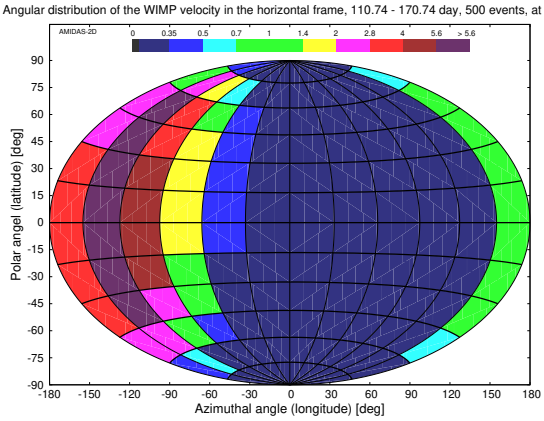

(c) 110.74 – 170.74 day

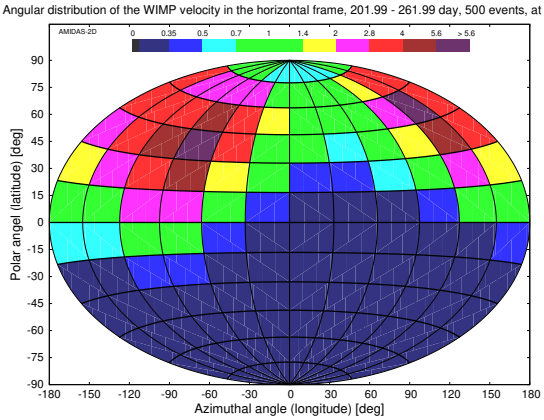

(d) 201.99 – 261.99 day

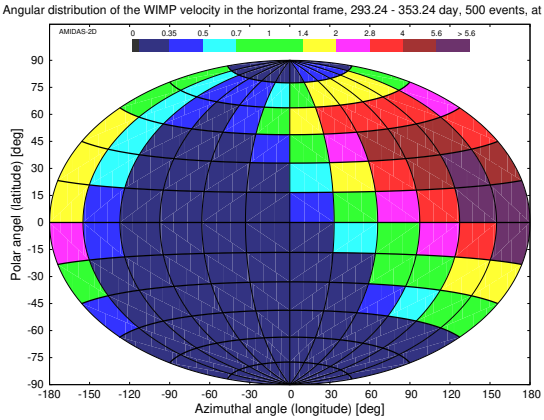

(e) 293.24 – 353.24 day

Figure A68: As in Figs. A67, except that 500 total events on average in one entire year (a) and in each 60-day observation period of four advanced seasons (b – e) have been simulated.

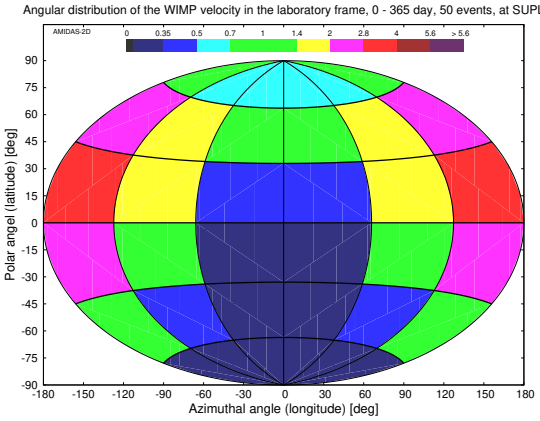

(a) 0 – 365 day

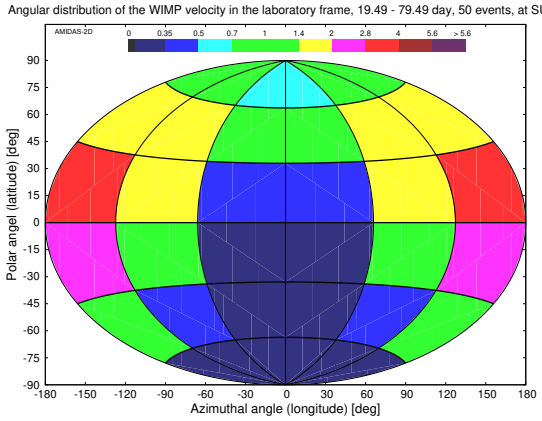

(b) 19.49 – 79.49 day

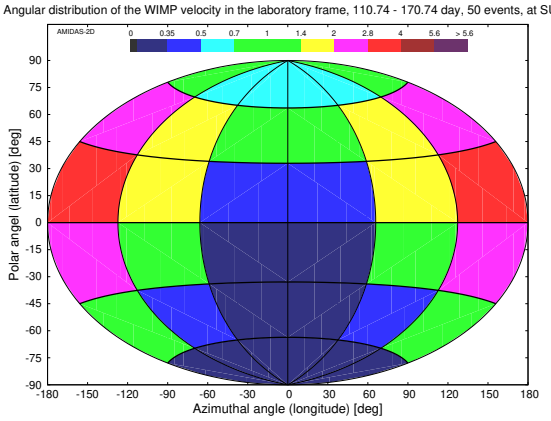

(c) 110.74 – 170.74 day

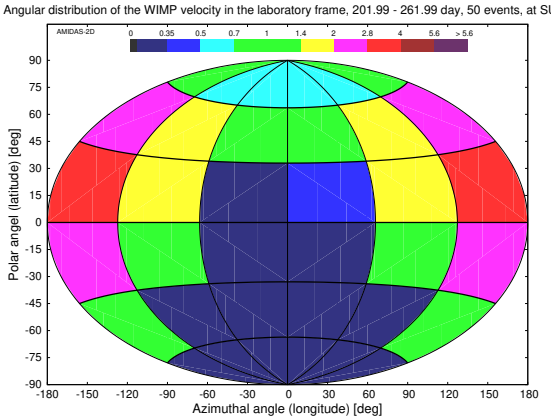

(d) 201.99 – 261.99 day

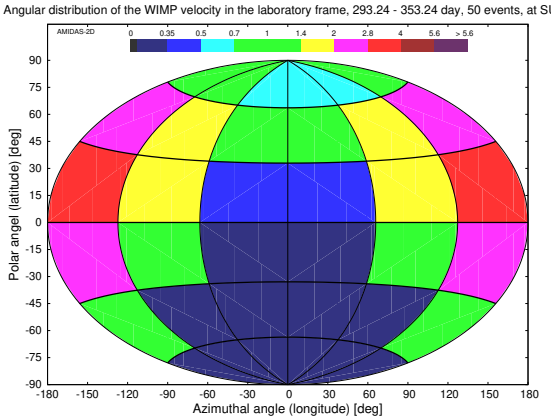

(e) 293.24 – 353.24 day

Figure A69: The angular distributions of the 3-D WIMP velocity transformed from events shown in Fig. A67 to the laboratory coordinate system at the location of the SUPL laboratory. All simulation setup and notations are the same as in Fig. A67.

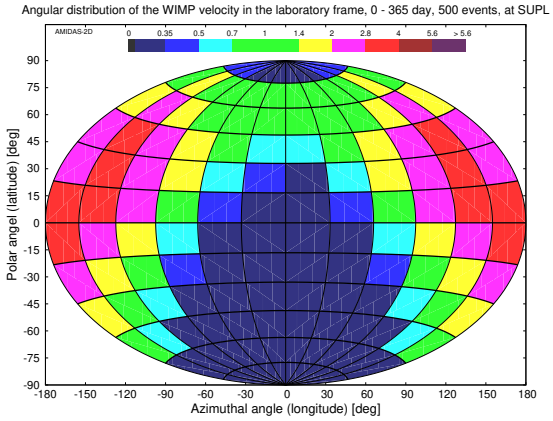

(a) 0 – 365 day

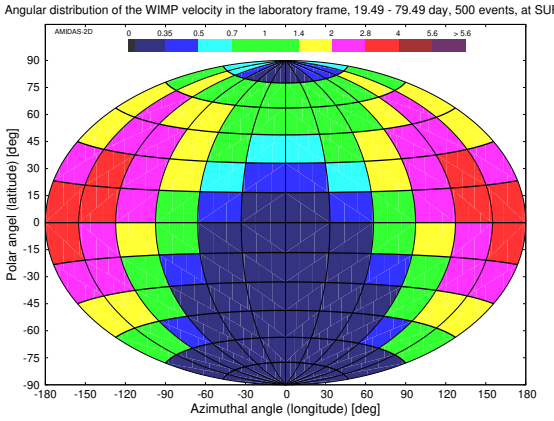

(b) 19.49 – 79.49 day

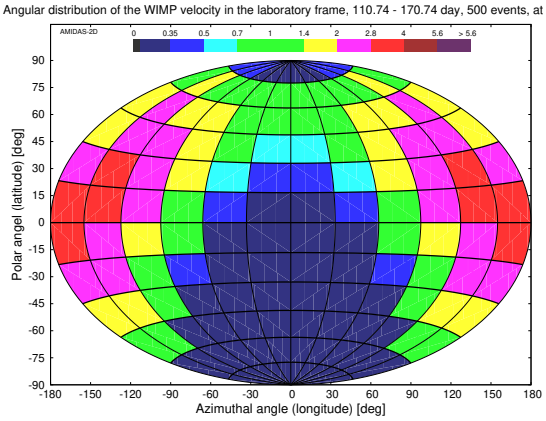

(c) 110.74 – 170.74 day

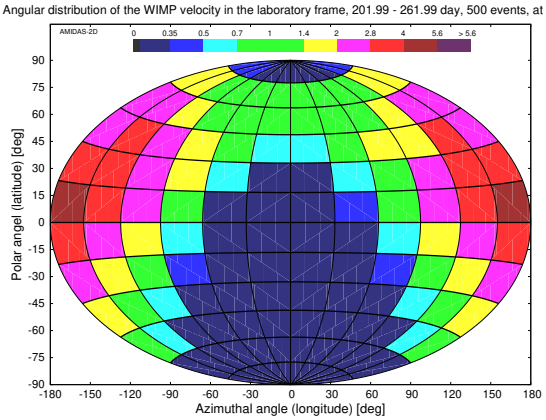

(d) 201.99 – 261.99 day

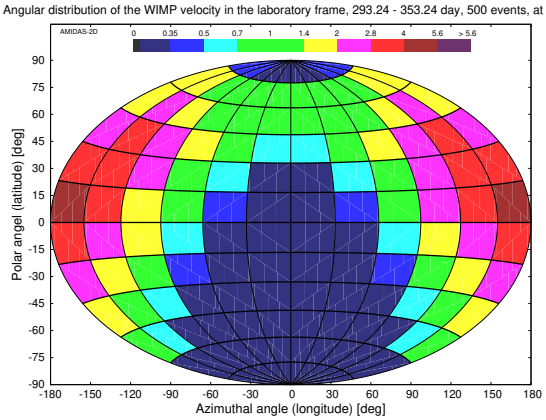

(e) 293.24 – 353.24 day

Figure A70: As in Figs. A69, except that 500 total events on average in one entire year (a) and in each 60-day observation period of four advanced seasons (b – e) have been simulated.

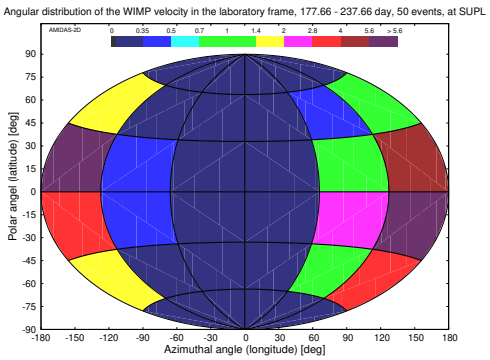

(a) 177.66 – 237.66 day, 22 – 2 hour

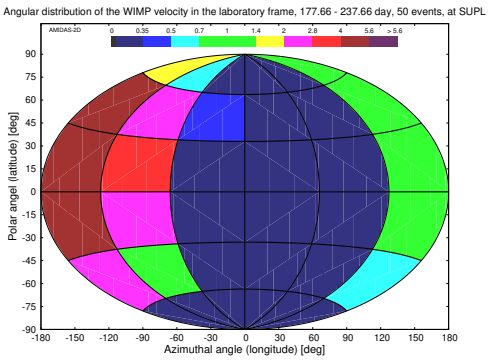

(b) 177.66 – 237.66 day, 4 – 8 hour

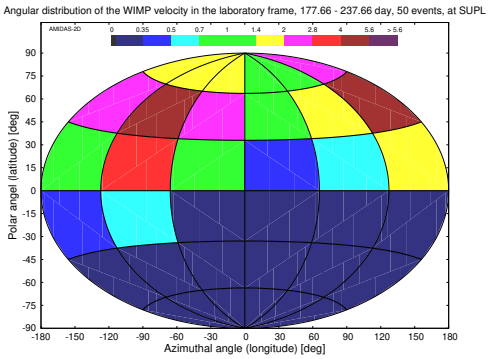

(c) 177.66 – 237.66 day, 10 – 14 hour

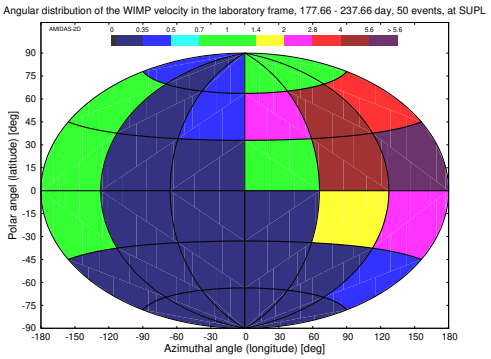

(d) 177.66 – 237.66 day, 16 – 20 hour

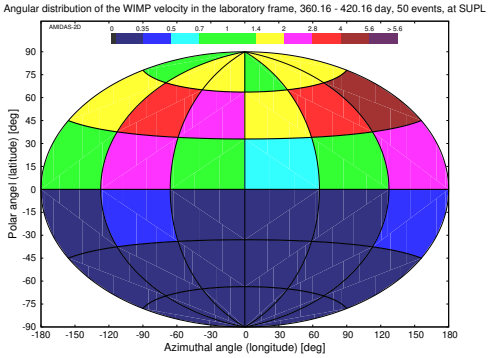

(e) 360.16 – 420.16 day, 22 – 2 hour

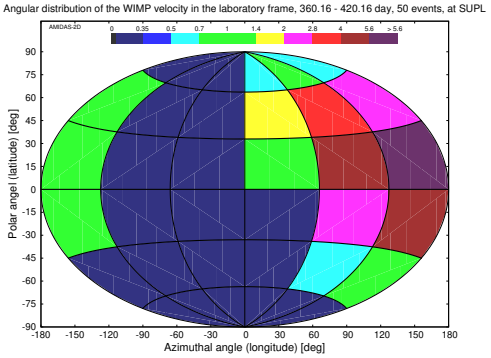

(f) 360.16 – 420.16 day, 4 – 8 hour

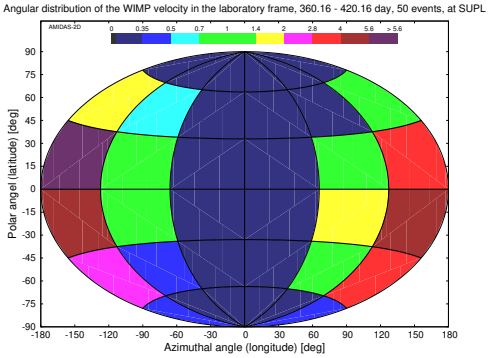

(g) 360.16 – 420.16 day, 10 – 14 hour

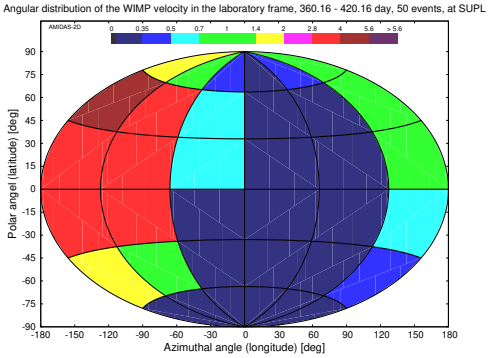

(h) 360.16 – 420.16 day, 16 – 20 hour

Figure A71: The angular distributions of the 3-D WIMP velocity observed at the location of the SUPL laboratory. 50 total events on average in each 4-hour daily shift in the 60-day observation periods of 177.66 – 237.66 day (a – d) and 360.16 – 420.16 (= 55.16) day (e – h) have been simulated.

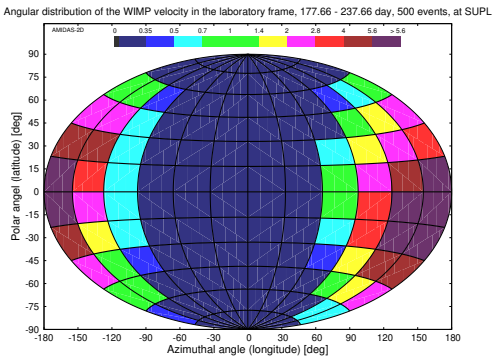

(a) 177.66 – 237.66 day, 22 – 2 hour

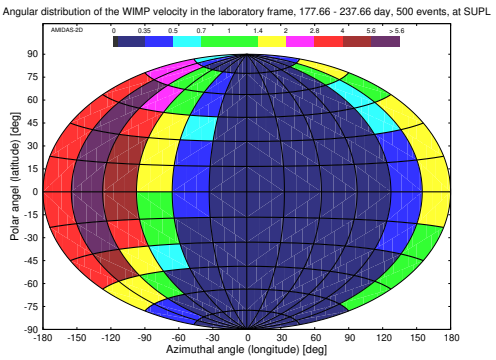

(b) 177.66 – 237.66 day, 4 – 8 hour

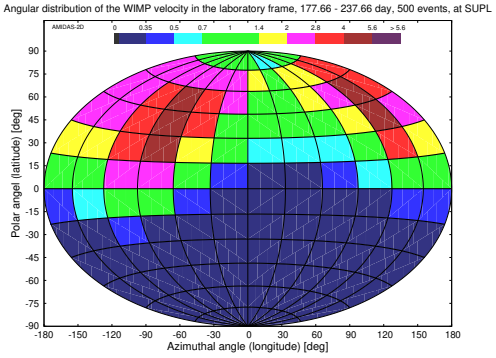

(c) 177.66 – 237.66 day, 10 – 14 hour

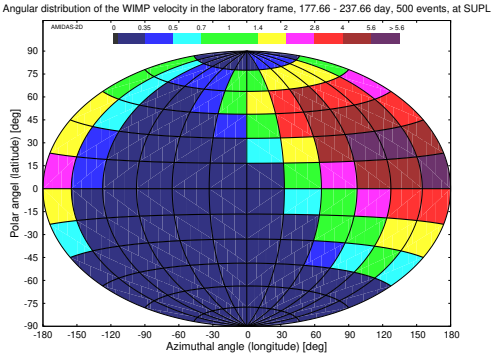

(d) 177.66 – 237.66 day, 16 – 20 hour

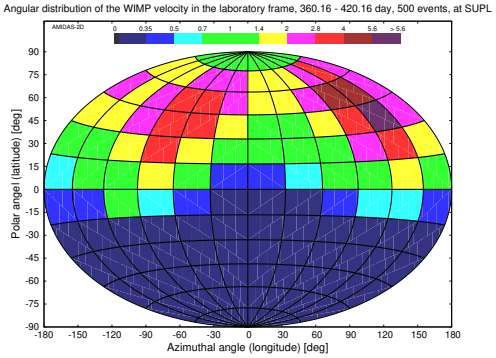

(e) 360.16 – 420.16 day, 22 – 2 hour

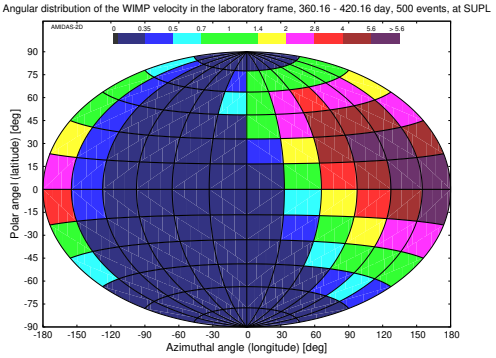

(f) 360.16 – 420.16 day, 4 – 8 hour

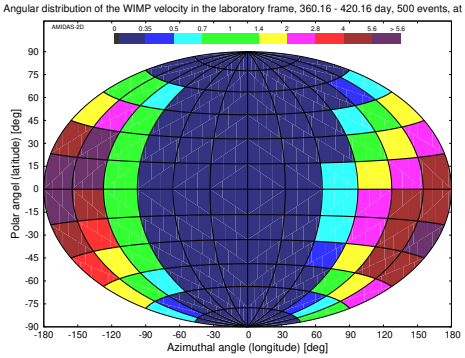

(g) 360.16 – 420.16 day, 10 – 14 hour

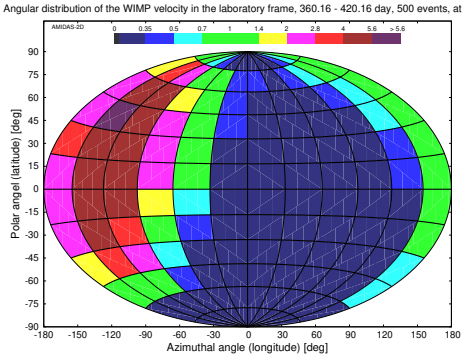

(h) 360.16 – 420.16 day, 16 – 20 hour

Figure A72: As in Figs. A71, except that 500 total events on average in each 4-hour daily shift in the 60-day observation periods have been simulated.

C Annual modulation of the radial WIMP velocity distribution in four normal seasons

For the sake of completeness and readers' reference, in this section, we provide the reconstruction results of the annual modulation of the radial distribution of the 3-D WIMP velocity in the Equatorial coordinate system in the observation periods of four normal seasons. 50 and 500 total events on average in each 60-day observation period have been simulated.

C.1 With the one–parameter velocity distribution $f_{1,\mathrm{sh},v_0}(v; v_0)$

As in Sec. 4.3.1, we start our reconstruction by using the one–parameter velocity distribution $f_{1,\mathrm{sh},v_0}(v; v_0)$ given by Eq. (24) with v_0 as the fitting parameter scanned in the ranges of 160 km/s $\leq v_0 \leq$ 270 km/s (50 events) and 190 km/s $\leq v_0 \leq$ 240 km/s (500 events) as well as the constraint that $v_\mathrm{e} = 1.05\, v_0$.

In Figs. A73 and A74, we show the reconstructed radial distributions of the 3-D WIMP velocity and the 1(2)σ statistical uncertainty bands by using $f_{1,\mathrm{sh},v_0}(v; v_0)$ as well as the distributions of the fitting parameter v_0 in all simulated experiments with 50 and 500 total events on average in each 60-day observation period of four normal seasons, respectively. Comparing with our results of the advanced seasons shown in Figs. 30 and 46, one can see here, as expected, an *asymmetric* periodic variation of the best–fit values of the fitting parameter v_0 (see the summary of the reconstructed results and the 1(2)σ statistical uncertainty ranges of the median values in Table A14).

C.2 With the v_0–fixed velocity distribution $f_{1,\mathrm{sh},v_\mathrm{e}}(v; v_\mathrm{e})$

As in Sec. 4.3.2, we now consider the v_0–fixed velocity distribution $f_{1,\mathrm{sh},v_\mathrm{e}}(v; v_\mathrm{e})$ given by Eq. (26) with v_e as the fitting parameter scanned in the ranges of 90 km/s $\leq v_\mathrm{e} \leq$ 330 km/s (50 events) and 180 km/s $\leq v_\mathrm{e} \leq$ 270 km/s (500 events) as well as the input condition that $v_0 = 220$ km/s.

In Figs. A75 and A76, we show the reconstructed radial distributions of the 3-D WIMP velocity and the 1(2)σ statistical uncertainty bands by using $f_{1,\mathrm{sh},v_\mathrm{e}}(v; v_\mathrm{e})$ as well as the distributions of the fitting parameter v_e in all simulated experiments with 50 and 500 total events on average in each 60-day observation period of four normal seasons, respectively. As in Sec. C.1, by comparing with our results of the advanced seasons shown in Figs. 31 and 47, we can also find here an asymmetric periodic variation of the best–fit values of the fitting parameter v_e (see the summary of the reconstructed results and the 1(2)σ statistical uncertainty ranges of the median values in Table A15).

C.3 With the simplified velocity distribution $f_{1,\mathrm{sh}}(v; v_0, v_\mathrm{e})$

As in Sec. 4.3.3, we release now the constraints on v_0 and v_e and consider the simplified velocity distribution $f_{1,\mathrm{sh}}(v; v_0, v_\mathrm{e})$ given by Eq. (27) with v_0 and v_e as two free fitting parameters scanned in the ranges of 80 km/s $\leq v_0 \leq$ 340 km/s (50 events) and 140 km/s $\leq v_0 \leq$ 240 km/s (500 events) as well as 0 $\leq v_\mathrm{e} \leq$ 380 km/s (50 events) and 200 km/s $\leq v_\mathrm{e} \leq$ 310 km/s (500 events), respectively.

In Figs. A77 and A78, we show the reconstructed radial distributions of the 3-D WIMP velocity and the 1(2)σ statistical uncertainty bands by using $f_{1,\mathrm{sh}}(v; v_0, v_\mathrm{e})$ as well as the distributions of the fitting parameters v_0 and v_e in all simulated experiments on the $v_0 - v_\mathrm{e}$ plane with 50 and 500 total events on average in each 60-day observation period of four normal seasons,

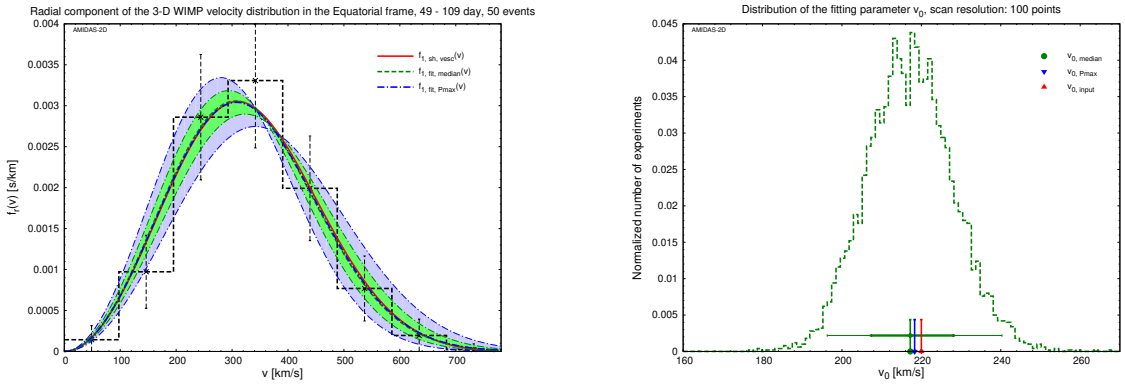

(a) 49.0 – 109.0 day

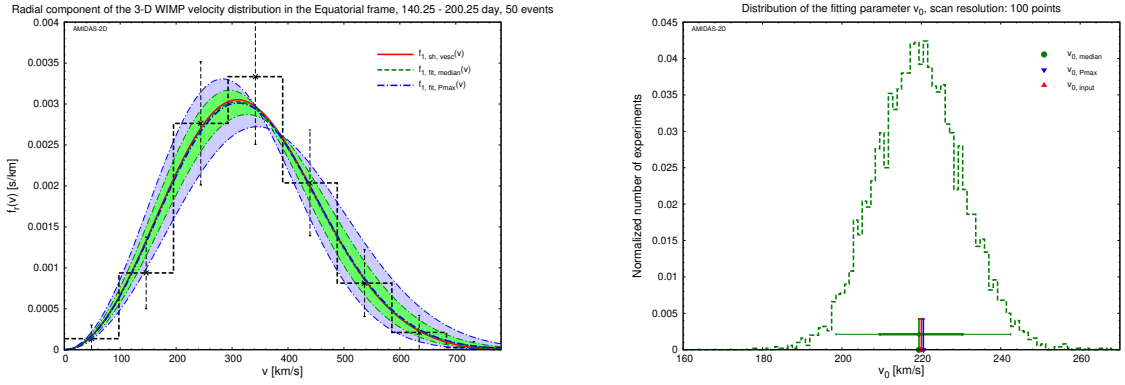

(b) 140.25 – 200.25 day

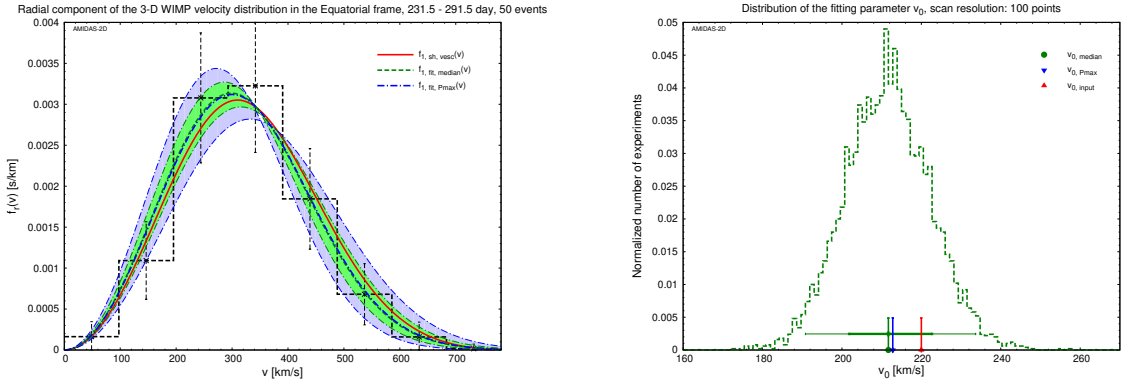

(c) 231.50 – 291.50 day

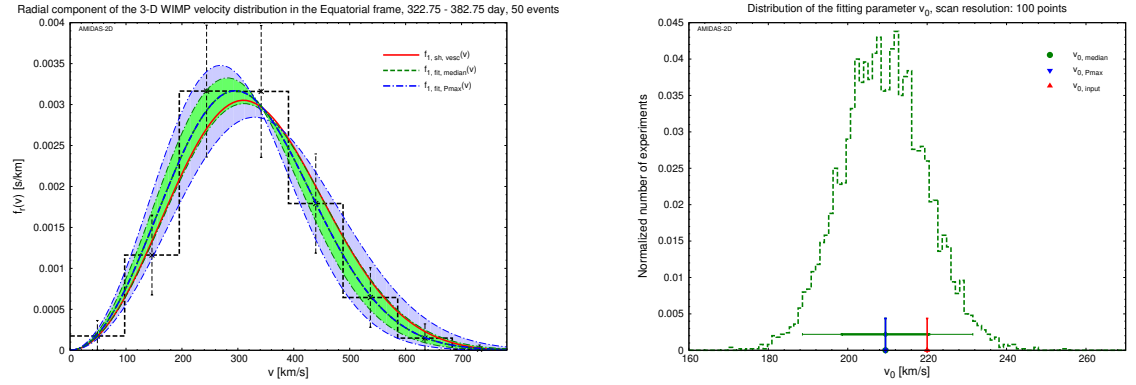

(d) 322.75 – 382.75 day

Figure A73: As in Figs. 30, reconstructed with the one–parameter velocity distribution $f_{1,\mathrm{sh},v_0}(v;v_0)$, except that four 60-day observation periods of the normal seasons have been considered.

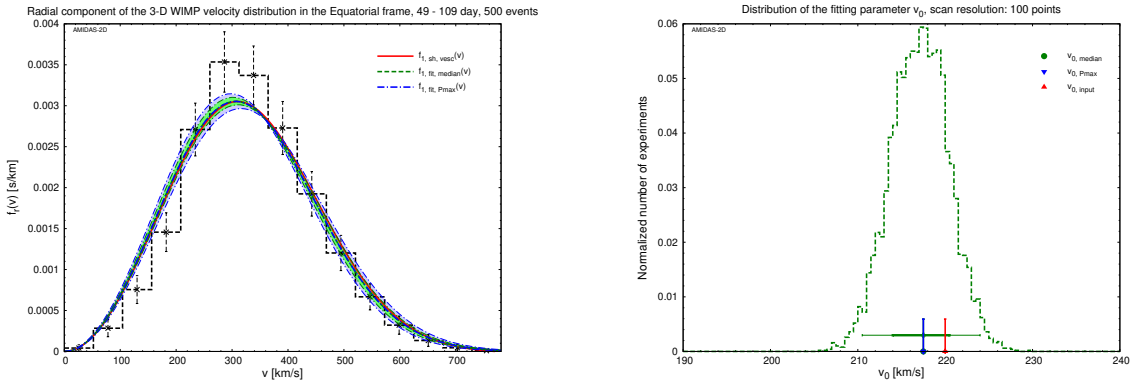

(a) 49.0 – 109.0 day

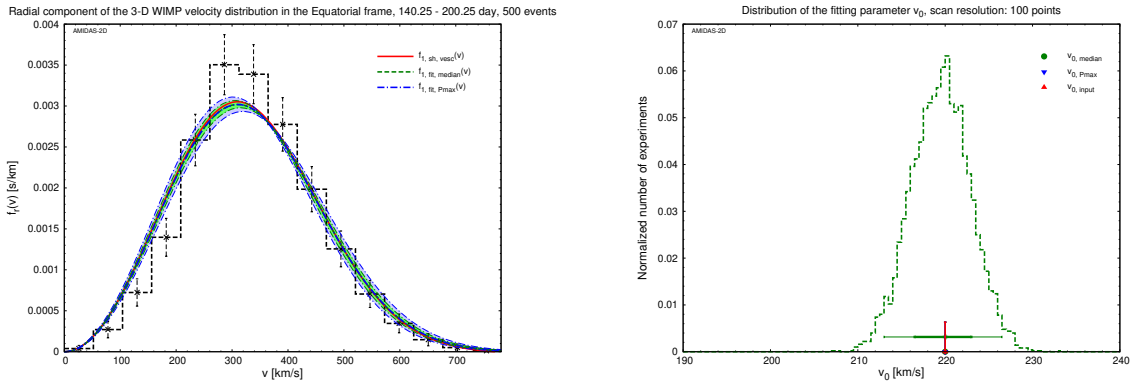

(b) 140.25 – 200.25 day

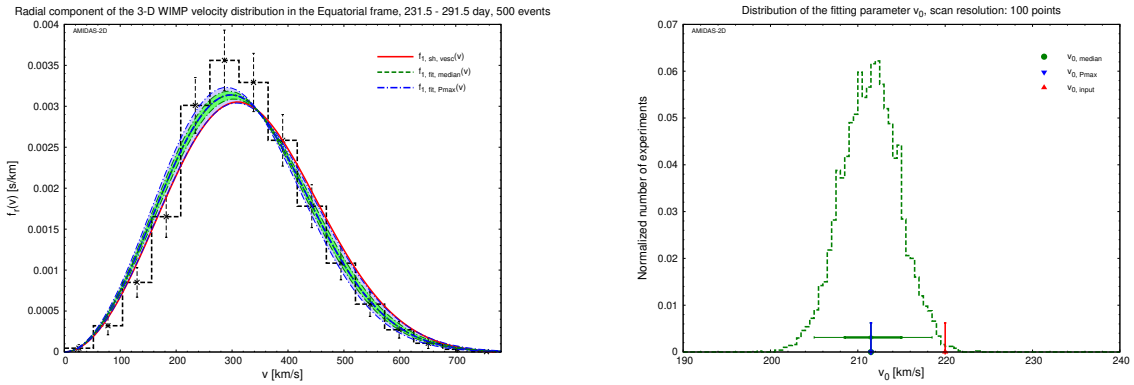

(c) 231.50 – 291.50 day

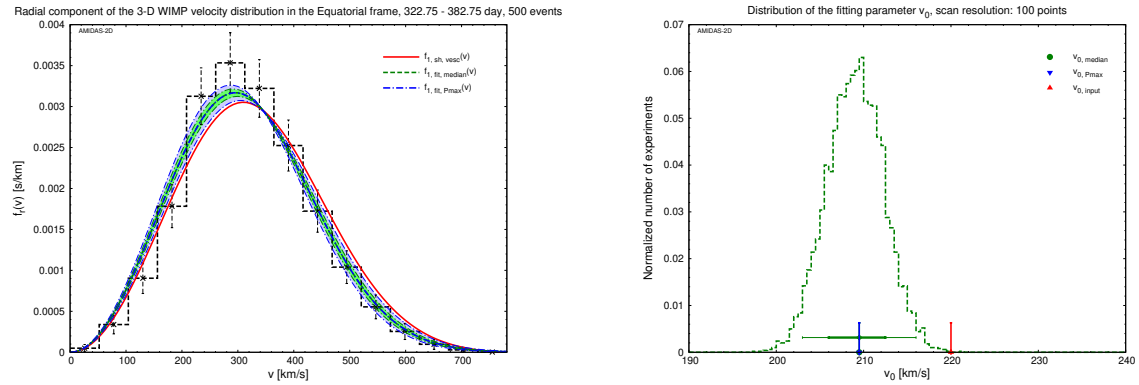

(d) 322.75 – 382.75 day

Figure A74: As in Figs. A73, except that 500 total events on average in one 60-day observation period have been simulated. Remind that the scanning range of the fitting parameter v_0 is shrunk to between 190 km/s and 240 km/s.

Fitting distribution: one–parameter velocity distribution $f_{1,\mathrm{sh},v_0}(v;v_0)$					
Central date (observation period) (day)	Parameter	Max. P_{median}	Median	1σ range	2σ range
79.0 (49.0 – 109.0)	v_0 [km/s]	218.3	$217.2\,^{+11.0}_{-\ 9.9}\,(^{+23.1}_{-20.9})$	[207.3, 228.2]	[196.3, 240.3]
170.25 (140.25 – 200.25)	v_0 [km/s]	220.5	$219.4\,^{+11.0}_{-\ 9.9}\,(^{+23.1}_{-20.9})$	[209.5, 230.4]	[198.5, 242.5]
261.5 (231.50 – 291.50)	v_0 [km/s]	212.8	$211.7\,^{+11.0}_{-\ 9.9}\,(^{+22.0}_{-20.9})$	[201.8, 222.7]	[190.8, 233.7]
352.75 (322.75 – 382.75)	v_0 [km/s]	209.5	$209.5 \pm 11.0\,(^{+22.0}_{-20.9})$	[198.5, 220.5]	[188.6, 231.5]
50 total events on average in one observation period of 60 days					

Central date (observation period) (day)	Parameter	Max. P_{median}	Median	1σ range	2σ range
79.0 (49.0 – 109.0)	v_0 [km/s]	217.5	$217.5\,^{+3.0}_{-3.5}\,(^{+6.5}_{-7.0})$	[214.0, 220.5]	[210.5, 224.0]
170.25 (140.25 – 200.25)	v_0 [km/s]	220.0	$220.0\,^{+3.0}_{-3.5}\,(^{+6.5}_{-7.0})$	[216.5, 223.0]	[213.0, 226.5]
261.5 (231.50 – 291.50)	v_0 [km/s]	211.5	$211.5\,^{+3.5}_{-3.0}\,(^{+7.0}_{-6.5})$	[208.5, 215.0]	[205.0, 218.5]
352.75 (322.75 – 382.75)	v_0 [km/s]	209.5	$209.5\,^{+3.0}_{-3.5}\,(\pm 6.5)$	[206.0, 212.5]	[203.0, 216.0]
500 total events on average in one observation period of 60 days					

Table A14: The summary of the reconstructed results of the fitting parameter v_0 and their $1(2)\sigma$ statistical uncertainty ranges of the median values by using the one–parameter velocity distribution $f_{1,\mathrm{sh},v_0}(v;v_0)$ with 50 (upper) and 500 (lower) total events on average in each 60–day observation period of the normal seasons.

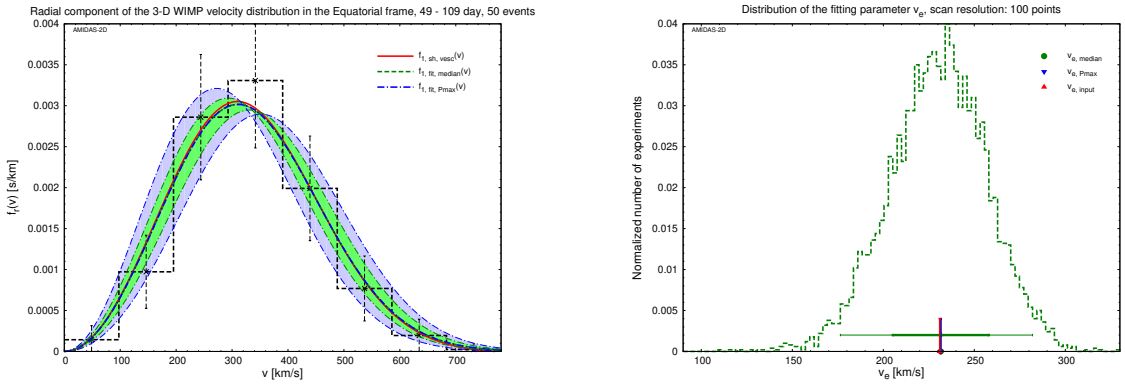

(a) 49.0 – 109.0 day

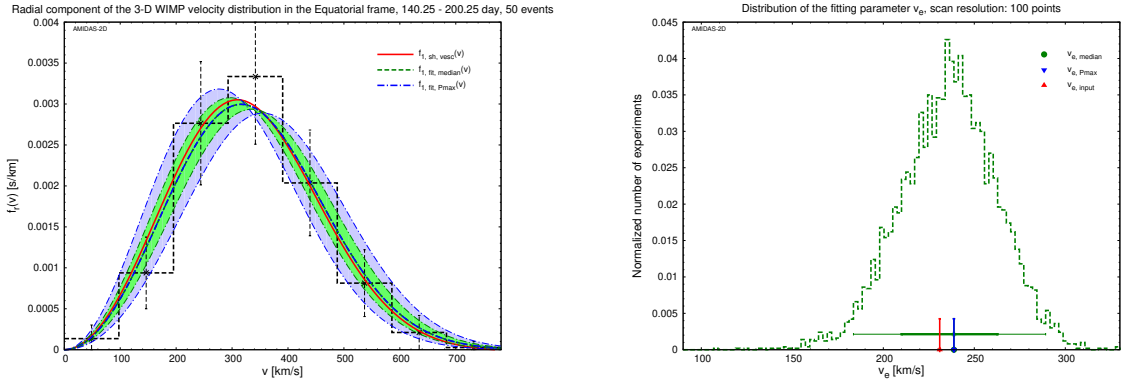

(b) 140.25 – 200.25 day

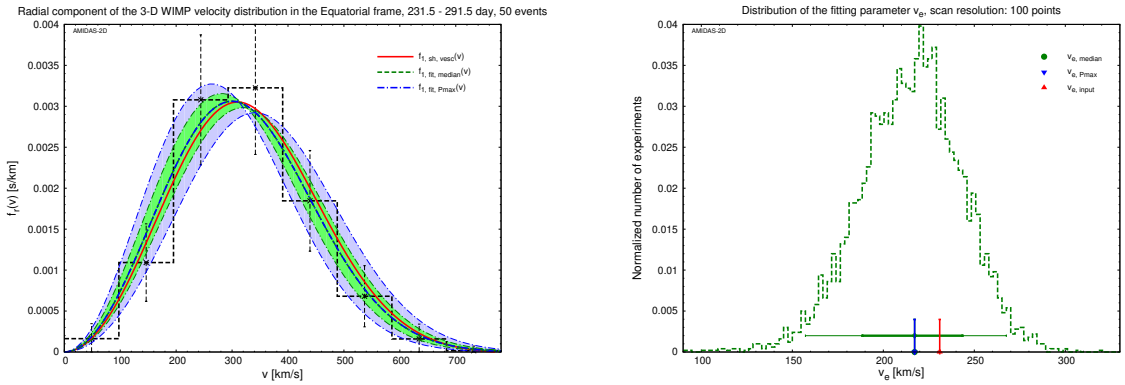

(c) 231.50 – 291.50 day

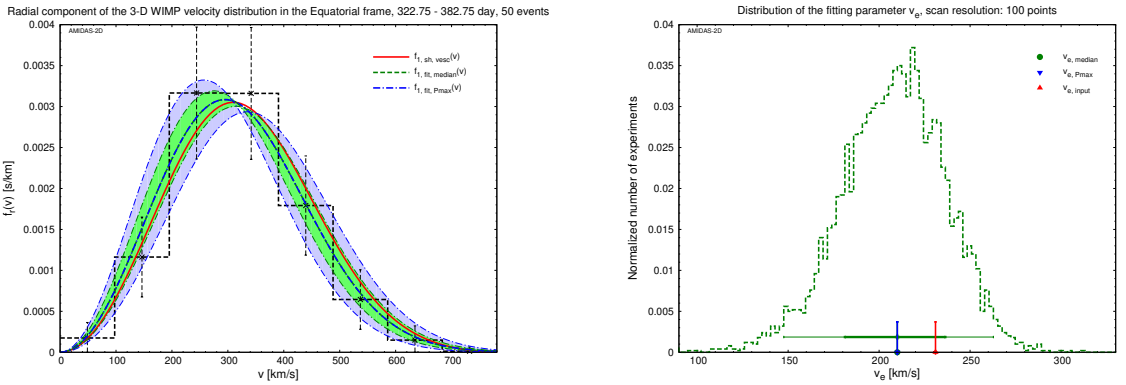

(d) 322.75 – 382.75 day

Figure A75: As in Figs. 31, reconstructed with the v_0–fixed velocity distribution $f_{1,\mathrm{sh},v_\mathrm{e}}(v;v_\mathrm{e})$, except that four 60-day observation periods of the normal seasons have been considered.

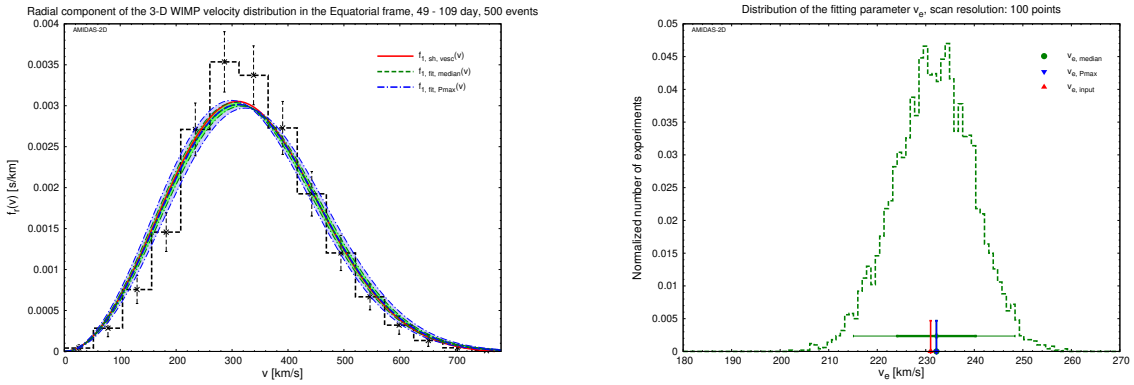

(a) 49.0 – 109.0 day

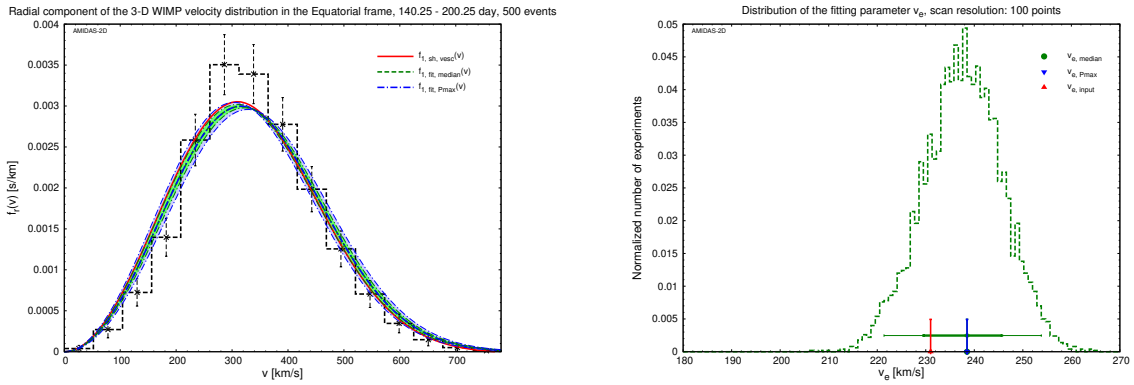

(b) 140.25 – 200.25 day

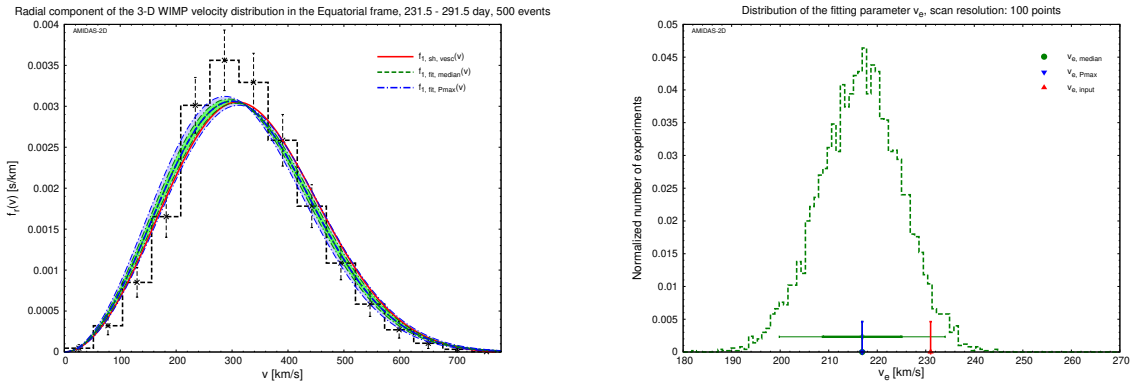

(c) 231.50 – 291.50 day

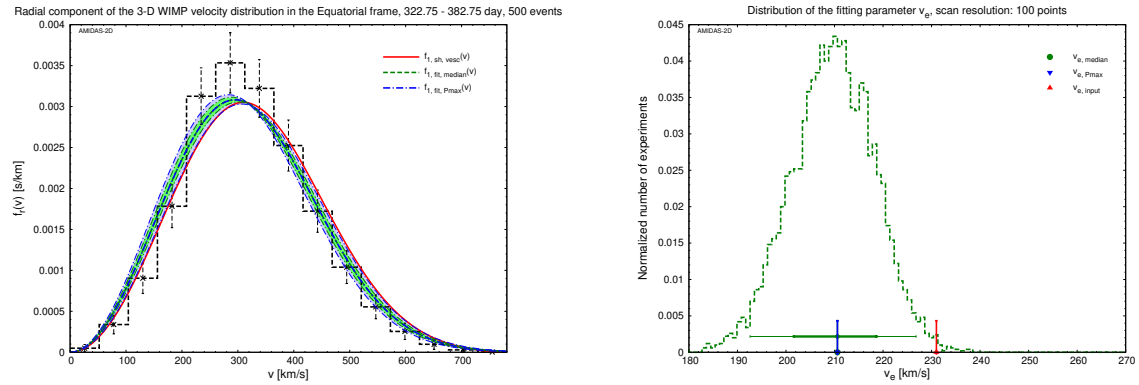

(d) 322.75 – 382.75 day

Figure A76: As in Figs. A75, except that 500 total events on average in one 60-day observation period have been simulated. Remind that the scanning range of the fitting parameter v_e is shrunk to between 180 km/s and 270 km/s.

Fitting distribution: v_0–fixed velocity distribution $f_{1,\mathrm{sh},v_\mathrm{e}}(v;v_\mathrm{e})$					
Central date (observation period) (day)	Parameter	Max. $\mathrm{P_{median}}$	Median	1σ range	2σ range
79.0 (49.0 – 109.0)	v_e [km/s]	231.6	$231.6 \pm 26.4\,(^{+50.4}_{-55.2})$	[205.2, 258.0]	[176.4, 282.0]
170.25 (140.25 – 200.25)	v_e [km/s]	238.8	$238.8\,^{+24.0}_{-28.8}\,(^{+50.4}_{-55.2})$	[210.0, 262.8]	[183.6, 289.2]
261.5 (231.50 – 291.50)	v_e [km/s]	217.2	$217.2\,^{+26.4}_{-28.8}\,(^{+50.4}_{-60.0})$	[188.4, 243.6]	[157.2, 267.6]
352.75 (322.75 – 382.75)	v_e [km/s]	210.0	$210.0\,^{+26.4}_{-28.8}\,(^{+52.8}_{-62.4})$	[181.2, 236.4]	[147.6, 262.8]
50 total events on average in one observation period of 60 days					

Central date (observation period) (day)	Parameter	Max. $\mathrm{P_{median}}$	Median	1σ range	2σ range
79.0 (49.0 – 109.0)	v_e [km/s]	232.2	$232.2 \pm 8.1\,(^{+16.2}_{-17.1})$	[224.1, 240.3]	[215.1, 248.4]
170.25 (140.25 – 200.25)	v_e [km/s]	238.5	$238.5\,^{+7.2}_{-9.0}\,(^{+15.3}_{-17.1})$	[229.5, 245.7]	[221.4, 253.8]
261.5 (231.50 – 291.50)	v_e [km/s]	216.9	$216.9 \pm 8.1\,(\pm 17.1)$	[208.8, 225.0]	[199.8, 234.0]
352.75 (322.75 – 382.75)	v_e [km/s]	210.6	$210.6\,^{+8.1}_{-9.0}\,(^{+16.2}_{-18..0})$	[201.6, 218.7]	[192.6, 226.8]
500 total events on average in one observation period of 60 days					

Table A15: The summary of the reconstructed results of the fitting parameter v_e and their $1(2)\sigma$ statistical uncertainty ranges of the median values by using the v_0–fixed velocity distribution $f_{1,\mathrm{sh},v_\mathrm{e}}(v;v_\mathrm{e})$ with 50 (upper) and 500 (lower) total events on average in each 60–day observation period of the normal seasons.

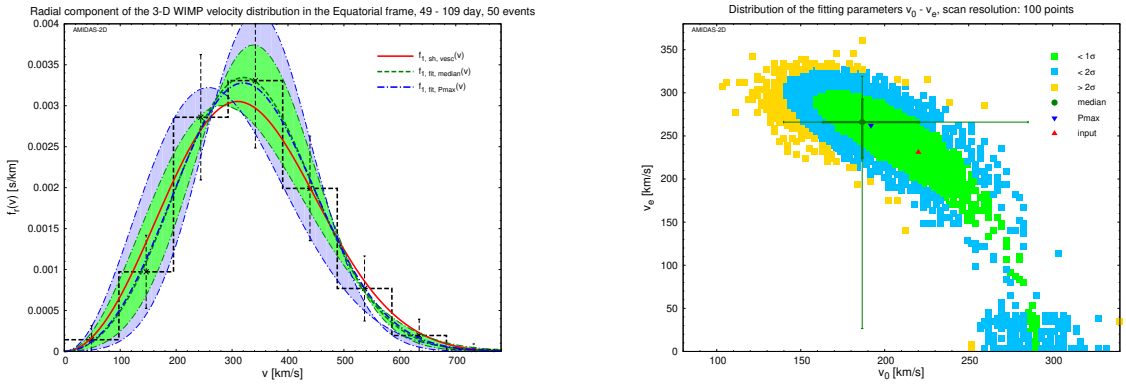

(a) 49.0 – 109.0 day

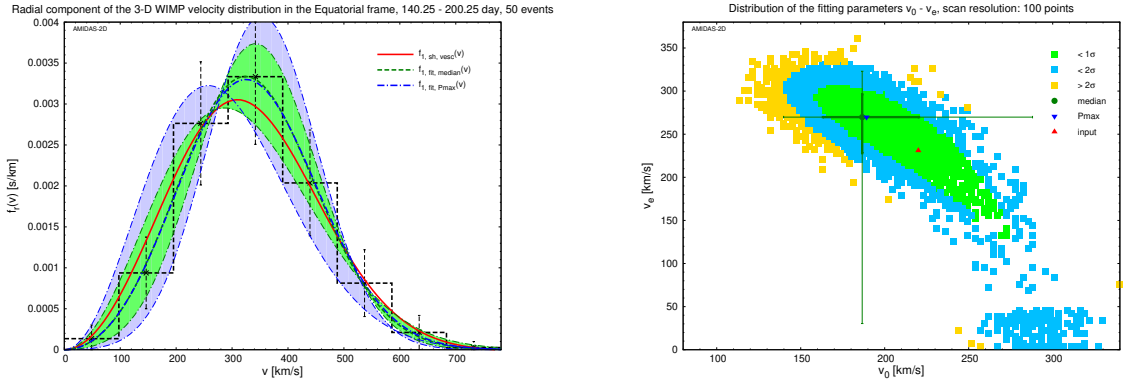

(b) 140.25 – 200.25 day

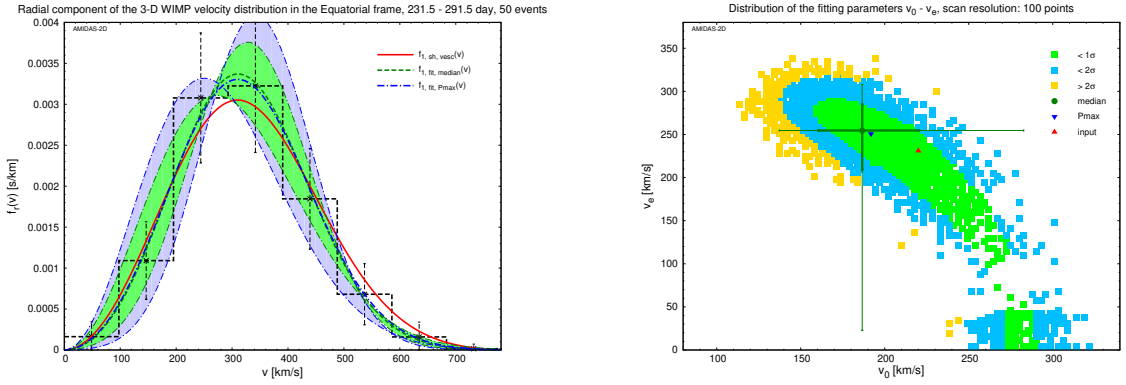

(c) 231.50 – 291.50 day

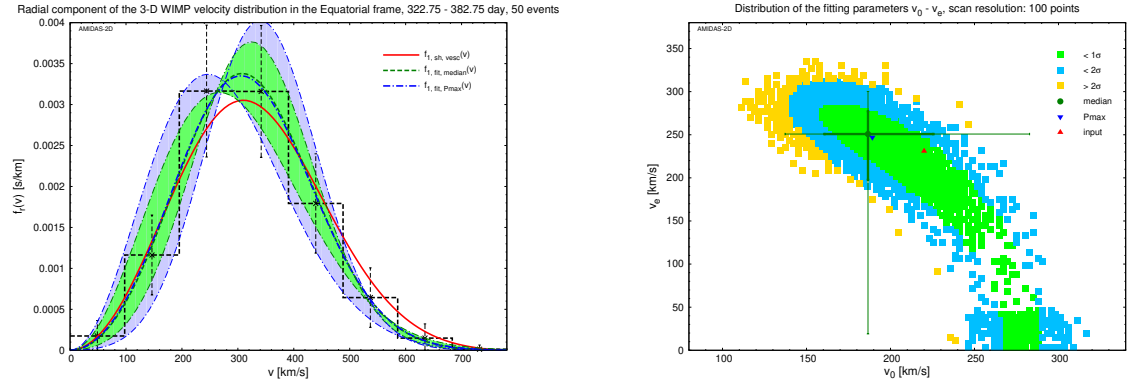

(d) 322.75 – 382.75 day

Figure A77: As in Figs. 32, reconstructed with the simplified velocity distribution $f_{1,\mathrm{sh}}(v; v_0, v_\mathrm{e})$, except that four 60-day observation periods of the normal seasons have been considered.

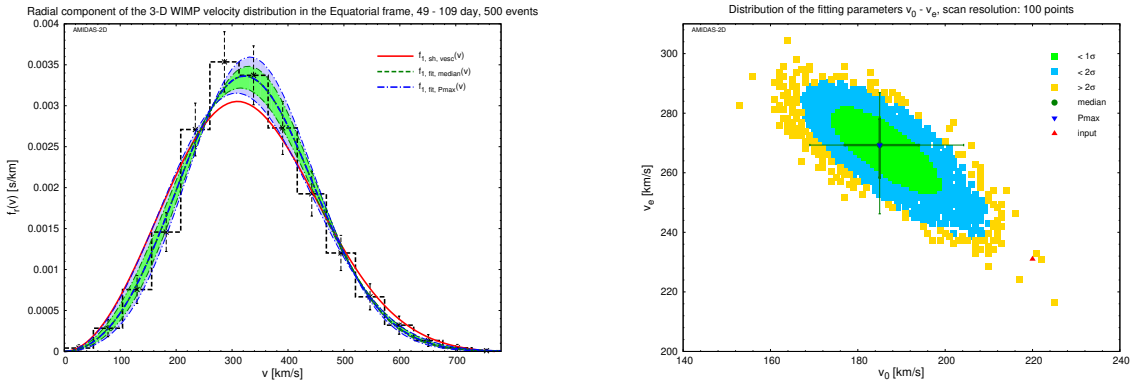

(a) 49.0 – 109.0 day

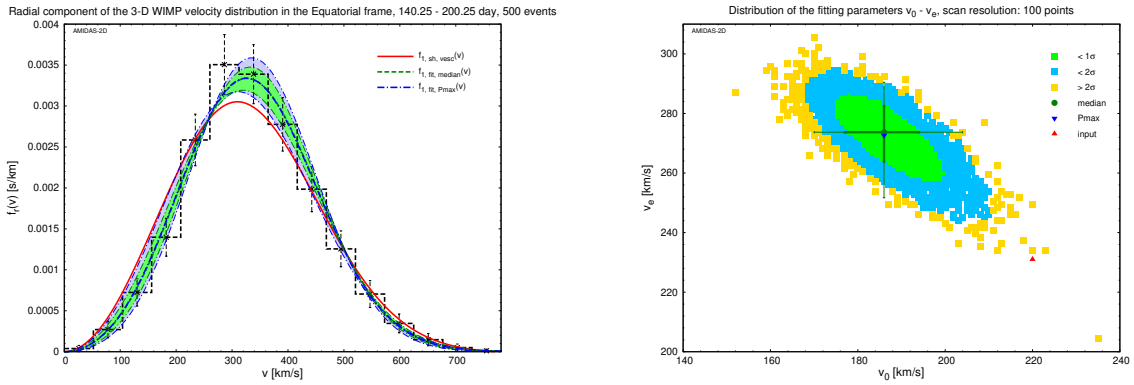

(b) 140.25 – 200.25 day

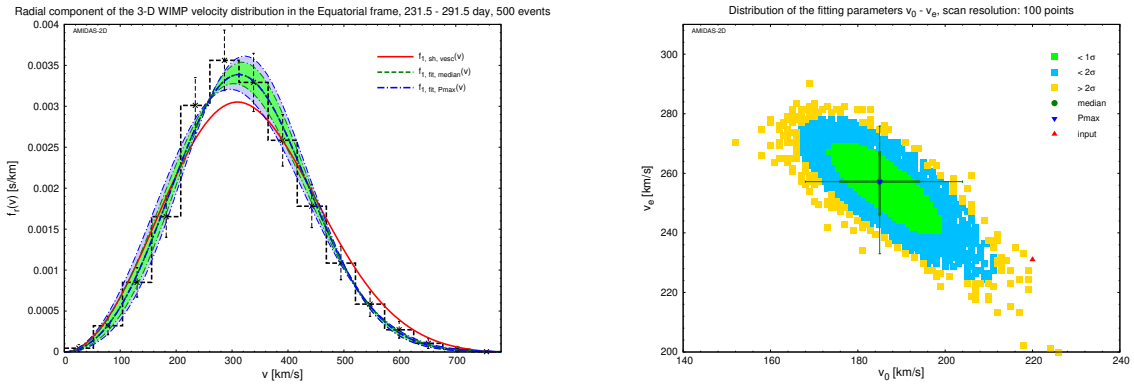

(c) 231.50 – 291.50 day

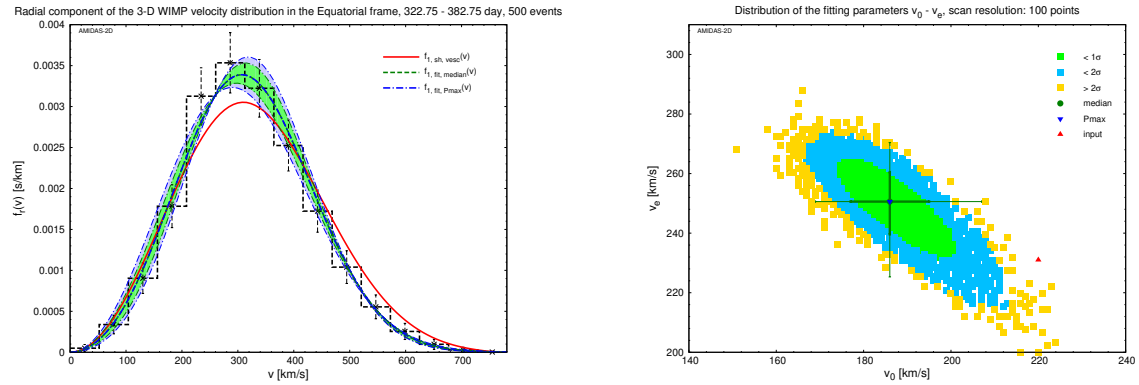

(d) 322.75 – 382.75 day

Figure A78: As in Figs. A77, except that 500 total events on average in one 60-day observation period have been simulated. Remind that the scanning ranges of the fitting parameters v_0 and v_e are shrunk to between 140 km/s and 240 km/s and between 200 km/s and 310 km/s, respectively.

Fitting distribution: simplified velocity distribution $f_{1,\mathrm{sh}}(v; v_0, v_\mathrm{e})$					
Central date (observation period) (day)	Parameter	Max. $\mathrm{P}_{\mathrm{median}}$	Median	1σ range	2σ range
79.0 (49.0 – 109.0)	v_0 [km/s]	191.8	$186.6\,^{+33.8}_{-23.4}\,(^{+98.8}_{-46.8})$	[163.2, 220.4]	[139.8, 285.4]
	v_e [km/s]	262.2	$266.0\,^{+26.6}_{-41.8}\,(^{+\ 53.2}_{-239.4})$	[224.2, 292.6]	[26.6, 319.2]
170.25 (140.25 – 200.25)	v_0 [km/s]	189.2	$186.6\,^{+33.8}_{-23.4}\,(^{+101.4}_{-\ 46.8})$	[163.2, 220.4]	[139.8, 288.0]
	v_e [km/s]	269.8	$269.8\,^{+26.6}_{-41.8}\,(^{+\ 53.2}_{-239.4})$	[228.0, 296.4]	[30.4, 323.0]
261.5 (231.50 – 291.50)	v_0 [km/s]	191.8	$186.6\,^{+33.8}_{-26.0}\,(^{+96.2}_{-49.4})$	[160.6, 220.4]	[137.2, 282.8]
	v_e [km/s]	250.8	$254.6\,^{+30.4}_{-45.6}\,(^{+\ 53.2}_{-231.8})$	[209.0, 285.0]	[22.8, 307.8]
352.75 (322.75 – 382.75)	v_0 [km/s]	189.2	$186.6\,^{+39.0}_{-26.0}\,(^{+96.2}_{-49.4})$	[160.6, 225.6]	[137.2, 282.8]
	v_e [km/s]	247.0	$250.8\,^{+26.6}_{-53.2}\,(^{+\ 49.4}_{-231.8})$	[197.6, 277.4]	[19.0, 300.2]
50 total events on average in one observation period of 60 days					

Central date (observation period) (day)	Parameter	Max. $\mathrm{P}_{\mathrm{median}}$	Median	1σ range	2σ range
79.0 (49.0 – 109.0)	v_0 [km/s]	185.0	$185.0\,^{+9.0}_{-8.0}\,(^{+19.3}_{-16.0})$	[177.0, 194.0]	[169.0, 204.3]
	v_e [km/s]	269.3	$269.3\,^{+\ 8.8}_{-11.0}\,(^{+17.6}_{-23.1})$	[258.3, 278.1]	[246.2, 286.9]
170.25 (140.25 – 200.25)	v_0 [km/s]	186.0	$186.0\,^{+8.0}_{-9.0}\,(^{+18.0}_{-16.0})$	[177.0, 194.0]	[170.0, 204.0]
	v_e [km/s]	272.6	$273.7\,^{+8.8}_{-9.9}\,(^{+16.8}_{-22.0})$	[263.8, 282.5]	[251.7, 290.5]
261.5 (231.50 – 291.50)	v_0 [km/s]	185.0	$185.0 \pm 9.0\,(^{+19.0}_{-17.0})$	[176.0, 194.0]	[168.0, 204.0]
	v_e [km/s]	257.2	$257.2\,^{+\ 9.9}_{-11.0}\,(^{+18.7}_{-24.2})$	[246.2, 267.1]	[233.0, 275.9]
352.75 (322.75 – 382.75)	v_0 [km/s]	186.0	$186.0 \pm 9.0\,(^{+21.0}_{-17.0})$	[177.0, 195.0]	[169.0, 207.0]
	v_e [km/s]	250.6	$250.6\,^{+\ 9.9}_{-11.0}\,(^{+19.8}_{-25.3})$	[239.6, 260.5]	[225.3, 270.4]
500 total events on average in one observation period of 60 days					

Table A16: The summary of the reconstructed results of the fitting parameters v_0 and v_e as well as their $1(2)\sigma$ statistical uncertainty ranges of the median values by using the simplified velocity distribution $f_{1,\mathrm{sh}}(v; v_0, v_\mathrm{e})$ with 50 (upper) and 500 (lower) total events on average in each 60–day observation period of the normal seasons.

respectively. Besides that the asymmetric periodic variation of the best–fit values of the fitting parameter $v_{\rm e}$ can be seen clearly here, the *invariability* of the best–fit values of v_0 as its annual average value can also be confirmed (see the summary of the reconstructed results and the $1(2)\sigma$ statistical uncertainty ranges of the median values in Table A16).

C.4 With the modified velocity distribution $f_{\rm 1,sh,\Delta v}(v; v_0, \Delta v)$

Finally, as in Sec. 4.3.4, we consider the modified velocity distribution $f_{1,{\rm sh},\Delta v}(v; v_0, \Delta v)$ given by Eq. (28) with v_0 and Δv as two free fitting parameters scanned in the ranges of 80 km/s $\leq v_0 \leq$ 340 km/s (50 events) and 140 km/s $\leq v_0 \leq$ 240 km/s (500 events) as well as -190 km/s $\leq \Delta v \leq$ 230 km/s (50 events) and -20 km/s $\leq \Delta v \leq$ 150 km/s (500 events), respectively.

In Figs. A79 and A80, we show the reconstructed radial distributions of the 3-D WIMP velocity and the $1(2)\sigma$ statistical uncertainty bands by using $f_{1,{\rm sh},\Delta v}(v; v_0, \Delta v)$ as well as the distributions of the fitting parameters v_0 and Δv in all simulated experiments on the $v_0 - \Delta v$ plane with 50 and 500 total events on average in each 60-day observation period of four normal seasons, respectively. Not surprisingly, one can find the asymmetric periodic variation of the best–fit values of the fitting parameter Δv as well as the invariability of the best–fit values of v_0 as its annual average value (see the summary of the reconstructed results and the $1(2)\sigma$ statistical uncertainty ranges of the median values given in Table A17).

D Analytic forms of the shift Maxwellian velocity distribution

In this section, we show the plots of the exact analytic expression of the shift Maxwellian velocity distribution $f_{1,{\rm sh,vesc}}(v)$ given in Eq. (19) and the simplified form $f_{1,{\rm sh}}(v)$ given in Eq. (22). The Galactic escape velocity has been set as $v_{\rm esc} = 500$ km/s in Figs. A81 and raised to $v_{\rm esc} = 600$ km/s in Figs. A82 [64]. Additionally, as a comparison of the shape difference between two expressions, their boundaries due to the annual modulation of the Earth's Galactic velocity $v_{\rm e}(t)$ given by Eq. (21) have also been given.

It can be seen clearly that, with the Galactic escape velocity of $v_{\rm esc} = 500$ km/s, the shape difference between the exact analytic expression of the shift Maxwellian velocity distribution $f_{1,{\rm sh,vesc}}(v)$ and the simplified form $f_{1,{\rm sh}}(v)$ is much smaller than the annual variation of two expressions. This tiny difference can also be neglected compared to the much larger statistical uncertainties on the recorded WIMP events (shown in e.g., Fig. 25). Moreover, once the Galactic escape velocity would be as large as $v_{\rm esc} = 600$ km/s, the tiny shape difference between two expressions could even vanish.

References

[1] G. Jungman, M. Kamionkowski and K. Griest, *"Supersymmetric Dark Matter"*, *Phys. Rep.* **267**, 195–373 (1996), `arXiv:hep-ph/9506380`.

[2] R. J. Gaitskell, *"Direct Detection of Dark Matter"*, *Ann. Rev. Nucl. Part. Sci.* **54**, 315–359 (2004).

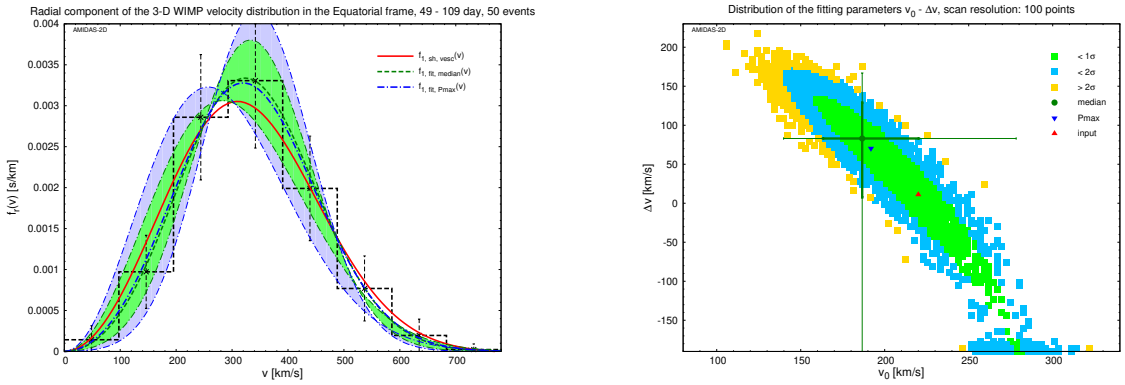

(a) 49.0 – 109.0 day

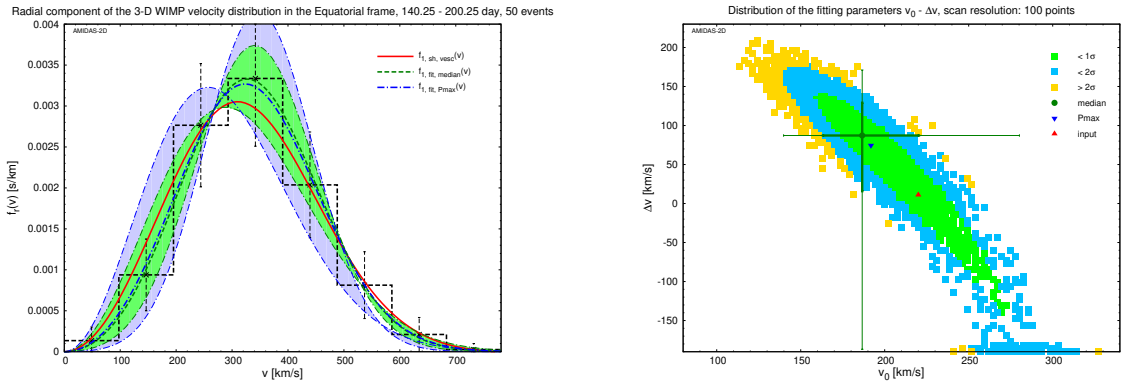

(b) 140.25 – 200.25 day

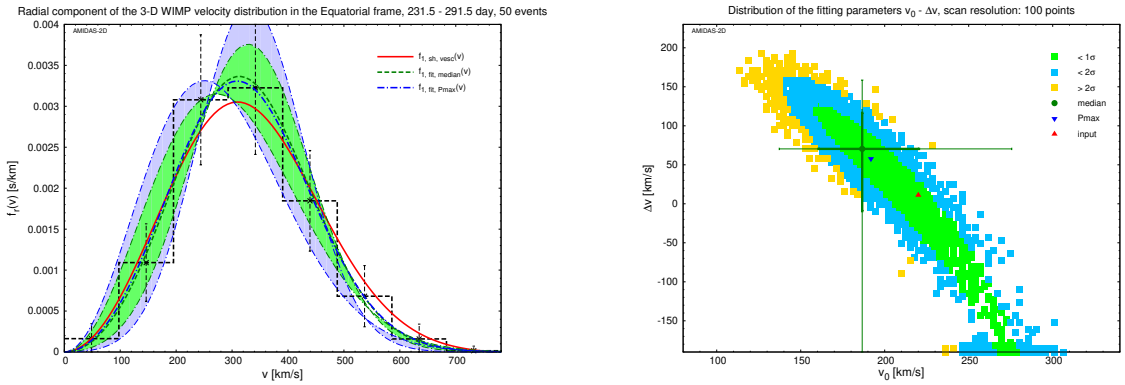

(c) 231.50 – 291.50 day

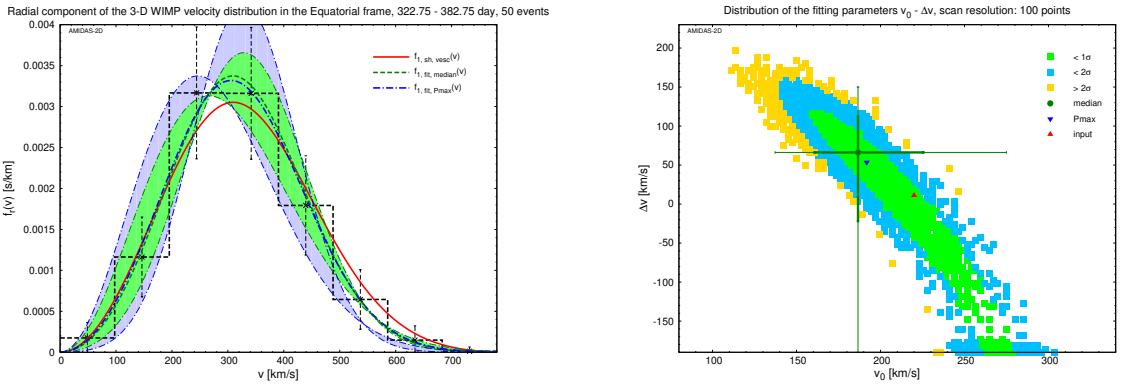

(d) 322.75 – 382.75 day

Figure A79: As in Figs. 33, reconstructed with the modified velocity distribution $f_{1,\mathrm{sh},\Delta v}(v; v_0, \Delta v)$, except that four 60-day observation periods of the normal seasons have been considered.

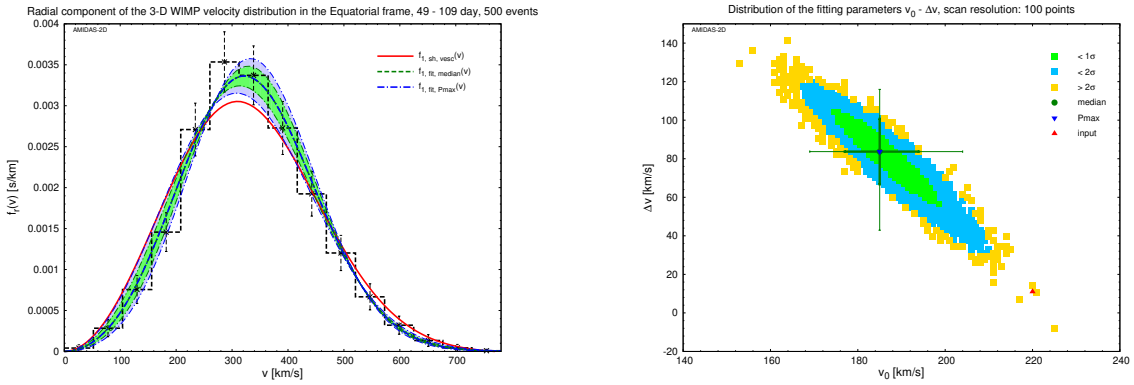

(a) 49.0 – 109.0 day

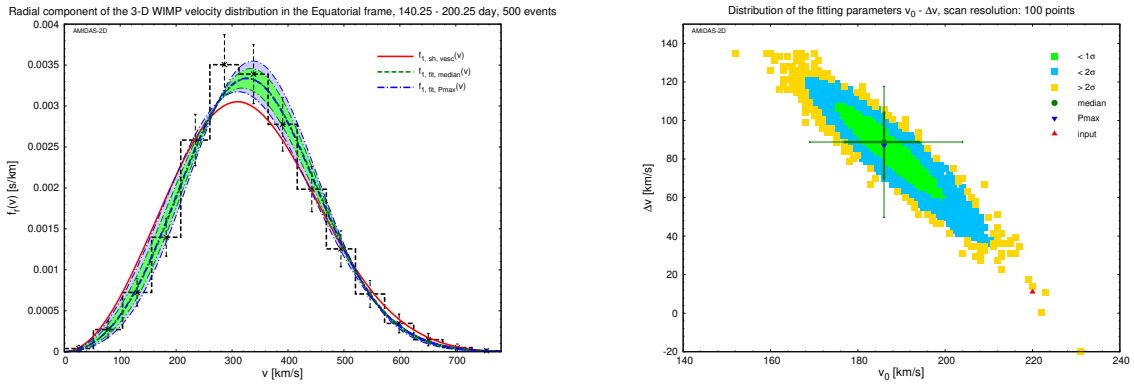

(b) 140.25 – 200.25 day

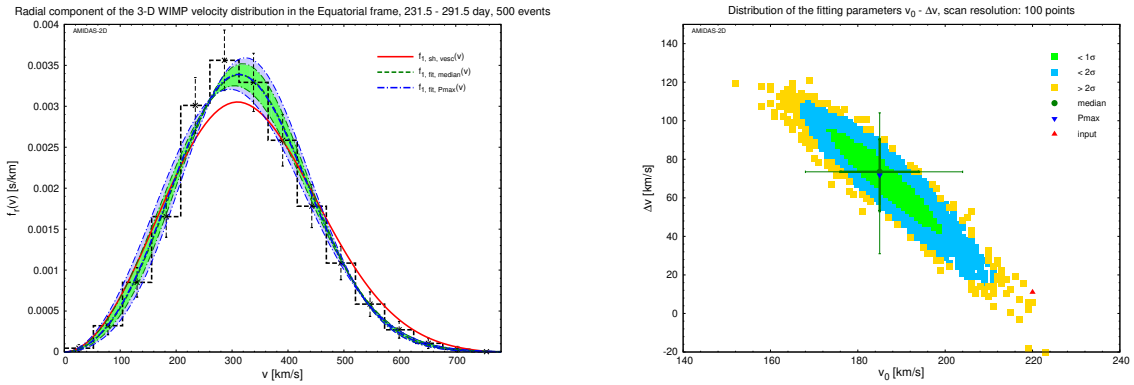

(c) 231.50 – 291.50 day

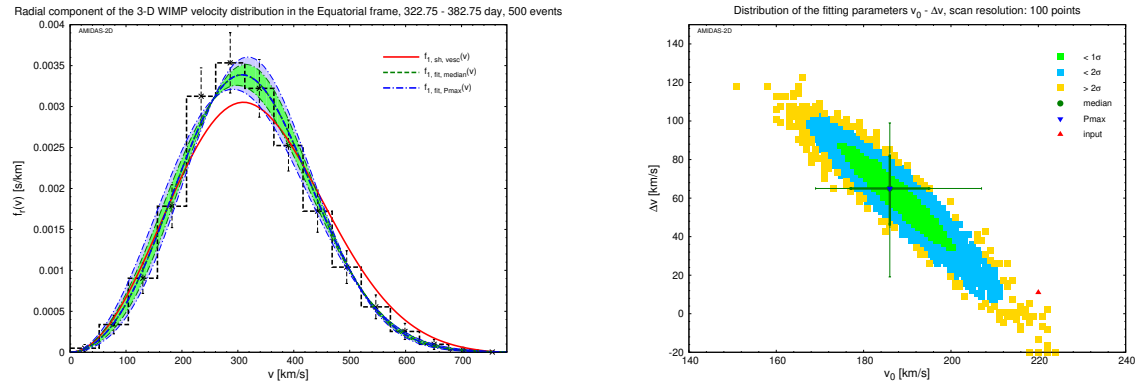

(d) 322.75 – 382.75 day

Figure A80: As in Figs. A79, except that 500 total events on average in one 60-day observation period have been simulated. Remind that the scanning ranges of the fitting parameters v_0 and v_e are shrunk to between 140 km/s and 240 km/s and between -20 km/s and 150 km/s, respectively.

Fitting distribution: modified velocity distribution $f_{1,\mathrm{sh},\Delta v}(v; v_0, \Delta v)$					
Central date (observation period) (day)	Parameter	Max. P_{median}	Median	1σ range	2σ range
79.0 (49.0 – 109.0)	v_0 [km/s]	191.8	$186.6\,^{+36.4}_{-26.0}\,(^{+88.4}_{-46.8})$	[163.2, 220.4]	[139.8, 278.3]
	Δv [km/s]	70.4	$83.0\,^{+46.2}_{-75.6}\,(^{+\ 84.0}_{-273.0})$	[7.4, 129.2]	[−190.0, 167.0]
170.25 (140.25 – 200.25)	v_0 [km/s]	191.8	$186.6\,^{+33.8}_{-23.4}\,(^{+93.6}_{-46.8})$	[163.2, 220.4]	[139.8, 280.2]
	Δv [km/s]	74.6	$87.2\,^{+42.0}_{-71.4}\,(^{+\ 84.0}_{-274.1})$	[15.8, 129.2]	[−186.9, 171.2]
261.5 (231.50 – 291.50)	v_0 [km/s]	191.8	$186.6\,^{+33.8}_{-26.0}\,(^{+89.1}_{-49.4})$	[160.6, 220.4]	[137.2, 275.7]
	Δv [km/s]	57.8	$70.4\,^{+46.2}_{-79.8}\,(^{+\ 88.2}_{-260.4})$	[−9.4, 116.6]	[−190.0, 158.6]
352.75 (322.75 – 382.75)	v_0 [km/s]	191.8	$186.6\,^{+39.0}_{-26.0}\,(^{+88.4}_{-49.4})$	[160.6, 225.6]	[137.2, 275.0]
	Δv [km/s]	53.6	$66.2\,^{+46.2}_{-88.2}\,(^{+\ 84.0}_{-256.2})$	[−22.0, 112.4]	[−190.0, 150.2]
50 total events on average in one observation period of 60 days					

Central date (observation period) (day)	Parameter	Max. P_{median}	Median	1σ range	2σ range
79.0 (49.0 – 109.0)	v_0 [km/s]	185.0	$185.0\,^{+9.0}_{-8.0}\,(^{+19.0}_{-16.0})$	[177.0, 194.0]	[169.0, 204.0]
	Δv [km/s]	83.7	$83.7 \pm 17\,(^{+32.3}_{-40.8})$	[66.7, 100.7]	[42.9, 116.0]
170.25 (140.25 – 200.25)	v_0 [km/s]	186.0	$186.0\,^{+8.0}_{-9.0}\,(^{+18.0}_{-17.0})$	[177.0, 194.0]	[169.0, 204.0]
	Δv [km/s]	87.1	$88.8\,^{+15.3}_{-18.7}\,(^{+28.9}_{-39.1})$	[70.1, 104.1]	[49.7, 117.7]
261.5 (231.50 – 291.50)	v_0 [km/s]	185.0	$185.0 \pm 9.0\,(^{+19.0}_{-17.0})$	[176.0, 194.0]	[168.0, 204.0]
	Δv [km/s]	71.8	$73.5\,^{+17.0}_{-20.4}\,(^{+30.6}_{-42.5})$	[53.1, 90.5]	[31.0, 104.1]
352.75 (322.75 – 382.75)	v_0 [km/s]	186.0	$186.0 \pm 9.0\,(^{+21.0}_{-17.0})$	[177.0, 195.0]	[169.0, 207.0]
	Δv [km/s]	65.0	$65.0\,^{+17.0}_{-18.7}\,(^{+34.0}_{-45.9})$	[46.3, 82.0]	[19.1, 99.0]
500 total events on average in one observation period of 60 days					

Table A17: The summary of the reconstructed results of the fitting parameters v_0 and Δv as well as their $1(2)\sigma$ statistical uncertainty ranges of the median values by using the modified velocity distribution $f_{1,\mathrm{sh},\Delta v}(v; v_0, \Delta v)$ with 50 (upper) and 500 (lower) total events on average in each 60–day observation period of the normal seasons.

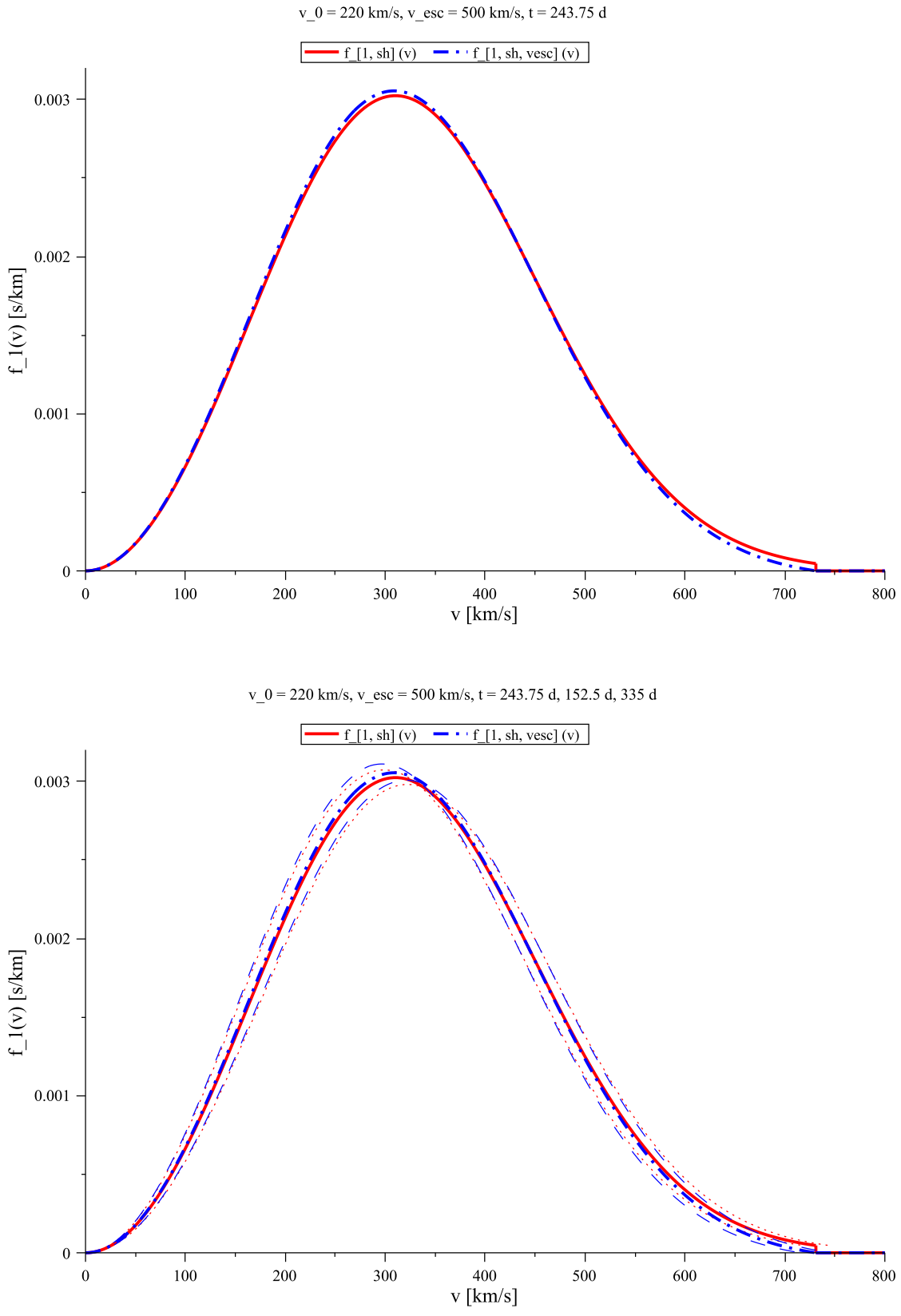

Figure A81: The exact analytic form of the shift Maxwellian velocity distribution $f_{1,\mathrm{sh,vesc}}(v)$ given in Eq. (19) (dash–dotted blue) and the simplified form $f_{1,\mathrm{sh}}(v)$ given in Eq. (22) (solid red) with the Galactic escape velocity of $v_{\mathrm{esc}} = 500$ km/s. In the lower frame, the boundaries of two velocity distributions due to the annual modulation of the Earth's Galactic velocity $v_{\mathrm{e}}(t)$ given by Eq. (21) have been additionally given as the dashed blue and the dotted red curves for the exact and the simplified expressions, respectively.

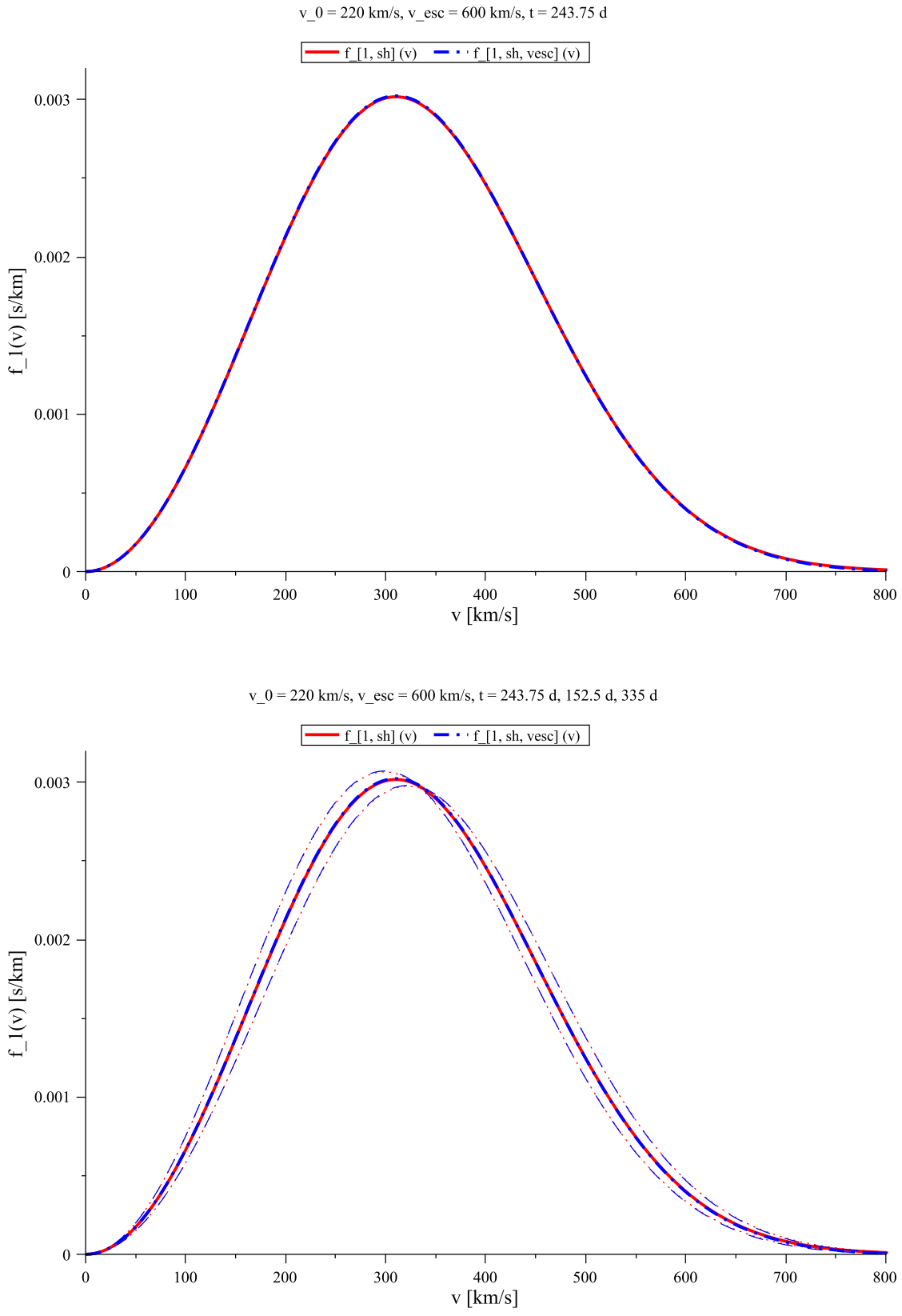

Figure A82: As in Figs. A81, except that the Galactic escape velocity has been raised to $v_{\rm esc} = 600$ km/s.

[3] L. Baudis, *"Direct Dark Matter Detection: the Next Decade"*, Issue on *"The Next Decade in Dark Matter and Dark Energy"*, *Phys. Dark Univ.* **1**, 94–108 (2012), arXiv:1211.7222 [astro-ph.IM].

[4] L. Baudis, *"Dark Matter Searches"*, *Annalen Phys.* **528**, 74–83 (2016), arXiv:1509.00869 [astro-ph.CO].

[5] M. Drees and G. Gerbier, contribution to *"The Review of Particle Physics 2018"*, *Phys. Rev.* **D98**, 030001 (2018), *26. Dark Matter.*

[6] M. Schumann, *"Direct Detection of WIMP Dark Matter: Concepts and Status"*, *J. Phys.* **G46**, 103003 (2019), arXiv:1903.03026 [astro-ph.CO].

[7] S. Ahlen *et al.*, *"The Case for a Directional Dark Matter Detector and the Status of Current Experimental Efforts"*, *Int. J. Mod. Phys.* **A25**, 1–51 (2010), arXiv:0911.0323 [astro-ph.CO].

[8] F. Mayet, J. Billard and D. Santos, *"Directional Detection of Dark Matter"*, *EAS Publ. Ser.* **53**, 3–10 (2012), arXiv:1110.1056 [astro-ph.IM].

[9] S. E. Vahsen *et al.*, *"3-D Tracking in a Miniature Time Projection Chamber"*, *Nucl. Instrum. Meth.* **A788**, 95–105 (2015), arXiv:1407.7013 [physics.ins-det].

[10] N. S. Phan, R. J. Lauer, E. R. Lee, D. Loomba, J. A. J. Matthews and E. H. Miller, *"GEM–Based TPC with CCD Imaging for Directional Dark Matter Detection"*, *Astropart. Phys.* **84**, 82–96 (2016), arXiv:1510.02170 [physics.ins-det].

[11] F. Mayet *et al.*, *"A Review of the Discovery Reach of Directional Dark Matter Detection"*, *Phys. Rept.* **627**, 1–49 (2016), arXiv:1602.03781 [astro-ph.CO].

[12] Y. Hochberg, Y. Kahn, M. Lisanti, C. G. Tully and K. M. Zurek, *"Directional Detection of Dark Matter with Two–Dimensional Targets"*, *Phys. Lett.* **B772**, 239–246 (2017), arXiv:1606.08849 [hep-ph].

[13] J. B. R. Battat *et al.*, *"Readout Technologies for Directional WIMP Dark Matter Detection"*, *Phys. Rept.* **662**, 1–46 (2016), arXiv:1610.02396 [physics.ins-det].

[14] DRIFT–III,
see https://web.archive.org/web/20130713090725/http://driftdarkmatter.org/.

[15] DRIFT Collab., S. Burgos *et al.*, *"Studies of Neutron Detection and Backgrounds with the DRIFT–IIa Dark Matter Detector"*, *Astropart. Phys.* **28**, 409–421 (2007), arXiv:0707.1488 [hep-ex].

[16] DRIFT Collab., S. Burgos *et al.*, *"First Measurement of the Head–Tail Directional Nuclear Recoil Signature at Energies Relevant to WIMP Dark Matter Searches"*, *Astropart. Phys.* **31**, 261–266 (2009), arXiv:0809.1831 [astro-ph].

[17] P. Majewski, D. Muna, D. P. Snowden-Ifft, N. J. C. Spooner, *"Simulations of the Nuclear Recoil Head–Tail Signature in Gases Relevant to Directional Dark Matter Searches"*, *Astropart. Phys.* **34**, 284–292 (2010), arXiv:0902.4430 [physics.ins-det].

[18] DRIFT Collab., J. B. R. Battat *et al.*, *"First Background–Free Limit from a Directional Dark Matter Experiment: Results from a Fully Fiducialised DRIFT Detector"*, *Phys. Dark Univ.* **9–10**, 1–7 (2015), arXiv:1410.7821 [hep-ex].

[19] DRIFT Collab., J. B. R. Battat *et al.*, *"First Measurement of Nuclear Recoil Head–Tail Sense in a Fiducialised WIMP Dark Matter Detector"*, *J. Inst.* **11**, P10019 (2016), arXiv:1606.05364 [physics.ins-det].

[20] DRIFT Collab., J. B. R. Battat *et al.*, *"Low Threshold Results and Limits from the DRIFT Directional Dark Matter Detector"*, *Astropart. Phys.* **91**, 65–74 (2017), arXiv:1701.00171 [astro-ph.IM].

[21] DRIFT Collab., J. B. R. Battat *et al.*, *"Measurement of Directional Range Components of Nuclear Recoil Tracks in a Fiducialised Dark Matter Detector"*, *J. Inst.* **12**, P10009 (2017), arXiv:1707.09431 [physics.ins-det].

[22] MIMAC Collaboration, see http://lpsc.in2p3.fr/mimac/.

[23] E. Moulin and D. Santos, *"MIMAC–He3, A Project for a Micro–TPC Matrix of Chambers of Helium 3 for Axial Direct Detection of Non–Baryonic Dark Matter"*, arXiv:astro-ph/0505458 (2005).

[24] D. Santos *et al.*, *"MIMAC–He3: MIcro–tpc MAtrix of Chambers of He3"*, arXiv:astro-ph/0701230 (2007).

[25] F. Mayet *et al.*, *"Micromegas μTPC for Direct Dark Matter Search with MIMAC"*, *J. Phys.: Conf. Ser.* **179**, 012011 (2009), arXiv:0905.4654 [astro-ph.CO].

[26] D. Santos *et al.*, *"MIMAC: A Micro–TPC Matrix for Directional Detection of Dark Matter"*, *PoS* **IDM2010**, 041 (2010), arXiv:1012.1166 [astro-ph.IM].

[27] J. Billard, F. Mayet and D. Santos, *"Three–Dimensional Track Reconstruction for Directional Dark Matter Detection"*, *J. Cosmol. Astropart. Phys.* **1204**, 006 (2012), arXiv:1202.3372 [astro-ph.IM].

[28] Q. Riffard *et al.*, *"MIMAC Low Energy Electron–Recoil Discrimination Measured with Fast Neutrons"*, *J. Inst.* **11**, P08011 (2016), arXiv:1602.01738 [astro-ph.IM].

[29] Y. Tao *et al.*, *"Angular Resolution of the MIMAC Dark Matter Directional Detector"*, arXiv:1903.02159 [physics.ins-det] (2019).

[30] K. Miuchi *et al.*, *"First Underground Results with NEWAGE-0.3a Direction–Sensitive Dark Matter Detector"*, *Phys. Lett.* **B686**, 11–17 (2010), arXiv:1002.1794 [astro-ph.CO].

[31] K. Miuchi *et al.*, *"NEWAGE"*, *EAS Publ. Ser.* **53**, 33–41 (2012), arXiv:1109.3099 [astro-ph.IM].

[32] K. Nakamura *et al.*, *"Direction–Sensitive Dark Matter Search with Gaseous Tracking Detector NEWAGE-0.3b"*, *Prog. Theor. Exp. Phys.* **2015**, 043F01 (2015).

[33] DMTPC Collaboration, see http://dmtpc.mit.edu/.

[34] DMTPC Collab., D. Dujmic *et al.*, *"Charge Amplification Concepts for Direction–Sensitive Dark Matter Detectors"*, *Astropart. Phys.* **30**, 58–64 (2008), arXiv:0804.4827 [astro-ph].

[35] G. Sciolla, *"Directional detection of Dark Matter"*, *Mod. Phys. Lett.* **A24**, 1793–1809 (2009), arXiv:0811.2764 [astro-ph].

[36] G. Sciolla and C. J. Martoff, *"Gaseous Dark Matter Detectors"*, *New J. Phys.* **11**, 105018 (2009), arXiv:0905.3675 [astro-ph.IM].

[37] DMTPC Collab., S. Ahlen *et al.*, *"First Dark Matter Search Results from a Surface Run of the 10-L DMTPC Directional Dark Matter Detector"*, *Phys. Lett.* **B695**, 124–129 (2011), arXiv:1006.2928 [hep-ex].

[38] C. Deaconu, G. Druitt, R. Eggleston, P. Fisher, J. Lopez, J. Monroe, H. Tomita and E. Zayas, *"Track Reconstruction Progress from the DMTPC Directional Dark Matter Experiment"*, *Phys. Procedia* **61**, 39–44 (2015).

[39] C. Deaconu *et al.*, *"Measurement of the Directional Sensitivity of DMTPC Detectors"*, *Phys. Rev.* **D95**, 122002 (2017), arXiv:1705.05965 [astro-ph.IM].

[40] S. E. Vahsen *et al.*, *"The Directional Dark Matter Detector (D^3)"*, *EAS Publ. Ser.* **53**, 43–50 (2012), arXiv:1110.3401 [astro-ph.IM].

[41] S. Ross, on behalf of the D^3 Collab., *"Recent Progress on D^3 – The Directional Dark Matter Detector"*, arXiv:1402.0043 [physics.ins-det] (2014).

[42] T. Naka *et al.*, *"R&D Status of Nuclear Emulsion for Directional Dark Matter Search"*, *EAS Publ. Ser.* **53**, 51–58 (2012), arXiv:1109.4485 [astro-ph.IM].

[43] NEWS Collab., A. Aleksandrov *et al.*, *"NEWS: Nuclear Emulsions for WIMP Search"*, arXiv:1604.04199 [astro-ph.IM] (2016).

[44] NEWSdm Collab., N. Agafonova *et al.*, *"Discovery Potential for Directional Dark Matter Detection with Nuclear Emulsions"*, *J. Phys.: Conf. Ser.* **869**, 012048 (2017), arXiv:1705.00613 [physics.ins-det].

[45] CYGNUS homepage: https://web.infn.it/cygnus/.

[46] P. Gondolo, *"Recoil Momentum Spectrum in Directional Dark Matter Detectors"*, *Phys. Rev.* **D66**, 103513 (2002), arXiv:hep-ph/0209110.

[47] M. S. Alenazi and P. Gondolo, *"Directional Recoil Rates for WIMP Direct Detection"*, *Phys. Rev.* **D77**, 043532 (2008), arXiv:0712.0053 [astro-ph].

[48] N. Bozorgnia, G. B. Gelmini and P. Gondolo, *"Ring–Like Features in Directional Dark Matter Detection"*, *J. Cosmol. Astropart. Phys.* **1206**, 037 (2012), arXiv:1111.6361 [astro-ph.CO].

[49] N. Bozorgnia, G. B. Gelmini and P. Gondolo, *"Aberration Features in Directional Dark Matter Detection"*, *J. Cosmol. Astropart. Phys.* **1208**, 011 (2012), arXiv:1205.2333 [astro-ph.CO].

[50] B. Morgan, A. M. Green and N. J. C. Spooner, *"Directional Statistics for (Realistic) WIMP Direct Detection"*, *Phys. Rev.* **D71**, 103507 (2005), arXiv:astro-ph/0408047.

[51] B. Morgan and A. M. Green, *"Directional Statistics for WIMP Direct Detection II. 2–D Read–Out"*, *Phys. Rev.* **D72**, 123501 (2005), arXiv:astro-ph/0508134.

[52] C. A. J. O'Hare and A. M. Green, *"Directional Detection of Dark Matter Streams"*, *Phys. Rev.* **D90**, 123511 (2014), arXiv:1410.2749 [astro-ph.CO].

[53] B. J. Kavanagh, *"Discretising the Velocity Distribution for Directional Dark Matter Experiments"*, *J. Cosmol. Astropart. Phys.* **1507**, 019 (2015), arXiv:1502.04224 [hep-ph].

[54] C. A. J. O'Hare, A. M. Green, J. Billard, E. Figueroa–Feliciano and L. E. Strigari, *"Readout Strategies for Directional Dark Matter Detection beyond the Neutrino Background"*, *Phys. Rev.* **D92**, 063518 (2015), arXiv:1505.08061 [astro-ph.CO].

[55] B. J. Kavanagh and C. A. J. O'Hare, *"Reconstructing the Three–Dimensional Local Dark Matter Velocity Distribution"*, *Phys. Rev.* **D94**, 123009 (2016), arXiv:1609.08630 [astro-ph.CO].

[56] C. A. J. O'Hare, B. J. Kavanagh and A. M. Green, *"Time–Integrated Directional Detection of Dark Matter"*, *Phys. Rev.* **D96**, 083011 (2017), arXiv:1708.02959 [astro-ph.CO].

[57] J. Billard, F. Mayet, J. F. Macias–Perez and D. Santos, *"Directional Detection as a Strategy to Discover Galactic Dark Matter"*, *Phys. Lett.* **B691**, 156–162 (2010), arXiv:0911.4086 [astro-ph.CO].

[58] J. Billard, F. Mayet and D. Santos, *"Exclusion Limits from Data of Directional Dark Matter Detectors"*, *Phys. Rev.* **D82**, 055011 (2010), arXiv:1006.3513 [astro-ph.CO].

[59] J. Billard, F. Mayet and D. Santos, *"A Markov Chain Monte Carlo Analysis to Constrain Dark Matter Properties with Directional Detection"*, *Phys. Rev.* **D83**, 075002 (2011), arXiv:1012.3960 [astro-ph.CO].

[60] S. K. Lee and A. H. G. Peter, *"Probing the Local Velocity Distribution of WIMP Dark Matter with Directional Detectors"*, *J. Cosmol. Astropart. Phys.* **1204**, 029 (2012), arXiv:1202.5035 [astro-ph.CO].

[61] S. K. Lee, *"Harmonics in the Dark–Matter Sky: Directional Detection in the Fourier–Bessel Basis"*, *J. Cosmol. Astropart. Phys.* **1403**, 047 (2014), arXiv:1401.6179 [astro-ph.CO].

[62] https://en.wikipedia.org/wiki/Galactic_coordinate_system.

[63] A. Bandyopadhyay and D. Majumdar, *"On Diurnal and Annual Variations of Directional Detection Rates of Dark Matter"*, *Astrophys. J.* **746**, 107 (2012), arXiv:1006.3231 [hep-ph].

[64] M. Tanabashi *et al.* (Particle Data Group), *"The Review of Particle Physics 2018"*, *Phys. Rev.* **D98**, 030001 (2018), *2. Astrophysical Constants and Parameters.*

[65] K. Freese, J. Frieman and A. Gould, *"Signal Modulation in Cold–Dark–Matter Detection"*, *Phys. Rev.* **D37**, 3388–3405 (1988).

[66] G. D'Agostini, *"Probability and Measurement Uncertainty in Physics: A Bayesian Primer"*, `arXiv:hep-ph/9512295` (1995).

[67] J. D. Lewin and P. F. Smith, *"Review of Mathematics, Numerical Factors, and Corrections for Dark Matter Experiments Based on Elastic Nuclear Recoil"*, *Astropart. Phys.* **6**, 87–112 (1996).

[68] C.-L. Shan, *"Bayesian Reconstruction of the Velocity Distribution of Weakly Interacting Massive Particles from Direct Dark Matter Detection Data"*, *J. Cosmol. Astropart. Phys.* **1408**, 009 (2014), `arXiv:1403.5610 [astro-ph.HE]`.